

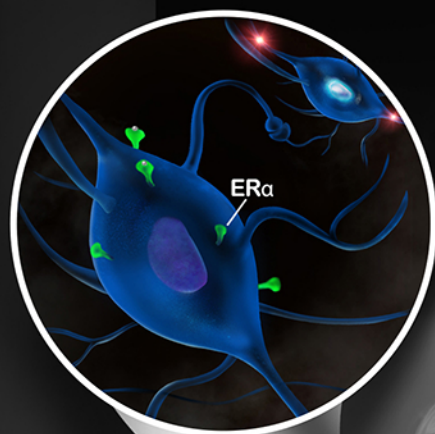
# Neuroscience Bulletin

The Official Journal of the Chinese Neuroscience Society

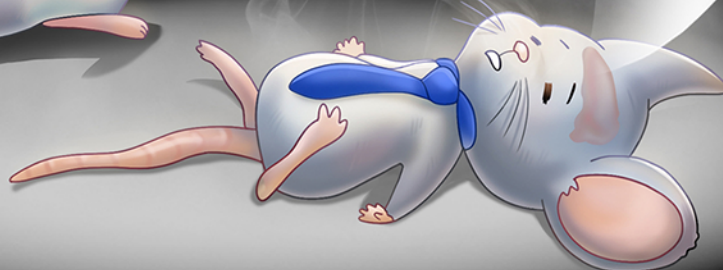
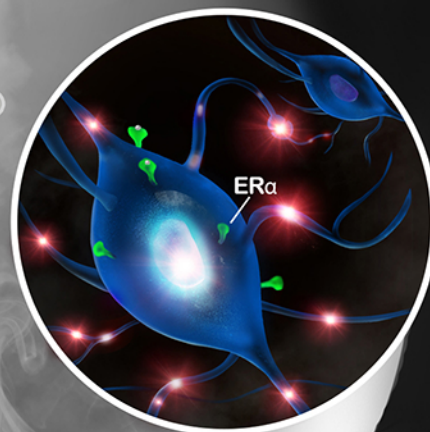
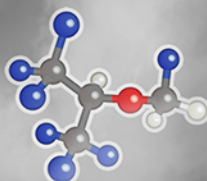
神经科学通报

Volume 38  
Number 7  
July 2022

## ER $\alpha$ in MPA Contributes to Sex Difference of Sevoflurane Anesthesia



SEVO



Springer

[www.neurosci.cn](http://www.neurosci.cn)

## About the Cover

Sex differences in response to general anesthesia have been reported previously, but the underlying neural mechanism remained unknown. In the current study, male mice were confirmed to be more sensitive to sevoflurane than females. This sex difference was mediated by estrogen receptor  $\alpha$  (ER $\alpha$ ) on GABAergic neurons in the medial preoptic area (MPA) of males. ER $\alpha$  signaling stimulated the GABAergic MPA neurons in males but had no effect on that in females. The activation of GABAergic neurons exerted an inhibitory effect on neural networks that, in turn, facilitated the anesthesia process. In the cover image, the female mouse is fighting against sevoflurane anesthesia, while the male mouse has already fallen asleep. In the brain, ER $\alpha$  has ignited the MPA GABAergic neurons in the male mouse, but in the female, the GABAergic neurons keep silent. See pages 703–719. (Cover provided by Dr. Hailong Dong)

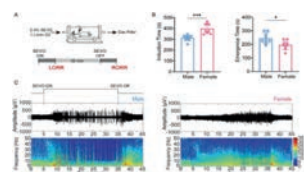


Volume 38 Number 7  
July 2022

## Original Articles

### 703 Estrogen Receptor-A in Medial Preoptic Area Contributes to Sex Difference of Mice in Response to Sevoflurane Anesthesia

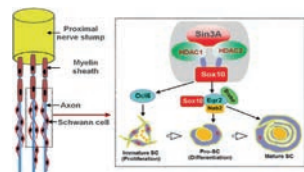
Yunyun Zhang · Huiming Li · Xinxin Zhang · Sa Wang ·  
Dan Wang · Jiajia Wang · Tingting Tong · Zhen Zhang ·  
Qianzi Yang · Hailong Dong



p 708

### 720 Transcriptome Analysis of Schwann Cells at Various Stages of Myelination Implicates Chromatin Regulator Sin3A in Control of Myelination Identity

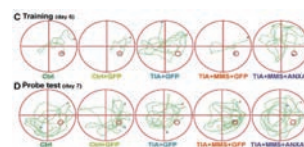
Bin Zhang · Wenfeng Su · Junxia Hu · Jinghui Xu ·  
Parizat Askar · Shuangxi Bao · Songlin Zhou · Gang Chen ·  
Yun Gu



p 738

### 741 Formation of the Looming-evoked Innate Defensive Response during Postnatal Development in Mice

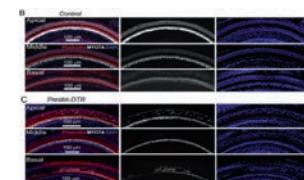
Shanping Chen · Huiying Tan · Zhijie Wang · Yu-ting Tseng ·  
Xiaotao Li · Liping Wang



p 765

### 753 Multiple Mild Stimulations Reduce Membrane Distribution of CX3CR1 Promoted by Annexin a1 in Microglia to Attenuate Excessive Dendritic Spine Pruning and Cognitive Deficits Caused by a Transient Ischemic Attack in Mice

Lu Zheng · Yi Wang · Bin Shao · Huijuan Zhou · Xing Li ·  
Cai Zhang · Ning Sun · Jing Shi



p 780

**769 Prestin-Mediated Frequency Selectivity Does not Cover Ultrahigh Frequencies in Mice**

Jie Li · Shuang Liu · Chenmeng Song · Tong Zhu · Zhikai Zhao · Wenzhi Sun · Yi Wang · Lei Song · Wei Xiong

**785 Cross-Modal Interaction and Integration Through Stimulus-Specific Adaptation in the Thalamic Reticular Nucleus of Rats**

Yumei Gong · Yuying Zhai · Xinyu Du · Peirun Song · Haoxuan Xu · Qichen Zhang · Xiongjie Yu

## Reviews

**796 From Parametric Representation to Dynamical System: Shifting Views of the Motor Cortex in Motor Control**

Tianwei Wang · Yun Chen · He Cui

**809 Factors Influencing Alzheimer's Disease Risk: Whether and How They are Related to the APOE Genotype**

Rong Zhang · Xiaojiao Xu · Hang Yu · Xiaolan Xu · Manli Wang · Weidong Le

## Insights

**820 Induced Dopaminergic Neurons for Parkinson's Disease Therapy: Targeting the Striatum or Midbrain/Substantia Nigra Pars Compacta?**

Huadong Xu · Xu Cheng · Qian Song · Yuxin Yang · Changhe Wang · Xinjiang Kang

**825 Expanding Views of Mitochondria in Parkinson's Disease: Focusing on *PINK1* and *GBA1* Mutations**

Yu Yuan · Xizhen Ma · Ning Song · Junxia Xie

**829 The Mechanism for Allocating Limited Working Memory Resources in Multitasking**

Lu Gan · Jinglong Wu · Ji Dai · Shintaro Funahashi

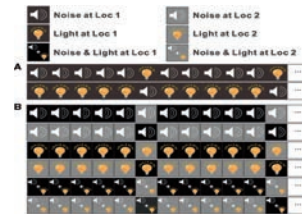
## Research Highlights

**834 Getting a Sense of ATP in Real Time**

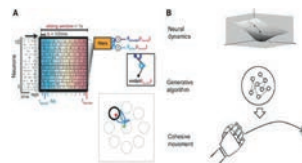
Anthony D. Umpierre · Koichiro Haruwaka · Long-Jun Wu

**837 Fundamental Neurocircuit of Anti-inflammatory Effect by Electroacupuncture Stimulation Identified**

Jiayu Hu · Wanye Hu · Lusheng Tang · Ying Wang



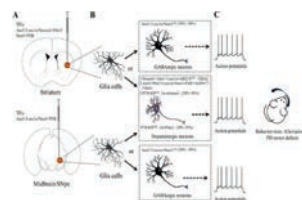
p 787



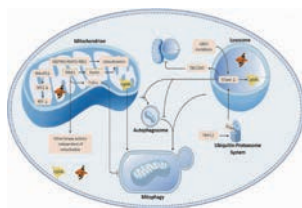
p 805



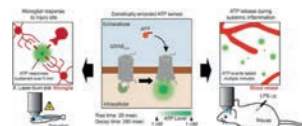
p 811



p 822



p 827



p 835



# Neuroscience Bulletin

## Copyright Information

### *For Authors*

As soon as an article is accepted for publication, authors will be requested to assign copyright of the article (or to grant exclusive publication and dissemination rights) to the publisher (respective the owner if other than Springer Nature). This will ensure the widest possible protection and dissemination of information under copyright laws.

More information about copyright regulations for this journal is available at [www.springer.com/12264](http://www.springer.com/12264)

### *For Readers*

While the advice and information in this journal is believed to be true and accurate at the date of its publication, neither the authors, the editors, nor the publisher can accept any legal responsibility for any errors or omissions that may have been made. The publisher makes no warranty, express or implied, with respect to the material contained herein.

All articles published in this journal are protected by copyright, which covers the exclusive rights to reproduce and distribute the article (e.g., as offprints), as well as all translation rights. No material published in this journal may be reproduced photographically or stored on microfilm, in electronic data bases, on video disks, etc., without first obtaining written permission from the publisher (respective the copyright owner if other than Springer Nature). The use of general descriptive names, trade names, trademarks, etc., in this publication, even if not specifically identified, does not imply that these names are not protected by the relevant laws and regulations.

Springer Nature has partnered with Copyright Clearance Center's RightsLink service to offer a variety of options for reusing Springer Nature content. For permission to reuse our content please locate the material that you wish to use on [link.springer.com](http://link.springer.com) or on [springerimages.com](http://springerimages.com) and click on the permissions link or go to [copyright.com](http://copyright.com) and enter the title of the publication that you wish to use. For assistance in placing a permission request, Copyright Clearance Center can be contacted directly via phone: +1-855-239-3415, fax: +1-978-646-8600, or e-mail: [info@copyright.com](mailto:info@copyright.com)

© Center for Excellence in Brain Science  
and Intelligence Technology, CAS 2022

## Journal Website

[www.springer.com/12264](http://www.springer.com/12264)

For the actual version of record please always check the online version of the publication.

## Subscription Information

Volume 38 (12 issues) will be published in 2022.

ISSN: 1673-7067 print

ISSN: 1995-8218 electronic

For information on subscription rates please contact Springer Nature Customer Service Center: [customerservice@springernature.com](mailto:customerservice@springernature.com)

The Americas (North, South, Central America and the Caribbean)  
Springer Nature Journal Fulfillment,  
Harborside Plaza II,  
200 Hudson Street, Jersey City,  
NJ 07302, USA  
Tel. 800-SPRINGER (777-4643);  
212-460-1500 (outside  
North America)

Outside the Americas

Springer Nature Customer Service  
Center GmbH, Tiergartenstr. 15,  
69121 Heidelberg, Germany  
Tel.: +49-6221-345-4303

## Advertisements

E-mail contact: [advertising@springer.com](mailto:advertising@springer.com) or [anzeigen@springer.com](mailto:anzeigen@springer.com) (Germany)

## Disclaimer

Springer Nature publishes advertisements in this journal in reliance upon the responsibility of the advertiser to comply with all legal requirements relating to the marketing and sale of products or services advertised. Springer Nature and the editors are not responsible for claims made in the advertisements published in the journal. The appearance of advertisements in Springer Nature publications does not constitute endorsement, implied or intended, of the product advertised or the claims made for it by the advertiser.

## Office of Publication

Springer Nature Singapore Pte Ltd.  
152 Beach Road, #21-01/04  
Gateway East, Singapore 189721,  
Singapore



# Estrogen Receptor- $\alpha$ in Medial Preoptic Area Contributes to Sex Difference of Mice in Response to Sevoflurane Anesthesia

Yunyun Zhang<sup>1</sup> · Huiming Li<sup>1</sup> · Xinxin Zhang<sup>1</sup> · Sa Wang<sup>1</sup> · Dan Wang<sup>1</sup> ·  
Jiajia Wang<sup>1</sup> · Tingting Tong<sup>1</sup> · Zhen Zhang<sup>1</sup> · Qianzi Yang<sup>1</sup> · Hailong Dong<sup>1</sup>

Received: 13 October 2021 / Accepted: 20 December 2021 / Published online: 17 February 2022  
© The Author(s) 2022

**Abstract** A growing number of studies have identified sex differences in response to general anesthesia; however, the underlying neural mechanisms are unclear. The medial preoptic area (MPA), an important sexually dimorphic structure and a critical hub for regulating consciousness transition, is enriched with estrogen receptor  $\alpha$  (ER $\alpha$ ), particularly in neuronal clusters that participate in regulating sleep. We found that male mice were more sensitive to sevoflurane. Pharmacological inhibition of ER $\alpha$  in the MPA abolished the sex differences in sevoflurane anesthesia, in particular by extending the induction time and facilitating emergence in males but not in females. Suppression of ER $\alpha$  *in vitro* inhibited GABAergic and glutamatergic neurons of the MPA in males but not in females. Furthermore, ER $\alpha$  knockdown in GABAergic neurons of the male MPA was sufficient to eliminate sex differences during sevoflurane anesthesia. Collectively, MPA ER $\alpha$  positively regulates the activity of MPA GABAergic neurons in males but not in females, which contributes to the sex difference of mice in sevoflurane anesthesia.

**Keywords** Sex difference · Anesthesia · Estrogen receptor  $\alpha$  · Medial preoptic area · Sevoflurane

## Introduction

General anesthesia, with the features of unconsciousness, analgesia, amnesia, and immobility, has been widely used in surgery for more than 170 years. However, the underlying mechanisms remain largely unknown. Accumulating evidence has shown that unconsciousness induced by general anesthetics shares the neural pathway with sleep [1], and many sleep-related nuclei and networks have been reported to be involved in anesthesia [2–4]. However, in both basic and clinical research, females have been primarily excluded for a long time because of the confounding variables of breeding, pregnancy, and hormonal fluctuations that are characteristic of this sex. Considering that half of the surgical population is female, the exclusion of this sex from anesthesia-related studies has produced a huge knowledge gap from the literature to the clinic.

In the past decade, a small but growing number of investigations have been focused on sex differences in response to general anesthesia [5–13]. Some clinical studies have demonstrated that women require a higher propofol infusion rate to maintain general anesthesia [5] and spend less time emerging from anesthesia than men do [6–8]. However, Kodaka *et al.* [9] reported that there was no difference in the minimum alveolar anesthetic concentration (MAC) requirement or bispectral index (BIS) value at loss of consciousness between men and women for sevoflurane anesthesia. A few basic studies with rodent models have reported that male rats require larger doses of anesthetics to produce general anesthesia [10, 11] and

Yunyun Zhang and Huiming Li have contributed equally to this work.

**Supplementary Information** The online version contains supplementary material available at <https://doi.org/10.1007/s12264-022-00825-w>.

✉ Qianzi Yang  
qianziyang@hotmail.com

✉ Hailong Dong  
hldong6@hotmail.com

<sup>1</sup> Department of Anesthesiology and Perioperative Medicine, Xijing Hospital, The Fourth Military Medical University, Xi'an 710032, China

emerge faster from a single intraperitoneal injection of propofol than female rats [12]. The discrepancy in previous studies has not yet provided a clear view of sex differences in general anesthesia. Nevertheless, the traditional explanations for the previously reported sex differences in clinical anesthetic effects involve sex-specific pharmacokinetic disparities [14–20] and hormonal differences [10, 21–28]. Whether gender-related neural mechanisms contribute to sex-specific responses to general anesthetics remains unclear.

The preoptic area (POA), one of the most celebrated sexually dimorphic structures [29–31], is enriched with estrogen receptor alpha ( $ER\alpha$ , gene *ESR1*) [32, 33].  $ER\alpha$  expression in the POA has a sex preference, and its expression is higher in females than in males [34]. The POA has also been identified as a critical hub for sleep generation. Inhibitory neurons in the POA, such as GABAergic [35] neurons, have sleep-promoting and sleep-active features and project inhibitory innervation to the arousal-promoting systems [36, 37]. In contrast, excitatory glutamatergic neurons in the POA promote wakefulness [38]. Single-cell RNA sequencing of the POA has revealed that *ESR1* is densely co-expressed in neuronal clusters that participate in regulating sleep-wakefulness [33]. The anesthesia-regulatory role of POA has been identified in the presence of dexmedetomidine [39], propofol [40, 41], and volatile anesthetics [4]. Therefore, the POA offers a potential target for coding sex differences in general anesthesia.

In the current study, we aimed to examine sex-specific differences in the murine response to sevoflurane. Considering that  $ER\alpha$  is expressed most densely in the medial POA (MPA) in both male and female mice [32, 33], the pharmacological technique, patch-clamp recordings, and short-hairpin RNA knockdown were applied to further investigate the role of MPA  $ER\alpha$  in sevoflurane anesthesia in both sexes in an attempt to partially explain the sex differences in the response to sevoflurane anesthesia.

## Materials and Methods

### Animals

C57BL/6J mice used in this study were purchased from the Beijing Vital River Laboratory Animal Technology Co., Ltd. *Vglut2-ires-Cre* (Stock No. 028863; Jackson Laboratories, Bar Harbor, ME, USA) or *Vgat-ires-Cre* mice (Stock No. 028862; Jackson Laboratories, Bar Harbor, ME, USA) were crossed with Cre-dependent tdTomato reporter knock-in mice (B-tdTomato cKI mice, provided by Beijing Biocytogen Inc.) to generate mice expressing red fluorescence in the major subset of glutamatergic (Vglut2-

TdTomato mice) or GABAergic (Vgat-tdTomato mice) neurons. Mice were housed at 18–23°C with 38%–42% humidity in a 12-h light–dark cycle (lights on 07:00–19:00) with free access to food and water. All experiments were performed on age-matched (8–12 weeks old) adult male (24–27 g) and female (22–25 g) mice during the light cycle (9:00–18:00). All studies were carried out in accordance with the protocols approved by the Animal Experiment Ethics Committee and strictly in compliance with the guidelines for animal experiments of the Fourth Military Medical University (Xi'an, China) as well as the ARRIVE guidelines.

### Short-hairpin RNA and Virus Preparation

$ER\alpha$  short-hairpin RNA sequences were designed based on the report by Musatov *et al.* [42, 43].  $ER\alpha$ -short-hairpin RNA (sh $ER\alpha$ , *ESR1*, 5'-GGCATGGAGCATCTCTACA-3'), or short-hairpin control (a scrambled sequence) was ligated into the designated plasmid vector construct (pAAV-GAD67-EGFP-3xFLAG-WPRE), which was designed to co-express the short-hairpin RNA driven by the GAD67 promoter and the enhanced green fluorescent protein. The reconstructed vector was packaged in adeno-associated virus 2/9 (AAV2/9) serotype with titers of  $1.0 \times 10^{12}$  genome copies/mL. The reconstruction and packaging processes were completed by Obio Technology Corp., Ltd. (Shanghai, China).

### Stereotaxic surgery

Mice were fixed in a stereotaxic frame (RWD, Shenzhen, China) under 1.4–1.5 vol% isoflurane anesthesia with erythromycin ophthalmic ointment applied for eye protection. After shaving and skin antisepsis, 1% lidocaine was subcutaneously injected and a sagittal incision was made in the scalp. During surgery, the mice were kept warm using a heating plate.

For pharmacological experiments, a custom-made double guide cannula (center-to-center distance 0.8 mm, 0.48 mm in diameter, RWD, Shenzhen, China) was inserted bilaterally into the MPA (AP: + 0.15 mm; ML:  $\pm$  0.4 mm; DV: – 4.5 mm from the brain surface) of C57BL/6J mice. A double dummy cannula (RWD, Shenzhen, China) secured with a dust cap was inserted into the guide cannula to prevent clogging during the recovery period.

For the  $ER\alpha$  knockdown test, AAV9-GAD67-EGFP-sh $ER\alpha$ -WPRE or AAV9-GAD67-EGFP-short-hairpin control was bilaterally injected (300 nL/side, 50 nL/min) into the MPA (AP: + 0.15 mm; ML:  $\pm$  0.4 mm; DV: – 5.0 mm from the brain surface). After microinjection, the micropipette was left in place for an additional 10 min

to minimize the spread of the virus along the injection track.

After cannula insertion and virus injection, three stainless steel screws ( $1 \times 5 \text{ mm}^2$ , RWD, Shenzhen, China) were secured on the skull surface as electroencephalogram (EEG) electrodes: the positive electrode on one side of the frontal cortex (AP:  $-1.5 \text{ mm}$ , ML:  $+1.5 \text{ mm}$ ), the negative electrode on the other side of the parietal cortex (AP:  $+1.5 \text{ mm}$ , ML:  $-1.5 \text{ mm}$ ), and a reference electrode at the occipital cortex (AP:  $-5.5 \text{ mm}$ , ML:  $0.0 \text{ mm}$ ). The cannula and skull screws were fixed using methyl methacrylate cement. After surgery, the mice were moved to a heating plate until they recovered consciousness. Meloxicam ( $0.03 \text{ mg/kg}$ ) was used for postoperative analgesia for 3 days.

### Measurement of Induction and Emergence Times

After habituation in a horizontal Plexiglas<sup>®</sup> cylinder (45 cm long, 12 cm in diameter) for 2 h for 3 consecutive days, the duration of sevoflurane induction or emergence was tested using the cylinder, in which mice were administered 2.4 vol% sevoflurane in 1 L/min 100% oxygen using a sevoflurane vaporizer (RWD, Shenzhen, China). The inhaled concentrations of sevoflurane were continuously monitored using a gas analyzer (G60; Philips, Shenzhen, China) with sampling from the outlet of the cylinder. The cylinder was rotated  $90^\circ$  every 15 s after the sevoflurane inhalation was started or stopped, and loss of the righting reflex (LORR) was defined if mice could not turn prone onto four limbs and remained in the supine position for  $>60 \text{ s}$ . Induction time was defined as the duration from the onset of anesthetic inhalation to LORR. After LORR, rotation of the cylinder was stopped, and 2.4 vol% sevoflurane was continuously administered for an additional 30 min to ensure equilibration. Mice were considered to have achieved recovery of the righting reflex (RORR) if they could turn themselves to the prone position. Emergence time was defined as the interval from the cessation of anesthetic inhalation to RORR. For the cannula microinjection experiment, considering the effective time of 1,3-bis (4-hydroxyphenyl)-4-methyl-5-[4-(2-piperidinylethoxy) phenol]-1H-pyrazole dihydrochloride (MPP), induction time and emergence time were assessed in two separate trials (Fig. 2B, C).

### Pharmacological Experiments

The ER $\alpha$  antagonist MPP was from Tocris Bioscience (Catalog number: 1991, United Kingdom). MPP was dissolved in dimethyl sulfoxide (DMSO; Sigma, Billerica, MA, USA) as a stock solution ( $1 \text{ mg/mL}$ ) and diluted to 1

ng/ $\mu\text{L}$  with artificial cerebrospinal fluid (ACSF) for the formal experiment (DMSO = 0.1%).

After mice had recovered from surgery for at least 5–7 days, MPP ( $1 \text{ ng}/\mu\text{L}$ ,  $0.3 \mu\text{L}/\text{side}$ ) was microinjected through the double injector cannula, which had a 0.5-mm extension beyond the tip of the guide cannula. Once the injection was completed, the injector cannula was left in place for an additional 5 min to prevent spread of the drug along the injection track.

### EEG Recording and Analysis

EEG signals were continuously recorded using the Power Lab 16/35 amplifier system (PL3516, AD Instruments, New Zealand) and LabChart Pro V8.1.13 software (MLU60/8, AD Instruments). Raw EEG data were digitized at 1000 Hz.

To calculate the burst-suppression ratio (BSR, a marker of deep anesthesia), EEG data were bandpass filtered at 5–30 Hz, and then analyzed using a custom Matlab script (R2019a, MathWorks, Natick, MA, USA). A suppression event, with an assignment of 1, was defined as when the EEG amplitude was less than its individual threshold for  $>0.5 \text{ s}$ . Otherwise, the amplitude above the threshold was defined as a burst event assigned a value of 0. The BSR was calculated every 1 min by the percentage of suppression events as required. The presence of a BSR was defined as a certain minute when the BSR was  $>20\%$ , and the extinction of BSR was defined as the time interval from the cessation of anesthetic administration to the end of the last suppression event.

For spectral analysis, the spectrum of frequencies throughout the entire procedure within the 0.3–50 Hz range was plotted for all mice. The relative power in the delta band (1–4 Hz), computed by averaging the signal power across the frequency range of the delta band and then dividing by the total power, was recorded for 5 min after the onset and cessation of sevoflurane administration.

### Slice Preparation and Whole-Cell Recordings

Acute coronal brain slices containing the MPA at  $300 \mu\text{m}$  thickness were cut on a vibratome in ice-cold cutting solution (in mmol/L): 92 NMDG, 2.5 KCl, 1.25  $\text{NaH}_2\text{PO}_4$ , 30  $\text{NaHCO}_3$ , 20 HEPES, 25 glucose, 2 thiourea, 5 Na-ascorbate, 3 Na-pyruvate, 0.5  $\text{CaCl}_2$ , and 10  $\text{MgSO}_4$  (bubbled with 95%  $\text{O}_2$  and 5%  $\text{CO}_2$ ). The slices were immersed in ACSF (in mmol/L): 124 NaCl, 2.5 KCl, 1.25  $\text{NaH}_2\text{PO}_4$ , 24  $\text{NaHCO}_3$ , 12.5 glucose, 5 HEPES, 2  $\text{CaCl}_2$ , and 2  $\text{MgSO}_4$  for 45 min at  $35^\circ\text{C}$  and then 1 h at room temperature ( $22^\circ\text{C}$ – $26^\circ\text{C}$ ) before being transferred to the recording chamber. Patch pipettes ( $3 \mu\text{m}$ – $5 \mu\text{m}$ ,  $4 \text{ M}\Omega$ – $6 \text{ M}\Omega$ ) for whole-cell recording were filled with an internal



solution containing (in mmol/L) 145 K-gluconate, 10 HEPES, 1 EGTA, 2 Mg-ATP, 0.3 Na<sub>2</sub>-GTP, and 2 MgCl<sub>2</sub>. Bright tdTomato-fluorescence or EGFP-fluorescence of glutamatergic or GABAergic neurons in the MPA were visually identified using an Olympus U-HGLGPS fluorescent source microscope. Whole-cell recordings were made while perfusing (3–5 mL/min) ACSF containing estradiol (10 nmol/L) at room temperature. Most of the MPA neurons exhibited spontaneous action potential (AP) firing; for these neurons, we waited for 5 min–10 min after the establishment of whole-cell patching configuration to record stable responses. In neurons without spontaneous firing, a positive current (10 pA–50 pA) was injected *via* the recording pipette to bring the resting membrane potential to 45 mV–50 mV and then to induce steady firing activity [44, 45]. MPP (1  $\mu$ mol/L or 5  $\mu$ mol/L, MPP was dissolved into DMSO as a stock solution (5 mmol/L), and diluted to 5  $\mu$ mol/L (DMSO = 0.1%) or 1  $\mu$ mol/L (DMSO = 0.02%) with ACSF for the formal experiment) was bath applied for 15 min after 5 min of baseline recording. We averaged the number of APs recorded during the 5 min baseline and the last 5 min of MPP application for comparison. All tested neurons were checked for the co-expression of ER $\alpha$  after patching, and only data from ER $\alpha$ -positive neurons were analyzed. Data were acquired using pClamp 10.6 (Molecular Devices, Foster City, CA, USA). AP numbers were calculated using Mini Analysis 6.0.1 (Synaptosoft Inc., Decatur, GA, USA).

### Histological Verification

Mice were deeply anesthetized with isoflurane and perfused with 4% paraformaldehyde (PFA) followed by 0.9% saline [46]. Brains were post-fixed for 2 h in 4% PFA at 4°C and then dehydrated in 30% sucrose in phosphate-buffered saline (PBS) at 4°C until sinking. Brains were coronally cut at 40  $\mu$ m on a cryostat microtome (CM1200 Leica, Wetzlar, Germany). The sections were washed three times for 10 min each in PBS and then blocked with 5% normal donkey serum in PBS with 0.3% Triton X-100 for 2 h at room temperature. The primary antibodies, rabbit anti-ER $\alpha$  (1:200, Abcam, ab32063, United Kingdom), were incubated at 4°C for 48 h, followed by incubation with donkey anti-rabbit Alexa Fluor 594 (1:500, Jackson ImmunoResearch, Code: 711-585-152, West Grove, PA, USA) as secondary antibodies for 2 h at room temperature. After another 3  $\times$  10 min wash with PBS, the sections were mounted in Fluoromount-G (Millipore Sigma, Billerica, MA, USA), and images of immunostaining were captured using a laser confocal microscope (FV1200, Olympus, Tokyo, Japan).

### Western Blotting

Mice were deeply anesthetized with isoflurane before transcardial infusion of 0.9% saline, and their brains were quickly removed. The MPA was dissected on ice using a mouse brain matrix (RWD, Shenzhen, China). Total proteins were isolated using RIPA lysis buffer supplemented with a protease inhibitor cocktail (catalog number: 78438, Thermo Fisher Scientific, Carlsbad, CA, USA). Equal amounts of protein ( $\sim$ 50  $\mu$ g) were loaded and separated on 10% Tris-Tricine SDS-PAGE gels and transferred to polyvinylidene difluoride membranes. The membranes were blocked in 5% nonfat milk for 1 h and incubated overnight with primary antibodies at 4°C. After incubation with secondary antibodies (1:5000, Zhuangzhi Biological Technology Co., Ltd, EK020/EK010, Xi'an, China) for 1 h at room temperature, the signals were visualized using enhanced chemiluminescence (Millipore Sigma, Billerica, MA, USA) and captured using a ChemiDocXRS system (Bio-Rad, Minnesota, USA). Western blot results were quantified using densitometry (Image Lab). The primary antibodies used were rabbit anti-ER $\alpha$  (1:1000, Abcam, ab32063, United Kingdom) and a glyceraldehyde-3-phosphate dehydrogenase antibody (1:10000, Zhuangzhi Biological Technology Co., Ltd, NC020, Xi'an, China).

### Measurement of Body Surface Temperature

The back skin surface temperature of males and females ( $n = 6$ ) was measured before and 10 min, 20 min, 30 min, 40 min, 50 min, and 60 min after injection of MPP to determine the temperature response to MPP in male and female mice. An infrared thermometer (YHW-2, Yuwell, Jiangsu, China) was used as previously described [47].

### Statistical Analysis

Prism 8.0 (GraphPad Software, San Diego, CA, USA) was used for statistical analysis. Data are presented as the mean  $\pm$  standard error of the mean or the mean  $\pm$  standard deviation as needed. All sets of data were verified for normality and homogeneity of variance using Kolmogorov–Smirnov and Brown–Forsythe tests before analysis. Student's *t*-test was used to assess the statistical significance for comparisons of two groups, followed by two-way analysis of variance (ANOVA) followed by Bonferroni's multiple comparisons for three or more groups. Statistical significance was set at  $P < 0.05$ .

## Results

### Sevoflurane Induces Sex Differences Across Anesthesia Induction, Maintenance, and Emergence

To determine whether there was a sex difference in the anesthetic effect of sevoflurane in mice, age-matched adult female and male mice were used to compare the time spent in losing and regaining consciousness (in terms of the righting reflex) from sevoflurane anesthesia (Fig. 1A). We found that female mice took longer to lose the righting reflex than male mice ( $398.9 \pm 46.8$  s vs  $313.3 \pm 26.5$  s,  $P = 0.0002$ ,  $n = 9$  per group; Fig. 1B), and less time to emerge from anesthesia after sevoflurane exposure ceased ( $196.7 \pm 33.9$  s vs  $245 \pm 38.2$  s,  $P = 0.0119$ ,  $n = 9$  per group; Fig. 1B).

To investigate the sex difference in response to sevoflurane in EEG patterns during anesthesia maintenance, we continuously recorded EEG signals over the peri-anesthesia period (Fig. 1C). Continuous inhalation of 2.4 vol% sevoflurane for 30 min after LORR kept animals anesthetized. However, female mice experienced fewer burst suppression patterns than male mice, suggesting lighter anesthesia. Although the BSR increased in both sexes as anesthesia continued, females displayed a rather lower BSR than males ( $F_{44, 528} = 2.341$ ,  $P < 0.0001$ ,  $n = 7$  per group; Fig. 1D). Moreover, the presence of burst suppression patterns was later in females than males ( $22.4 \pm 9.3$  min vs  $12.4 \pm 2.1$  min,  $P = 0.017$ ,  $n = 7$  per group; Fig. 1E). In addition, the extinction of burst suppression patterns in females was faster than in males ( $109.3 \pm 24.3$  s vs  $149.9 \pm 30.0$  s,  $P = 0.0116$ ,  $n = 7$  per group; Fig. 1F). The enhancement of delta oscillation also represents the deepening of anesthesia; therefore, we analyzed the relative power in the delta band every 30 s during induction and emergence. Delta power gradually increased in both males and females from the start of sevoflurane inhalation, but males had a stronger delta oscillation than females (Fig. 1G). Also, delta power increased faster in males than females during induction ( $1.9 \pm 0.9\%/min$  vs  $0.9 \pm 0.6\%/min$ ,  $P = 0.0338$ ,  $n = 7$  per group; Fig. 1H). During emergence, delta power gradually decreased in both sexes, but males maintained a higher power than females (Fig. 1I), and the rate of decrease in power was significantly slower in males than in females ( $-0.7 \pm 0.3\%/min$  vs  $-1.3 \pm 0.6\%/min$ ,  $P = 0.0387$ ,  $n = 7$  per group; Fig. 1J). The above results suggest that sevoflurane anesthesia has a sex-dependent effect in mice, and males are more sensitive to sevoflurane than females.

### Inhibition of ER $\alpha$ in the MPA Alters Anesthesia Sensitivity and Depth in Male Mice

To determine the regulatory role of MPA ER $\alpha$  in the sevoflurane anesthesia-induced sex difference, MPP, a highly selective ER $\alpha$  antagonist, was bilaterally microinjected into the MPA of male and female mice (Fig. 2A). MPP was administered 10 min before starting or stopping sevoflurane inhalation to assess the changes in LORR or RORR, since MPP requires 5 min–10 min to take effect (Fig. 2B, C). We found that the sex differences in induction time ( $402.3 \pm 37.2$  s vs  $437.7 \pm 41.3$  s,  $P = 0.2310$ ,  $n = 11$  per group; Fig. 2B) and emergence time ( $199.4 \pm 30.8$  s vs  $208.3 \pm 37.1$  s,  $P > 0.9999$ ,  $n = 11$  per group; Fig. 2C) were abolished in the MPP group, and the primary change occurred in the males rather than in the females. When ER $\alpha$  was inhibited, males took longer to be anesthetized ( $341.3 \pm 28.6$  s,  $n = 8$  vs  $402.3 \pm 37.2$  s,  $n = 11$ ,  $P = 0.0104$ ; Fig. 2B) and a shorter time to wake up from anesthesia ( $248.3 \pm 37.6$  s vs  $199.4 \pm 30.8$  s,  $P = 0.0338$ ,  $n = 9$  per group; Fig. 2C), while females did not show much change (induction time:  $449.1 \pm 44.9$  s,  $n = 8$  vs  $437.7 \pm 41.3$  s,  $n = 11$ ,  $P > 0.9999$ ; emergence time:  $196.7 \pm 33.9$  s vs  $208.3 \pm 37.1$  s,  $P > 0.9999$ ,  $n = 9$  per group; Fig. 2B, C).

To obtain a comparable BSR among male and female mice during maintained deep anesthesia, the concentration of sevoflurane was individually adjusted to 2.4%–2.6% to keep the BSR stable at  $\sim 70\%$ . We compared the burst suppression patterns of EEG 15 min after the administration of MPP (Fig. 2D). Representative changes in the EEG spectra are shown in Fig. 2F–I. A significant decrease in burst suppression pattern occurred only in male mice after MPP microinjection. Statistical analysis of the BSR for 5 min before and 15 min after MPP administration confirmed that the BSR in males significantly declined  $\sim 7$  min after MPP treatment and lasted for at least 8 min ( $F_{57, 323} = 6.426$ ,  $P < 0.0001$ ; Fig. 2E), while that in females did not change significantly. These results suggest a sex-specific regulation of ER $\alpha$  in the MPA under sevoflurane anesthesia. ER $\alpha$  is likely to be involved in the sevoflurane sensitivity in men rather than in women.

Given the involvement of MPA in regulating body temperature [34, 35, 48], and temperature being an important factor for sensitivity to anesthesia, the changes in body surface temperature of male and female mice after MPP injection were measured. As shown in Fig. S1, inhibition of the ER $\alpha$  signal in the MPA significantly increased body surface temperature in males and females ( $F_{6, 60} = 40.28$ ,  $P < 0.0001$ ,  $n = 6$  per group), and it took 10–20 min to reach the peak temperature, after which it declined gradually.

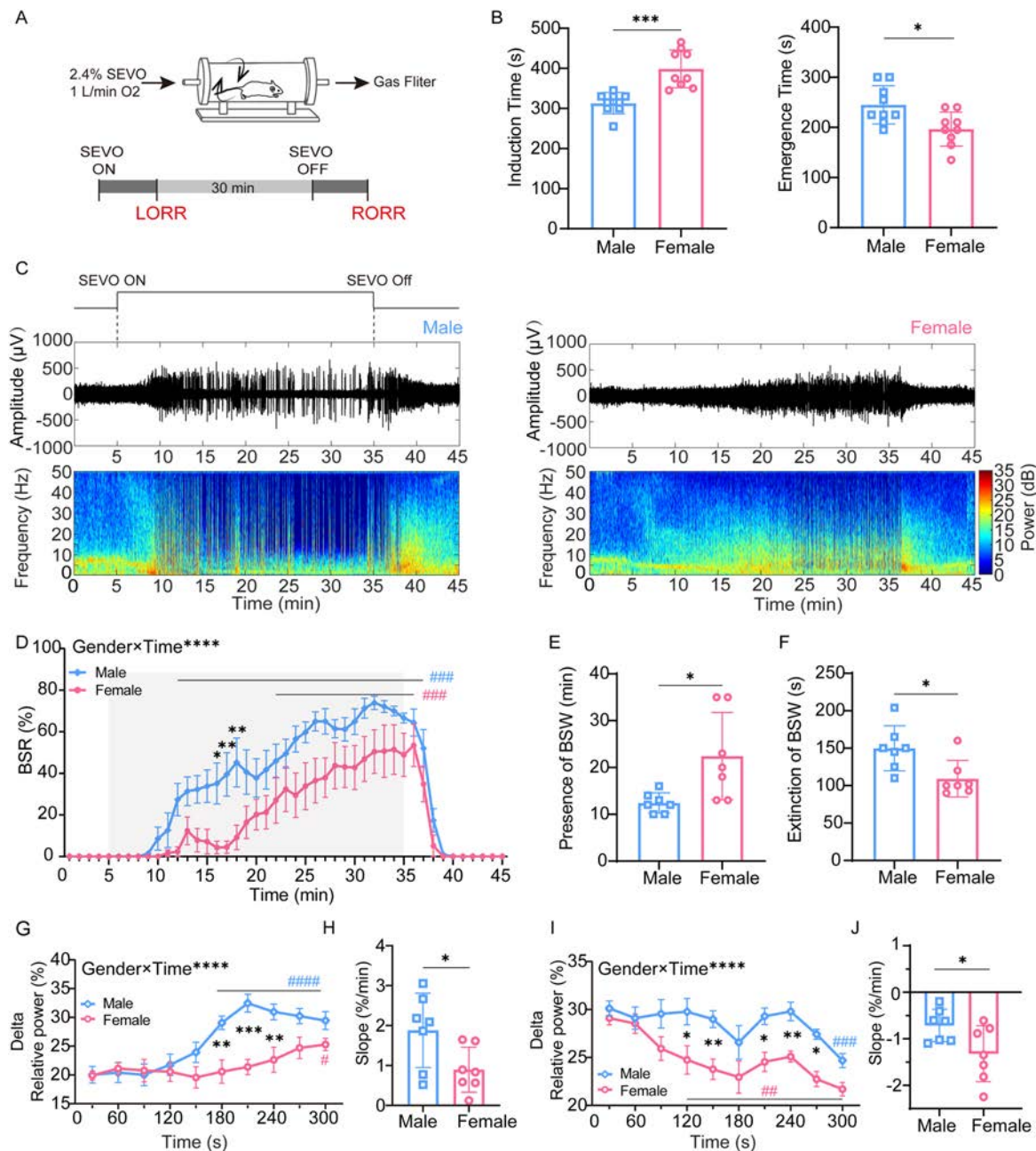


**Fig. 1** Sex-specific differences in behavioral response and electroencephalogram pattern in mice during sevoflurane anesthesia. **A** Schematic of Plexiglas cylinder and protocol used in behavioral observations. **B** Induction time (left) and emergence time (right) in male and female mice ( $t_{16} = 4.772$ ,  $P = 0.0002$  for induction time;  $t_{16} = 2.837$ ,  $P = 0.0119$  for emergence time; two-tailed unpaired Student's  $t$ -test). **C** Representative electroencephalogram traces and corresponding power spectrograms in a male and a female recorded throughout the process of sevoflurane anesthesia. **D** BSR throughout the electroencephalogram recording (45 min) in males and females. BSR is calculated every minute ( $F_{44,528} = 2.341$ ,  $P < 0.0001$ ; two-way analysis of variance (ANOVA) followed by *post hoc* Bonferroni's multiple comparisons). **E**, **F** Presence (**E**) and extinction (**F**) of BSR in male and female groups ( $t_{12} = 2.770$ ,  $P = 0.0170$  for presence of BSR,  $t_{12} = 2.781$ ,  $P = 0.0166$  for extinction of BSR; two-tailed

unpaired Student's  $t$ -test). **G**, **I** Spectral analysis of relative power in the delta band between male and female groups during induction (**G**, 5 min after administration of sevoflurane) and emergence (**I**, 5 min after cessation of administration). The relative delta power is computed every 30 s ( $F_{9,108} = 4.997$ ,  $P < 0.0001$  for induction;  $F_{9,108} = 1.987$ ,  $P = 0.0476$  for emergence; two-way ANOVA followed by *post hoc* Bonferroni's multiple comparisons). **H**, **J** Relative power transition rate in delta wave between male and female groups during induction (**H**) and emergence (**J**) ( $t_{12} = 2.395$ ,  $P = 0.0338$  for induction;  $t_{12} = 2.320$ ,  $P = 0.0387$  for emergence; two-tailed unpaired Student's  $t$ -test; \*significant difference between males and females; #significant difference from initial value). SEVO, sevoflurane; BSR, burst suppression ratio; BSW, burst suppression wave; LORR, loss of righting reflex; RORR, recovery of righting reflex.



### MPP Reduces Spikes in Glutamatergic and GABAergic Neurons in the MPA in Males but not in Females

GABAergic and glutamatergic neurons are the major neuronal subsets in the MPA, both of which have been suggested to play a critical role in modulating arousal behaviors. To examine the specific neuronal effect of ER $\alpha$  in the MPA, whole-cell patch-clamp recordings were performed on the MPA GABAergic and glutamatergic neurons with MPP interventions in acute brain slices from both male and female mice. We identified GABAergic and glutamatergic neurons based on bright tdTomato-fluorescence before patching and checked the co-expression of ER $\alpha$  after recording (Fig. 3A). In male mice, bath application of MPP (1  $\mu$ mol/L) significantly decreased the number of spike in GABAergic neurons ( $23.1 \pm 3.5$  vs  $11.5 \pm 2.2$ ,  $P = 0.0059$ ,  $n = 5$  per group; Fig. 3B, D, E) and also slightly reduced the firing rate of glutamatergic neurons ( $46.8 \pm 3.2$  vs  $32.4 \pm 5.3$ ,  $P = 0.0089$ ,  $n = 5$  per group; Fig. 3C, F, G). Notably, GABAergic neurons fired less by  $52 \pm 10\%$ , while the spike number of glutamatergic neurons decreased by  $30 \pm 13\%$  ( $P = 0.0195$ ; Fig. 3H). However, after application of MPP (1  $\mu$ mol/L) in the slices from females, there was no significant change in the firing rate of the GABAergic neurons ( $30.6 \pm 4.0$  vs  $29.7 \pm 5.0$ ,  $P = 0.7474$ ,  $n = 5$  per group; Fig. 3I, K, L) or glutamatergic neurons ( $19.0 \pm 3.2$  vs  $15.9 \pm 2.1$ ,  $n = 5$ ,  $P = 0.1809$ ; Fig. 3J, M, N). We further increased the MPP concentration to 5  $\mu$ mol/L, but still did not find a change in the firing activity of GABAergic ( $47.1 \pm 4.2$  vs  $43.9 \pm 3.5$ ,  $P = 0.1577$ ,  $n = 5$  per group; Fig. 3O, P) or glutamatergic neurons ( $33.0 \pm 2.2$  vs  $32.2 \pm 5.4$ ,  $P = 0.6897$ ,  $n = 5$  per group; Fig. 3Q, R) in females. These results provide evidence for sex differences in the responses of MPA neurons to ER $\alpha$  inhibition. MPA GABAergic neurons in males exhibited a more profound suppression than glutamatergic neurons.

### ER $\alpha$ Knockdown in GABAergic Neurons of the Male MPA is Sufficient to Eliminate the Sex Difference During Sevoflurane Anesthesia

Inhibitory GABAergic neurons in the MPA are well known for their sleep-promoting nature while excitatory glutamatergic neurons promote wakefulness. Considering that MPP administration in the MPA area produced a stronger suppression in GABAergic neurons and an arousal-facilitation effect on behaviors in male mice, we speculated that ER $\alpha$  in the MPA GABAergic neurons of males could principally mediate the sex difference during sevoflurane anesthesia. To test this hypothesis, we generated and microinjected into the MPA recombinant AAV2/9

expressing a short-hairpin RNA targeting ER $\alpha$  (AAV-GAD67-shER $\alpha$ ) driven by the GAD67 promoter (Fig. 4A, B). After a period of 3 weeks for virus expression, double immunofluorescence and western blotting showed a prominent efficiency of ER $\alpha$  knockdown in GABAergic neurons of the MPA (Fig. 4C, D). We also examined the neuronal activity in acute brain slices, and found that the ER $\alpha$  knockdown in the MPA GABAergic neurons eliminated the inhibitory effect of MPP on GABAergic neurons in males (Fig. S2).

Consistent with the results of pharmacological manipulation with MPP, knocking down the ER $\alpha$  in MPA GABAergic neurons eliminated the sex difference in sevoflurane induction time ( $390.0 \pm 18.4$  s vs  $416.7 \pm 34.2$  s,  $P = 0.2888$ ,  $n = 9$  per group; Fig. 5B) and emergence time ( $223.3 \pm 37.1$  s vs  $220.0 \pm 38.2$  s,  $P > 0.9999$ ,  $n = 9$  per group; Fig. 5B). Specifically, male mice with GABAergic ER $\alpha$  knockdown in the MPA required more time to be anesthetized ( $338.3 \pm 23.9$  s vs  $390 \pm 18.4$  s,  $P = 0.0022$ ,  $n = 9$  per group; Fig. 5B) and less time to wake up from anesthesia ( $280.0 \pm 31.9$  s vs  $223.3 \pm 37.1$  s,  $P = 0.0044$ ,  $n = 9$  per group; Fig. 5B) than mice expressing scrambled shRNA (EGFP). In females, there was no significant difference in either induction time ( $415.0 \pm 30.9$  s vs  $416.7 \pm 34.2$  s,  $P > 0.9999$ ,  $n = 9$  per group; Fig. 5B) or emergence time ( $205.0 \pm 28.1$  s vs  $220.0 \pm 38.2$  s,  $P > 0.9999$ ,  $n = 9$  per group; Fig. 5B) between the EGFP and shRNA-ER $\alpha$  groups.

Furthermore, MPA GABAergic ER $\alpha$  knockdown significantly decreased the BSR during the maintenance period in male mice, but not in females, which resulted in the disappearance of sex differences in anesthesia depth ( $F_{132, 880} = 2.901$ ,  $P < 0.0001$ ,  $n = 6$  per group; Fig. 5D). Compared with the EGFP group, MPA GABAergic ER $\alpha$  knockdown also postponed the presence of a burst suppression pattern in the EEG ( $14.5 \pm 4.5$  min vs  $29.5 \pm 7.5$  min,  $P = 0.0088$ ,  $n = 6$  per group; Fig. 6B) and accelerated the extinction of the pattern ( $230.8 \pm 40.1$  s vs  $115.0 \pm 54.3$  s,  $P = 0.0050$ ,  $n = 6$  per group; Fig. 6F) in males, while females with MPA GABAergic ER $\alpha$  knockdown showed no significant changes in the presence ( $27.5 \pm 8.9$  min vs  $22.77 \pm 6.6$  min,  $P > 0.9999$ ,  $n = 6$  per group; Fig. 6B) or extinction (EGFP:  $146.7 \pm 65.3$  s vs shRNA-ER $\alpha$ :  $123.3 \pm 44.1$  s,  $P > 0.9999$ ,  $n = 6$  per group; Fig. 6F) of the pattern. As shown in Fig. 6A, with the onset of sevoflurane inhalation, delta waves gradually increased in the EGFP groups in a sex-specific manner. However, MPA GABAergic ER $\alpha$  knockdown largely eliminated this sex difference. We measured the relative power of the delta band every 30 s during the induction stage for 5 min. The male ER $\alpha$  knockdown group showed a decline in both delta power (Fig. 6C) and the rate of increase of delta power ( $2.6 \pm 0.6\%/min$  vs  $1.3 \pm 0.8\%/min$ ,  $P = 0.0395$ ,  $n = 6$  per

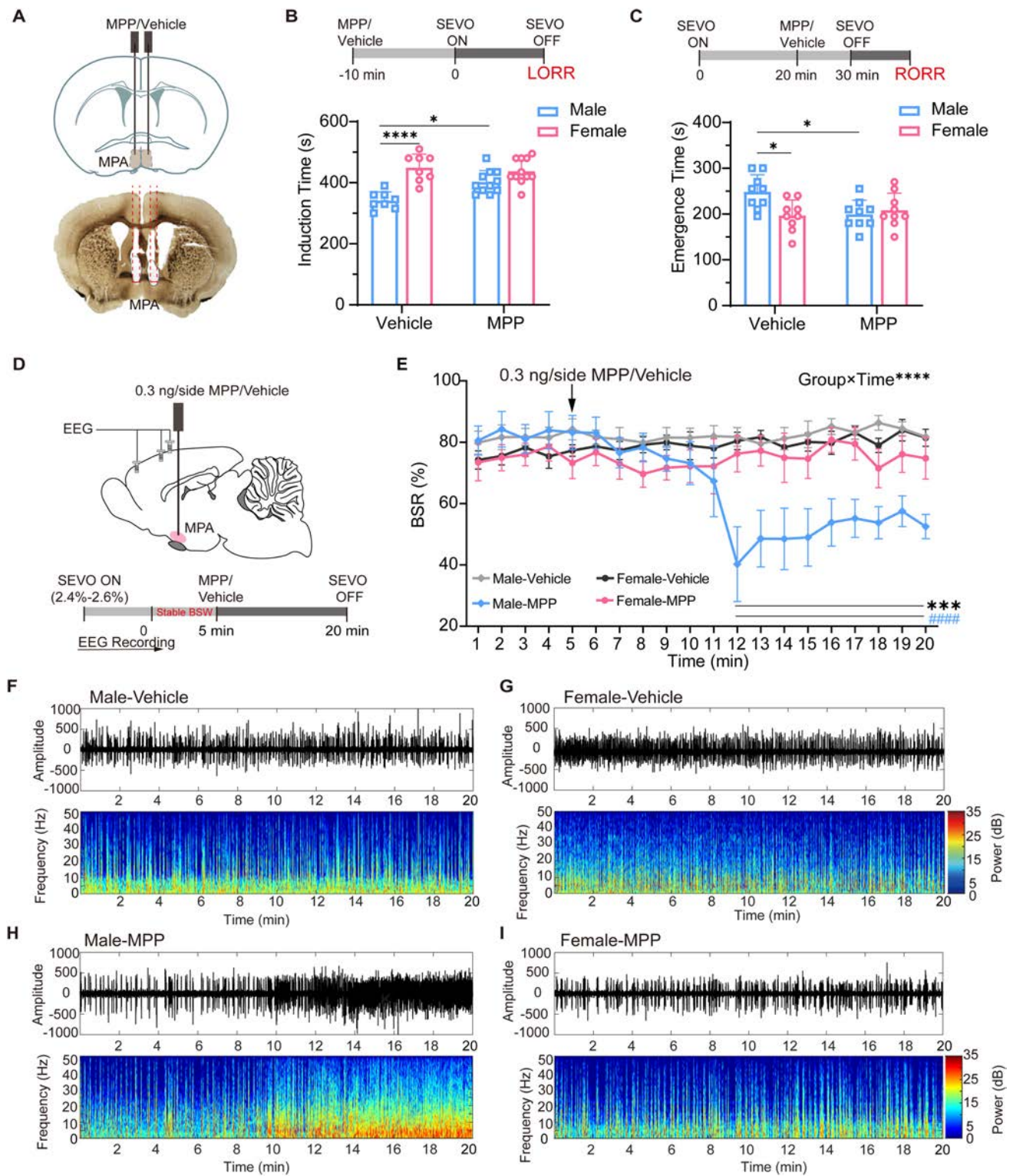


**Fig. 2** Inhibition of ER $\alpha$  in the MPA reduces the anesthesia sensitivity and anesthesia depth in male mice. **A** Diagram of coronal brain section (upper) showing cannula insertion and histological image (lower) showing the bilateral location of cannulas in the MPA. **B, C** Schematics of protocols (upper) and results (lower) for induction (**B**) and emergence (**C**) times in male and female mice in the vehicle and MPP groups ( $F_{1,34} = 8.144$ ,  $P = 0.0073$ ;  $t_{34} = 5.587$  (Vehicle: male vs Vehicle: female),  $P < 0.0001$ ;  $t_{34} = 3.401$  (Vehicle: male vs MPP: male),  $P = 0.0104$  for induction time (**B**);  $F_{1,32} = 6.757$ ,  $P = 0.0140$ ;  $t_{32} = 3.137$  (Vehicle: male vs Vehicle: female),  $P = 0.0219$ ;  $t_{32} = 2.968$  (Vehicle: male vs MPP: male),  $P = 0.0338$  for emergence time (**C**); two-way analysis of variance (ANOVA) followed by *post hoc* Bonferroni's multiple comparisons). **D** Diagram of sagittal brain section showing the site of cannula implantation and schematic protocol for EEG recording. **E** BSR at 5 min before and 15 min after MPP/vehicle injection into the MPA in male and female mice. BSR is computed each minute (male-vehicle:  $n = 5$ ; female-vehicle:  $n = 5$ ; male-MPP:  $n = 6$ ; female-MPP:  $n = 5$ ;  $F_{57,323} = 6.426$ ,  $P < 0.0001$ ; two-way ANOVA followed by *post hoc* Bonferroni's multiple comparisons; \*significant difference between male-vehicle and male-MPP groups; #significant difference from initial value). **F–I** Representative EEG traces and power spectrograms over time after MPP (lower) or vehicle (upper) injection in male (left) and female (right) mice. MPA, medial preoptic area; SEVO, sevoflurane; BSW, burst suppression wave; BSR, burst suppression ratio; LORR, loss of righting reflex; RORR, recovery of righting reflex; EEG, electroencephalogram.

group; Fig. 6D) in males, while there was no such effect in females ( $1.1 \pm 0.4\%/min$  vs  $1.1 \pm 0.9\%/min$ ,  $P > 0.9999$ ,  $n = 6$  per group; Fig. C, D). During the emergence stage, delta oscillation gradually weakened in the EGFP groups in a sex-dependent manner (Fig. 6E). This sex dependence was abolished in the ER $\alpha$  knockdown groups. ER $\alpha$  knockdown reduced the delta power at most time points (Fig. 6G) and accelerated the rate of weakening of the delta wave in males ( $-0.6 \pm 0.4\%/min$  vs  $-1.5 \pm 0.3\%/min$ ,  $P = 0.0106$ ,  $n = 6$  per group; Fig. 6H), while the ER $\alpha$  knockdown groups showed no effect on the delta power dynamics in females (EGFP:  $-1.0 \pm 0.5\%/min$  vs shRNA-ER $\alpha$ :  $-0.8 \pm 0.4\%/min$ ,  $P > 0.9999$ ,  $n = 6$  per group; Fig. 6G, H). Combined with the pharmacological results, MPA GABAergic ER $\alpha$  regulated the sensitivity to sevoflurane anesthesia in males more than females, which could make a pivotal contribution to the differences in behaviors and EEG patterns between male and female mice during general anesthesia.

## Discussion

In the present study, we found sex differences in the behavioral responses and EEG signatures in sevoflurane anesthesia in mice. In particular, males were more prone to lose consciousness during anesthesia induction and maintain a deeper anesthesia and were harder to wake up than females at the same concentration of sevoflurane.

Pharmacological inhibition of ER $\alpha$  in the MPA extended the induction time and facilitated the emergence from sevoflurane in males but did not have such effects in females, which consequently abolished the sex bias in sevoflurane anesthesia. *In vitro* electrophysiological tests revealed that the firing activity of GABAergic and glutamatergic neurons of the MPA was inhibited in males but not in females after bath application of an ER $\alpha$  inhibitor, and GABAergic neurons showed greater suppression than glutamatergic neurons. Selective downregulation of ER $\alpha$  in GABAergic neurons of the MPA was sufficient to eliminate the sex difference during sevoflurane anesthesia.

In the last few decades, female rodents have often been neglected in preclinical neuroscience research. A groundbreaking evaluation of biomedical research even reported that male bias was most prominent in terms of neural regulation [49]. The exclusion of females from anesthesia studies also hinders the anesthesia management of female patients because of a lack of knowledge about sex-specific mechanisms. Although a few studies have confirmed that sex plays a role in determining anesthetic requirements and emergence, they have reported conflicting results [5–13]. In our study, we systemically recorded the behavioral and EEG differences during single sevoflurane anesthesia in mice, and found that males were more sensitive to sevoflurane anesthesia and entered deeper anesthesia more easily. Our results are consistent with those of most clinical studies, in which women were found to require a higher propofol infusion rate to maintain general anesthesia [5], a shorter time to emerge from general anesthesia administered with propofol/alfentanil/nitrous oxide complex [6] or inhalational anesthetic [8], and a higher concentration of inhalational anesthesia to maintain BIS levels equivalent to those of men [13]. However, a few basic studies have reported that male rats require larger doses of anesthetics to produce general anesthesia [10, 11], and emerge faster after a single intraperitoneal injection of propofol than female rats [12]. The discrepancy between these studies and our findings could be attributed to the differences in anesthetics, species, and drug delivery strategies [10–12].

Estrogen has been believed to be the leading cause of sex differences in general anesthesia effects for a long time [10]. However, the neuronal targets of this hormone are unclear. The MPA, one of the most established sexually dimorphic structures and a well-known sleep-generating site, is densely enriched in ER $\alpha$ . By microinjection of the selective ER $\alpha$  antagonist MPP into the MPA, we found that the sex difference in sevoflurane anesthesia was completely abolished, which provided evidence for the key role of MPA ER $\alpha$  in the sex difference of sevoflurane anesthesia. Surprisingly, MPP only changed the anesthesia behaviors and EEG signals in males but not in females. Of note, sex



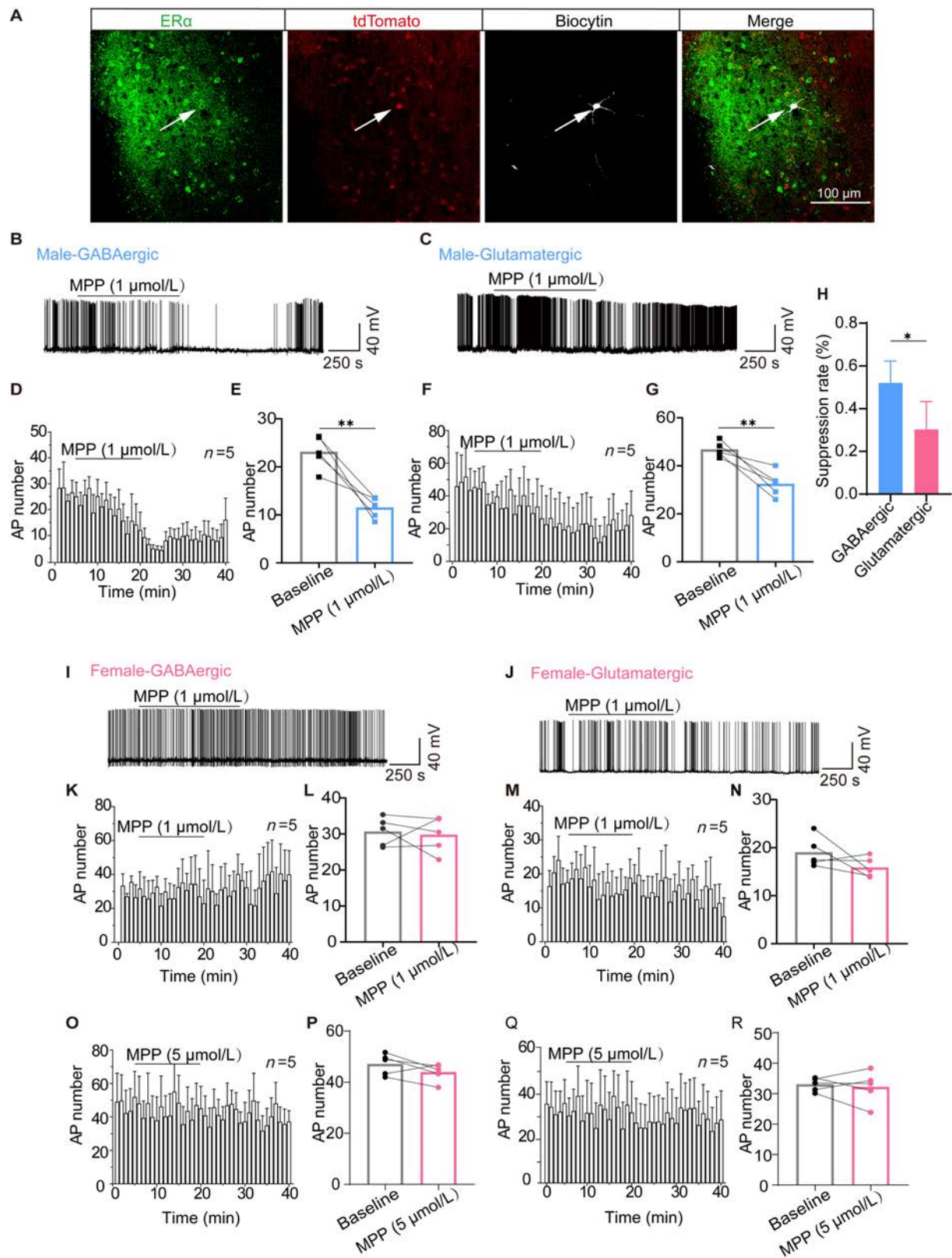


**Fig. 3** MPP decreases the firing activity of MPA neurons in male but not in female mice. **A** Immunofluorescence test for the co-expression of ER $\alpha$  (scale bar, 100  $\mu$ m). **B, C, I, J** Representative firing activity over 5 min before, 15 min perfusion, and 20 min wash with MPP (1  $\mu$ mol/L) application of GABAergic neurons in male (**B**) and female (**I**) mice, and of glutamatergic neurons in male (**C**) and female (**J**) mice. **D, F** Time course of AP number averaged from GABAergic (**D**) and glutamatergic (**F**) neurons in male mice with MPP (1  $\mu$ mol/L) perfusion. **K, M, O, Q** Time course of AP number averaged from GABAergic (**K, O**) and glutamatergic (**M, Q**) neurons in female mice with MPP (1  $\mu$ mol/L) and MPP (5  $\mu$ mol/L) perfusion. **E, G, L, N, P, R** Averaged spike number before 5 min and after 10–15 min of MPP perfusion. Using two-tailed paired Student's *t*-test:  $t_4 = 5.347$ ,  $P = 0.0059$  for GABAergic neurons in males with MPP (1  $\mu$ mol/L) (**E**);  $t_4 = 4.757$ ,  $P = 0.0089$  for glutamatergic neurons in males with MPP (1  $\mu$ mol/L) (**G**);  $t_4 = 0.3451$ ,  $P = 0.7474$  for GABAergic neurons in females with MPP (1  $\mu$ mol/L) (**L**);  $t_4 = 1.618$ ,  $P = 0.1809$  for glutamatergic neurons in females with MPP (1  $\mu$ mol/L) (**N**);  $t_4 = 1.735$ ,  $P = 0.1577$  for GABAergic neurons in females with MPP (5  $\mu$ mol/L) (**P**);  $t_4 = 0.4295$ ,  $P = 0.6897$  for glutamatergic neurons in females with MPP (5  $\mu$ mol/L) (**R**). **H** Suppression rate of GABAergic and glutamatergic neurons of male mice after injection of MPP ( $t_8 = 2.914$ ,  $P = 0.0195$ ; two-tailed unpaired Student's *t*-test). AP, action potential.

differences in the response to manipulation of estradiol signaling are not unprecedented. Indeed, estrogen and its receptors have been traditionally considered to contribute greatly to the unique characteristics of females that are different from those in males, such as reward [50, 51], pain [52, 53], skeletal metabolism [53], emotion-related behaviors [54], and stroke [55]. Vandegrift *et al.* [51] reported that knockdown of ER $\alpha$  in the VTA reduces binge-like ethanol drinking in female mice, but not in males. Indeed, we also expected to find an ER $\alpha$ -mediated anesthesia difference in female mice. However, our findings suggested a regulatory contribution of MPA ER $\alpha$  to the higher sensitivity in male, but not female mice to sevoflurane anesthesia. In the present study, a higher estimated estrogen level in female mice may not fully explain the different responses to MPP between females and males. The differential effects of MPP in female and male mice during sevoflurane anesthesia could be largely attributed to the distinct nature and regulatory mechanism of MPA ER $\alpha$  in the sexes. Although many studies have revealed the various regulatory effects of ER $\alpha$  in males under both physiological and pathological conditions, such as sexual [56] and aggressive behavior [57], pain [43], and temperature regulation [34], only a few studies have compared the roles of ER $\alpha$  or other estrogen receptors between males and females.

In the 1970s, several studies reported that estradiol alters neuronal activity in the preoptic area of the hypothalamus within seconds to minutes [58–61]. Satta *et al.* [50] recently reported that acute treatment with an ER $\beta$  agonist induces the expression of the immediate early gene *c-fos* in

the nucleus accumbens. In our study, we inhibited the MPA ER $\alpha$  by bath application of MPP in the acute brain slice, and found a significant depression of neuronal activity of GABAergic neurons and glutamatergic neurons of the MPA in male mice, suggesting that ER $\alpha$  activation mediates the excitation of these two types of neurons. However, no changes in firing rate were recorded in the MPA neurons of female mice. In consideration of the possible need for higher MPP by female ER $\alpha$ , we increased the MPP concentration to 5  $\mu$ mol/L but still found no significant change in the MPA neuronal activity of female mice. A sex-difference of ER $\alpha$  in regulating inhibitory neurotransmission has been reported in the hippocampus. ER $\alpha$  activates postsynaptic mGluR1 to facilitate endocannabinoid release, which then inhibits presynaptic GABAergic terminals [62]. The functional coupling of ERs with metabotropic glutamate receptors (mGluRs) seems to occur only in females, although ER–mGluR complexes exist in both sexes [63]. These reports may not be identical to our findings but provide some hints on the underlying mechanism. With regard to excitatory neurotransmission, the subtypes of ER that mediate hippocampal neural excitation differ between males and females, and presynaptic glutamatergic neurotransmission is regulated by ER $\beta$  in females but ER $\alpha$  in males [64], which provides a plausible explanation for the weaker response of glutamatergic neurons to MPP. In addition, GABAergic neurons directly inhibit glutamatergic neurons in the MPA; thus, the greater the suppression of GABAergic neurons by MPP, the greater the disinhibition of glutamatergic neurons [65]. Therefore, the overall effect of MPP may be due to the combination of the direct effect of MPP on glutamatergic neurons and feedforward disinhibition from GABAergic neurons. The classical mechanism of estrogen action involves the slow regulation of gene transcription by acting as a transcription factor [66]. However, more recent studies [67] have confirmed many non-classical estrogen signaling mechanisms that are initiated at the cell membrane and regulate rapid non-genomic action. Estrogen receptors physically interact with mGluRs [68–70], receptor tyrosine kinases [71–73], G proteins [74], and kinases [75] at the cell membrane, forming a functional signaling complex, consequently triggering numerous intracellular signaling cascades, such as gene expression, local protein synthesis, actin polymerization, ion channel dynamics, synaptic physiology, and dendritic spine morphology [76–80]. In our study, the effects of MPP recorded *in vivo* and *in vitro* probably resulted from the rapid non-classical estrogen signaling pathways.

It has been reported that selectively activating estrogen-sensitive MPA ER $\alpha^+$  neurons is sufficient to induce a coordinated depression of metabolic rate and body temperature [34]. Body temperature can affect the MAC of

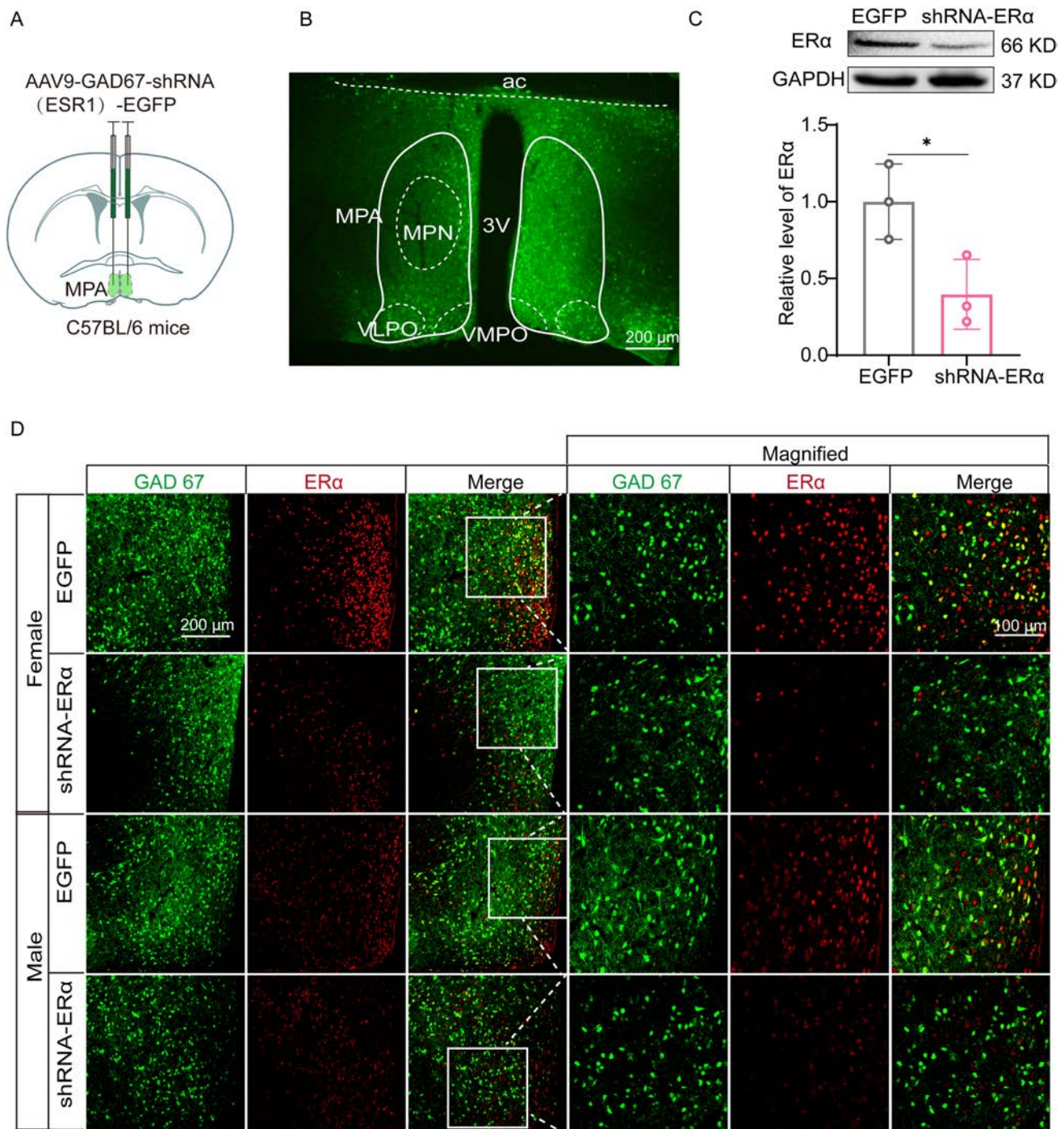


**Fig. 4** Validation of knockdown efficiency of ERα in the MPA. **A** Schematic of intra-MPA injection in C57BL/6 mice. **B** Expression of the virus (EGFP) in GAD67<sup>+</sup> neurons in the MPA. **C, D** Western blots (**C**) and immunofluorescence (**D**) showing efficient ERα knockdown in the MPA ( $n = 3$ ; scale bar, 200 μm;  $t_4 = 3.117$ ,  $P =$

0.0356; two-tailed unpaired Student's  $t$ -test). 3V third ventricle; ac, anterior commissure; MPA, medial preoptic area; MPN, medial preoptic nucleus; VLPO, ventrolateral preoptic nucleus; VMPO, ventromedial preoptic nucleus.

inhaled anesthetics, and hypothermia decreases the isoflurane requirement [81]. In our study, inhibition of ERα signaling by microinjection of MPP increased the body surface temperature not only in males but also in females,

suggesting that the ERα-mediated body temperature increase may not be a contributor to the sex difference in sevoflurane anesthesia. Interestingly, because the female mice did not show an MPA neuronal response to MPP, the



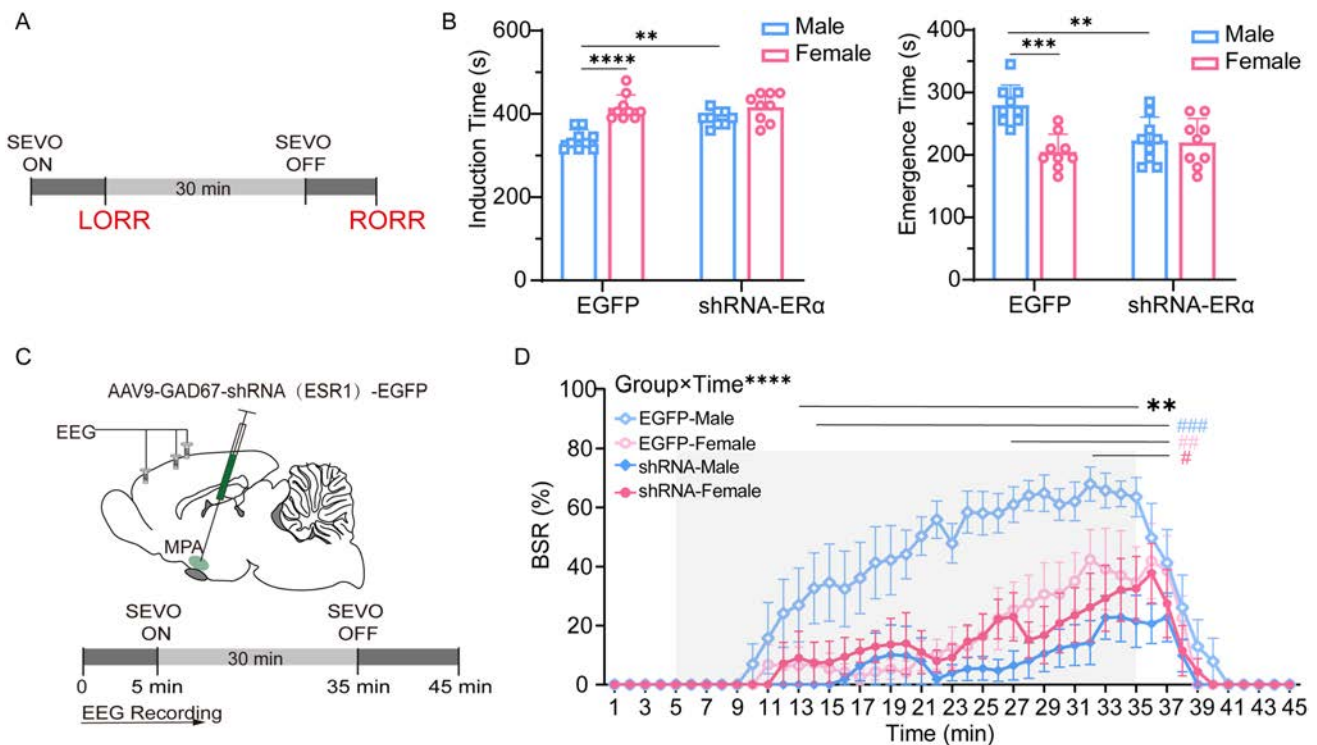


**Fig. 5** ER $\alpha$  knockdown in MPA GABAergic neurons eliminates the significant gender difference of sevoflurane anesthesia in mice. **A** Protocol for measurement of induction and emergence times. **B** Induction (left) and emergence (right) times in male and female mice in the EGFP and shRNA-ER $\alpha$  group. Using two-way ANOVA followed by *post hoc* Bonferroni's multiple comparisons:  $F_{1,32} = 7.423$ ,  $P = 0.0103$ ;  $t_{32} = 5.908$  (EGFP: male vs EGFP: female),  $P < 0.0001$ ;  $t_{32} = 3.981$  (EGFP: male vs shRNA-ER $\alpha$ : male),  $P = 0.0022$  for induction time (left);  $F_{1,32} = 9.968$ ,  $P = 0.0035$ ;  $t_{32} = 4.673$  (EGFP: male vs EGFP: female),  $P = 0.0003$ ;  $t_{32} = 3.530$  (EGFP: male vs shRNA-ER $\alpha$ : male),  $P = 0.0077$  for emergence time (right).

underlying relationship between MPA ER $\alpha$  and temperature elevation in females requires further discussion. First, MPA neurons that regulate anesthesia may not completely overlap with those regulating body temperature. We only recorded the APs in a small population of glutamatergic and GABAergic neurons co-expressing ER $\alpha$ . More importantly, we only recorded APs in neurons that were confined to the MPA, but did not observe that in ventrolateral preoptic nucleus (VLPO). Because of the diffusion of MPP, the VLPO might be involved in the change of temperature in male and female mice, and previous research has reported that modulation of neurons in the VLPO does not alter anesthetic induction or recovery time, while the body temperature changes strikingly [35].

This study has some limitations. We only found sex differences in mice under sevoflurane anesthesia, while different anesthetics with distinct molecular or neural targets may have different effects in the sexes. Because we did not monitor the estrus cycle of the female mice, we do not know yet how much dispersion the fluctuations of sex

**C** Diagram of a coronal brain section showing virus injection into the MPA of a C57BL/6 mouse (upper) and schematic protocol for EEG recording (lower). **D** BSR throughout a 45-min electroencephalogram recording in EGFP-Male, EGFP-Female, shRNA-Male, and shRNA-Female groups. BSR is calculated every one minute. Using two-way ANOVA followed by *post hoc* Bonferroni's multiple comparisons:  $F_{132,880} = 2.901$ ,  $P < 0.0001$ . \*Significant difference between male-vehicle and male-MPP groups; #significant difference from the initial value. SEVO, sevoflurane; BSR, burst suppression ratio; LORR, loss of righting reflex; RORR, recovery of righting reflex; MPA, medial preoptic area; EEG, electroencephalogram.

hormone levels could have contributed to the results in females. In addition, we only focused on the role of ER $\alpha$  in the MPA, but other subtypes of ER, such as ER $\beta$  and G protein-coupled ER (also known as GPR30) may have their own effect on sex differences in general anesthesia. Pharmacokinetic gender disparities are prevalent within the respiratory, renal, and endocrine systems. As we did not assess these differences, we could not determine how much the peripheral pharmacokinetic differences affect the sex differences in response to general anesthesia in this study. All of these limitations need to be addressed in future studies.

In conclusion, our study confirmed sex differences in response to sevoflurane anesthesia and found that male mice were more sensitive to sevoflurane anesthesia than females. The ER $\alpha$  of GABAergic neurons in the MPA plays a regulatory role in the anesthesia sensitivity of male mice, which contributes to the sex difference in sevoflurane anesthesia.

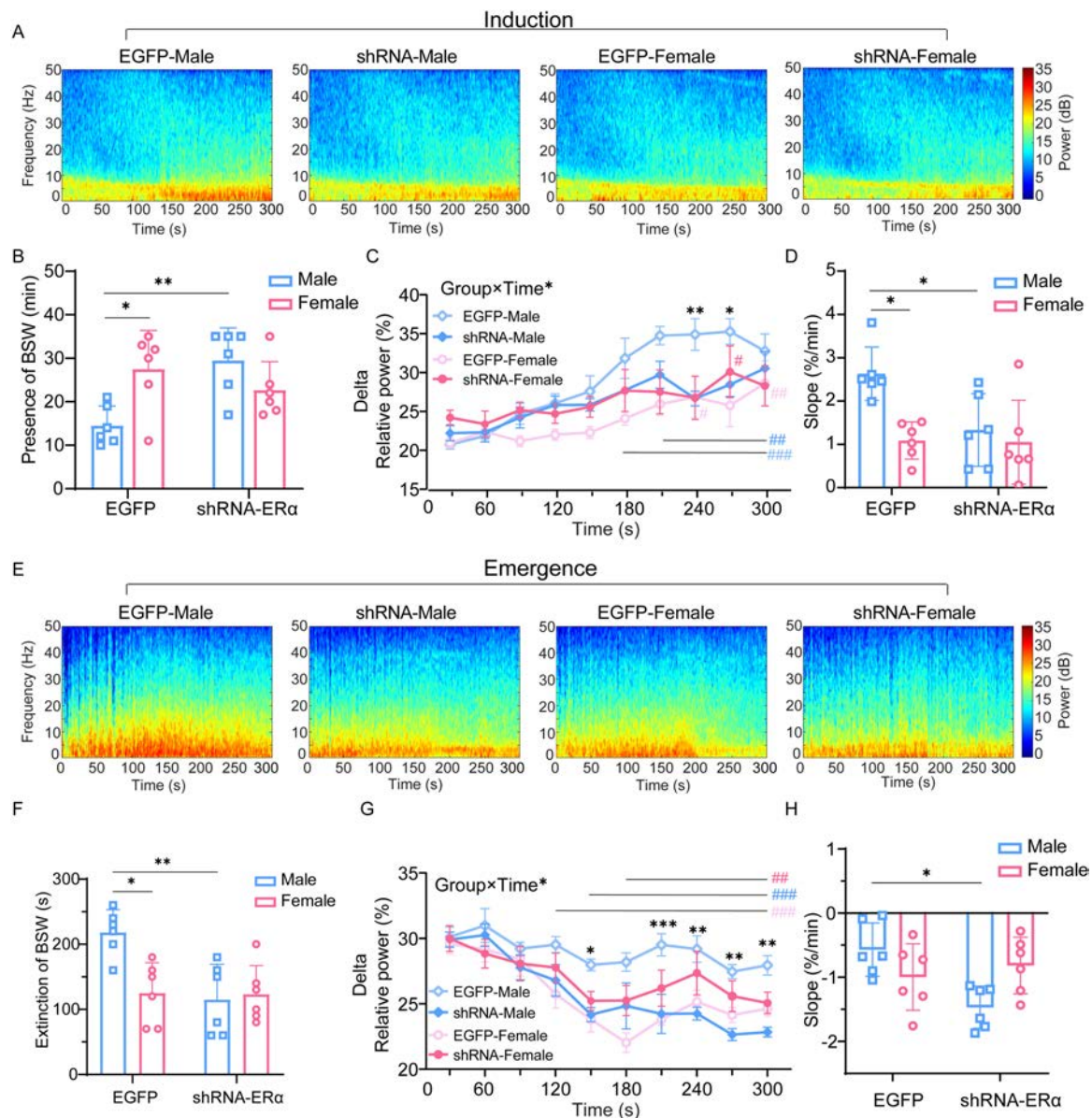


**Fig. 6** ER $\alpha$  knockdown in MPA GABAergic neurons affects the evolution of EEG signatures during sevoflurane anesthesia in males. **A**, **E** Averaged spectra in EGFP-Male, EGFP-Female, shRNA-Male, shRNA-Female groups during induction (**A**, 5 min after administration of sevoflurane) and emergence (**E**, 5 min after cessation of administration). **B**, **F** Presence (**B**) and extinction (**F**) of BSR in male and female mice in the EGFP and shRNA-ER $\alpha$  groups. Using two-way ANOVA followed by *post hoc* Bonferroni's multiple comparisons:  $F_{1,20} = 11.87$ ,  $P = 0.0026$ ;  $t_{20} = 3.194$  (EGFP: male vs EGFP: female),  $P = 0.0273$ ;  $t_{20} = 3.686$  (EGFP: male vs shRNA-ER $\alpha$ : male),  $P = 0.0088$  for presence of BSR;  $F_{1,20} = 7.469$ ,  $P = 0.0128$ ;  $t_{20} = 3.548$  (EGFP: male vs EGFP: female),  $P = 0.0121$ ;  $t_{20} = 3.928$  (EGFP: male vs shRNA-ER $\alpha$ : male),  $P = 0.0050$  for extinction of BSR. **C**, **G** Spectral analysis of relative power in the delta band in EGFP-Male, EGFP-Female, shRNA-Male, shRNA-Female groups ( $n = 6$ ) during induction

(**C**, 5 min after administration of sevoflurane) and emergence (**G**, 5 min after cessation of administration). The relative delta power is computed every 30 s. Using two-way ANOVA followed by *post hoc* Bonferroni's multiple comparisons:  $F_{27,180} = 1.750$ ,  $P = 0.0171$  for induction (**C**);  $F_{27,180} = 1.550$ ,  $P = 0.0496$  for emergence (**G**). **D**, **H** Relative power transition rate in the delta band in EGFP-Male, EGFP-Female, shRNA-Male, shRNA-Female groups ( $n = 6$ ) during induction (**D**) and emergence (**H**). Using two-way ANOVA followed by *post hoc* Bonferroni's multiple comparisons:  $F_{1,20} = 4.335$ ,  $P = 0.0504$ ;  $t_{20} = 3.600$  (EGFP: male vs EGFP: female),  $P = 0.0107$ ;  $t_{20} = 3.033$  (EGFP: male vs shRNA-ER $\alpha$ : male),  $P = 0.0395$  for induction (**D**);  $F_{1,20} = 9.373$ ,  $P = 0.0062$ ;  $t_{20} = 3.606$  (EGFP: male vs shRNA-ER $\alpha$ : male),  $P = 0.0106$  for emergence (**H**). \*Significant difference between male-vehicle and male-MPP groups; #significant difference from initial value. BSW, burst suppression wave.



**Acknowledgements** This work was supported by the National Natural Science Foundation of China (82071554 and 81620108012).

**Conflict of interest** The authors declare no potential conflict of interest.

**Open Access** This article is licensed under a Creative Commons Attribution 4.0 International License, which permits use, sharing, adaptation, distribution and reproduction in any medium or format, as long as you give appropriate credit to the original author(s) and the source, provide a link to the Creative Commons licence, and indicate if changes were made. The images or other third party material in this article are included in the article's Creative Commons licence, unless indicated otherwise in a credit line to the material. If material is not included in the article's Creative Commons licence and your intended use is not permitted by statutory regulation or exceeds the permitted use, you will need to obtain permission directly from the copyright holder. To view a copy of this licence, visit <http://creativecommons.org/licenses/by/4.0/>.

## References

1. Franks NP. General anaesthesia: From molecular targets to neuronal pathways of sleep and arousal. *Nat Rev Neurosci* 2008, 9: 370–386.
2. Brown EN, Lydic R, Schiff ND. General anesthesia, sleep, and coma. *N Engl J Med* 2010, 363: 2638–2650.
3. Wang D, Guo QC, Zhou Y, Xu Z, Hu SW, Kong XX. GABAergic neurons in the dorsal-intermediate lateral septum regulate sleep-wakefulness and anesthesia in mice. *Anesthesiology* 2021, 135: 463–481.
4. Reitz SL, Wasilczuk AZ, Beh GH, Proekt A, Kelz MB. Activation of preoptic tachykinin 1 neurons promotes wakefulness over sleep and volatile anesthetic-induced unconsciousness. *Curr Biol* 2021, 31: 394–405.e4.
5. Pleym H, Spigset O, Kharasch ED, Dale O. Gender differences in drug effects: Implications for anesthesiologists. *Acta Anaesthesiol Scand* 2003, 47: 241–259.
6. Gan TJ, Glass PS, Sigl J, Sebel P, Payne F, Rosow C, *et al.* Women emerge from general anesthesia with propofol/alfentanil/nitrous oxide faster than men. *Anesthesiology* 1999, 90: 1283–1287.
7. Hoymork SC, Raeder J. Why do women wake up faster than men from propofol anaesthesia? *Br J Anaesth* 2005, 95: 627–633.
8. Myles PS, McLeod AD, Hunt JO, Fletcher H. Sex differences in speed of emergence and quality of recovery after anaesthesia: Cohort study. *BMJ* 2001, 322: 710–711.
9. Kodaka M, Johansen JW, Sebel PS. The influence of gender on loss of consciousness with sevoflurane or propofol. *Anesth Analg* 2005, 101: 377–381.
10. Fink G, Sarkar DK, Dow RC, Dick H, Borthwick N, Malnick S, *et al.* Sex difference in response to alphaxalone anaesthesia may be oestrogen dependent. *Nature* 1982, 298: 270–272.
11. Torbati D, Ramirez J, Hon E, Camacho MT, Sussmane JB, Raszynski A, *et al.* Experimental critical care in rats: Gender differences in anesthesia, ventilation, and gas exchange. *Crit Care Med* 1999, 27: 1878–1884.
12. Mansouri MT, Fidler JA, Meng QC, Eckenhoff RG, García PS. Sex effects on behavioral markers of emergence from propofol and isoflurane anesthesia in rats. *Behav Brain Res* 2019, 367: 59–67.
13. Buchanan FF, Myles PS, Cicuttini F. Effect of patient sex on general anaesthesia and recovery. *Br J Anaesth* 2011, 106: 832–839.
14. Sarangapani R, Gentry PR, Covington TR, Teeguarden JG, Clewell HJ 3rd. Evaluation of the potential impact of age- and gender-specific lung morphology and ventilation rate on the dosimetry of vapors. *Inhal Toxicol* 2003, 15: 987–1016.
15. Reckelhoff JF, Hennington BS, Moore AG, Blanchard EJ, Cameron J. Gender differences in the renal nitric oxide (NO) system: Dissociation between expression of endothelial NO synthase and renal hemodynamic response to NO synthase inhibition. *Am J Hypertens* 1998, 11: 97–104.
16. Loryan I, Lindqvist M, Johansson I, Hiratsuka M, van der Heiden I, van Schaik RH, *et al.* Influence of sex on propofol metabolism, a pilot study: Implications for propofol anesthesia. *Eur J Clin Pharmacol* 2012, 68: 397–406.
17. Kotani K, Tokunaga K, Fujioka S, Kobatake T, Keno Y, Yoshida S, *et al.* Sexual dimorphism of age-related changes in whole-body fat distribution in the obese. *Int J Obes Relat Metab Disord* 1994, 18: 207–202.
18. Tontisirin N, Muangman SL, Suz P, Pihoker C, Fisk D, Moore A, *et al.* Early childhood gender differences in anterior and posterior cerebral blood flow velocity and autoregulation. *Pediatrics* 2007, 119: e610–e615.
19. Vuyk J, Oostwouder CJ, Vletter AA, Burm AG, Bovill JG. Gender differences in the pharmacokinetics of propofol in elderly patients during and after continuous infusion. *Br J Anaesth* 2001, 86: 183–188.
20. Gandhi M, Aweeka F, Greenblatt RM, Blaschke TF. Sex differences in pharmacokinetics and pharmacodynamics. *Annu Rev Pharmacol Toxicol* 2004, 44: 499–523.
21. Chan MT, Gin T. Postpartum changes in the minimum alveolar concentration of isoflurane. *Anesthesiology* 1995, 82: 1360–1363.
22. Erden V, Yangn Z, Erkalp K, Delatioğlu H, Bahçeci F, Seyhan A. Increased progesterone production during the luteal phase of menstruation may decrease anesthetic requirement. *Anesth Analg* 2005, 101: 1007–1011.
23. Gin T, Chan MT. Decreased minimum alveolar concentration of isoflurane in pregnant humans. *Anesthesiology* 1994, 81: 829–832.
24. Manber R, Armitage R. Sex, steroids, and sleep: A review. *Sleep* 1999, 22: 540–555.
25. Palahniuk RJ, Shnider SM, Eger EI 2nd. Pregnancy decreases the requirement for inhaled anesthetic agents. *Anesthesiology* 1974, 41: 82–83.
26. Pfaff DW, McEwen BS. Actions of estrogens and progestins on nerve cells. *Science* 1983, 219: 808–814.
27. Söderpalm AH, Lindsey S, Purdy RH, Hauger R, de Wit H. Administration of progesterone produces mild sedative-like effects in men and women. *Psychoneuroendocrinology* 2004, 29: 339–354.
28. Walle UK, Fagan TC, Topmiller MJ, Conradi EC, Walle T. The influence of gender and sex steroid hormones on the plasma binding of propranolol enantiomers. *Br J Clin Pharmacol* 1994, 37: 21–25.
29. McCarthy MM, Arnold AP. Reframing sexual differentiation of the brain. *Nat Neurosci* 2011, 14: 677–683.
30. Wei YC, Wang SR, Jiao ZL, Zhang W, Lin JK, Li XY, *et al.* Medial preoptic area in mice is capable of mediating sexually dimorphic behaviors regardless of gender. *Nat Commun* 2018, 9: 279.
31. Xu XH, Coats JK, Yang CF, Wang A, Ahmed OM, Alvarado M, *et al.* Modular genetic control of sexually dimorphic behaviors. *Cell* 2012, 148: 596–607.
32. Merchenthaler I, Lane MV, Numan S, Dellovade TL. Distribution of estrogen receptor alpha and beta in the mouse central nervous system: *In vivo* autoradiographic and immunocytochemical analyses. *J Comp Neurol* 2004, 473: 270–291.

33. Moffitt JR, Bambah-Mukku D, Eichhorn SW, Vaughn E, Shekhar K, Perez JD, *et al.* Molecular, spatial, and functional single-cell profiling of the hypothalamic preoptic region. *Science* 2018, 362: eaau5324.
34. Zhang Z, Reis FMCV, He YL, Park JW, DiVittorio JR, Sivakumar N, *et al.* Estrogen-sensitive medial preoptic area neurons coordinate torpor in mice. *Nat Commun* 2020, 11: 6378.
35. Vanini G, Bassana M, Mast M, Mondino A, Cerda I, Phyle M, *et al.* Activation of preoptic GABAergic or glutamatergic neurons modulates sleep-wake architecture, but not anesthetic state transitions. *Curr Biol* 2020, 30: 779–787.e4.
36. Walter A, van der Spek L, Hardy E, Bemelmans AP, Rouach N, Rancillac A. Structural and functional connections between the median and the ventrolateral preoptic nucleus. *Brain Struct Funct* 2019, 224: 3045–3057.
37. Weber F, Dan Y. Circuit-based interrogation of sleep control. *Nature* 2016, 538: 51–59.
38. Mondino A, Hambrecht-Wiedbusch VS, Li D, York AK, Pal D, González J, *et al.* Glutamatergic neurons in the preoptic hypothalamus promote wakefulness, destabilize NREM sleep, suppress REM sleep, and regulate cortical dynamics. *J Neurosci* 2021, 41: 3462–3478.
39. McCarren HS, Chalifoux MR, Han B, Moore JT, Meng QC, Baron-Hionis N, *et al.*  $\alpha$ 2-adrenergic stimulation of the ventrolateral preoptic nucleus destabilizes the anesthetic state. *J Neurosci* 2014, 34: 16385–16396.
40. Li KY, Guan YZ, Krnjević K, Ye JH. Propofol facilitates glutamatergic transmission to neurons of the ventrolateral preoptic nucleus. *Anesthesiology* 2009, 111: 1271–1278.
41. Yuan J, Luo Z, Zhang Y, Zhang Y, Wang Y, Cao S, *et al.* GABAergic ventrolateral pre-optic nucleus neurons are involved in the mediation of the anesthetic hypnosis induced by propofol. *Mol Med Rep* 2017, 16: 3179–3186.
42. Musatov S, Chen W, Pfaff DW, Kaplitt MG, Ogawa S. RNAi-mediated silencing of estrogen receptor alpha in the ventromedial nucleus of hypothalamus abolishes female sexual behaviors. *Proc Natl Acad Sci USA* 2006, 103: 10456–10460.
43. Zang KK, Xiao X, Chen LQ, Yang Y, Cao QL, Tang YL, *et al.* Distinct function of estrogen receptors in the rodent anterior cingulate cortex in pain-related aversion. *Anesthesiology* 2020, 133: 165–184.
44. Zhang HP, Cilz NI, Yang CX, Hu BQ, Dong HL, Lei SB. Depression of neuronal excitability and epileptic activities by group II metabotropic glutamate receptors in the medial entorhinal cortex. *Hippocampus* 2015, 25: 1299–1313.
45. Cilz NI, Kurada L, Hu BQ, Lei SB. Dopaminergic modulation of GABAergic transmission in the entorhinal cortex: Concerted roles of  $\alpha$ 1 adrenoreceptors, inward rectifier  $K^+$ , and T-type  $Ca^{2+}$  channels. *Cereb Cortex* 2014, 24: 3195–3208.
46. Zhao SY, Wang S, Li HM, Guo J, Li JN, Wang D, *et al.* Activation of orexinergic neurons inhibits the anesthetic effect of desflurane on consciousness state via paraventricular thalamic nucleus in rats. *Anesth Analg* 2021, 133: 781–793.
47. Saegusa Y, Tabata H. Usefulness of infrared thermometry in determining body temperature in mice. *J Vet Med Sci* 2003, 65: 1365–1367.
48. Harding EC, Yu X, Miao A, Andrews N, Ma Y, Ye ZW, *et al.* A neuronal hub binding sleep initiation and body cooling in response to a warm external stimulus. *Curr Biol* 2018, 28: 2263–2273.e4.
49. Beery AK, Zucker I. Sex bias in neuroscience and biomedical research. *Neurosci Biobehav Rev* 2011, 35: 565–572.
50. Satta R, Certa B, He DH, Lasek AW. Estrogen receptor  $\beta$  in the nucleus accumbens regulates the rewarding properties of cocaine in female mice. *Int J Neuropsychopharmacol* 2018, 21: 382–392.
51. Vandegrift BJ, Hilderbrand ER, Satta R, Tai R, He DH, You C, *et al.* Estrogen receptor  $\alpha$  regulates ethanol excitation of ventral tegmental area neurons and binge drinking in female mice. *J Neurosci* 2020, 40: 5196–5207.
52. Khariv V, Acioglu C, Ni L, Ratnayake A, Li L, Tao YX, *et al.* A link between plasma membrane calcium ATPase 2 (PMCA2), estrogen and estrogen receptor  $\alpha$  signaling in mechanical pain. *Sci Rep* 2018, 8: 17260.
53. Rowan MP, Berg KA, Roberts JL, Hargreaves KM, Clarke WP. Activation of estrogen receptor  $\alpha$  enhances bradykinin signaling in peripheral sensory neurons of female rats. *J Pharmacol Exp Ther* 2014, 349: 526–532.
54. Ter Horst JP, de Kloet ER, Schächinger H, Oitzl MS. Relevance of stress and female sex hormones for emotion and cognition. *Cell Mol Neurobiol* 2012, 32: 725–735.
55. Wilson ME, Westberry JM, Trout AL. Estrogen receptor-alpha gene expression in the cortex: Sex differences during development and in adulthood. *Horm Behav* 2011, 59: 353–357.
56. Paredes RG. Medial preoptic area/anterior hypothalamus and sexual motivation. *Scand J Psychol* 2003, 44: 203–212.
57. Yamaguchi T, Wei DY, Song SC, Lim B, Tritsch NX, Lin DY. Posterior amygdala regulates sexual and aggressive behaviors in male mice. *Nat Neurosci* 2020, 23: 1111–1124.
58. Kelly MJ, Moss RL, Dudley CA. The effects of microelectrophoretically applied estrogen, cortisol and acetylcholine on medial preoptic-septal unit activity throughout the estrous cycle of the female rat. *Exp Brain Res* 1977, 30: 53–64.
59. Kelly MJ, Moss RL, Dudley CA. Differential sensitivity of preoptic-septal neurons to microelectrophoresed estrogen during the estrous cycle. *Brain Res* 1976, 114: 152–157.
60. Kubo K, Gorski RA, Kawakami M. Effects of estrogen on neuronal excitability in the hippocampal-septal-hypothalamic system. *Neuroendocrinology* 1975, 18: 176–191.
61. Kelly MJ, Moss RL, Dudley CA, Fawcett CP. The specificity of the response of preoptic-septal area neurons to estrogen: 17 $\alpha$ -estradiol versus 17 $\beta$ -estradiol and the response of extrahypothalamic neurons. *Exp Brain Res* 1977, 30: 43–52.
62. Huang GZ, Woolley CS. Estradiol acutely suppresses inhibition in the hippocampus through a sex-specific endocannabinoid and mGluR-dependent mechanism. *Neuron* 2012, 74: 801–808.
63. Tabatadze N, Huang GZ, May RM, Jain A, Woolley CS. Sex differences in molecular signaling at inhibitory synapses in the hippocampus. *J Neurosci* 2015, 35: 11252–11265.
64. Oberlander JG, Woolley CS. 17 $\beta$ -estradiol acutely potentiates glutamatergic synaptic transmission in the hippocampus through distinct mechanisms in males and females. *J Neurosci* 2016, 36: 2677–2690.
65. Kim NR, Jardí F, Khalil R, Antonio L, Schollaert D, Deboel L, *et al.* Estrogen receptor alpha signaling in extrahypothalamic neurons during late puberty decreases bone size and strength in female but not in male mice. *FASEB J* 2020, 34: 7118–7126.
66. Balthazart J, Choleris E, Remage-Healey L. Steroids and the brain: 50 years of research, conceptual shifts and the ascent of non-classical and membrane-initiated actions. *Horm Behav* 2018, 99: 1–8.
67. Taxier LR, Gross KS, Frick KM. Oestradiol as a neuromodulator of learning and memory. *Nat Rev Neurosci* 2020, 21: 535–550.
68. Boulware MI, Weick JP, Becklund BR, Kuo SP, Groth RD, Mermelstein PG. Estradiol activates group I and II metabotropic glutamate receptor signaling, leading to opposing influences on cAMP response element-binding protein. *J Neurosci* 2005, 25: 5066–5078.
69. Dewing P, Boulware MI, Sinchak K, Christensen A, Mermelstein PG, Micevych P. Membrane estrogen receptor-alpha interactions with metabotropic glutamate receptor 1a modulate female sexual receptivity in rats. *J Neurosci* 2007, 27: 9294–9300.

70. Boulware MI, Heisler JD, Frick KM. The memory-enhancing effects of hippocampal estrogen receptor activation involve metabotropic glutamate receptor signaling. *J Neurosci* 2013, 33: 15184–15194.
71. Kahlert S, Nuedling S, van Eickels M, Vetter H, Meyer R, Grohe C. Estrogen receptor alpha rapidly activates the IGF-1 receptor pathway. *J Biol Chem* 2000, 275: 18447–18453.
72. Mendez P, Azcoitia I, Garcia-Segura LM. Estrogen receptor alpha forms estrogen-dependent multimolecular complexes with insulin-like growth factor receptor and phosphatidylinositol 3-kinase in the adult rat brain. *Brain Res Mol Brain Res* 2003, 112: 170–176.
73. Kramár EA, Babayan AH, Gall CM, Lynch G. Estrogen promotes learning-related plasticity by modifying the synaptic cytoskeleton. *Neuroscience* 2013, 239: 3–16.
74. Lu Q, Pallas DC, Surks HK, Baur WE, Mendelsohn ME, Karas RH. Striatin assembles a membrane signaling complex necessary for rapid, nongenomic activation of endothelial NO synthase by estrogen receptor alpha. *Proc Natl Acad Sci U S A* 2004, 101: 17126–17131.
75. Cabodi S, Moro L, Baj G, Smeriglio M, Di Stefano P, Gippone S, *et al.* p130Cas interacts with estrogen receptor alpha and modulates non-genomic estrogen signaling in breast cancer cells. *J Cell Sci* 2004, 117: 1603–1611.
76. Akama KT, McEwen BS. Estrogen stimulates postsynaptic density-95 rapid protein synthesis via the Akt/protein kinase B pathway. *J Neurosci* 2003, 23: 2333–2339.
77. Zhao ZR, Fan L, Frick KM. Epigenetic alterations regulate estradiol-induced enhancement of memory consolidation. *Proc Natl Acad Sci U S A* 2010, 107: 5605–5610.
78. Phan A, Gabor CS, Favaro KJ, Kaschack S, Armstrong JN, MacLusky NJ, *et al.* Low doses of 17 $\beta$ -estradiol rapidly improve learning and increase hippocampal dendritic spines. *Neuropsychopharmacology* 2012, 37: 2299–2309.
79. Woolley CS. Acute effects of estrogen on neuronal physiology. *Annu Rev Pharmacol Toxicol* 2007, 47: 657–680.
80. Kramár EA, Chen LY, Brandon NJ, Rex CS, Liu F, Gall CM, *et al.* Cytoskeletal changes underlie estrogen's acute effects on synaptic transmission and plasticity. *J Neurosci* 2009, 29: 12982–12993.
81. Liu M, Hu X, Liu J. The effect of hypothermia on isoflurane MAC in children. *Anesthesiology* 2001, 94: 429–432.

# Transcriptome Analysis of Schwann Cells at Various Stages of Myelination Implicates Chromatin Regulator Sin3A in Control of Myelination Identity

Bin Zhang<sup>1</sup> · Wenfeng Su<sup>1</sup> · Junxia Hu<sup>1</sup> · Jinghui Xu<sup>1</sup> · Parizat Askar<sup>1</sup> ·  
Shuangxi Bao<sup>1</sup> · Songlin Zhou<sup>1</sup> · Gang Chen<sup>1</sup> · Yun Gu<sup>1</sup>

Received: 29 July 2021 / Accepted: 13 December 2021 / Published online: 10 April 2022  
© Center for Excellence in Brain Science and Intelligence Technology, Chinese Academy of Sciences 2022

**Abstract** Enhancing remyelination after injury is of utmost importance for optimizing the recovery of nerve function. While the formation of myelin by Schwann cells (SCs) is critical for the function of the peripheral nervous system, the temporal dynamics and regulatory mechanisms that control the progress of the SC lineage through myelination require further elucidation. Here, using *in vitro* co-culture models, gene expression profiling of laser capture-microdissected SCs at various stages of myelination, and multilevel bioinformatic analysis, we demonstrated that SCs exhibit three distinct transcriptional characteristics during myelination: the immature, promyelinating, and myelinating states. We showed that suppressor interacting 3a (*Sin3A*) and 16 other transcription factors and chromatin regulators play important roles in the progress of myelination. *Sin3A* knockdown in the sciatic nerve or specifically in SCs reduced or delayed the myelination of regenerating axons in a rat crushed sciatic nerve model, while overexpression of *Sin3A* greatly

promoted the remyelination of axons. Further, *in vitro* experiments revealed that *Sin3A* silencing inhibited SC migration and differentiation at the promyelination stage and promoted SC proliferation at the immature stage. In addition, SC differentiation and maturation may be regulated by the *Sin3A*/histone deacetylase2 (HDAC2) complex functionally cooperating with Sox10, as demonstrated by rescue assays. Together, these results complement the recent genome and proteome analyses of SCs during peripheral nerve myelin formation. The results also reveal a key role of *Sin3A*-dependent chromatin organization in promoting myelinogenic programs and SC differentiation to control peripheral myelination and repair. These findings may inform new treatments for enhancing remyelination and nerve regeneration.

**Keywords** (Re)myelination · Schwann cells · *Sin3A* · Transcriptome · Peripheral nerve injury

Bin Zhang and Wenfeng Su contributed equally to this work.

**Supplementary Information** The online version contains supplementary material available at <https://doi.org/10.1007/s12264-022-00850-9>.

✉ Gang Chen  
chengang6626@ntu.edu.cn

✉ Yun Gu  
guyun@ntu.edu.cn

<sup>1</sup> Jiangsu Key Laboratory of Neuroregeneration, Co-innovation Center of Neuroregeneration, Jiangsu Clinical Medicine Center of Tissue Engineering and Nerve Injury Repair, NMPA Key Laboratory for Research, Evaluation of Tissue Engineering Technology Products, Nantong University, Nantong 226001, China

## Introduction

Myelination is a vital aspect of the development and function of the peripheral nervous system (PNS). The myelin sheath, formed by Schwann cells (SCs), is a specialized lamellar structure surrounding the axon that provides insulation and trophic support for the axon. Many pathological states, such as inherited neuropathies, infection, toxic agents, or trauma, can lead to myelin deficiency, and hence to severe neurological disability [1,2]. Despite the regenerative capacity of the PNS after injury, remyelination always occurs at a slow rate and is ultimately compromised. Consequently, the newly formed myelin sheath is thinner than the original myelin sheath, incapacitating sensorimotor functions [3,4]. Therefore, enhancing

remyelination after an injury is of utmost importance to optimize the recovery of nerve function. Currently, remyelinating therapies are being pursued as a repair strategy for preventing axonal degeneration by stimulation of endogenous cells, such as SCs, to improve their plasticity and/or remyelination capacity [5–8].

Remyelination is a coordinated molecular and cellular multistage process that occurs over a protracted period of time [9]. In response to injury, SCs dedifferentiate to an SC precursor state (immature SCs), undergo proliferation and expansion to break down myelin, and secrete various molecules to support axonal survival. They then differentiate into promyelinating cells to establish a one-to-one relationship with the axon, and further differentiate and eventually remyelinate axons in the regenerating nerve [3]. The efficacy of remyelination after the injury is therefore highly dependent on SC plasticity. Enhancing the knowledge of SC plasticity is key to the development of therapies that increase SC remyelination capacity. Previous studies have provided important insights into myelination and remyelination, based on gene expression profiling during PNS development and injury [10–12]. However, the temporal dynamics of extrinsic and intrinsic signals that govern SC plasticity and transitions are only partially understood.

The chromatin regulator suppressor interacting 3a (Sin3A) is a well-known master scaffold protein involved in the Sin3A/histone deacetylase (HDAC) complex and other histone deacetylase complexes, including nucleosome remodeling deacetylase and corepressor of repressor element-1 silencing transcription factor. Sin3A modifies chromatin structure and regulates multiple biological processes, such as cell proliferation, differentiation, apoptosis, and cell cycle progression, as well as early embryonic development [13–16]. Although initially identified as a repressor, Sin3A is now implicated in both positive and negative transcriptional regulation by tethering other factors to induce transcriptional silencing or promotion in a cell context-dependent manner [17]. Sin3A/HDAC is critical for mediating stage-specific neuronal gene expression and the sequential stages of neurogenesis [18,19]. Depletion of Sin3A in pluripotent P19 cells results in down-regulation of the repressive activity of repressor element-1 silencing transcription factor, which enhances the differentiation of pluripotent P19 cells into electrophysiologically active neurons [19]. Notably, no role of Sin3A in myelin formation and SC plasticity has been described to date.

Here, we present transcriptome analysis of the definitive SC lineage progression during myelination, gleaned from rigorously characterized immature (i.e., proliferating), promyelinating, and myelinating SC populations. We demonstrated that *Sin3A* is essential for SC myelination

and myelin regeneration after nerve injury. We found that Sin3A established chromatin interaction loops between HDAC2 and Sox10 (a key pro-myelinogenic factor) to activate the transcriptional program associated with positive regulation of SC maturation. These findings demonstrate that enhancement of *Sin3A* expression in SCs within a specific time window after nerve injury may be an effective approach to facilitate nerve regeneration and remyelination.

## Materials and Methods

### Schwann Cell–DRG Neuron Co-culture

Purified SCs and DRG neurons were isolated and co-cultured as previously described [20]. Briefly, DRGs from embryonic day 14.5 (E14.5) were plated in Dulbecco's modified Eagle medium (DMEM)- high glucose (HG) (Gibco, Carlsbad, USA) containing 10% foetal bovine serum (FBS) (Gibco) and allowed to adhere within 24 h, then the medium was replaced with DRG purification medium, consisting of Neurobasal medium (NB, Gibco), 2% B27 (Invitrogen, Carlsbad, USA), 50 ng/mL nerve growth factor (NGF) (Sigma, St Louis, USA), and 2 mmol/L L-glutamine (Gln) (Life Technologies, Carlsbad, USA). Cultures were cycled on purification medium supplemented with 5-fluorodeoxyuridine and uridine (Sigma), both at 10  $\mu$ mol/L, with medium changes every 3 days, repeated 3 times to remove non-neuronal cells, and then kept in growth medium (NB, 2% B27, 50 ng/mL NGF, 2 mmol/L Gln) before the purified SCs were added.

SCs were isolated from sciatic nerves from 2-day-old rat pups as previously described [21]. Nerves were enzymatically dissociated in 1% collagenase and 0.125% trypsin (Roche, Indianapolis, USA). The mixture was triturated, filtered, centrifuged, and re-suspended in 5 mL of SC medium (DMEM, 10% FBS, and penicillin-streptomycin), and then plated into poly-L-lysine (PLL, Sigma) pre-coated dishes. The next day, 10 mmol/L cytosine arabinoside was added and the cells were incubated for an additional 24 h to remove fibroblasts. After this, the medium was replaced with DMEM supplemented with 10% FBS, 2 mmol/L forskolin (Sigma), and 2 ng/mL heregulin (R&D, Minneapolis, USA) to stimulate cell proliferation. When the cells covered 90% of the dish surface, they were purified with an anti-Thy1 antibody (1:1000, AbDSerotec, Raleigh, USA). The purified SCs were typically cultured for an additional week before plating onto DRG neurons.

Myelinating co-cultures of SCs and DRG neurons were generated as previously described [20]. Approximately 50,000 SCs were seeded onto purified neuronal cultures and allowed to attach overnight in DMEM-HG medium



with 10% FBS. On the following day, the medium was replaced with DRG growth medium for 2 days to allow the SCs to repopulate the neurites and then switched to DMEM supplemented with 50 ng/mL NGF, ITS (a mixture of recombinant human insulin, human transferrin, and sodium selenite; Sigma), and 0.2% bovine serum albumin (Sigma) for ~4 days to initiate basal lamina formation, then the premyelinated co-cultures were maintained in DMEM containing 15% FBS, 50 ng/mL NGF, and 50 µg/mL L-ascorbic acid (Sigma) for 2–3 weeks until myelination was achieved.

### Myelinating SC Isolation by Laser Capture Microdissection (LCM)

DRG neuron-SC co-cultures were cultivated and multiplied in special Petri dishes with a polyethylene naphthalate (PEN) film bottom; they were microdissected in live-cell cutting (LCC) modules. In the co-cultures, appropriate SCs (myelinating SCs at different stages) were selected on a computer-controlled inverted microscope with a stage incubator that created a physiological atmosphere for the preparations (Cell Observer, Zeiss, Oberkochen, Germany); their coordinates were recorded to serve as a reference. During selection, any SCs exhibiting signs of stress, such as vacuoles, blebs, or deformed membranes, were excluded. LCM (LMD7000, Leica) was used to dissect the myelinating SCs at different stages by ultraviolet laser (laser power set to 2.2–3.2 mW) and attached to CapSure LCM caps with the help of infrared laser (power set to 80%). Caps were collected in 0.5 mL tubes containing 100 µL of RNeasy lysis buffer (Qiagen, Valencia, USA) and stored upside down at –80°C until RNA isolation.

### Microarray Hybridization and Analysis

The RNeasy Micro Kit (Qiagen) was used to collect and prepare total RNA for microarray analysis. The Input Quick Amp Labeling Kit (Agilent Technologies, Santa Clara, USA) was used for amplification and labeling. Gene expression profiling was performed on Agilent G4130F gene chips (design ID: 014879) per standard protocol. Each sample of the co-culture's six time-points (1, 3, 7, 14, and 21 days) and control (0 day, i.e. purified SCs) was tested in triplicate. All microarray experiments were conducted in the National Engineering Center for Biochips in Shanghai, China. The GeneChip microarray data have been deposited in the NCBI Gene Expression Omnibus (GEO; <http://www.ncbi.nlm.nih.gov/geo/>) and are accessible through GEO Series accession number GSE163132.

### Bioinformatics Analysis

Unsupervised principal component analysis (PCA) clustering was performed in R (v3.6.0, R Foundation for Statistical Computing, TUNA Team, Tsinghua University, Beijing, China). Gene expression correlation between samples was calculated as the Pearson correlation coefficient and viewed as a heatmap. The R/BHC [22], fast Bayesian hierarchical clustering, was first used to analyze the data. In detail, the “limma R” package (linear models and empirical Bayes methods) was used to statistically analyze differentially expressed genes (DEGs) as previously described [23,24]. The expression levels of mRNAs at each time point were compared with control. Genes with a fold change >1.5 or <–1.5 and an adjusted  $P < 0.05$  after analysis were assigned as DEGs (Table S1.1). DEGs were clustered into 5 profiles through hierarchical clustering and agglomeration methods according to their expression (Table S1.2). Gene Ontology (GO) was applied to analyze the biological functions of the significantly different tendencies by using the “enrichment Analysis” function from the R Richment package (Table S1.3). Considering the correlation between different time points and gene expression, the algorithm in the time course (R package), a multivariate empirical Bayes statistic for replicated microarray time-course data was used to rank the genes in order by the significance of difference from high to low [22,25]. The probes with a limma  $P$ -value < 0.01 were filtered for the following weighted gene co-expression network analysis (WGCNA).

The gene co-expression network was constructed using R package WGCNA analysis [26]. After filtering genes, 3393 probes with Entrez gene annotations from the 18 samples were imported into WGCNA to construct co-expression modules. Briefly, expression correlation coefficients of the genes were calculated to select a threshold power of 14 that resulted in a scale-free topology. The network tree diagram was created using the average linkage hierarchical clustering of topological overlapping different similarity matrices (1-TOM). The genes with similar expression patterns were hierarchically clustered according to TOM dissimilarity, and genes were assigned to modules by using the “cutreeHybrid” function from the R package WGCNA analysis. The resulting 17 modules (Table S2.1) or groups of co-expressed genes ranging in size from 524 genes to 32 genes were used to calculate the module eigengenes (MEs), and the hub genes (highly connected genes) in a given module were filtered according to the intra-modular connectivity and correlation with MEs. Pearson correlations between MEs and time points were calculated. Modules with eigengene connectivity (kME) >0.6 and a Bonferroni corrected  $P$ -value < 0.001 were considered to be time-specific modules, and nine modules

strongly associated with SC myelination were identified. GO and KEGG (Kyoto Encyclopedia of Genes and Genomes) pathway enrichment analyses were applied using the “enrichmentAnalysis” function from an R Richment package to identify the biological function of the significant modules associated with myelination at different stages (Table S2.2). All analysis results were summarized and visualized using Graph Visualization Software with the “circo” layout [27].

The upstream regulator analysis of the 9 specific modules obtained from WGCNA was performed using Ingenuity Pathway Analysis (IPA). The regulators, especially transcription factors (TFs), regulate the co-expressed genes participating in the same biological process (e.g. myelination). Here, we identified the upstream TFs in each module with a fold change of overlap  $\geq 1.5$  to explain the biological activity of each module (Table S3). For visual analysis of the constructed networks by hard thresholding of edge distances, the closest 150 edges were represented using Cytoscape 3.0.0 (The Cytoscape Consortium; <http://cytoscape.org/>, USA) [28].

### Animals, Surgical Procedure, and Virus Infection

All experimental procedures involving animals were performed in accordance with the National Institutes of Health Guide for the Care and Use of Laboratory Animals, and approved by the Nantong University Administration Committee of Experimental Animals.

Adult female Sprague-Dawley rats weighing 200–250 g provided by the Experimental Animal Center of Nantong University are used for sciatic nerve crush and virus infection; they were anesthetized with 3% isoflurane prior to surgery and during surgery. The sciatic nerve was exposed by making a skin incision and splitting apart the underlying muscles in the left lateral thigh. The virus, including adeno-associated virus (pAAV2/8-RNAi vector; Genechem Co., Shanghai, China) carrying the desired shRNA (at a final titer of  $5 \times 10^8$ , 5  $\mu$ L) or control sequence (at a final titer of  $5 \times 10^8$ , 5  $\mu$ L), the lentivirus vectors (LV, GL120, Genechem) carrying the coding sequence of the *Sin3A* (gene ID: NM\_001108761.1; at a final titer of  $2 \times 10^8$ , 5  $\mu$ L), and empty LV (at a final titer of  $2 \times 10^8$ , 5  $\mu$ L), were pressure-injected into the sciatic nerve as previously described [20,29]. Before suture, the syringe was held still for 2 min and then slowly retracted. The rats were kept on a heating pad throughout the surgery and recovery from anesthesia. The nerve crush experiments were carried out 3 weeks after virus injection. The sciatic nerve was exposed as above and crushed at the level of the sciatic notch for 30 s using a fine hemostat. In each sham rat, the sciatic nerve was exposed but not injured, and then the incision was sutured. Animals were housed and fed

routinely, and monitored for changes in their general condition.

### Cell Migration, Proliferation, and Differentiation Assays

SC migration was routinely assessed by using culture-inserts (Ibidi, DE, Germany) plated on 24-well plates. SCs (5,000 cells in 80  $\mu$ L of medium/side of Ibidi insert) were seeded and cultured in growth medium until attachment (24 h). After removing the culture-inserts, a cell-free gap is created in which the cell migration can be visualized. The two cell islands were washed with phosphate-buffered saline (PBS) to remove debris, and then cultured at 37°C in medium containing 2  $\mu$ g/mL mitomycin C (Sigma) for 24 h. Images were captured with a microscope (Leica Imaging Systems, Cambridge, England); the width of the separation wall was measured using ImageJ (National Institutes of Health, Bethesda, USA).

To mimic physiological conditions, SC migration was also assayed by using fasciculated DRG axons and reaggregated SCs as previously described [30]. DRGs were plated onto one side of a PLL-coated dish, in which axons extended and became fasciculated after 2–3 weeks. SC reagggregates were achieved by plating SCs on a non-permissive substrate overnight with gentle agitation every 2–3 h, and were then plated onto the fasciculated axons or PLL-coated coverslips. Individual SCs were allowed to migrate out of the reagggregates along the axons of DRGs for 24 h. Images were captured with a microscope (Leica); the distance of migration was calculated by measuring the size of the reagggregates using ImageJ.

The EdU DNA Cell Proliferation Kit (Ribobio, Guangzhou, China) was used to measure the proliferation rate of SCs as previously described [31]. Approximately 40,000 SCs were plated onto the fasciculated axons or PLL-coated coverslips in DMEM containing 10% FBS for 1 day, after which 50  $\mu$ mol/L EdU was added to the medium and incubated for 24 h. Then the cells were fixed with 4% formaldehyde in PBS for 30 min. EdU labeling was applied according to the manufacturer's instructions. Hoechst 33342 (1  $\mu$ g/mL, Sigma) was applied for cell nucleus staining. Images were captured with a deuterium magnetic resonance (DMR) fluorescence microscope (Leica Microsystems, Bensheim, Germany), and the percentage of cell proliferation was analyzed in 3 randomly-selected fields from 3 different wells (3 fields/well), and experiments were repeated 5–10 times.

SC differentiation was induced as previously described [31]. SCs were plated onto 24-well culture plates with PLL-coated coverslips at a density of  $\sim 10,000$  cells per 500  $\mu$ L in DMEM containing 10% FBS for 24 h. Afterwards, the medium was replaced with DMEM/F12

plus 1% FBS, 1 mmol/L db-cAMP (Sigma), and 20 ng/mL heregulin for 3 days to acquire a differentiated phenotype. Western blotting (WB) was carried out to analyze the expression of protein markers for myelinating/non-myelinating SCs, and cell morphology was analyzed by immunocytochemistry (ICC).

### RNA Interference

Short interfering RNA (siRNA) oligonucleotide duplexes targeting *Sin3A* used in this study were synthesized and purified by RiboBio (Guangzhou, China). The sequences of *Sin3A*-siRNAs were as follows: siRNA #1, 5'-CCCAAAGTATTAGTCTAA-3'; siRNA #2, 5'-CCAAATTTTCGCTTAGATAA-3'; siRNA #3, 5'-GCCTACATTGCCTTTACTA-3'. The siRNA transfection was performed using Lipofectamine RNAiMAX transfection reagent (Invitrogen, Carlsbad, USA) according to the manufacturer's instructions. Purified SCs were seeded at a density of  $3 \times 10^6$  cells/mL in 24-well plates and cultured for 24 h, after which they were transfected with siRNAs for *Sin3A* and non-targeting negative control. The knockdown efficiency was verified 48 h after transfection by WB. All the siRNAs were used at a final concentration of 10 nmol/L.

### Lentivirus Transfection *In Vitro*

Purified SCs were inoculated in 24-well plates at a density of  $1 \times 10^5$  cells per well and cultured for 24 h before infection. Lentiviral supernatant with the multiplicity of infection (MOI) at 20 and polybrene at a final concentration of 6  $\mu$ g/mL were added, after 12 h the lentiviral supernatant was replaced with fresh complete cell culture medium, and the cells were incubated for 72 h. The transfection efficiency was verified by WB.

### Western Blotting Analysis and Immunoprecipitation

For WB analysis, protein samples were prepared as previously described [31], after which they were separated by sodium dodecyl sulfate-polyacrylamide gel electrophoresis (SDS-PAGE) and transferred onto poly(vinylidene fluoride) (PVDF) membranes (Millipore, Bedford, USA). Following blocking in Tris-buffered saline (TBS, pH 7.6) containing 5% non-fat milk and 0.1% Tween-20, the blots were probed with primary antibodies at 4°C overnight, further incubated with horseradish peroxidase (HRP)-conjugated secondary antibody, and detected using a SuperSignal West Pico Chemiluminescent Substrate kit (Pierce). The images were scanned with a Bio-Rad GS800 Densitometer Scanner and processed for data analysis using PDQuest 7.2.0 software (Bio-Rad).

Immunoprecipitation (IP) was carried out using an IP assay kit following the manufacturer's instructions (Cell Signaling Technology, Beverly, USA). Briefly, 500  $\mu$ g of total cell or tissue lysates was incubated with appropriate antibodies overnight and subsequently rotated with proteinA/G beads for 2–4 h at 4°C. Beads were washed three times using NP-40 lysis buffer, and then resolved in  $2 \times$  SDS-PAGE sample buffer to be subjected to WB analysis.

### Immunocyto/Histochemistry

Cells were fixed with 4% paraformaldehyde (PFA) and then processed for ICC. After blocking in 5% normal donkey serum plus 0.1% Triton X-100 in PBS at room temperature (RT) for 30 min, the cells were incubated with primary antibodies (appropriate dilution) overnight at 4°C, followed by incubation with fluorescence-conjugated secondary antibodies (Jackson Immuno Research, West Grove, USA) at RT for 1 h. The cells were counterstained with Hoechst 33342 (Sigma) prior to visualization under a Zeiss fluorescence microscope and images were captured with a CCD Spot camera.

For immunohistochemistry (IHC), the animals were deeply anesthetized and perfused through the ascending aorta with PBS and 4% PFA. DRGs or sciatic nerves were then harvested and post-fixed in the same fixative overnight. Tissue sections (12  $\mu$ m) were cut on a cryostat and processed for IHC in a manner similar to the ICC protocol.

### Electron Microscopic Analysis

Scanning electron microscopy and transmission electron microscopy (TEM) were used to examine the co-cultures and nerve specimens treated with siRNA. Electron microscopy experiments were performed as previously described [21]. For scanning electron microscopy, samples were coated with gold using a JEOL JFC-110E Ion Sputter before observation under a Philips XL-30 scanning electron microscope (Eindhoven, The Netherlands). The TEM process was as follows: Samples (cell co-cultures embedded in an orientation of 1% agar; regenerated nerves), were fixed, dehydrated, embedded in Epon 812 epoxy resin, and cut into ultra-thin sections for staining with lead citrate and uranyl acetate. The stained specimens were observed under a TEM (JEOL Ltd., Tokyo, Japan), and subjected to morphometric analysis using Image-Pro Plus software (NIH Image, National Institutes of Health, Bethesda, USA).

### Quantification and Statistical Analysis

Data are expressed as the mean  $\pm$  SEM. One-way analysis of variance (ANOVA), two-way ANOVA, Mann-Whitney

two-tailed test, or *t*-test was used as indicated in the figure legends to test for statistical significance using GraphPad Prism (GraphPad Software Inc., San Diego, USA), *n*-values are indicated in the corresponding figure legends. Significance was placed at  $P < 0.05$  unless otherwise noted in the figure legends.

## Results

### Experimental Setup for the Analysis of Gene Expression in SCs Throughout Myelination in an SC-DRG Co-culture System

The SC-DRG co-culture system enables the observation and analysis of various stages of SC myelination [32]. In the current study, the purified DRG tissue (Fig. S1A) and SCs (Fig. S1B) were co-cultured for 21 days to assess the dynamics of myelinating SCs in this system. Specifically, upon contact with the axon (co-culture days 1–3), SCs proliferated and migrated rapidly along the available axons, and myelination was then induced by the addition of ascorbic acid. By day 7 of co-cultivation, SCs lined up along the axons and even enclosed them, but a myelin sheath was not formed. As the culture continued, on about day 14 of co-culture, the SC membrane began to spin a second cytoplasmic layer around the axon on some nerve fibers, which wrapped and spiraled until multiple myelin sheaths were formed by day 21 (Fig. 1A, B), as determined by immunofluorescence staining of the myelin-associated glycoprotein (MAG) and myelin basic protein (MBP) (Fig. 1C) or double-labeling of MAG and NF200 (Fig. S1C). In addition, TEM revealed the presence of a typical compact myelin structure on day 21 of co-culture (Fig. 1D). Based on these findings, we defined days 0–1, 3–7, and 14–21 of co-culture as the three stages of SC myelination (i.e., proliferation, promyelination, and myelination), which were further evidenced by the ensuing transcriptome analyses (see below).

Next, we used LCM to dissociate SCs at the different time points of co-culture (days 0, 1, 3, 7, 14, and 21), following a strict purification scheme based on morphological characteristics. We collected three biological replicates for each population. We then generated gene expression profiles using the Agilent gene chip and performed computational analyses, as described below.

### SCs Exist in Three Predominant Transcriptional States During Myelination

We used several bioinformatics (multivariate analysis) tools to identify transcriptional changes in SCs during myelination. Using Pearson's correlation coefficient of

transcriptomes for sample pairs in all combinations and unbiased hierarchical clustering of the complete dataset (18 samples), we divided the samples into three groups: group one, 0- and 1-day samples; group two, 3- and 7-day samples; and group three, 14- and 21-day samples (Fig. 2A). PCA revealed three distinct clusters of expression (0 and 1, 3 and 7, and 14 and 21 day clusters) during the 21-day co-culture period (Fig. 2B). These two approaches indicated the possibility of three main waves of transcription during the time course of SC myelination. Comparative analysis using the “limma R” package revealed 3,717 DEGs (Fig. 2C and Table S1.1) partitioned into five co-expression clusters (Bayesian hierarchical clustering, see Methods for details) with distinct temporal profiles (Table S1.2). We used GO to annotate the biological functions of these clusters (Table S1.3) and found that they corresponded to the following SC myelination stages: (I) proliferation (immature); (II) promyelination; and (III) myelination (Fig. 2D). Specifically, stage I was characterized by the cell cycle and cell division (Cluster 1). Stage II was marked by the c-Jun N-terminal kinases (JNK) cascade and cell morphogenesis involved in differentiation (Cluster 2), and other functions, including neutral lipid metabolic process, glial cell differentiation, and the myelin sheath (Cluster 3), which are associated with SC differentiation (i.e., promyelination). Finally, during the transition to stage III, establishment or maintenance of actin cytoskeleton polarity, ensheathment of neurons, and myelination were induced (Clusters 4 and 5); these processes play an important role in the formation and maturation of the myelin sheath. Consequently, we reasoned that SCs exhibit three predominant transcriptional states (proliferation, promyelination, and myelination) during myelination, which was in agreement with the SC behavior and the time course of myelination in the SC-DRG co-culture system.

Next, we used WGCNA to elucidate the stage-specific genes contributing to SC myelination. The analysis revealed 17 co-expression modules, each containing between 32 and 524 genes (Fig. S2A and Table S2.1). These were divided into three clusters based on module correlation (Fig. S2B). We summarized their expression patterns by calculating MEs (the first principal component of a given module, which can be considered as a representative of the gene expression profiles in a module; Fig. S2C). Based on ME correlation with the time-dependent changes during SC myelination, we identified nine modules that were significantly (Bonferroni corrected  $P$ -value  $< 0.001$ ) and positively associated with different stages of myelination, as follows (Fig. 3A, Table S2): two modules (turquoise and purple) were related to days 0 and 1 (stage I); five modules (green, brown, yellow, cyan, and salmon) were related to days 3 and 7 (stage II); and the

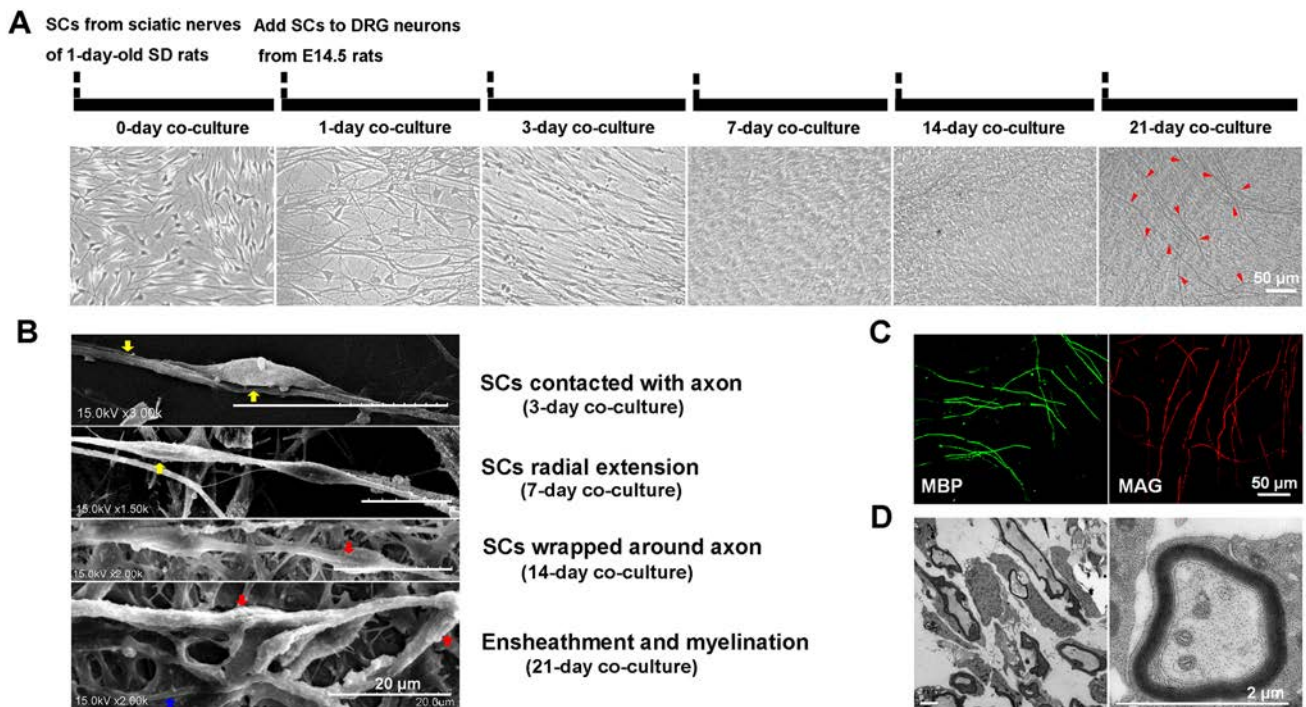


**Fig. 1** Time-course of SC myelination in the SC-DRG co-culture system. **A** Timeline for setting up the SC-DRG neuron co-culture. Representative phase-contrast microscopy images from the different stages of co-culture are shown under the timeline. Red arrowheads, myelin segments. Scale bar, 50  $\mu$ m. **B** Representative scanning electron micrographs of SCs at various time points of co-culture: yellow arrows, SCs that have contacted the axon and exhibit radial

extension; red arrows, SCs wrapped around and sheathing the axon; blue arrow, the axon unwrapped by myelin sheath. Scale bars, 20  $\mu$ m. **C** Immunocytochemistry with anti-MAG (red) and MBP (green) antibodies demonstrating myelin segments on day 21 of co-cultivation. Scale bar, 50  $\mu$ m. **D** Representative transmission electron micrographs from day 21 of co-culture, showing the myelin sheaths. Scale bars, 2  $\mu$ m.

remaining two modules (blue and magenta) were related to days 14 and 21 (stage III). We then annotated the shared functions of genes within these stage-specific modules using GO enrichment, as follows: stage I modules were enriched in the regulation of transcription, cell cycle, and cell proliferation/growth/migration functions; stage II modules were related to cell fraction/projection organization, cofactor binding, and myelination; and stage III modules corresponded to cell morphogenesis, ensheathment of neurons, and myelination. Data from the WGCNA transcriptome further evidenced three main waves of transcription during SC myelination in the SC-DRG co-culture system.

Considering the above, we concluded that three transcriptional phases occur in SCs, as the cells transition from an immature state ( $t = 0$  days) to myelination ( $t = 21$  days): stage I (days 0 and 1, proliferation), stage II (days 3 and 7, promyelination), and stage III (days 14 and 21, myelination).

### Identification of Known and Novel Transcriptional Regulators of SC Myelination

Differential regulation of many TFs during SC myelination has been reported in a number of studies [33–36]. To delineate the potential transcriptional regulatory network contributing to the reproducible co-expression of multiple genes during SC myelination, we first screened the known myelination-related genes in the nine specific modules by testing their association with the key terms “SC differentiation” and “myelination” in the PubMed database. We then applied TF binding site enrichment analysis of the resultant 117 genes and the top 20 DEGs identified in the current study (Table S3.1) by using two TF datasets (JASPAR and ConTraV3) to identify potential or novel myelin-related TFs. We thus identified 17 TFs significantly enriched in the nine modules (number of target genes >15, and fold change >1.5 compared with day 0; Table S3.2) and reconstructed a regulatory network by using IPA to screen the potential TF-target gene relationships during SC myelination (Fig. 3Bb2 and Table S3.3). Remarkably, seven TFs were associated with stage I (Kif7, E2f1, E2f8, Lef1, Fos11, and EGR1); six TFs were present in stage II (Sin3A, Egr2, Stat1, Etv1, ATF4, and Tcf712), the major



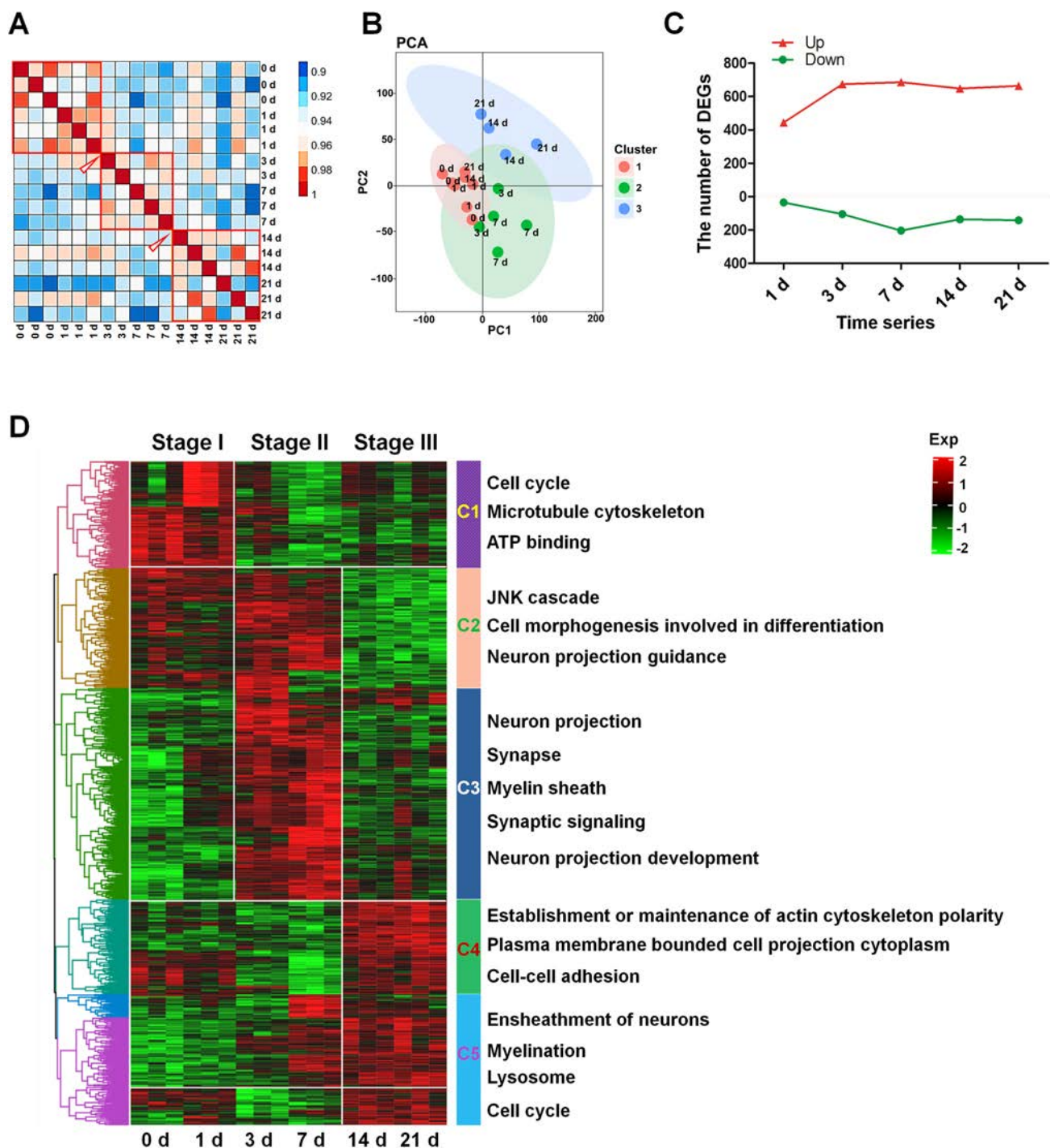


**Fig. 2** Overview of temporal expression profiles of SC myelination. **A** Pearson correlation coefficient analysis of the correlations of gene expression in SCs at various time points of co-culture with neurons. Two nodal transitions are detected between days 1 and 3 of co-culture and between days 7 and 14 of co-culture. Arrowheads, the transitions. **B** PCA plot of unsupervised clustering of 18 samples, demonstrating three distinct clusters, with some overlaps. **C** Differential gene expression (DEG) analysis vs day 0, showing the number of up-regulated (red) and down-regulated (green) DEGs. **D** Gene expression

profiles during SC myelination. Shown is the differential expression of genes (rows) at six time points (columns) relative to gene expression in the control [Exp, upper right,  $\log_2(\text{ratio})$ ]. The genes are partitioned into five clusters (c1–c5, color bars, right). GO-enriched functional annotations are denoted on the right, indicating three major transcriptional stages: stage I (c1; days 0–1, proliferation), stage II (c2 and c3; days 3 and 7, promyelination and myelination), and stage III (c4 and c5; days 14 and 21, myelination and maturation).

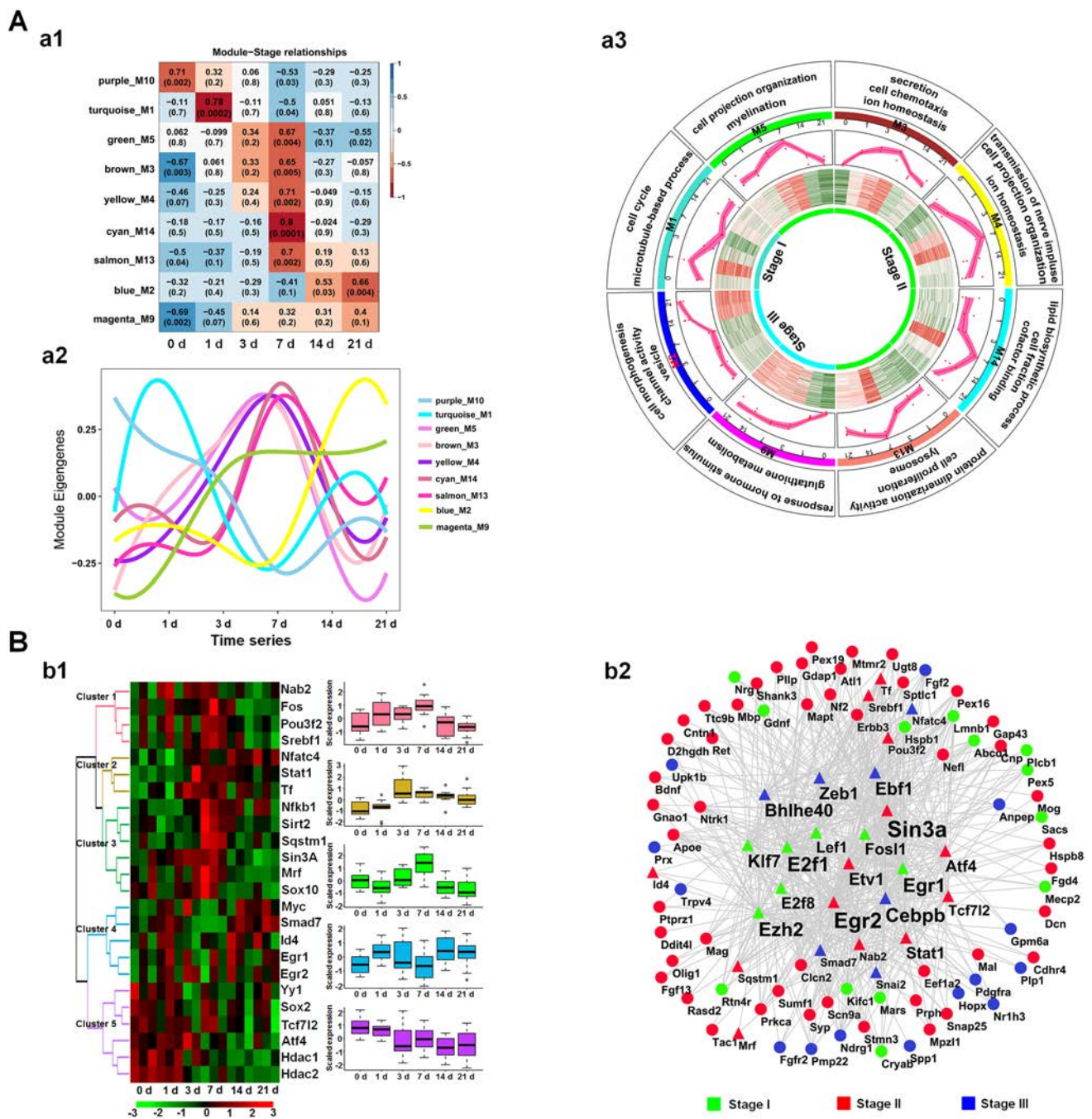


**Fig. 3** Establishment of gene modules underlying SC myelination using weighted gene co-expression network analysis (WGCNA), and identification of known and novel transcriptional regulators. **Aa1** Module-trait (time-point) associations. Each row corresponds to a module eigengene; each column corresponds to a time point. The colors, from blue through white to red, indicate low to high correlations. **Aa2** Eigengene expression of nine selected modules across six time points. **Aa3** Circular graph combining the information for the nine modules. First layer, the major function of genes in the module; second layer, the corresponding module and time-point information; third layer, the expression trend of the module over time;

fourth layer, the heat map of the changes of gene expression in the module; fifth layer, the three major transcriptional phases of SC myelination. **Bb1** Heat map of the changes in the expression of 24 signature TFs (rows) during SC myelination (columns). The genes are partitioned into five clusters. The box plots on the right: the expression of the cluster genes (X-axis, time points; Y-axis, scaled expression). **Bb2** Cascade network of genes for 17 differentially expressed TFs for SC myelination. The interaction network of TFs (solid triangles) and target genes (dots) at each stage of SC myelination (green: stage I; red: stage II; blue: stage III).

phase during SC myelination; and four TFs were related to stage III (Zeb1, Ebf1, Cebpb, and Bhlhe40). Among them, Sin3A, which had not been reported as related to myelination prior to the current study, aroused our interest. Accordingly, we proceeded to explore its effects on myelination in detail.

### Dynamic Expression and Cellular Location of Sin3A Following Sciatic Nerve Crush

We used a rat model of sciatic nerve crush (i.e., an *in vivo* myelination model) to determine the potential role of Sin3A in the control of SC remyelination *in vivo*. Initially, we examined Sin3A expression in a sciatic nerve lesion from days 1–28 after nerve crush by WB. We also assessed the levels of Egr2 (also known as Krox20) and MAG (myelin-associated glycoprotein), which are both involved in myelin formation. As shown in Fig. 4A, the relative Sin3A and Egr2 levels showed similar dynamics i.e., decreased levels on day 1 followed by a progressive increase until day 28. In addition, the expression of MAG started to decrease on day 1, reached a nadir on day 7, and then increased to reach peak expression on day 28. This was consistent with the myelin sheath decomposition and clearance at an early stage of nerve injury and with axon regeneration and remyelination at a late stage, and indicated that Sin3A might play a role similar to Egr2 in remyelination. Furthermore, the results of double immunostaining for Sin3A and S100 $\beta$  (an SC marker) in the crushed portion of the injured sciatic nerve revealed co-localization of Sin3A and S100 $\beta$  on day 1 until day 28 following the nerve crush (Fig. 4B), suggesting that Sin3A localized in SCs may affect demyelination early after nerve crush and during the ensuing remyelination.

### Sin3A Knockdown Inhibits Remyelination in a Regenerating Sciatic Nerve

To address the role of Sin3A in SC remyelination during peripheral nerve regeneration, we designed three different non-overlapping shRNAs against *Sin3A* and co-expressed them with GFP in an AAV expression system. The viruses carrying *Sin3A*-shRNAs and scrambled shRNA were injected into rat sciatic nerves to confirm the validity of the shRNAs and the virus transfection system. Sin3A expression was assessed 21 days after transfection. Sin3A expression was significantly attenuated by shRNA-1, -2, and -3, as demonstrated by WB analysis (Fig. S4). Since shRNA-3 led to an approximately four-fold decrease in Sin3A levels compared with the effect of scrambled shRNA, we used shRNA-3 in the ensuing experiments.

We subjected rats with Sin3A knockdown in the sciatic nerve to a nerve crush injury, and then assessed MAG and

P0 levels in the crushed nerve by WB (Fig. 5Aa1) and immunohistochemistry (Fig. 5Aa2) 28 days after the injury. The analysis revealed that both MAG and P0 levels were decreased in rats with Sin3A knockdown compared with those in controls. In addition, we used electron microscopy to observe the distribution of myelin sheaths in the experimental and control groups, and detected some myelinated nerve fibers, characterized by a clear, electron-dense myelin sheath and perfect SC basal membrane in both groups. Quantitative analysis revealed that the number of myelin sheath layers and the thickness of the myelin sheath were lower in the Sin3A knockdown rats than in those in the control group. Sin3A knockdown also significantly increased the *g*-ratio, which is a reliable index for assessing axonal myelination (Fig. 5Aa3). These results suggested that Sin3A affects SC remyelination.

Considering the diversity of cells in the sciatic nerve (SCs and fibroblasts), we then specifically knocked down Sin3A in SCs by using the 2',3'-cyclic nucleotide-3'-phosphodiesterase (CNPase) promoter to assess the role of Sin3A in SCs in remyelination. The CNPase promoter has been demonstrated to control gene expression restricted to cells of the oligodendroglia and Schwann lineages [37]. In this study, the green fluorescence (EGFP) was mainly co-localized with S100 $\beta$  (Fig. S4Bb1), and the double immunostaining results of Sin3A and S100 $\beta$  showed that CNPase-AAV-*Sin3A*-siRNA effectively knocked down the expression of Sin3A in SCs (Fig. S4Bb2), suggesting that CNPase-AAV is specific for SC infection. The effect of the SC-specific Sin3A knockdown was similar to that of the global Sin3A knockdown, showing a reduction in MAG and P0 levels, the number of myelin sheath layers, and the thickness of myelin sheath, as well as an increased *g*-ratio compared to those in the control group (Fig. 5B). Collectively, these results suggest that in SCs, Sin3A plays a major role in the initiation or formation of the myelin sheath during nerve regeneration.

### Sin3A Enhances SC Migration and Differentiation and Reduces SC Proliferation to Promote Myelination

Myelination is an organized process that includes SC proliferation, migration, differentiation, and wrapping. Accordingly, we next separately investigated the effects of Sin3A on SC proliferation, migration, and differentiation.

We first used insert-based scratch migration assays to investigate whether Sin3A affects SC migration. The wound area was analyzed 24 h post-migration. Sin3A knockdown in SCs resulted in an approximately six-fold increase in the percentage wound area compared with that in the negative control (Fig. 6Aa1, a2), indicating that Sin3A promotes SC migration. To mimic physiological



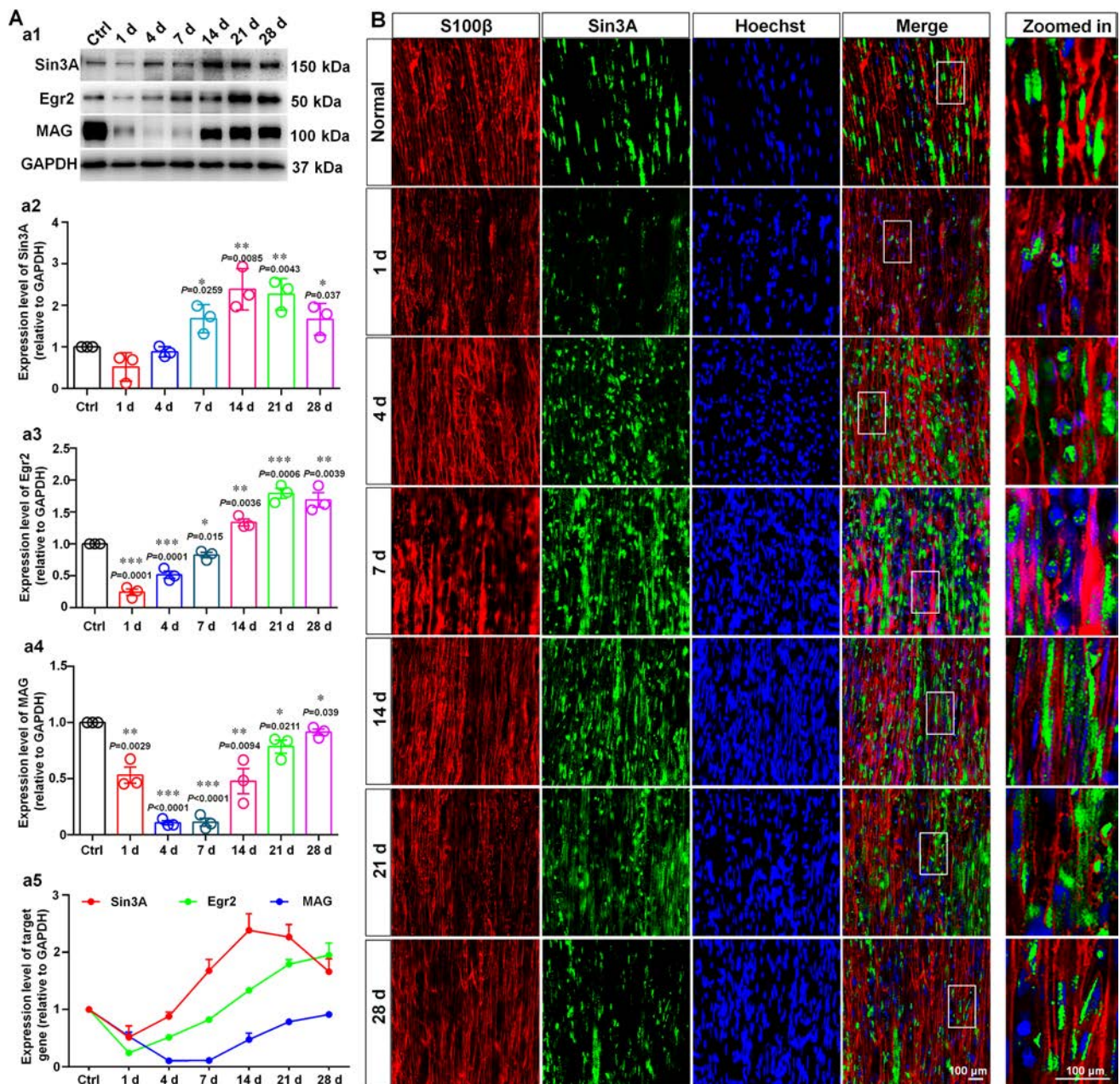


**Fig. 4** Expression dynamics and cellular location of Sin3A in a rat model of sciatic nerve crush. **Aa1** Representative Western blots showing Sin3A, MAG, and Egr2 levels in a regenerating nerve segment at days 1, 4, 7, 14, 21, and 28 following a nerve crush, with normal nerve used as the control (Ctrl). GAPDH served as the loading control. **Aa2–5** Histogram comparing the changes in protein levels of Sin3A, MAG, and Egr2 in a regenerating nerve segment at the indicated time points following a nerve crush.  $*P < 0.05$ ,  $**P < 0.01$ ,  $***P < 0.001$  vs control, one-way ANOVA,  $n = 3$  per group.

conditions, we then conducted another migration assay by incubating reaggregated SCs on fasciculated DRG axons or PLL, as previously described [30,31]. Similar to what was found in the scratch migration assays, Sin3A knockdown significantly inhibited SC migration from the reaggregates after 24 h of incubation under both culture conditions

(Fig. 6Aa3–6). These results suggested that endogenous Sin3A is a key regulator of SC migration because low Sin3A expression in SCs inhibited cell migration. We then evaluated the effect of Sin3A on SC proliferation by using an EdU labeling proliferation assay. SCs were transfected with *Sin3A*-siRNA or a non-targeting

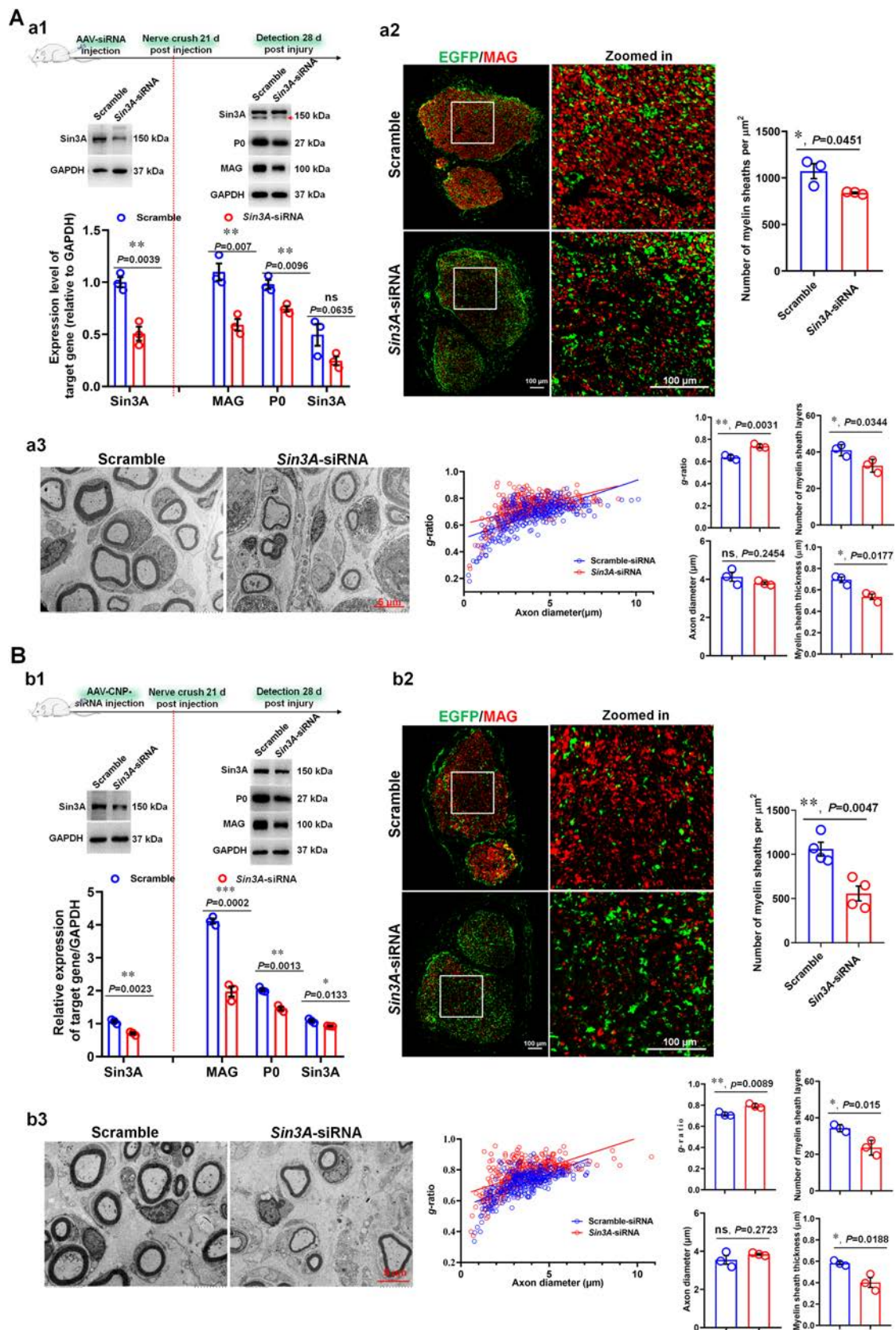




**Fig. 5** Sin3A knockdown inhibits remyelination in a rat model of sciatic nerve crush. **Aa1, Bb1** Western blots confirming the validity of the *Sin3A*-siRNA and virus transfection system 21 days after virus injection (on the left of the red dotted line), and comparison of the MAG, P0, and *Sin3A* levels in regenerated nerves treated with AAV-*Sin3A*-siRNA (**a1**) and AAV-CNP-*Sin3A*-siRNA (**b1**), 28 days after nerve injury (on the right of the red dotted line). Also shown are representative Western blots, with GAPDH serving as the internal standard. **Aa2, Bb2** Immunostaining with anti-MAG (red) antibody and EGFP fluorescence (green) indicating axon remyelination in regenerated nerves treated with AAV-*Sin3A*-siRNA (**a2**) and AAV-CNP-*Sin3A*-siRNA (**b2**). Also shown are high magnification images of the boxed areas. Scale bars, 100  $\mu$ m. Histograms comparing the density of myelin sheaths. \* $P < 0.05$  vs LV-Ctrl,  $t$ -test,  $n = 3$  per group. **Aa3, Bb3** Representative transmission electron micrographs, 28 days after surgery, of the regenerated nerve in rats treated with AAV-*Sin3A*-siRNA (**a3**) and AAV-CNP-*Sin3A*-siRNA (**b3**). Scale bars, 5  $\mu$ m. Histograms comparing the  $g$ -ratio, axon diameter, the number of myelin sheath layers, and the thickness of the myelin sheath. \* $P < 0.05$ , \*\* $P < 0.01$ , \*\*\* $P < 0.001$  vs scrambled,  $t$ -test,  $n = 3$  per group; ns, not significant.

negative control and cultured on PLL or fasciculated DRG axons. This was followed by EdU labeling and cell counting 24 h after the start of the culture. The number of cells double-labeled with EdU and Hoechst among SCs transfected with *Sin3A*-siRNA was significantly higher than that among SCs transfected with the negative control (Fig. 6B). This result suggests that *Sin3A* acts as a negative regulator of SC proliferation, regardless of whether the cells are cultured on PLL or DRG axons.

Finally, we examined the effect of *Sin3A* on SC differentiation using an *in vitro* SC differentiation assay [38]. First, 1 mmol/L dB-cAMP and 20 ng/mL HRG were added to SC culture to promote cell differentiation. After 3 days of induction, the cells were analyzed by WB and immunocytochemistry. The analysis revealed that the levels of myelin protein MAG and P0 were high and enriched in differentiated SCs (Fig. 6Cc1, c2), and that the expression of *Sin3A* increased with cell differentiation (Fig. 6Cc3). To characterize the effects of *Sin3A* on SC differentiation, we transfected SCs with *Sin3A*-siRNA or negative control and evaluated the expression of MAG after 48 h. We found that the expression of MAG during differentiation was lower in SCs with *Sin3A* knockdown than that in the control cells, indicating that *Sin3A* promotes SC differentiation (Fig. 6Cc4).

Taken together, the above results indicate that *Sin3A* is required for myelin formation, most likely because of its role in promoting SC migration and differentiation and inhibiting SC proliferation.

### **Sin3A Overexpression Enhances Remyelination *In Vivo* and SC Differentiation *In Vitro***

To further investigate the actions of *Sin3A* on remyelination, the lentivirus carrying the coding sequence of *Sin3A*

(LV-*Sin3A*) and lentivirus vector (LV-Ctrl) was injected into rat sciatic nerves and the *Sin3A* expression was assessed 14 days after transfection. As shown in Fig. 7Aa1, WB analysis showed the *Sin3A* expression was significantly stronger than that of the control, suggesting the validity of the virus transfection system. Next, rats that had been injected with LV-*Sin3A* or control virus for 14 days were subjected to sciatic nerve crush injury, and 28 days after the injury, the level of MAG in the crushed nerve was assessed by WB (Fig. 7Aa1) and immunohistochemistry (Fig. 7Aa2). The analysis revealed that MAG levels were increased in rats with *Sin3A* overexpression compared with those in controls. In addition, we evaluated the influence of *Sin3A* overexpression in SCs on their proliferation and differentiation. The results showed that the proportion of proliferative cells among SCs that had been transfected with LV-*Sin3A* was significantly lower than in SCs transfected with LV-Ctrl (Fig. 7B). Moreover, we also found that *Sin3A*-overexpressing SCs exhibited higher MAG expression levels during the process of differentiation compared to those of controls (Fig. 7C). Together, these results further suggest that *Sin3A* enhances myelin formation by promoting SC differentiation and inhibiting proliferation.

### **Sin3A Cooperates with HDAC2 and Sox10 to Promote SC Differentiation and Myelination**

*Sin3A* tethers HDAC1/2 to mediate the transcription of *Sin3A* target genes [17] and is associated with several TFs to modulate their activity [13]. Here, we first examined HDAC1/2 expression during nerve regeneration (Fig. 8Aa1) and in differentiating SCs (Fig. 8Bb1). As anticipated, HDAC1/2 expression was similar to that of *Sin3A*; namely, the expression levels gradually increased as the nerve regeneration and SC differentiation progressed. To explore other factors associated with *Sin3A* that might promote the transcriptional co-activation function of this complex, we applied co-immunoprecipitation and probed nerves that had been regenerating for 14 days (Fig. 8Aa2) and differentiating SCs (Fig. 8Bb2) with antibodies against *Sin3A*. This was followed by immunoblotting with antibodies against HDAC1, HDAC2, Sox10, and Egr2. As expected, the experiment confirmed the interaction of *Sin3A* with HDAC1/2 in the regenerating nerves and differentiating SCs, indicating the preservation of the *Sin3A*/HDAC complex in these cells. Surprisingly, we found that *Sin3A* and Egr2 do not physically interact; instead, *Sin3A* binds to Sox10. This suggested that *Sin3A* regulates SC differentiation and myelination by interacting with HDAC1/2 and Sox10, but not Egr2.

To further address the role of *Sin3A* in the complex (including *Sin3A*, HDAC1/2, and Sox10) in synergistically

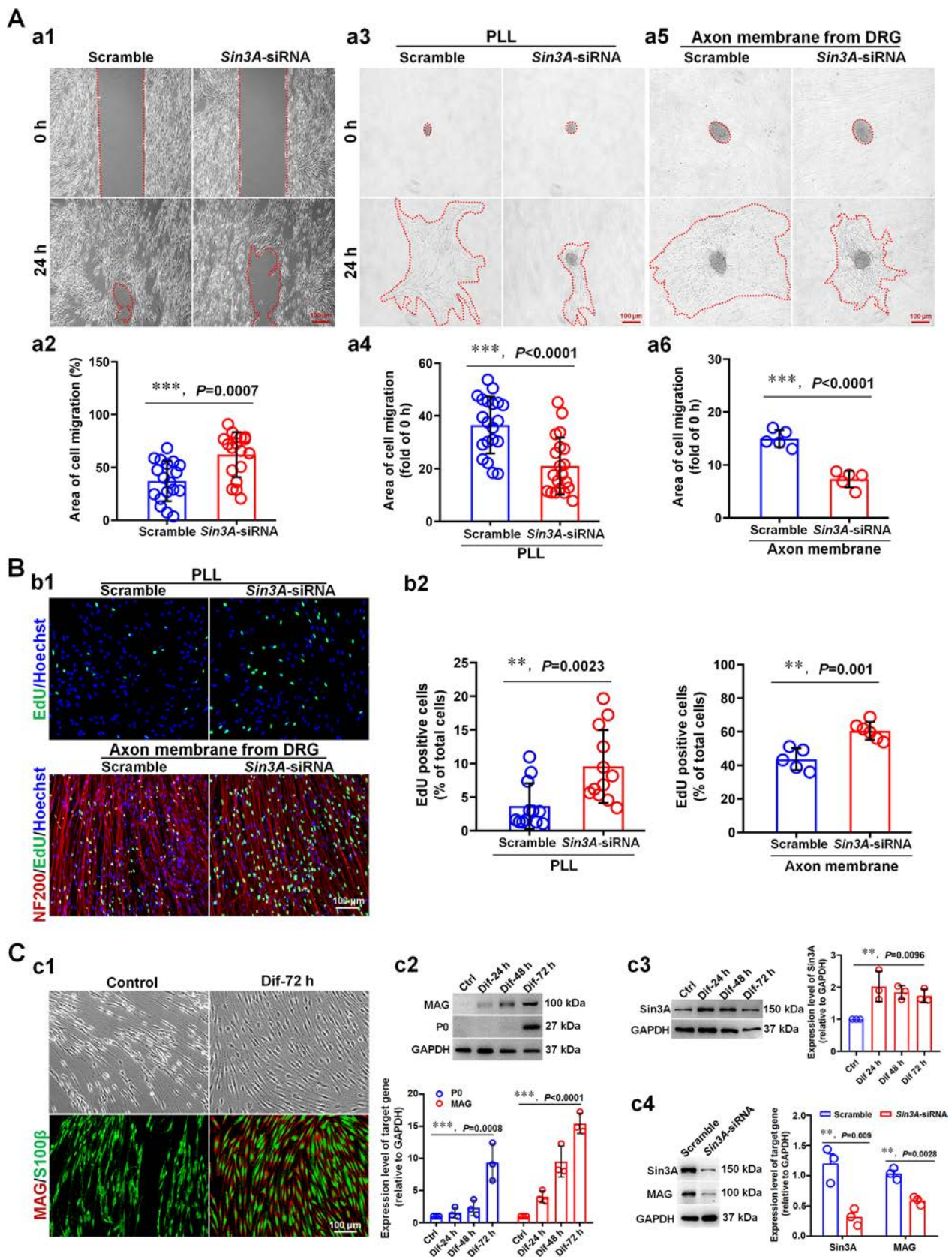


**Fig. 6** Sin3A enhances SC migration and differentiation, and reduces SC proliferation to promote myelination. **A** Sin3A knockdown in SCs reduces SC migration. **Aa1, a2** Results of an insert-based scratch migration assay. SC transfection with *Sin3A*-siRNA decreased SC migration in comparison with that of cells transfected with a negative control construct ( $n = 18$ ,  $t$ -test,  $***P = 0.0007$  vs scrambled). **Aa3–a6** Following transfection with *Sin3A*-siRNA and scrambled, SCs reaggregate on fasciculated DRG axons (**a5, a6**) or PLL (**a3, a4**), and the area of migration is measured. Red dashed circles indicate the extent of SC migration. Scale bars, 100  $\mu\text{m}$ . The histograms show that Sin3A knockdown in SCs significantly decreases SC migration from the reaggregates on fasciculated DRG axons ( $n = 5$ ,  $t$ -test,  $***P < 0.001$  vs scrambled) and PLL ( $n = 20$ ,  $t$ -test,  $***P < 0.001$  vs scrambled). **B** Sin3A knockdown in SCs increases SC proliferation. **Bb1** Proliferation ratio of SCs seeded on PLL or fasciculated DRG axons transfected with *Sin3A*-siRNA or scrambled. Green dots, proliferating SCs; blue dots, all cell nuclei; and red, NF200 immunostaining of the fasciculated DRG axons. Scale bar, 100  $\mu\text{m}$ . **Bb2** Histograms showing that Sin3A knockdown significantly increases SC proliferation on PLL ( $n = 12$ ,  $t$ -test,  $**P = 0.0023$  vs scrambled) and fasciculated DRG axons ( $n = 5$ ,  $t$ -test,  $**P = 0.001$  vs scrambled). **C** Sin3A knockdown in SCs decreases SC differentiation. **Cc1** Representative phase-contrast microscopy images, and immunocytochemical analyses of S100 $\beta$  (green) and MAG (red), indicating the differentiation efficacy of SCs cultured with vehicle or dibutyryl cyclic adenosine phosphate (dBcAMP) for 72 h. Scale bar, 100  $\mu\text{m}$ . **Cc2** Western blots comparing MAG and P0 levels in differentiated cells treated with dBcAMP for 24, 48, and 72 h, or vehicle as the control ( $n = 3$ , one-way ANOVA, P0:  $***P = 0.008$ , vs control; MAG:  $***P < 0.001$ , vs control). Also shown are representative Western blots, with GAPDH as the internal standard. **Cc3** Changes in Sin3A levels during SC differentiation ( $n = 3$ , one-way ANOVA,  $**P = 0.0096$  vs control). **Cc4** Western blots showing Sin3A and MAG levels in differentiated SCs following Sin3A knockdown. The histograms show that Sin3A knockdown decreases the expression of MAG compared with that in cells transfected with scrambled control ( $n = 3$ ,  $t$ -test,  $**P < 0.01$ ).

modulating SC differentiation and myelination, we evaluated the expression of HDAC1/2 and Sox10 following Sin3A knockdown during SC differentiation *in vitro*. Not surprisingly, we found that Sin3A knockdown dramatically reduced HDAC2 and Sox10 expression, indicating that HDAC2 is critical for the ability of Sin3A to functionally cooperate with Sox10 during SC differentiation (Fig. 8Cc1). Similarly, Sin3A knockdown in SCs resulted in a significant reduction in Sox10 expression in the regenerating nerve (14 days, SC remyelination), but did not affect Egr2 expression (Fig. 8Cc2). To confirm the function of Sin3A/HDAC2/Sox10 in the SC differentiation, we also performed rescue assays in SCs by co-transfecting *Sin3A*-siRNA and lentivirus vectors carrying the coding sequence of *Sin3A* (i.e. *Sin3A*-siRNA + LV-Ctrl, scrambled + LV-Ctrl, *Sin3A*-siRNA + LV-*Sin3A*, and scrambled + LV-*Sin3A*). Three days after differentiation, the expression of related molecules, such as MAG, Sox10, and HDAC1/2, was detected with WB. As expected, the results showed that knockdown of Sin3A repressed the expression levels of MAG, HDAC2, and Sox10 in differentiating SCs, and

was partially restored by co-transfection with LV-*sin3A* (Fig. 8D). These findings demonstrate that the Sin3A/HDAC2 complex promotes SC differentiation and myelination in the context of Sox10, and that Sin3A and HDAC2 are dependent on one another to functionally cooperate with Sox10 (Fig. 9).

## Discussion

Myelination in the PNS is temporally and spatially regulated in a precise manner during development and nerve regeneration after injury [34,39]. Accordingly, the transition of the SC lineage from immature to promyelinating and myelinating SCs allows them to assume a variety of critical roles to support myelination, including proliferation, migration along the axon, differentiation, and ensheathing of individual axons, ultimately leading to the formation of the myelin sheath [40,41]. SC subtype is the driving force behind efficient regeneration in an uncompromised nerve injury [11]. In the current study, we aimed to delineate the transcriptional networks that govern SC behavior during myelination. We show that SCs progress through three distinct transcription stages during myelination, and that the TF Sin3A plays a major role in controlling SC myelination identity. Understanding the temporal and spatial molecular dynamics that govern SC lineage development will provide insights for the development of treatments for myelinopathies and related diseases.

Here, we defined specific gene expression patterns that are characteristic for different SC development stages (i.e., immature, promyelinating, and myelinating) using gene expression profiling of laser capture-microdissected SCs at various stages of myelination, combined with multilevel bioinformatic analyses (Figs 1–3). We found three distinct transcriptional states of SCs, which were consistent with the SC lineage transition during myelination. The earliest SC stage (immature or proliferation stage) was characterized by the up-regulation of genes that mainly contribute to cell cycle, cell division, and cell motion, and whose expression decreases 3 days after the start of co-culture in the SC-DRG model. A distinct feature of the late immature/promyelinating SCs (stage II) coalescing in the co-culture is the initiation of the expression of genes involved in cell differentiation and myelination, with a concomitant loss of the expression of genes related to cell proliferation after 7 days of co-culture. Further, in stage II SCs, genes related to functions such as regulation of axon growth, synaptic signaling, and ensheathment of neurons, were expressed at high levels, which suggests a dialogue between SCs and neurons and their mutual interactions. Myelinating SCs in the co-culture system at 14 and 21 days



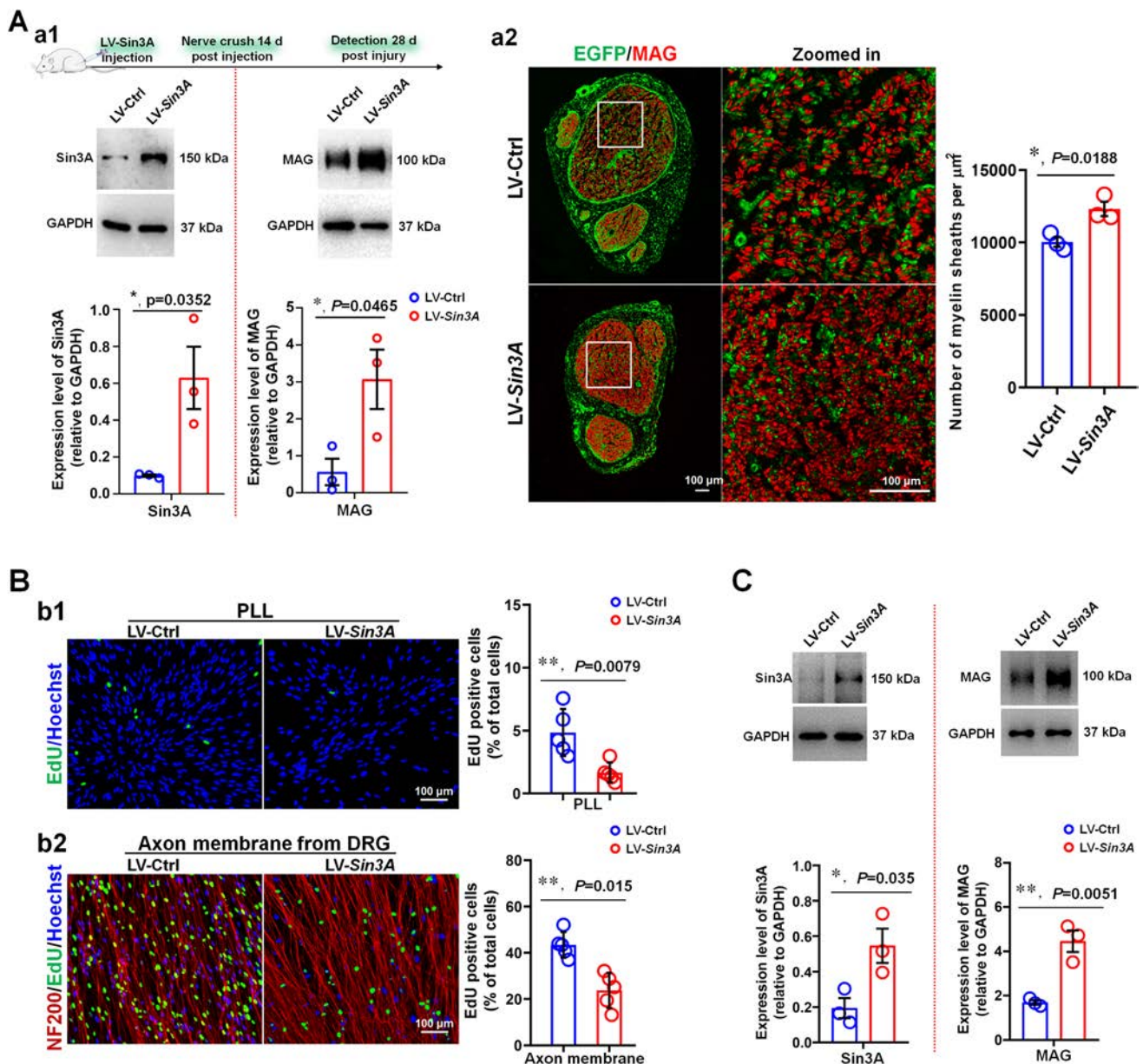


**Fig. 7** Sin3A overexpression enhances remyelination *in vivo* and SC differentiation *in vitro*. **Aa1** Western blots confirming the validity of the lentivirus (LV) transfection system carrying the *Sin3A* coding region sequence (LV-*Sin3A*) in nerves 14 days after transfection (on the left of the red dotted line), with an empty LV used as the control (LV-Ctrl), and comparison of the MAG expression in regenerated nerves treated with LV-*Sin3A* and LV-Ctrl, 28 days after nerve injury (on the right of the red dotted line). Also shown are representative Western blots, with GAPDH serving as the internal standard.  $*P < 0.05$  vs LV-Ctrl, *t*-test,  $n = 3$  per group. **Aa2** Immunostaining with anti-MAG (red) antibody and EGFP fluorescence (green) indicating axon remyelination in regenerated nerves treated with LV-*Sin3A* and LV-Ctrl. Also shown are high magnification images of the boxed areas. Scale bars, 100  $\mu\text{m}$ . Histograms comparing the density of myelin sheaths.  $*P < 0.05$  vs LV-Ctrl, *t*-test,  $n = 3$  per group. **B** Sin3A overexpression in SCs decreases SC proliferation. Proliferation ratio

of SCs following transfection with LV-*Sin3A* and LV-Ctrl and reseeded on fasciculated DRG axons (**b2**) or PLL (**b1**). Green dots, proliferating SCs; blue dots, all cell nuclei; and red, NF200 immunostaining of the fasciculated DRG axons. Scale bars, 100  $\mu\text{m}$ . Histograms showing that Sin3A overexpression significantly decreases SC proliferation on PLL ( $n = 5$ , *t*-test,  $**P = 0.0079$  vs LV-Ctrl) and fasciculated DRG axons ( $n = 5$ , *t*-test,  $**P = 0.015$  vs LV-Ctrl). **C** Sin3A overexpression in SCs increases SC differentiation. Western blots confirming the validity of the virus transfection system carrying *Sin3A* coding region sequence (LV-*Sin3A*) in SCs 3 days after transfection (on the left of the red dotted line), with an empty LV used as the control (LV-Ctrl), and comparison of the MAG expression in LV-*Sin3A* and LV-Ctrl-treated SCs after 3 days of differentiation *in vitro* (on the right of the red dotted line). Also shown are representative Western blots, with GAPDH serving as the internal standard.  $*P < 0.05$ ,  $**P < 0.01$ , vs LV-Ctrl, *t*-test,  $n = 3$  per group.

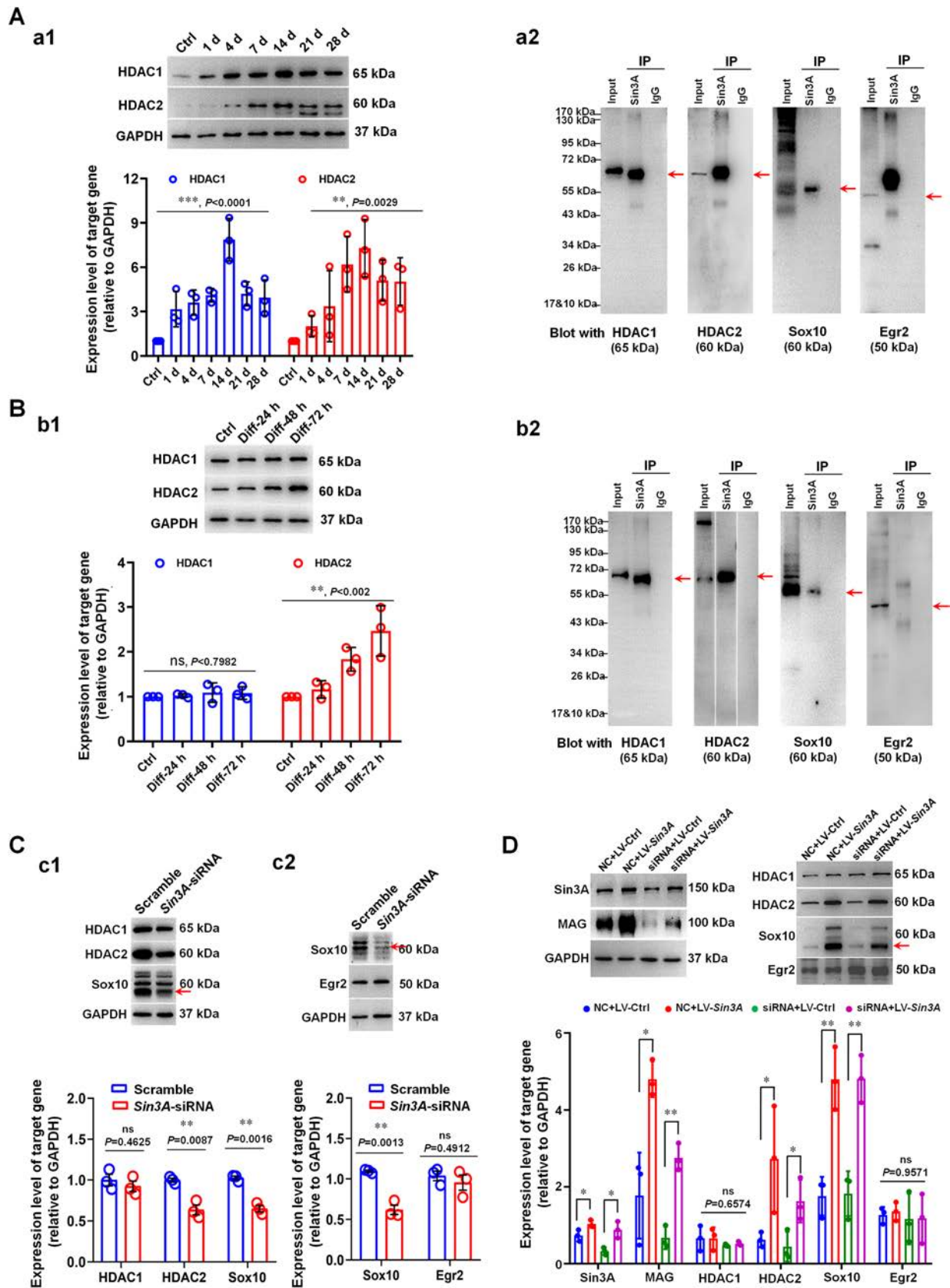


**Fig. 8** Sin3A coordinates with HDAC1/2 and Sox10 to promote SC differentiation and myelination. **Aa1** Representative Western blots showing HDAC1 and HDAC2 levels in a regenerating nerve segment, at 1, 4, 7, 14, 21, and 28 days following nerve crush, with the normal nerve used as the control. GAPDH is the loading control. The histogram compares protein levels of HDAC1 and HDAC2 in the regenerating nerve segment at the indicated time points following nerve crush.  $**P < 0.01$ ,  $***P < 0.001$  vs control, one-way ANOVA,  $n = 3$  per group. **Aa2** Co-IP of regenerating nerves using antibodies against Sin3A, followed by immunoblotting with antibodies against HDAC1, HDAC2, Sox10, or Egr2. Red arrows indicate target proteins. **Bb1** Representative Western blots showing HDAC1 and HDAC2 levels during SC differentiation stimulated by dBcAMP, with untreated SCs used as the control. GAPDH serves as the loading control. The histogram compares protein levels of HDAC1 and HDAC2 in differentiating SCs at different time points after induction.  $**P < 0.01$ ,  $***P < 0.001$  vs control, one-way ANOVA,  $n = 3$  per group. **Bb2** Co-IP of differentiating SCs using antibodies against Sin3A, followed by immunoblotting with antibodies against HDAC1, HDAC2, Sox10, or Egr2. Red arrows indicate target proteins. **Cc1** Western blots showing HDAC1, HDAC2, and Sox10 levels in differentiating SCs following Sin3A knockdown. The histograms show that Sin3A knockdown decreases the expression of HDAC2 and Sox10, but does not affect HDAC1 expression ( $n = 3$ ,  $t$ -test,  $**P < 0.01$ ). **Cc2** Egr2 and Sox10 expression in regenerated nerves after Sin3A knockdown in SCs in a rat sciatic nerve crush model. Also shown are representative Western blots, with GAPDH serving as the internal standard. The histograms show that Sin3A knockdown decreases the expression of Sox10 ( $n = 3$ ,  $t$ -test,  $**P = 0.0013$ ), but not that of Egr2 ( $n = 3$ ,  $t$ -test, ns,  $P = 0.4912$ ). **D** Western blots showing the expression of Sin3A, MAG, HDAC1, HDAC2, Sox10, and Egr2 in Sin3A-Scrambled (negative control, NC) + LV-Ctrl (NC + LV-Ctrl), Sin3A-Scrambled + LV-Sin3A (NC + LV-Sin3A), Sin3A-siRNA + LV-Ctrl (siRNA + LV-Ctrl), and Sin3A-siRNA + LV-Sin3A (siRNA + LV-Sin3A) treated SCs after 3 days of differentiation *in vitro*. The histogram showed that Sin3A overexpression restores the decreased expression of Sox10, MAG, and HDAC2 in SCs with Sin3A knockdown, but not Egr2 and HDAC1.  $n = 3$ ,  $t$ -test,  $*P < 0.05$ ,  $**P < 0.01$ .

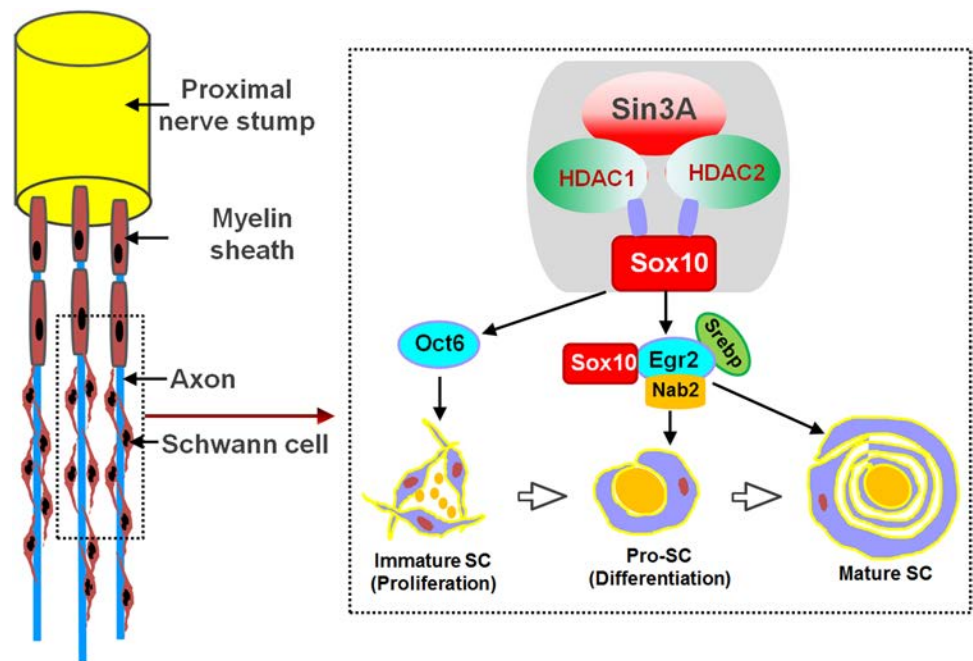
after the start of the culture (stage III) retained the expression of genes involved in the ensheathment of neurons and myelination. This was accompanied by the expression of genes related to myelin maturation, such as those involved in the regulation of SC plasma membrane surrounding the axon. The genome and proteome analyses of the entire co-cultures (SCs and neurons) maintained for 0, 10, and 22 days have been reported in another study [12], similarly delineating the dynamic changes that occur in the system at these time points. However, there are several key differences between the current and previous studies. First, we analyzed the transcriptomes of purified SCs isolated from the myelinating co-cultures by LCM, whereas in the previous study, all cells were analyzed together. Second, unlike the previous study, we performed global and detailed analyses of gene expression in SC lineages on days 0, 1, 3, 7, 14, and 21 in co-culture. Hence, the present data are an important complement for the mechanism of SC lineage transition during myelination.

Based on the available data, the SC lineage specificity of gene expression can best be explained by the combined action of multiple TFs [35,36,42,43]. Therefore, we analyzed TFs that exhibited a strong regulatory relationship with DEGs in the nine identified gene co-expression modules. We identified 17 TFs that temporally control the SC development and reconstructed a network of these TFs and their target genes (Fig. 3B and Table S3). Several of the 17 TFs (e.g., Egr2, Sox10, Sox2, and Yy1) have been implicated in the regulation of SC lineage progression, with a coordinated input from positive and negative factors to control the transition of SC to an SC precursor state, or to promote cell cycle exit and initiate differentiation. For example, a hierarchy of positive TFs, including Egr2, Sox10, and Oct6 (a.k.a. Pou3F1), is required for the sequential progression from immature SCs to promyelinating SCs and eventually to myelinating SCs [9,34]. This is accompanied by a suppression of negative regulatory factors that inhibit SC differentiation, including Notch, Sox2, and c-Jun [9,36,42,44,45]. Based on the functions of the known TFs, we here used co-expression analysis to classify the newly discovered TFs according to the three stages of myelination (Fig. 3Bb2) and focused on a core set of TFs important for stage II. Based on WGCNA data, Sin3A contributes more than Egr2 to SC development from the immature to promyelination stages. Sin3A is a well-characterized general chromatin regulator that plays an important role in vertebrate tissue diversity by maintaining tissue homeostasis and stem cell pluripotency [15,46–48]. However, the function of Sin3A in SC lineage transition during myelination and remyelination after nerve injury has not been investigated prior to the current study.

To determine the possible role of Sin3A in myelination, we first identified the expression and localization of Sin3A in the PNS, double immunohistochemistry for S100 $\beta$ , an SC marker, or  $\beta$ -tubulin III, a neuronal marker, and Sin3A in DRG tissue, sciatic nerves, or cultured DRG neurons and SCs revealed that Sin3A was expressed in both the neurons and SCs, and mainly in the nucleus (Fig. S3). We further analyzed the expression of Sin3A, Egr2, and MAG in an injured segment at different time points following nerve crush. Sin3A expression dynamics were similar to those of Egr2 and positively correlated with MAG levels (Fig. 4A), suggesting that Sin3A and Egr2 play a similar role during nerve regeneration. It is well known that SCs assume a transient "dedifferentiated" phenotype to help clear the myelin debris at early post-nerve crush stages, and then redifferentiate to promyelinating and myelinating phenotypes to form new myelin sheaths and perform axon regeneration [4,43]. During this process, Egr2 is a key TF associated with myelin formation, and its expression is specifically related to SC development or plasticity in the PNS [49,50]. In addition, MAG is an essential component



**Fig. 9** Schematic showing the preliminary mechanism of Sin3A in SCs regulating myelination or remyelination. The Sin3A/HDACs complex promotes SC differentiation and myelination in the Sox10 context, and Sin3A and HDAC2 are mutually dependent for their functional cooperation with Sox10. The area denoted in gray indicates the findings of the current study.



of the myelin sheath; it is expressed by myelinated glial cells and is involved in the formation and maintenance of myelin sheath [9,45]. Based on the similar expression trends of Sin3A and Egr2 and the consistent co-localization of Sin3A and S100 $\beta$  (an SC marker) from days 1–28 after nerve crush (Fig. 4B), we concluded that, in the PNS, Sin3A may participate in the remyelination following acute nerve injury. We also analyzed myelin-formation in a rat sciatic nerve injury model after Sin3A knockdown in the sciatic nerve or specifically in SCs by injecting viruses carrying specific shRNAs (Fig. S4). We found that low Sin3A expression decreases the myelinating capacity of SCs, resulting in decreased MAG expression during myelin sheath reformation (Fig. 5). Furthermore, we found that overexpression of Sin3A increases the expression of MAG (Fig. 7A). These results further confirm that Sin3A is involved in controlling SC remyelination following nerve injury.

SCs produce insulating myelin sheaths around large axons at a one-to-one ratio in the course of a very complex process involving SC proliferation, migration, and differentiation [45,51]. Therefore, we also explored the effect of Sin3A on myelin formation by analyzing specific SC behavior using a Sin3A knockdown or overexpression approach in SCs. As a myelination substrate, the axon is the logical candidate and a source of extrinsic cues that might precisely regulate the timing of myelination [52]; therefore, we investigated the role of Sin3A in SC proliferation and migration on two substrates: PLL and axons. We found that Sin3A knockdown promoted SC proliferation while inhibiting SC migration and

differentiation, regardless of whether the cells were cultured on PLL or DRG axons (Fig. 6). Correspondingly, Sin3A overexpression resulted in the opposite outcomes, manifested as inhibition of SC proliferation and promotion of SC differentiation (Fig. 7). In addition, we also analyzed SC proliferation in a rat model of sciatic nerve injury through the double immunostaining of Ki67 (a marker of cell proliferation) and S100 $\beta$ , and found that the number of cells co-labeled with ki67 and S100 $\beta$  increased rapidly at 4 days after injury (Fig. S5), which is associated with SC dedifferentiation and proliferation at the early stage of nerve injury. Next, we analyzed the proliferation of SCs in sciatic nerves with knockdown or overexpression of Sin3A. The results showed that the number of proliferating SCs in the Sin3A knockdown sciatic nerve was significantly greater than that in the control (Fig. S6), while it was lower in the Sin3A-overexpressing sciatic nerve (Fig. S7), suggesting that Sin3A negatively regulates SC proliferation after nerve injury. Combined with the *in vivo* data, we thus concluded that Sin3A regulates the ability of SCs to undergo proliferation, migration, and morphological differentiation during myelination or remyelination.

Sin3A is generally thought to be responsible for the recruitment of HDACs to form an HDAC-associated transcriptional complex to regulate the transcription of specific genes [15,16,48]. Further, according to previous studies, HDAC1 and HDAC2 control the transcriptional program of myelination and SC survival [53,54]. Hence, we proposed that Sin3A might interact with HDAC1/2 to balance transcription activation or repression to regulate myelination. Indeed, the expression of HDAC1/2 was

consistent with that of Sin3A during nerve regeneration after injury (Fig. 8Aa1) and SC differentiation (Fig. 7Bb1). Furthermore, Sin3A co-immunoprecipitated with HDAC1/2 in nerves that had been regenerating for 14 days (Fig. 8Aa2) and in differentiating SCs (Fig. 8Bb2). Interestingly, we found that Sin3A interacted with Sox10, but not with Egr2, in the regenerating nerve and differentiating SCs. That may be because the complex TF network that controls the timely development of SCs proceeds in a cascade-like manner, and Sox10 may act upstream of Egr2. According to previous studies, Sox10 induces the specification and terminal differentiation of SCs by directly activating Egr2 expression and acting synergistically with Oct6 and Nab2 [55,56]. Further, deletion of Sox10 results in loss of Egr2 expression and myelin sheath degeneration [11,57]. Here, we showed that inhibition of Sin3A expression led to a decrease in Sox10 levels in differentiating SCs and the regenerating nerve, but did not affect Egr2 levels (Fig. 8C). Moreover, the rescue experiments provided further evidence for the above phenomena (Fig. 8D). Hence, we reasoned that the Sin3A/HDAC1/2 complex cooperates with Sox10, rather than with Egr2, to regulate the differentiation of SCs to promyelinating and myelinating phenotypes. Another interesting discovery was that HDAC1/2 both associate with Sin3A in SCs upon induction of differentiation. However, only HDAC2 expression was enhanced under these conditions (Fig. 8Bb1), while that of HDAC1 was relatively stable. This suggests that Sin3A preferentially binds HDAC2 to regulate SC differentiation. HDAC1 and HDAC2 are essential for SC myelination and survival; HDAC2 is a principal inducer of differentiation, whereas HDAC1 regulates SC survival [53]. This is consistent with the findings of the current study. Taken together, the current and previous studies suggest that Sin3A is a key regulator in the TF network that controls SC development and myelination. It may act by activating its own transcription and the transcription of Sox10 in synergy with HDAC2, and by recruiting Sox10 to its target gene Egr2 (Fig. 9).

In summary, in agreement with recent studies [11,12,58], we demonstrated that SCs pass through three distinct transcriptional stages consistent with SC lineage transition (immature, promyelination, and myelination) during myelination. Even though the temporal expression data presented here provide a comprehensive glimpse into the expression profiles of the various TFs involved in SC development and myelination, the expression and function of a large number of developmentally important TF families should be analyzed further. In addition, we identified Sin3A as a critical regulator of SC lineage transition and remyelination, and showed that Sin3A increases remyelination speed and efficiency after lesions in the PNS. This knowledge is important for the general

understanding of neurobiology related to myelination. Furthermore, our findings provide important information for potential medical applications in future translational studies on accelerating remyelination after traumatic lesions or in the context of demyelinating disorders.

**Acknowledgments** This work was supported by the National Key Research and Development Program of China (2017YFA0104702); the National Natural Science Foundation of China (81771339 and 82001296); the Natural Science Foundation of Jiangsu Province (BK20202013); the Priority Academic Program Development of Jiangsu Higher Education Institutions; the “226 High-level Talent Training Project” in Nantong city, and the Nantong Health commission Science project (MA2020004).



**Conflict of interest** The authors declare no conflict of interest.

## References

1. Taveggia C, Feltri ML, Wrabetz L. Signals to promote myelin formation and repair. *Nat Rev Neurol* 2010, 6: 276–287.
2. Saab AS, Nave KA. Myelin dynamics: protecting and shaping neuronal functions. *Curr Opin Neurobiol* 2017, 47: 104–112.
3. Zhou Y, Notterpek L. Promoting peripheral myelin repair. *Exp Neurol* 2016, 283: 573–580.
4. Liu B, Xin W, Tan JR, Zhu RP, Li T, Wang D. Myelin sheath structure and regeneration in peripheral nerve injury repair. *Proc Natl Acad Sci U S A* 2019, 116: 22347–22352.
5. Villoslada P, Martinez-Lapiscina EH. Remyelination: a good neuroprotective strategy for preventing axonal degeneration? *Brain* 2019, 142: 233–236.
6. Mei F, Lehmann-Horn K, Shen YAA, Rankin KA, Stebbins KJ, Lorrain DS, *et al.* Accelerated remyelination during inflammatory demyelination prevents axonal loss and improves functional recovery. *eLife* 2016, 5: e18246.
7. Monje M. Myelin plasticity and nervous system function. *Annu Rev Neurosci* 2018, 41: 61–76.
8. Lu FF, Yin D, Pu YY, Liu WL, Li ZH, Shao Q, *et al.* Shikimic acid promotes oligodendrocyte precursor cell differentiation and accelerates remyelination in mice. *Neurosci Bull* 2019, 35: 434–446.
9. Pereira JA, Lebrun-Julien F, Suter U. Molecular mechanisms regulating myelination in the peripheral nervous system. *Trends Neurosci* 2012, 35: 123–134.
10. Nagarajan R, Le N, Mahoney H, Araki T, Milbrandt J. Deciphering peripheral nerve myelination by using Schwann cell expression profiling. *Proc Natl Acad Sci U S A* 2002, 99: 8998–9003.
11. Balakrishnan A, Stykel MG, Touahri Y, Stratton JA, Biernaskie J, Schuurmans C. Temporal analysis of gene expression in the murine Schwann cell lineage and the acutely injured postnatal nerve. *PLoS One* 2016, 11: e0153256.
12. Kangas SM, Ohlmeier S, Sormunen R, Jouhilahti EM, Peltonen S, Peltonen J, *et al.* An approach to comprehensive genome and proteome expression analyses in Schwann cells and neurons during peripheral nerve myelin formation. *J Neurochem* 2016, 138: 830–844.
13. Silverstein RA, Ekwall K. Sin3: a flexible regulator of global gene expression and genome stability. *Curr Genet* 2005, 47: 1–17.
14. Laugesen A, Helin K. Chromatin repressive complexes in stem cells, development, and cancer. *Cell Stem Cell* 2014, 14: 735–751.
15. Saunders A, Huang X, Fidalgo M, Reimer MH Jr, Faiola F, Ding JJ, *et al.* The SIN3A/HDAC corepressor complex functionally cooperates with NANOG to promote pluripotency. *Cell Rep* 2017, 18: 1713–1726.

16. Zhao PP, Li S, Wang HN, Dang YN, Wang LF, Liu T, *et al.* Sin3a regulates the developmental progression through morula-to-blastocyst transition via Hdac1. *FASEB J* 2019, 33: 12541–12553.
17. Kadamb R, Mittal S, Bansal N, Batra H, Saluja D. Sin3: insight into its transcription regulatory functions. *Eur J Cell Biol* 2013, 92: 237–246.
18. Castelo-Branco G, Lilja T, Wallenborg K, Falcão AM, Marques SC, Gracias A, *et al.* Neural stem cell differentiation is dictated by distinct actions of nuclear receptor corepressors and histone deacetylases. *Stem Cell Rep* 2014, 3: 502–515.
19. Halder D, Lee CH, Hyun JY, Chang GE, Cheong E, Shin I. Suppression of Sin3A activity promotes differentiation of pluripotent cells into functional neurons. *Sci Rep* 2017, 7: 44818.
20. Chen RY, Yang XM, Zhang B, Wang SR, Bao SX, Gu Y, *et al.* EphA4 negatively regulates myelination by inhibiting Schwann cell differentiation in the peripheral nervous system. *Front Neurosci* 2019, 13: 1191.
21. Gu Y, Zhu JB, Xue CB, Li Z, Ding F, Yang YM, *et al.* Chitosan/silk fibroin-based, Schwann cell-derived extracellular matrix-modified scaffolds for bridging rat sciatic nerve gaps. *Biomaterials* 2014, 35: 2253–2263.
22. Savage RS, Heller K, Xu Y, Ghahramani Z, Truman WM, Grant M, *et al.* R/BHC: fast Bayesian hierarchical clustering for microarray data. *BMC Bioinformatics* 2009, 10: 242.
23. Ritchie ME, Phipson B, Wu D, Hu YF, Law CW, Shi W, *et al.* Limma Powers differential expression analyses for RNA-sequencing and microarray studies. *Nucleic Acids Res* 2015, 43: e47.
24. Smyth GK. Linear models and empirical Bayes methods for assessing differential expression in microarray experiments. *Stat Appl Genet Mol Biol* 2004, 3: 3.
25. Tai YC, Speed TP. On gene ranking using replicated microarray time course data. *Biometrics* 2009, 65: 40–51.
26. Langfelder P, Horvath S. WGCNA: an R package for weighted correlation network analysis. *BMC Bioinformatics* 2008, 9: 559.
27. Carolina Sparavigna A. Graph visualization software for networks of characters in plays. *IJ Sciences* 2014, 46: 69–79.
28. Shannon P, Markiel A, Ozier O, Baliga NS, Wang JT, Ramage D, *et al.* Cytoscape: a software environment for integrated models of biomolecular interaction networks. *Genome Res* 2003, 13: 2498–2504.
29. Van Hameren G, Gonzalez S, Fernando RN, Perrin-Tricaud C, Tricaud N. *In vivo* introduction of transgenes into mouse sciatic nerve cells using viral vectors. *Methods Mol Biol* 2018, 1791: 263–276.
30. Yamauchi J, Chan JR, Shooter EM. Neurotrophins regulate Schwann cell migration by activating divergent signaling pathways dependent on Rho GTPases. *Proc Natl Acad Sci U S A* 2004, 101: 8774–8779.
31. Gu Y, Wu YM, Su WF, Xing LY, Shen YT, He XW, *et al.* 17 $\beta$ -estradiol enhances Schwann cell differentiation via the ER $\beta$ -ERK1/2 signaling pathway and promotes remyelination in injured sciatic nerves. *Front Pharmacol* 2018, 9: 1026.
32. Lewallen KA, Shen YAA, de la Torre AR, Ng BK, Meijer D, Chan JR. Assessing the role of the cadherin/catenin complex at the Schwann cell-axon interface and in the initiation of myelination. *J Neurosci* 2011, 31: 3032–3043.
33. Jaegle M, Ghazvini M, Mandemakers W, Piirsoo M, Driegen S, Levavasseur F, *et al.* The POU proteins Brn-2 and Oct-6 share important functions in Schwann cell development. *Genes Dev* 2003, 17: 1380–1391.
34. Boerboom A, Dion V, Chariot A, Franzen R. Molecular mechanisms involved in Schwann cell plasticity. *Front Mol Neurosci* 2017, 10: 38.
35. Wegner M. Transcriptional control in myelinating glia: the basic recipe. *Glia* 2000, 29: 118–123.
36. Sock E, Wegner M. Transcriptional control of myelination and remyelination. *Glia* 2019, 67: 2153–2165.
37. Yuan XQ, Chittajallu R, Belachew S, Anderson S, McBain CJ, Gallo V. Expression of the green fluorescent protein in the oligodendrocyte lineage: a transgenic mouse for developmental and physiological studies. *J Neurosci Res* 2002, 70: 529–545.
38. Bacallao K, Monje PV. Requirement of cAMP signaling for Schwann cell differentiation restricts the onset of myelination. *PLoS One* 2015, 10: 0116948.
39. Trapp BD, Kidd GJ, Pfeiffer SE, Anitei M. *Cell Biology of Myelin Assembly*. San Diego, CA: Elsevier Academic Press, 2004.
40. Taveggia C. Schwann cells-axon interaction in myelination. *Curr Opin Neurobiol* 2016, 39: 24–29.
41. Mirsky R, Jessen KR. Schwann cell development, differentiation and myelination. *Curr Opin Neurobiol* 1996, 6: 89–96.
42. Stolt CC, Wegner M. Schwann cells and their transcriptional network: evolution of key regulators of peripheral myelination. *Brain Res* 2016, 1641: 101–110.
43. Nave KA, Werner HB. Myelination of the nervous system: mechanisms and functions. *Annu Rev Cell Dev Biol* 2014, 30: 503–533.
44. Salzer JL. Switching myelination on and off. *J Cell Biol* 2008, 181: 575–577.
45. Snaidero N, Simons M. Myelination at a glance. *J Cell Sci* 2014, 127: 2999–3004.
46. Dobi KC, Halfon MS, Baylies MK. Whole-genome analysis of muscle founder cells implicates the chromatin regulator Sin3A in muscle identity. *Cell Rep* 2014, 8: 858–870.
47. Nascimento EM, Cox CL, MacArthur S, Hussain S, Trotter M, Blanco S, *et al.* The opposing transcriptional functions of Sin3a and c-Myc are required to maintain tissue homeostasis. *Nat Cell Biol* 2011, 13: 1395–1405.
48. Zhu FG, Zhu QS, Ye D, Zhang QQ, Yang YW, Guo XD, *et al.* Sin3a-Tet1 interaction activates gene transcription and is required for embryonic stem cell pluripotency. *Nucleic Acids Res* 2018, 46: 6026–6040.
49. Topilko P, Schneider-Maunoury S, Levi G, Baron-Van Evercooren A, Chennoufi AB, Seitanidou T, *et al.* Krox-20 controls myelination in the peripheral nervous system. *Nature* 1994, 371: 796–799.
50. Nagarajan R, Svaren J, Le N, Araki T, Watson M, Milbrandt J. *EGR2* mutations in inherited neuropathies dominant-negatively inhibit myelin gene expression. *Neuron* 2001, 30: 355–368.
51. Salzer JL, Zalc B. Myelination. *Curr Biol* 2016, 26: R971–R975.
52. Osso LA, Chan JR. Architecting the myelin landscape. *Curr Opin Neurobiol* 2017, 47: 1–7.
53. Jacob C, Christen CN, Pereira JA, Somandin C, Baggiolini A, Lötscher P, *et al.* HDAC1 and HDAC2 control the transcriptional program of myelination and the survival of Schwann cells. *Nat Neurosci* 2011, 14: 429–436.
54. Gomis-Coloma C, Velasco-Aviles S, Gomez-Sanchez JA, Casillas-Bajo A, Backs J, Cabedo H. Class IIa histone deacetylases link cAMP signaling to the myelin transcriptional program of Schwann cells. *J Cell Biol* 2018, 217: 1249–1268.
55. Jones EA, Jang SW, Mager GM, Chang LW, Srinivasan R, Gokey NG, *et al.* Interactions of Sox10 and Egr2 in myelin gene regulation. *Neuron Glia Biol* 2007, 3: 377–387.
56. LeBlanc SE, Ward RM, Svaren J. Neuropathy-associated Egr2 mutants disrupt cooperative activation of myelin protein zero by Egr2 and Sox10. *Mol Cell Biol* 2007, 27: 3521–3529.
57. Bremer M, Fröb F, Kichko T, Reeh P, Tamm ER, Suter U, *et al.* Sox10 is required for Schwann-cell homeostasis and myelin maintenance in the adult peripheral nerve. *Glia* 2011, 59: 1022–1032.
58. Wu XM. Genome expression profiling predicts the molecular mechanism of peripheral myelination. *Int J Mol Med* 2018, 41: 1500–1508.

# Formation of the Looming-evoked Innate Defensive Response during Postnatal Development in Mice

Shanping Chen<sup>1,3</sup> · Huiying Tan<sup>1,3</sup> · Zhijie Wang<sup>1</sup> · Yu-ting Tseng<sup>1</sup> · Xiaotao Li<sup>1,2</sup>  · Liping Wang<sup>1</sup> 

Received: 6 July 2021 / Accepted: 18 November 2021 / Published online: 5 February 2022

© Center for Excellence in Brain Science and Intelligence Technology, Chinese Academy of Sciences 2022

**Abstract** Environmental threats often trigger innate defensive responses in mammals. However, the gradual development of functional properties of these responses during the postnatal development stage remains unclear. Here, we report that looming stimulation in mice evoked flight behavior commencing at P14–16 and had fully developed by P20–24. The visual-evoked innate defensive response was not significantly altered by sensory deprivation at an early postnatal stage. Furthermore, the percentages of wide-field and horizontal cells in the superior colliculus were notably elevated at P20–24. Our findings define a developmental time window for the formation of the visual innate defense response during the early postnatal period

and provide important insight into the underlying mechanism.

**Keywords** Innate defensive response · Postnatal stage · Superior colliculus

## Introduction

Innate defensive responses to imminent threatening environmental stimuli are essential for the survival of animals [1, 2]. More importantly, visually-evoked innate defensive responses are of fundamental importance for many species because visual information may better convey the likelihood of an attack [3, 4]. It is known that visually-evoked defensive responses are highly conserved across species, ranging from *Drosophila* to mammals [5–10]. In addition, brain structures based on this predatory defense system are also highly conserved in vertebrate species and within mammals [11–13]. However, when the formation of this visually-evoked defensive response first occurs at the early postnatal stage remains unclear.

In many species, defensive responses do not emerge at pups until later in development. For example, rat pups do not exhibit an odor-evoked defensive response until ~P10 [14] and mice display defensive components to contextual fear conditioning at ~P23 [15]. The Jackson Laboratory report that mouse eyes open at ~P12. After eye-opening, at ~P14, the mouse visual system receives patterned information [16]. Furthermore, many studies and laboratory guidelines suggest that litters should be weaned by postnatal days 21–23 [17, 18]. At this age, young mice begin to venture away from the nest and become nutritionally independent of their parents [19]. These studies indicate that after P21–23, mice become increasingly

Shanping Chen and Huiying Tan have contributed equally to this work.

**Supplementary Information** The online version contains supplementary material available at <https://doi.org/10.1007/s12264-022-00821-0>.

✉ Liping Wang  
lp.wang@siat.ac.cn

<sup>1</sup> Shenzhen Key Lab of Neuropsychiatric Modulation, Guangdong Provincial Key Laboratory of Brain Connectome and Behavior, CAS Key Laboratory of Brain Connectome and Manipulation, the Brain Cognition and Brain Disease Institute, Shenzhen Institute of Advanced Technology, Chinese Academy of Sciences, Shenzhen-Hong Kong Institute of Brain Science-Shenzhen Fundamental Research Institutions, Shenzhen 518055, China

<sup>2</sup> Department of Brain and Cognitive Sciences, McGovern Institute for Brain Research, Massachusetts Institute of Technology, Cambridge, MA 02139, USA

<sup>3</sup> University of Chinese Academy of Sciences, Beijing 100049, China



independent and imply that having an appropriate defensive response to threatening signals received from multi-sensory modalities may become important. Therefore, it is possible that P10–23 may be the critical period for the firstly emergence of visually-evoked defensive responses.

Looming stimuli are used in a laboratory-based experimental paradigm to mimic the signal of an approaching aerial predator and to induce an innate defensive response in animals [1, 20]. This paradigm has recently been used to investigate the neural mechanisms underlying innate defensive behaviors. When an animal is exposed to an open field with a dark nest in one corner, looming stimuli lead to an innate defensive response, which manifests as flight-into-nest and hiding behavior [20, 21]. The superior colliculus (SC) is an integrative structure in the midbrain, and it is reported to mediate the expression of defensive responses in adult mice following looming stimuli [21–24]. There are four neuronal types in the superficial layer of the SC: wide-field cells, horizontal cells, stellate cells, and narrow-field cells that can be distinguished by electrophysiological characteristics [25]. In this study, we report that defensive responses to looming stimuli become fully established in mice during the specific developmental time window from P20 to P24, demonstrating functional and instinctive conservation, and they are not significantly affected by sensory deprivation. We also found a notable elevation in the percentage of wide-field and horizontal cells in the SC in the corresponding time period. Our findings help shed light on SC function in the formation of innate defensive responses to threatening visual stimuli.

## Materials and Methods

### Mice

All husbandry and experimental procedures in this study were approved by the Animal Care and Use Committees at the Shenzhen Institute of Advanced Technology, Chinese Academy of Sciences. Pregnant female C57BL/6J mice (Vital River Laboratory, Zhejiang, China) were group-housed, given access to food pellets and water *ad libitum*, and maintained on a 12:12-h light/dark cycle (lights on at 07:00). The body weights of mice at different ages are shown in Table S1. The transgenic mouse line expressing the genetically encoded  $\text{Ca}^{2+}$  indicator GCaMP6f under the control of the neuronal Thy1 promoter (Thy1-GCaMP6f) [26]. The Thy1-GCaMP6f transgenic mice (C57BL/6J-Tg(Thy1-GCaMP6f)GP5.17Dkim/J, Jackson Laboratories, jax 025393) were used for *in vivo* two-photon imaging [26]. The Thy1-GCaMP6f transgenic mice were a gift from Ning-Long Xu (Chinese Academy of Sciences, Shanghai).

### Looming Test

The looming test was applied in a closed Plexiglas box (40 cm long, 40 cm wide, and 30 cm high) with a dark sheltered nest in one corner, as described previously [21, 22]. An LCD monitor was placed on the ceiling to present the looming stimulus, which was a black disc expanding from a 4° to 40° visual angle in 0.25 s on a gray background. Mouse behavior was recorded using an infrared camera. Mice were handled and habituated to the looming box for 15 min one day before the test. On the day of the test, each mouse was given 5 min of free exploration in the box. Then, each mouse was presented with looming stimuli for a minimum of 3 trials. The stimuli were triggered by the experimenter when the mouse entered an area at the far end of the arena (away from the nest). The following measures were recorded as indices of looming-evoked defensive behavior: (1) flight latency (ms), defined as the time from looming stimulus presentation until the mouse entered the nest, (2) time spent in the nest (ms), defined as the time that the mouse hid in the nest following its flight action until it came out of the nest, (3) crouch response, defined as exhibiting a squat posture a short time from the onset of the black disk, (4) rearing response, characterized by persistent raising of the head, and (5) non-response, the mouse did not convert to other behavior during the looming stimuli. These data were recorded and analyzed using Anymaze software with additional analyses using Adobe Premiere and MatLab (MathWorks, USA).

### Sensory Deprivation

In all experiments, control mice were housed in plastic cages in our laboratory with *ad libitum* access to food and water and on a 12:12-h light/dark cycle. In the whisker-deprivation protocol littermates in the same cage were randomly assigned to the control or whisker-deprivation group. While each pup was under isoflurane anesthesia, only those in the whisker-deprivation group had their whiskers trimmed from P0 until the time of the experiment [27]. In a dark-rearing protocol, pregnant mothers and pups were randomly assigned to either a standard plastic cage or a plastic cage with a black cover. This cover was present until the time of the experiment [27].

### Two-photon Excitation Microscopy and Calcium Imaging

For two-photon imaging of the SC *in vivo*, a craniotomy 2.5–3 mm in diameter was made at lambda in each mouse. During the craniotomy, a circular area of the skull was first drilled to a thin layer. After that, the thinned skull was carefully removed from the craniotomy area in small pieces

to avoid bleeding from the transverse sinus. Sharp forceps were used to perform durotomy. A silicone plug was positioned to gently push the transverse sinus anteriorly so that the caudal pole of SC was revealed. This silicone plug was glued to a 2.5 mm glass coverslip, using ultraviolet cured optical adhesive (Norland optical adhesive 81). And the 2.5 mm glass coverslip was then glued to an outer 4-mm glass coverslip, which would be fixed to the skull with Vetbond (3M) and dental cement.

After surgery, body temperature was maintained at 37°C using a heating blanket until the mouse recovered. Two-photon imaging was performed 3 h after waking. During imaging, the mouse was head-fixed on a spherical styroform ball that allows mouse run on it. A screen (60-Hz refresh rate) was positioned 40 cm above the mouse for displaying looming stimulus.

Images were captured under a two-photon resonant scanning microscope (Ultima Investigator, Bruker Nano, FMBU) equipped with a 16× water-immersion objective (Nikon, 0.8 NA). The excitation light used was a femtosecond laser (Mai Tai, DeepSee) with a wavelength of 940 nm. The images were captured using Prairie View software with 1× optical zoom. The final size of the field-of-view was  $837.4 \times 837.4 \mu\text{m}$  with a resolution of  $512 \times 512$  pixels, and the imaging rate was 30 Hz. The depth of imaging in the SC was 100–250  $\mu\text{m}$  from the SC surface.

### Whole-Cell Patch Recording

Brains were harvested quickly under halothane anesthesia and immersed in ice-cold oxygenated (95% O<sub>2</sub>–5% CO<sub>2</sub>) cutting solution (in mmol/L: 228 sucrose, 11 glucose, 26 NaHCO<sub>3</sub>, 1 NaH<sub>2</sub>PO<sub>4</sub>, 2.5 KCl, 7 MgSO<sub>4</sub>, 0.5 CaCl<sub>2</sub>). Coronal slices containing the SC (350  $\mu\text{m}$  thick) were prepared on a vibratome (model 752; Campden Instruments Ltd., Leicester, UK). The slices were incubated at 32°C for 30 min in artificial cerebrospinal fluid containing: (in mmol/L) 125 NaCl, 2.5 KCl, 1.3 NaH<sub>2</sub>PO<sub>4</sub>, 25 NaHCO<sub>3</sub>, 1.3 Na-ascorbate, 0.6 Na-pyruvate, 10 glucose, 2 CaCl<sub>2</sub>, and 1.3 MgCl<sub>2</sub> (pH 7.35 when saturated with 95% O<sub>2</sub>/5% CO<sub>2</sub>) [21]. After incubation for 1 h, the slices were transferred to the recording chamber and continuously perfused with ACSF at 1 mL/min. Single-cell recordings were made using either sharp electrodes or whole-cell patch recordings. We pulled recording electrodes from borosilicate glass capillary tubing (Sutter Instrument Co., Novato, CA) using a Flaming-Brown vertical microelectrode puller (model PC-10; Narishige). For whole-cell patch recordings, we filled pipettes (input resistance, 4–6 M $\Omega$ ) with the following recording solution: (in mmol/L) 135 K-methanesulfonate, 10 HEPES, 1 EGTA, 1 Na-GTP, 4 Mg-ATP, and 2% neurobiotin (pH 7.4, 280 mOsm). Brain slices in the recording chamber were illuminated by a

40× water-immersion objective lens (NIR-Apo, Nikon) and a fluorescent pathway with excitation (473 nm) filters. Data were analyzed offline using Clampfit 10 software (Molecular Devices).

To distinguish the different SC neuron types, Gale and Murphy determined the cumulative probability distributions of the resting potentials in SC neurons and found that different neurons had different resting potentials [25]. They found that the resting potential of wide-field neurons was from  $-50$  to  $-60$  mV, horizontal neurons from  $-60$  to  $-70$  mV, stellate neurons from  $-60$  to  $-70$  mV, and narrow-field neurons had the most hyperpolarized resting potentials, from  $-65$  to  $-75$  mV [25]. Moreover, these neurons had a specific response to injection of an 800-ms current step ( $\pm 600$  pA/ $\pm 100$  pA) [25]. Wide-field neurons had the largest and fastest depolarizing sag in response to  $-600$  pA current injection and high-frequency spikes to  $+600$  pA [28]. Horizontal neurons exhibited the lowest 100 spikes/s firing rate with  $+100$  pA current steps. Narrow-field neurons exhibited high-frequency spikes to  $+600$  pA current injection and the most hyperpolarized resting potential [25]. Stellate neurons were characterized by spike after-depolarization following  $-100$  pA current injection [25].

### Histology

Mice were sacrificed 1.5 h after looming stimulus testing for c-fos staining. Mice were transcardially perfused with cold 4% paraformaldehyde in phosphate-buffered saline (PBS). Brains were submerged in 30% sucrose in PBS to equilibrate and then cut into coronal sections (40  $\mu\text{m}$ ) on a cryostat (Leica CM1950, Germany). Immunohistochemistry was applied to map c-Fos activation in the brain with antiserum (rabbit anti-c-Fos, 2250, Cell Signaling Technology; 1:500). Sections were incubated for 48 h in antiserum at 4°C followed by overnight incubation with secondary antibodies at 4°C. Sections were then photographed and analyzed with a Leica TCS SP5 laser scanning confocal microscope and ImageJ, Image Pro-plus, and Photoshop software.

### Data Acquisition and Analysis

Behavioral data were analyzed using Anymaze software (Stoelting Co.). Speed and distance data were extracted using Anymaze software. All statistics were performed using Graph Pad Prism (GraphPad Software, Inc., San Diego, CA). No statistical methods were used to predetermine sample sizes, but our sample sizes were similar to those generally used in this paradigm. Student's *t*-test and one-way analyses of variance (ANOVA) were used where

appropriate. In all statistical data, statistical significance was set at  $*P < 0.05$ ,  $**P < 0.01$ ,  $***P < 0.001$ .

## Results

### Innate Defensive Responses to Visual Threats are Established in Mice by P20–24

We first examined the formation of visually-evoked defensive responses spanning different developmental periods. There are several critical time points during development: first, at P14 pups start eye-opening but have undeveloped motor ability [19]; second, young mice at P21 become nutritionally independent of their parents [19] and their whole brain volume rapidly approaches the adult size [29]; third, the prepubescent stage starts at P23 [30]. Therefore, the first group of mice was tested at P14–19, the second group at P20–29, and the third group at P30–39. Because mice appear to develop motor ability at different postnatal stages [19], we first tested their spontaneous locomotion of mice in the three stages. The mice were placed in the looming paradigm box and allowed to move freely for 5 min. The average speed and total distance travelled were recorded (Fig. 1A, B). We found that the average speed of P14–19 pups was lower than that of mice at P20–29 ( $P < 0.05$ ) and at P30–39 ( $P < 0.001$ ). Mice at P20–29 had a lower average speed than mice at P30–39 ( $P < 0.01$ ). The total distance travelled by P14–19 pups was the shortest among the postnatal groups (P14–19 vs P20–29,  $P < 0.05$ ; P14–19 vs P30–39,  $P < 0.001$ ). The total distance travelled by mice at P30–39 was higher than that by mice at P20–29 (P20–29 vs P30–39,  $P < 0.01$ ). These data showed that the spontaneous locomotion levels of mice at the three stages are different.

Next, to determine the postnatal period at which the formation of innate defensive responses to visual threats emerges, we narrowed the age-range groups for analysis. Mice were further separated into three groups (P14–16, P20–24, and P30–37), all of which were tested with looming stimuli (Fig. 2A). Initial behaviors in response to the looming stimuli were categorized as either flight, freezing, crouching, rearing, or non-response (Fig. 2B). The P14–16 pups displayed varied initial behaviors: 15% showing flight, 32.5% crouch, and 22.5% rearing, while 30% did not respond. Furthermore, the distribution patterns of initial defensive behaviors in the P20–24 and P30–37 groups were similar: 47.3% flight, 10.9% freezing, 36.3% rearing, and 5.5% no response in the P20–24 group; 53.3% flight, 16.7% freezing, 20% rearing, and 10% no response in the P30–37 group. In general, the proportion of mice displaying defensive behaviors increased at the P20–24 and P30–37 stages compared to the P14–16 group. We further quantified the innate defensive responses to looming. In the looming box, P20–24 ( $n = 55$ ) and P30–37 ( $n = 30$ ) mice typically escaped into the nest quickly with a shorter latency following looming stimuli than P14–16 pups ( $n = 40$ ) (Fig. 2C, Movie 1). We also found that the maximum speed of P14–16 pups during flight-to-nest behavior was the lowest amongst the three groups (P14–16 vs P20–24,  $P < 0.001$ ; P14–16 vs P30–37,  $P < 0.001$ ). The maximum speed of the P20–24 mice was not statistically different from that of P30–37 mice (Fig. 2D, P20–24 vs P30–37, ns). These results suggest that the defensive responses of mice in threatening situations start to be better established in P20–24 mice compared to P14–16 pups after initial eye-opening. In summary, our results showed that the innate defensive response to looming stimuli depends on age at the early postnatal stage.

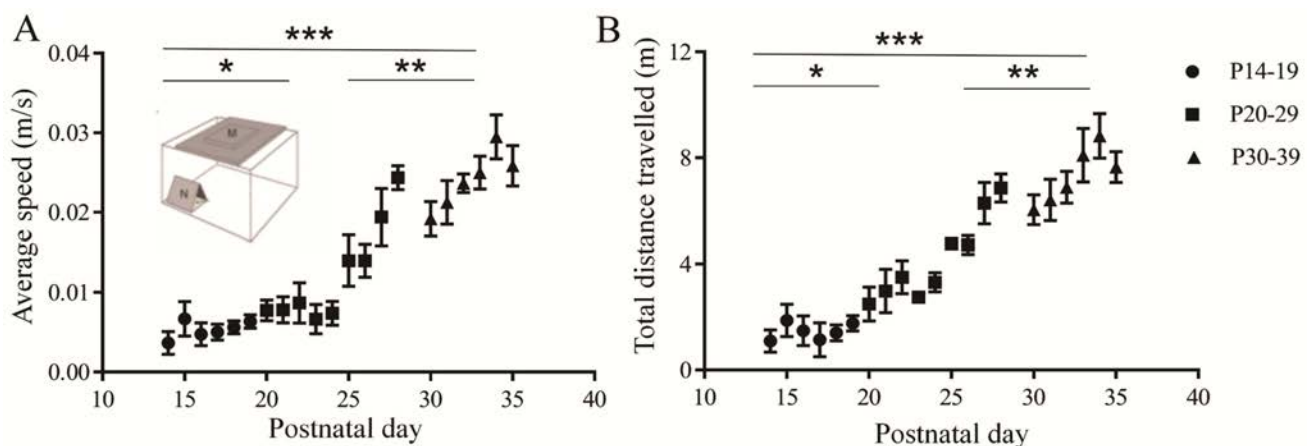


**Fig. 1** Motor skill development at different early postnatal ages. **A, B** Quantitative analysis of average speed **A** and total distance travelled **B** at difference ages.

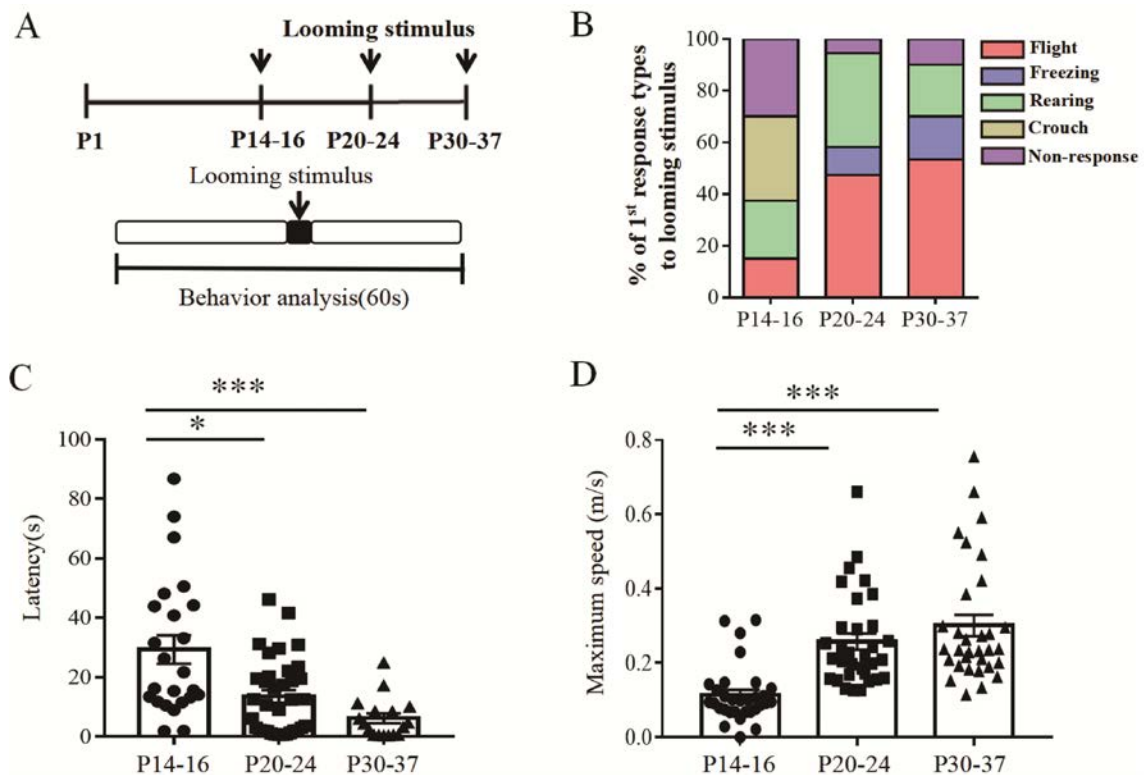


**Fig. 2** The formation of innate defensive responses to visual stimuli begins at P14–16 and is established by P20–24. **A** Schematic showing the three groups and behavioral testing timeline. **B** The percentages of initial behavior of mice at P14–16, P20–24, and P30–37 upon

exposure to looming. **C**, **D** Latency from onset of looming to return-to-nest **C** and maximum speed **D** of responsive mice at different stages.

To exclude individual differences and investigate whether the formation of the visual-evoked innate defensive response is age-dependent and fully formed at P20–24, we tracked looming-induced behavioral responses in each mouse of a cohort at different developmental stages (Fig. 3A). The even timeline showing defensive behaviors during the looming test was plotted for each mouse during a 10-s observation period beginning at the onset of the looming stimulus (Fig. 3B–D). A high frequency of crouching (Fig. 3B, 66.6%, 6/9) was found at P14–16 and a lower frequency (11.1%, 1/9) of flight. In contrast, flight was markedly higher at P20–24 (Fig. 3C, 77.7%, 7/9) and P30–37 (Fig. 3D, 77.7%, 7/9) with almost no crouching responses. When they did occur, brief periods of crouching were followed by either pre-looming behavior or some rearing before eventually walking as normal. This crouching behavior then subsided as the pups grew, and at P20–24, all mice switched to flight behavior (Fig. 3C, D). In summary, subsequent analysis of behavioral responses at three age ranges indicates that the formation of innate defensive responses in mice depends on age. There was one specific time window in which these responses began to develop, P14–16, and the development was relatively established at P20–24.

### Sensory Deprivation does not Affect the Formation of Visual Innate Fear Responses in Mice

Previous research has shown that visual deprivation at an early postnatal stage influences visual function and behavior [31]; dark-rearing prolongs the critical period for ocular dominance plasticity [32]. In addition, whisker deprivation reduces excitatory synaptic transmission and neuronal excitability in S1 and cross-modally in V1 cortex [27]. Therefore, we applied the dark-rearing and whisker deprivation at an early postnatal stage in mice to determine whether they will alter the emergence of the visually-evoked defensive responses. Figure 4A shows the timeline of sensory deprivation and the looming test. We maintained dark-rearing for three weeks during early postnatal development, and then tracked the innate defensive responses from P20 to P37. After three weeks of dark-rearing, we compared the behavioral responses to looming stimuli in young control and dark-reared mice. The latency to return to the nest of the dark-reared group (DR-P20-24) was similar to the control group and the same was found in another older dark-reared group (DR-P30–37) (Fig. 4B). Next, we investigated the defensive responses of whisker-clipped mice at P14–16 and P20–24 and found that they



**Fig. 3** Looming-evoked flight behavior commences at P14–16 and is expressed at P20–24 in most mice. **A** Schematic showing the behavioral testing timeline in the same mouse cohort. **B–D** Subsequent analyses of behavioral responses at **B** P14–16, **C** P20–24, and **D** P30–37.

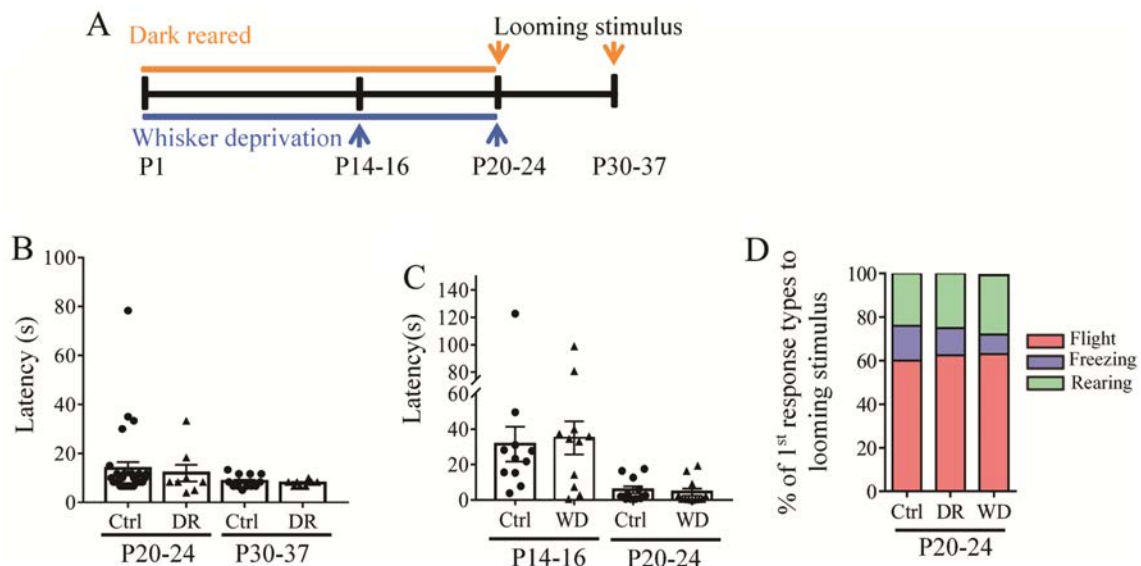
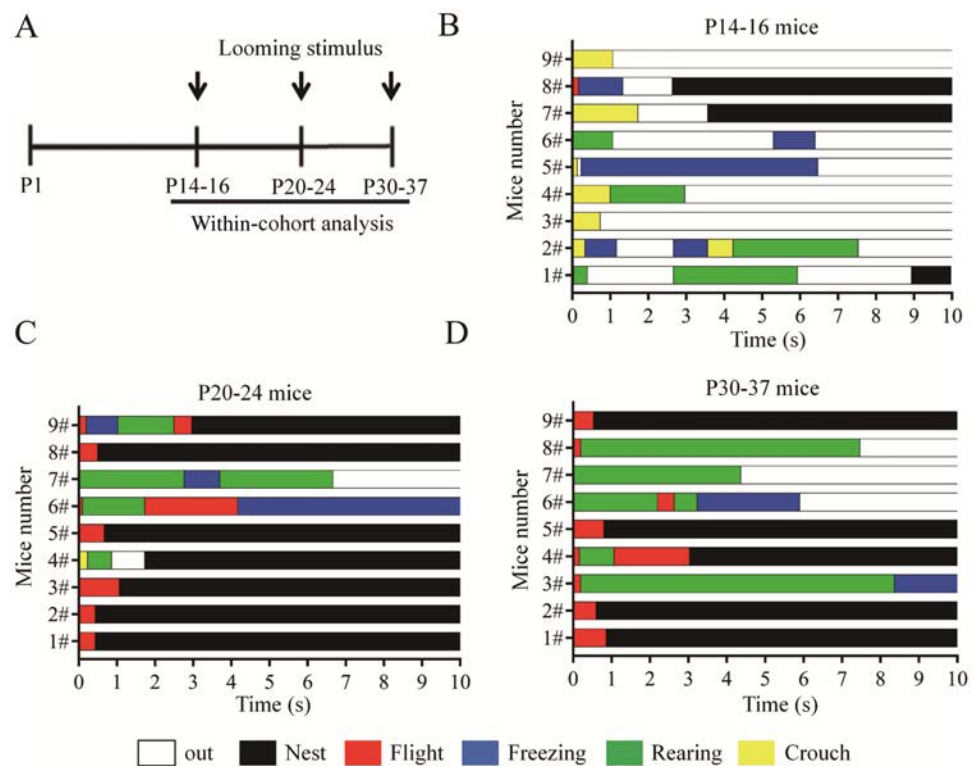


**Fig. 4** Dark-rearing and whisker deprivation during the early postnatal period does not affect the formation of visual looming-evoked innate fear responses in mice. **A** Schematic showing the timeline of sensory deprivation and behavioral tests. **B**, **C** Latency-to-

nest of **B** dark-reared and **C** whisker-deprived mice. **D** Percentages of initial behavior of mice after sensory deprivation upon exposure to looming at P20–24.

exhibited latencies similar to the control group (Fig. 4C). Visual or whisker deprivation from birth to 3 weeks of age did not dramatically alter the distribution pattern of defensive behaviors of P20–24 mice following looming

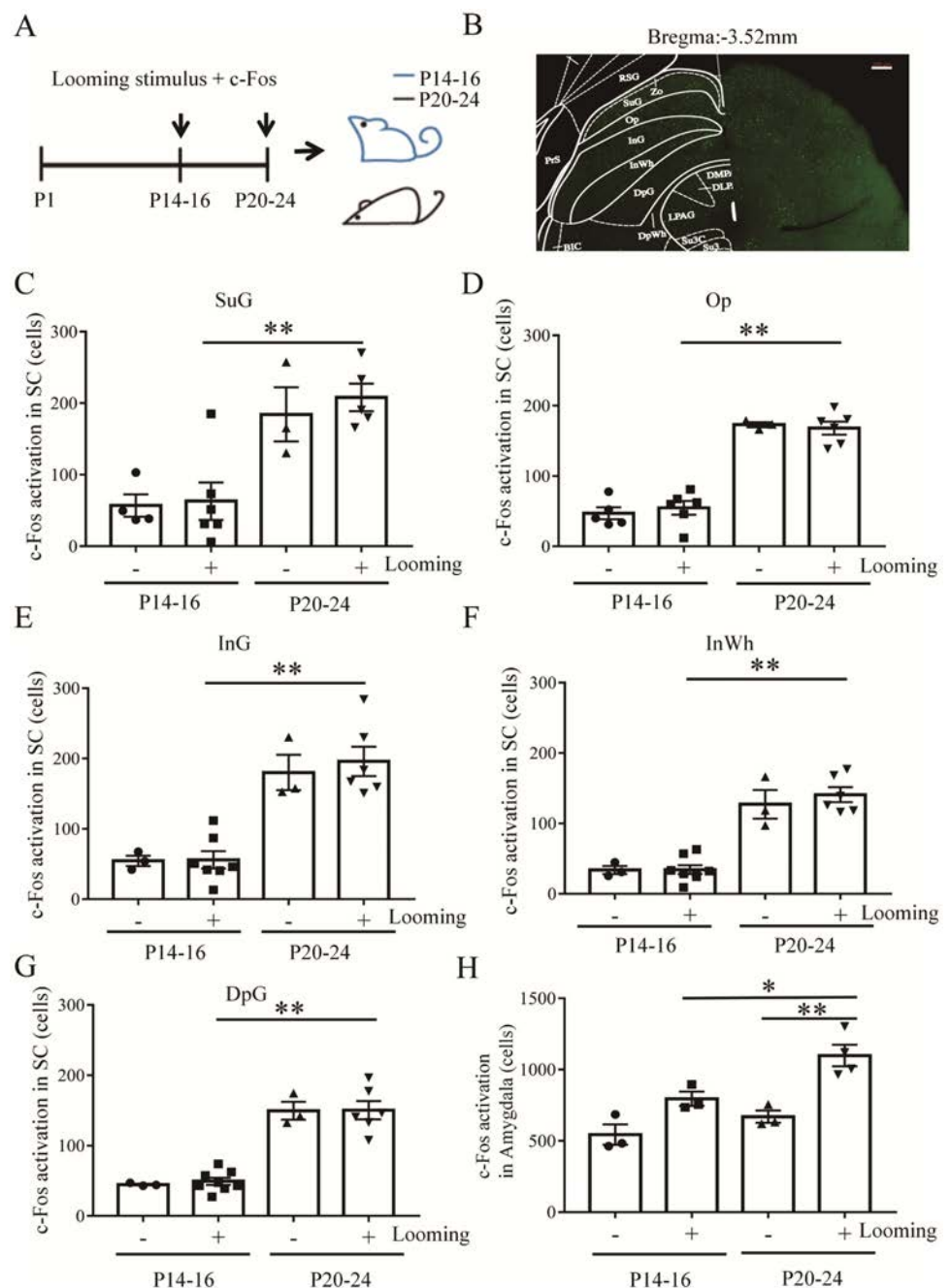
stimuli (Fig. 4D). Therefore, the development of functional properties in mice, and their expression, are uncoupled from light and whisker deprivation during postnatal development.

### SC Neurons play an Important Role in the Development of Innate Defensive Responses to Visual Threats

The SC is an important node for detecting threatening overhead looming information in rats [33]. In addition, work from our group has demonstrated that neurons in the SC are essential for innate defensive responses to overhead looming stimuli in adult mice [21, 23]. To investigate innate SC-mediated visual defensive responses in early postnatal mice, we analyzed c-Fos in the SC of pups

(P14–16) and young mice (P20–24) (Fig. 5A). The SC is composed of alternating gray and white layers that can be easily identified the living slice; these are the zonal, superficial gray, optic nerve, intermediate gray, intermediate white, deep gray, and deep white layers [34] (Fig. 5B). Previous studies have shown that the superficial SC receives projections from retinal ganglion cells and middle/deeper SC layers [35]. We assessed c-Fos expression in neurons from all layers shortly after a looming stimulus test (Fig. 5C–G, looming group at P14–16 vs looming group at P20–24,  $P < 0.01$ ). The expression of c-Fos in all SC

**Fig. 5** The c-Fos expression in the SC region of pups is lower than that of prepubescent mice following looming stimuli. **A** Schematic showing the timeline of behavioral testing and c-Fos examination. **B** Representative images of c-Fos expression in the SC following a looming stimulus (scale bar, 200  $\mu$ m). **C–G** c-Fos expression in pups and prepubescent mice in **C** the superficial layer (SuG), **D** the optic nerve layer (Op), **E** the intermediate gray layer (InG), **F** the intermediate white layer (InWh) and **G** in the deep gray layer of the SC (DpG). **H** Cells with c-Fos activation in the amygdala of pups and prepubescent.



substructures in pups (P14–16) was significantly lower than in young mice (P20–24). These data indicated that SC neurons do not respond to a looming stimulus until the prepubescent stage (P20–24). Moreover, the SC is one of the relays from the retina to the amygdala [36, 37], so we assessed c-Fos expression in neurons in the amygdala after a looming stimulus (Fig. 5H). We found that the expression of c-Fos in the control group was lower than that of the looming group at P14–16, but the difference was not statistically significant. But at P20–24, the number of neurons with c-Fos expression in the looming group was higher than that of control group (Control *vs* looming,  $P < 0.01$ ). In addition, looming stimuli induced more c-Fos expression in neurons in amygdala at P20–24 than at P14–16 ( $P < 0.05$ ). These data implied that the developments of SC and amygdala in concert establish the innate defensive responses to visual threats at early postnatal stage.

To determine the visual processing functions of SC neurons in the critical developmental time window, we applied  $\text{Ca}^{2+}$  imaging *in vivo* in Thy1-GCaMP6f transgenic mice, which were born with a  $\text{Ca}^{2+}$  indicator present in the brain. Two groups of Thy1-GCaMP6f transgenic mice, P14–16 and P20–24, were used (Fig. 6A). After surgery, Thy1-GCaMP6f transgenic mice were head-fixed on a spherical styroform ball. An LCD monitor was positioned above the mice to display the looming stimulus (Fig. 6B). Using a two-photon resonant scanning microscope, we observed that some SC neurons in P16 pups were excited during the looming stimulus, but the  $\text{Ca}^{2+}$  signals were weak (Fig. 6C–E). Moreover, the  $\text{Ca}^{2+}$  signals from SC neurons rose with the onset of the looming stimulus and decayed following its offset in P24 mice (Fig. 6D). The mean peak amplitude of SC neurons in young mice was higher than that of pups following looming presentation (Fig. 6E, P16 *vs* P24,  $P < 0.001$ ). Furthermore,  $\text{Ca}^{2+}$  imaging statistical data in Thy1-GCaMP6f transgenic mice (Fig. 6F) revealed that a large number (69%) of SC neurons were excited by a looming stimulus at P20–24 and around half (53%) were excited at P14–16. These data demonstrated that SC neurons in P14–16 pups and P20–24 young mice receive visual stimulus information from the retina, but more SC neurons in P20–24 mice respond to a looming stimulus. That the P20–24 mice have a flight-into-nest response to a looming stimulus suggests that SC neurons in these mice are involved in mediating looming-evoked defense responses.

In addition, we investigated the expression of different cell types in the SC at early postnatal (P14–16) and prepubescent (P20–24) stages. Previous estimates of cell types in the superficial SC were based on intrinsic electrophysiological properties using patch clamp recordings from slices [25]. Here, we found, using whole-cell

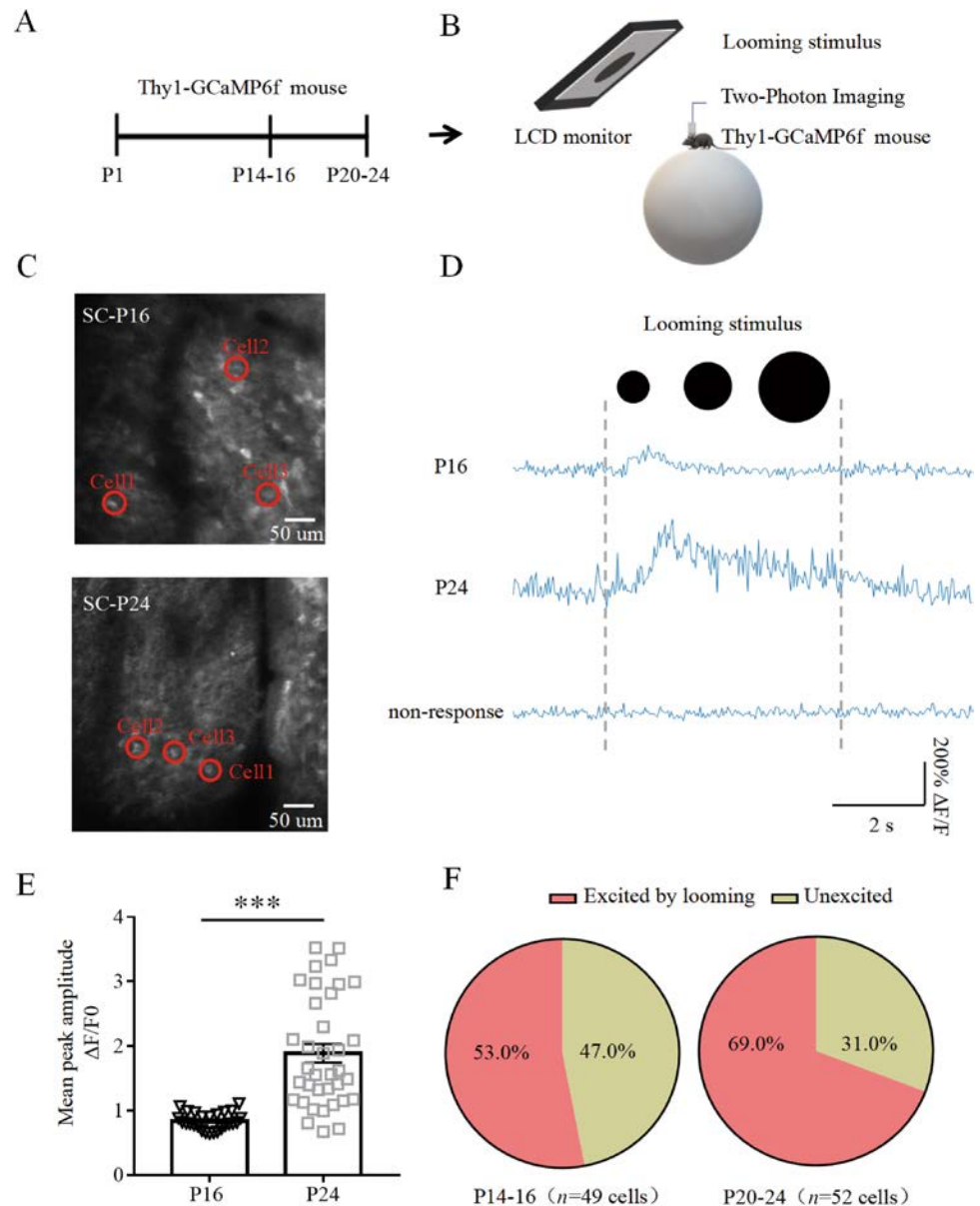
patch recording in SC slices, a significant difference in cell types between the early postnatal and prepubescent stages. The experimental timeline and electrophysiological protocol are shown in Fig. 7A and B. To investigate the intrinsic electrophysiological properties of SC cells, we injected current ( $\pm 100$  pA and  $\pm 600$  pA) for 800 ms to distinguish SC cell types in pups and prepubescent mice (Fig. 7C, D). Moreover, we calculated the number of different cell types in each of the two age ranges (Fig. 7E, F). Half of the SC cells recorded during the early postnatal stage had no spiking with current injection. These were likely to be immature cells, of which there was a higher percentage during the early postnatal stage than the prepubescent stage. Interestingly, there was a higher percentage of horizontal and wide-field cells in P20–24 mice than in P14–16 pups. As our results showed that the percentage of wide-field and horizontal cells of all recorded cells in the superior colliculus were notably elevated at P20–24, it is likely that they contribute to the function underlying innate defensive responses.

## Discussion

Several studies have investigated the adult mouse behavioral responses to looming stimuli [21, 23]. However, it remains unclear during which developmental stage the innate defense response to looming stimuli first occurs in mice. In this study, we explored the expression of innate defensive responses in different development epochs after initial eye-opening in mice. Not until the P20–24 stage did mice rapidly display flight-to-nest behavior induced by looming stimuli, which has been observed in adult mice in several reports [21, 23]. Here, we found that the development of these responses to looming stimuli occurred in a specific time window (P14–16) and was gradually established at P20–24 accompanied by the development of locomotion. The gradually-developed defensive ability during P20–24 may correlate strongly with the young mice at this stage becoming independent of maternal care and protection [19]. Our findings contribute to a better understanding of the early postnatal development of defensive behaviors that have been shaped by evolutionary pressure.

We provided a detailed description of looming-evoked defensive responses during early postnatal (P14–16), prepubescent (P20–24), and mid-pubescent (P30–37) stages in mice. Pups at P14–16 had a stronger tendency to display a crouching response to looming stimuli, whereas young mice at P20–24 and P30–37 had an increasing tendency for flight-to-nest behaviors (Fig. 2). This may be partially explained by the fact that the locomotion of pups was still under development, as we found that pups at this stage exhibited reduced spontaneous locomotion and a slower

**Fig. 6** More SC neurons in prepubescent mice respond to looming stimuli than in pups. **A** Schematic showing the two groups of Thy1-GCaMP6f transgenic mice. **B** *In vivo* two-photon  $\text{Ca}^{2+}$  imaging in the SC of Thy1-GCaMP6f transgenic mice. **C** Representative images showing that SC neurons are excited by a looming stimulus in pups and young mice. **D**  $\text{Ca}^{2+}$  signals in SC neurons of P20–24 mice are stronger than in P14–16 pups. **E** Mean peak amplitude of SC neurons responding to looming stimuli at P14–16 and P20–24. **F** Summary of the proportion of SC neurons activated by looming stimuli in pups and young mice.



maximal speed during a flight response (Fig. 1). However, a prominent percentage of pups at P14–16 did not respond to looming stimuli compared to young mice starting at P20, suggesting that the neural mechanisms underlying responses to threat in pups are likely not as established as those in young mice.

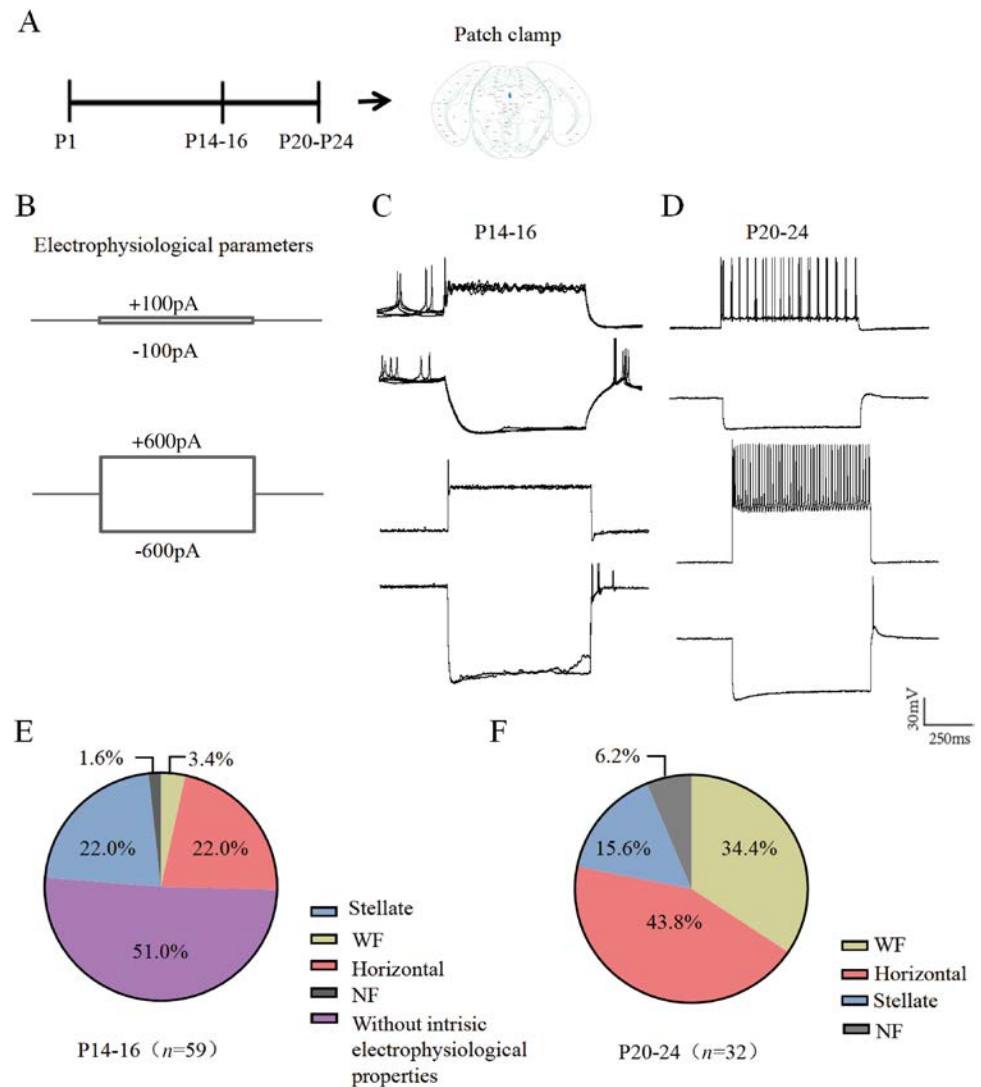
Previous studies have reported that, during the development of RGCs at P10–12, retinal ganglion cells receive visual information from the environment and directly deliver information into the mouse SC [38]. In this study, we applied looming stimuli with parameters within the range that has been reported to induce flight behaviors and saturated responses of SC neurons in adult mice (angular size, 4–40° and expanding at 144°/s) [39, 40]. We found that these looming parameters evoked higher c-Fos

expression in the SC of young mice (P20–24) than in pups (P14–16) (Fig. 5). Moreover, *in vivo*  $\text{Ca}^{2+}$  imaging data demonstrated that SC neurons were already excited by looming stimulus in pups at P14–16, consistent with the previous study showing that the RGCs at this developmental stage project visual information into the SC [38], but the percentage of SC neurons activated by looming at P14–16 was less than that at P20–24. In addition, the mean  $\text{Ca}^{2+}$  activity of the responsive cells at P14–16 was significantly weaker than that at P20–24. These results suggested that there are more mature cells in the SC at P20–24. Furthermore, electrophysiological recording from SC neurons revealed a higher percentage of horizontal and wide-field cells at P20–24 than at P14–16. As we discovered that P20–24 was the period when flight-to-nest



**Fig. 7** The percentages of wide-field and horizontal cells are notably elevated in the superficial SC at P20–24.

**A** Schematic showing the timeline of the patch-clamp recordings. **B** Representative images showing electrophysiological parameters in the SC. **C**, **D** Patch-clamp records from the SC region of **C** pups and **D** pre-pubescent mice. **E** Summary of the proportions of different cell types in the SC of pups. Half of the cells were without spiking activity. **F** Percentages of the four cell types in the SC of young mice.



responses to looming were better established, the elevated responses of cells in the SC and the increased percentage of horizontal cells and wide-field cells imply that they have important functions in the formation of innate defensive responses during the early developmental stage. All together, our results suggest the establishment of defensive responses at the early postnatal stage requires the development of both motor ability and brain functions.

Previous studies have shown that sensory deprivation during early postnatal development can induce developmental impairment of neuronal morphology and connectivity and reduce responsiveness in the corresponding brain region [31, 41–43]. Visual deprivation, such as dark-rearing from birth, permanently impairs visual function [44]. Although dark-rearing during early development delays the maturation of RGCs in mice, our results indicate that the innate defensive responses of dark-reared mice are not significantly influenced by visual deprivation since no

notable differences between dark-reared mice and control mice were observed. In adult mice, whisker deprivation markedly improves behavioral visual acuity and contrast sensitivity [45]. Our results showed that whisker deprivation had no prominent effect on the expression of innate defensive responses in early-neonatal-stage mice, which produce strong flight-to-nest behavior following looming stimuli. These results suggest that innate defensive responses are an inherent ability in mice and cannot be altered by sensory deprivation during the early neonatal stage.

Clinically, some autism patients exhibit a “lack of fear in response to real dangers” and difficulty reading fearful emotions [46]. Furthermore, previous studies on human children have suggested that autistic children lack defensive responses to looming stimuli [47]. However, little is known about when or how development becomes disrupted at early stages in autism. We have discovered a remarkable

time window in mice (P20–24), during which the formation of innate defensive responses occurs. In addition, we found that they are inherent characteristics that are not affected by sensory deprivation during the early postnatal period. Moreover, the percentage of horizontal and wide-field cells increased notably in the superficial layers of the SC during this specific window. Our findings increase the understanding of the interaction between developmental factors and defensive responses, and provides an evidence base for future research on neurodevelopmental disorders.

**Acknowledgements** This work was supported by the National Natural Science Foundation of China (31930047, 91732304 and 31630031); The Strategic Priority Research Program of the Chinese Academy of Science (XDB32030100); Guangdong Provincial Key Laboratory of Brain Connectome and Behavior (2017B030301017); the National Science Foundation of Guangdong Province (2018A030313439); a Shenzhen Government grant (JCYJ20170413164535041); Shenzhen Key Science and Technology Infrastructure Planning Project (ZDKJ20190204002); Key Laboratory of CAS (2019DP173024); The Ten Thousand Talents Program; The Guangdong Special Support Program; Chang Jiang Scholars Program; International Partnership Program of the Chinese Academy of Sciences (172644KYS820170004); and the Key-Area Research and Development Program of Guangdong Province (2018B030331001).

**Conflict of interest** The authors declare no competing interests.

## References

- Tovote P, Esposito MS, Botta P, Chaudun F, Fadok JP, Markovic M. Midbrain circuits for defensive behaviour. *Nature* 2016, 534: 206–212.
- Ydenberg RC, Dill LM. The economics of fleeing from predators. *Adv Study Behav* 1986, 16: 229–249.
- Fischer S, Oberhammer E, Cunha-Saraiva F, Gerber N, Taborsky B. Smell or vision? The use of different sensory modalities in predator discrimination. *Behav Ecol Sociobiol* 2017, 71: 1–10.
- Pereira AG, Moita MA. Is there anybody out there? Neural circuits of threat detection in vertebrates. *Curr Opin Neurobiol* 2016, 41: 179–187.
- Albano JE, Humphrey AL, Norton TT. Laminar organization of receptive-field properties in tree shrew superior colliculus. *J Neurophysiol* 1978, 41: 1140–1164.
- McIlwain JT, Buser P. Receptive fields of single cells in the cat's superior colliculus. *Exp Brain Res* 1968, 5: 314–325.
- Stewart DL, Birt D, Towns LC. Visual receptive-field characteristics of superior colliculus neurons after cortical lesions in the rabbit. *Vision Res* 1973, 13: 1965–1977.
- Fortin S, Chabli A, Dumont I, Shumikhina S, Itaya SK, Molotchnikoff S. Maturation of visual receptive field properties in the rat superior colliculus. *Brain Res Dev Brain Res* 1999, 112: 55–64.
- Dräger UC, Hubel DH. Responses to visual stimulation and relationship between visual, auditory, and somatosensory inputs in mouse superior colliculus. *J Neurophysiol* 1975, 38: 690–713.
- Sen R, Wu M, Branson K, Robie A, Rubin GM, Dickson BJ. Moonwalker descending neurons mediate visually evoked retreat in *Drosophila*. *Curr Biol* 2017, 27: 766–771.
- LeDoux J. Rethinking the emotional brain. *Neuron* 2012, 73: 653–676.
- LeDoux JE. Coming to terms with fear. *Proc Natl Acad Sci U S A* 2014, 111: 2871–2878.
- Mobbs D, Hagan CC, Dalgleish T, Silston B, Prévost C. The ecology of human fear: Survival optimization and the nervous system. *Front Neurosci* 2015, 9: 55.
- Moriceau S, Roth TL, Okotoghaide T, Sullivan RM. Corticosterone controls the developmental emergence of fear and amygdala function to predator odors in infant rat pups. *Int J Dev Neurosci* 2004, 22: 415–422.
- Arakawa H. Age and sex differences in the innate defensive behaviors of C57BL/6 mice exhibited in a fear conditioning paradigm and upon exposure to a predatory odor. *Physiol Behav* 2019, 204: 264–274.
- Sharma A, LeVaillant CJ, Plant GW, Harvey AR. Changes in expression of Class 3 Semaphorins and their receptors during development of the rat *Retina* and superior colliculus. *BMC Dev Biol* 2014, 14: 34.
- Williams E, Scott JP. The development of social behavior patterns in the mouse, in relation to natural periods 1). *Behaviour* 1954, 6: 35–64.
- Barbara K. Components of lifetime reproductive success in communally and solitarily nursing house mice—a laboratory study. *Behav Ecol Sociobiol* 1994, 34: 275–283.
- Latham N, Mason G. From house mouse to mouse house: The behavioural biology of free-living *Mus musculus* and its implications in the laboratory. *Appl Animal Behav Sci* 2004, 86: 261–289.
- Yilmaz M, Meister M. Rapid innate defensive responses of mice to looming visual stimuli. *Curr Biol* 2013, 23: 2011–2015.
- Zhou Z, Liu XM, Chen SP, Zhang ZJ, Liu YM, Montardy Q, *et al.* A VTA GABAergic neural circuit mediates visually evoked innate defensive responses. *Neuron* 2019, 103: 473–488.e6.
- Wei P, Liu N, Zhang Z, Liu X, Tang Y, He X, *et al.* Processing of visually evoked innate fear by a non-canonical thalamic pathway. *Nat Commun* 2015, 6: 6756.
- Li L, Feng X, Zhou Z, Zhang H, Shi Q, Lei Z, *et al.* Stress accelerates defensive responses to looming in mice and involves a locus coeruleus-superior colliculus projection. *Curr Biol* 2018, 28: 859–871.e5.
- Shang CP, Liu ZH, Chen ZJ, Shi YC, Wang Q, Liu S, *et al.* BRAIN CIRCUITS A parvalbumin-positive excitatory visual pathway to trigger fear responses in mice. *Science* 2015, 348: 1472–1477.
- Gale SD, Murphy GJ. Distinct representation and distribution of visual information by specific cell types in mouse superficial superior colliculus. *J Neurosci* 2014, 34: 13458–13471.
- Dana H, Chen TW, Hu A, Shields BC, Guo CY, Looger LL, *et al.* Thy1-GCaMP6 transgenic mice for neuronal population imaging *in vivo*. *PLoS One* 2014, 9: e108697. <https://doi.org/10.1371/journal.pone.0108697>.
- Zheng JJ, Li SJ, Zhang XD, Miao WY, Zhang DH, Yao HS, *et al.* Oxytocin mediates early experience-dependent cross-modal plasticity in the sensory cortices. *Nat Neurosci* 2014, 17: 391–399.
- Endo T, Tarusawa E, Notomi T, Kaneda K, Hirabayashi M, Shigemoto R, *et al.* Dendritic Ih ensures high-fidelity dendritic spike responses of motion-sensitive neurons in rat superior colliculus. *J Neurophysiol* 2008, 99: 2066–2076.
- Chuang N, Mori S, Yamamoto A, Jiang HY, Ye X, Xu X, *et al.* An MRI-based atlas and database of the developing mouse brain. *Neuroimage* 2011, 54: 80–89.
- Brust V, Schindler PM, Lewejohann L. Lifetime development of the behavioural phenotype in the house mouse (*Mus musculus*). *Front Zool* 2015, 12: S17.
- Fox K, Wong RO. A comparison of experience-dependent plasticity in the visual and somatosensory systems. *Neuron* 2005, 48: 465–477.

32. Gianfranceschi L, Siciliano R, Walls J, Morales B, Kirkwood A, Huang ZJ, *et al.* Visual cortex is rescued from the effects of dark rearing by overexpression of BDNF. *Proc Natl Acad Sci U S A* 2003, 100: 12486–12491.
33. Dean P, Redgrave P, Westby GW. Event or emergency? Two response systems in the mammalian superior colliculus. *Trends Neurosci* 1989, 12: 137–147.
34. Basso MA, May PJ. Circuits for action and cognition: A view from the superior colliculus. *Ann Rev Vis Sci* 2017, 3: 197–226.
35. Ito S, Feldheim DA. The mouse superior colliculus: An emerging model for studying circuit formation and function. *Front Neural Circuits* 2018, 12: 10.
36. Chen YM, Ni YL, Zhou JH, Zhou H, Zhong Q, Li XY, *et al.* The amygdala responds rapidly to flashes linked to direct retinal innervation: A flash-evoked potential study across cortical and subcortical visual pathways. *Neurosci Bull* 2021, 37: 1107–1118.
37. Tamietto M, Pullens P, de Gelder B, Weiskrantz L, Goebel R. Subcortical connections to human amygdala and changes following destruction of the visual cortex. *Curr Biol* 2012, 22: 1449–1455.
38. Gribizis A, Ge X, Daigle TL, Ackman JB, Zeng H, Lee D, *et al.* Visual cortex gains independence from peripheral drive before eye opening. *Neuron* 2019, 104: 711–723.e3.
39. Yang X, Liu Q, Zhong J, Song R, Zhang L, Wang L. A simple threat-detection strategy in mice. *BMC Biol* 2020, 18: 93.
40. Zhao X, Liu M, Cang J. Visual cortex modulates the magnitude but not the selectivity of looming-evoked responses in the superior colliculus of awake mice. *Neuron* 2014, 84: 202–213.
41. Wiesel TN. Postnatal development of the visual cortex and the influence of environment. *Nature* 1982, 299: 583–591.
42. Feldman DE, Brecht M. Map plasticity in somatosensory cortex. *Science* 2005, 310: 810–815.
43. Espinosa JS, Stryker MP. Development and plasticity of the primary visual cortex. *Neuron* 2012, 75: 230–249.
44. Gianfranceschi L, Siciliano R, Walls J, Morales B, Kirkwood A, Huang ZJ, *et al.* Visual cortex is rescued from the effects of dark rearing by overexpression of BDNF. *Proc Natl Acad Sci U S A* 2003, 100: 12486–12491.
45. Teichert M, Isstas M, Wenig S, Setz C, Lehmann K, Bolz J. Cross-modal refinement of visual performance after brief somatosensory deprivation in adult mice. *Eur J Neurosci* 2018, 47: 184–191.
46. Adolphs R, Sears L, Piven J. Abnormal processing of social information from faces in autism. *J Cogn Neurosci* 2001, 13: 232–240.
47. Hu Y, Chen ZM, Huang L, Xi Y, Li BX, Wang H, *et al.* A translational study on looming-evoked defensive response and the underlying subcortical pathway in autism. *Sci Rep* 2017, 7: 14755.

# Multiple Mild Stimulations Reduce Membrane Distribution of CX3CR1 Promoted by Annexin a1 in Microglia to Attenuate Excessive Dendritic Spine Pruning and Cognitive Deficits Caused by a Transient Ischemic Attack in Mice

Lu Zheng<sup>1,2,3</sup> · Yi Wang<sup>1,2,3</sup> · Bin Shao<sup>1,2,3</sup> · Huijuan Zhou<sup>1,2,3</sup> · Xing Li<sup>1,2,3</sup> · Cai Zhang<sup>4,5</sup> · Ning Sun<sup>1,2,3</sup> · Jing Shi<sup>1,2,3</sup>

Received: 21 June 2021 / Accepted: 25 November 2021 / Published online: 30 March 2022

© Center for Excellence in Brain Science and Intelligence Technology, Chinese Academy of Sciences 2022

**Abstract** A transient ischemic attack (TIA) can cause reversible and delayed impairment of cognition, but the specific mechanisms are still unclear. Annexin a1 (ANXA1) is a phospholipid-binding protein. Here, we confirmed that cognition and hippocampal synapses were impaired in TIA-treated mice, and this could be rescued by multiple mild stimulations (MMS). TIA promoted the interaction of ANXA1 and CX3CR1, increased the membrane distribution of CX3CR1 in microglia, and thus enhanced the CX3CR1 and CX3CL1 interaction. These phenomena induced by TIA could be reversed by MMS. Meanwhile, the CX3CR1 membrane distribution and CX3CR1–CX3CL1 interaction were upregulated in

primary cultured microglia overexpressing ANXA1, and the spine density was significantly reduced in co-cultured microglia overexpressing ANXA1 and neurons. Moreover, ANXA1 overexpression in microglia abolished the protection of MMS after TIA. Collectively, our study provides a potential strategy for treating the delayed synaptic injury caused by TIA.

**Keywords** Annexin a1 · CX3CR1 · Microglia · Dendritic spine pruning · Transient ischemic attack · Multiple mild stimulations

**Supplementary Information** The online version contains supplementary material available at <https://doi.org/10.1007/s12264-022-00847-4>.

✉ Ning Sun  
nsun@hust.edu.cn

✉ Jing Shi  
sj@mails.tjmu.edu.cn

<sup>1</sup> Department of Neurobiology, School of Basic Medicine, Tongji Medical College, Huazhong University of Science and Technology, Wuhan 430030, China

<sup>2</sup> Key Laboratory of Neurological Diseases, Ministry of Education, Wuhan 430030, China

<sup>3</sup> The Institute for Brain Research, Collaborative Innovation Center for Brain Science, Huazhong University of Science and Technology, Wuhan 430030, China

<sup>4</sup> Department of Clinical Laboratory, The First Affiliated Hospital of Zhengzhou University, Zhengzhou 450052, China

<sup>5</sup> Department of Immunology, School of Basic Medicine, Tongji Medical College, Huazhong University of Science and Technology, Wuhan 430030, China

## Introduction

Transient ischemic attack (TIA) is a transient attack of reversible neurological dysfunctions caused by ischemia of the brain, spinal cord, or retina without acute infarction [1]. TIA is usually associated with cognitive deficits caused by potential cerebrovascular diseases and easily leads to recurrent stroke [2], coronary heart disease [3], epilepsy [4] and even death. Clinical treatments for TIA involve early thrombolysis, antiplatelet therapy, and the control of risk factors such as hypertension, dyslipidemia, diabetes, and heart disease following risk assessment and stratification [5]. Considering that TIA or ischemic stroke is extremely prone to recurrence because of peripheral adverse factors, it is imperative to explore the pathogenesis of TIA and to propose corresponding interventions.

Microglia plays an essential role in the development and homeostasis of the central nervous system (CNS). Many studies have shown that microglia regulate neuronal survival and apoptosis, axonal growth, and synaptic homeostasis by interacting with neurons and other glia, potentially affecting the maturation of neuronal circuits



[6, 7]. Microglia can regulate synapses directly (contact and phagocytosis) [8, 9] or indirectly (cytokine secretion) [10]. Notably, microglia modulate brain function by engulfing non-functional synapses and cellular debris through phagocytosis (also known as synaptic pruning) [11]. In addition, the excessive phagocytosis of stressed but viable neurons by microglia is also one reason for developmental disorders and neurodegenerative diseases [12, 13]. Therefore, the synaptic pruning by microglia may be a potential target for neurological dysfunction after TIA.

C-X3-C motif chemokine receptor 1 (CX3CR1) is a member of the G protein-coupled receptor superfamily that is expressed in microglia and macrophages. Previous studies have shown that CX3CR1 mediates the phagocytosis of PSD95 by microglia [14]. Meanwhile, CX3CR1 can mediate synaptic integration through the phagocytosis of postsynaptic components [15]. Another study found that the number of hippocampal microglia is temporarily decreased and the dendritic spine density is correspondingly increased in *Cx3cr1*-knockout mice, and this delays the maturation of the hippocampal loop [14], indicating that CX3CR1 is a vital regulator in microglia to maintain the development of neuronal circuits. The specific ligand of CX3CR1, chemokine C-X3-C motif ligand 1 (CX3CL1, also known as fractalkine), is a chemokine family member with a CX3C motif that exists in membrane-bound and soluble forms. CX3CL1 is mainly expressed in neurons in the CNS [16]. CX3CL1/CX3CR1 signal transduction is involved in the activation and chemotaxis of microglia and plays a vital role in the interactions between microglia and neurons that participate in brain development, aging, and diseases [14, 17]. Thus, whether CX3CL1/CX3CR1 signaling between microglia and neurons is involved in the transient but recurring synaptic and learning and memory impairment after TIA is still unclear and needs further study.

A member of the annexin family, Annexin A1 (ANXA1, also known as Lipocortin I) can reversibly interact with cell membranes in a  $\text{Ca}^{2+}$ -dependent manner [18]. Besides mediating neutrophil migration [19], macrophage phagocytosis [20], and the anti-inflammatory effects of glucocorticoids [21], ANXA1 also participates in intracellular signal transduction through its membrane-linked characteristics [22]. Due to different subcellular localizations and post-translational modifications, ANXA1 interacts with different chaperone proteins and plays different physiological roles. Cytoplasmic phospholipase A2 interacts with full-length ANXA1 in the cytoplasm and with N terminal-cleaved ANXA1 in the membrane fraction to cause pro-inflammatory action during mast-cell activation [23]. Whether ANXA1 interacts with CX3CR1 and involves membrane transduction in transient and reversible TIA needs to be confirmed.

Given the lack of specific therapies for TIA, we hypothesized that multiple mild stimulations (MMS), some of which have been reported to improve learning and memory, might be effective in resisting neurological damage after TIA. In this study, we first evaluated the therapeutic effects of MMS on TIA. Furthermore, we studied the molecular mechanisms by which MMS affects the plasticity of neurons through modulating microglia. Overall, we propose that MMS is effective for TIA, and expect to find a new and potential treatment strategy for resisting the damage caused by transient cerebral ischemia.

## Materials and Methods

### Animals and Treatments

#### Animals

The *Cx3cr1*-cre mice (B6J.B6N(Cg)-Cx3cr1tm1.1(cre) Jung/J (RRID: IMSR\_JAX: J025524)) in the C57BL/6 strain background were from the Jackson Laboratory. Male wild-type (WT) C57BL/6 mice were purchased from Beijing Vital River Laboratory Animal Technology. Considering that estrogen expression differences between the sexes might influence cognitive function, we only used male mice. Mice were kept under a 12-h light/dark cycle at room temperature (RT;  $22 \pm 1^\circ\text{C}$ ) with food and water *ad libitum* unless indicated otherwise. All experiments were conducted following guidelines approved by the Institutional Animal Care and Use Committee of Huazhong University of Science and Technology and complied with the US National Institute of Health guidelines for animal research.

#### Transient Ischemic Attack (TIA)

To simulate slight ischemic impairment in mice, we selected transient global cerebral ischemia by bilateral common carotid artery (BCCA) occlusion from among the various models of ischemia [24] because of its repetitiveness and delayed neuronal damage [25]. Mice were deprived of food and water at least 6 h before surgery and then anesthetized with chloral hydrate (350 mg/kg) by intraperitoneal injection. The body temperature was maintained at  $37 \pm 0.5^\circ\text{C}$  with a homeothermic blanket (Harvard Apparatus) during the surgery. First, an incision was made in the middle ventral neck and the BCCA was gently separated from the vagus nerve. The BCCA was tightly occluded with 7–0 silk for 5 min to induce a slight ischemic injury and then the silk was withdrawn for reperfusion. Next, the incision was sutured and treated with antibiotic ointment, then each mouse was left on a

homeothermic blanket until awaking. Finally, mice were transferred to home cages with free access to food and water. Control mice underwent the same surgical procedure without occlusion.

#### *Multiple Mild Stimulations (MMS)*

MMS was adapted from the chronic mild stress (CMS) paradigm as previously reported [26]. Mice were subjected to unpredictable MMS for 5 weeks as follows: (1) light/dark cycle inversion (continuous illumination or darkness) for 24 h; (2) food deprivation for 12 h; (3) cage tilt on a 45° angle for 3 h; (4) damp bedding (100 mL water poured into sawdust bedding) for 3 h; (5) no bedding for 3 h; (6) warm water swimming ( $35 \pm 2^\circ\text{C}$ , 1 cm in depth) for 3 h; and (7) singly housed for 12 h. One or two stimulations per day were carried out in random order. Food and water were available *ad libitum* when not undergoing food deprivation.

#### *Viral Vector Transduction*

AAV2/6 viruses encoding Cx3cr1-DIO-EGFP or Cx3cr1-DIO-ANXA1-EGFP were generated by BrainVTA (China). The viral titers ranged from  $2\text{--}3 \times 10^{12}$  genome copies/mL. To specifically overexpress ANXA1 in hippocampal microglia, stereotaxic surgery was performed on *Cx3cr1-cre* mice. Briefly, mice were anesthetized and immobilized on a stereotaxic apparatus (RWD Life Science) and the skull was perforated. Four hundred nanoliters of virus were injected into the dentate gyrus (DG) region of the hippocampus with a stepper-motorized micro-syringe (Hamilton) at 50 nL/min. The injection coordinates were anterior-posterior  $-1.77$  mm, mediolateral  $\pm 1.15$  mm, and dorsal-ventral  $-2.13$  mm from the dura relative to bregma. After injection, the syringe was left for 10 min. Animals were transferred to clean home cages and allowed to recover for 10 days to ensure virus expression.

#### **Behavioral Tests**

##### *Morris Water Maze (MWM) Test*

The MWM test was adapted from previous reports [27]. Briefly, a complete MWM test included spatial training (days 1–6, 4 trials per day at at least 20-min interval), a first probe test (day 7), reversed spatial training (days 8–10), and a reversed probe test (day 11). Probe tests were conducted without the platform. The reversed spatial training was similar to the spatial training except that the hidden platform was fixed in the opposite quadrant and was removed for the reversed probe test. The swimming tracks were monitored by a camera mounted above the maze and

connected to a digital tracking device (Xinruan Information Technology).

##### *Novel Object Recognition (NOR) Task*

The NOR task was performed as described [28]. Briefly, mice were acclimated to the open-field apparatus for 10 min per day from 2 days before tests. During the training session, mice were presented with two identical objects (Objects 1 and 2) on diagonal quarters of the apparatus. Mice were allowed to freely explore the objects for 15 min. Fourteen hours later, Object 2 was replaced by a novel object (with a different material and shape), and the mouse was placed in the apparatus again and allowed to freely explore for 15 min (test session). The time mice spent exploring all objects was recorded by a digital video-tracking system (Xinruan Information Technology). Learning and memory were evaluated as exploratory time [time to explore new object / (time to explore new object + time to explore Object 1)  $\times 100\%$ ].

#### **Synaptic Function and Structure**

##### *Electrophysiology*

Acute hippocampal slices were prepared to investigate long-term potentiation (LTP). After mice were anesthetized and decapitated, one hemisphere was quickly removed into ice-cold artificial cerebrospinal fluid (ACSF; in mmol/L): 124 NaCl, 3 KCl, 2 CaCl<sub>2</sub>, 1.2 MgCl<sub>2</sub>, 1.25 NaH<sub>2</sub>PO<sub>4</sub>, 2 H<sub>2</sub>O, 26 NaHCO<sub>3</sub>, 10 glucose, pH 7.4 (oxygenated with 95% O<sub>2</sub> and 5% CO<sub>2</sub>). The brains were rapidly cut into 400  $\mu\text{m}$  slices and transferred into ACSF, followed by incubation at 32 °C for 30 min, and then at 22 °C for 1 h. A single slice was transferred to  $8 \times 8$  microelectrode arrays (MED-P515A probe, Alpha MED Scientific) and continuously perfused by ACSF (34 °C) at 2 mL/min throughout experiments. A 64-channel multi-electrode system (MED64, Alpha MED Scientific) was used to record field excitatory postsynaptic potentials (fEPSPs). One site at the Schaffer collaterals was selected for the delivery of stimuli from 10  $\mu\text{A}$  to 45  $\mu\text{A}$  (in 5- $\mu\text{A}$  increments) to construct the input-output curves, and then the intensity to evoke 30–50% of the maximal synaptic response was calculated and the fEPSPs were recorded by the microelectrodes. fEPSPs were recorded for 10 min before LTP induction as the baseline. High-frequency stimulation (HFS) was applied to induce LTP, which was induced by 3 consecutive trains every 10 s (10 bursts at 5 Hz for each train, and four 100-Hz pulses per burst).

### *Golgi-Cox Staining*

According to the super Golgi kit guidelines (#003010, Bioenno Tech), half of each freshly-harvested brain was silver-impregnated for 11 days at RT in the dark, followed by post-impregnation with 30% (weight/volume) sucrose for another 2 days. Then the brain tissue was coronally cut at 150  $\mu\text{m}$  on a vibratome, and the sections were mounted on gelatin-coated slides with light pressure. Next, the sections were stained, dehydrated, clarified, and coverslipped according to the manufacturer's instructions. The sections were dried for two weeks before neuronal tracing and photography under a Nikon Ni-E microscope. Only hippocampal neurons with fully visible processes were traced. Dendritic segments on tertiary branches were selected for spine counts and classification. The average spine density was expressed as the total number of spines divided by the dendritic segment length. The dendritic spines were classified into 4 categories based on their length and head/neck width: mushroom, stubby, thin, or branched [29].

### *Sholl Analysis*

An estimate of dendritic complexity was obtained using the Sholl ring method [30]. Z-stack images were processed by ImageJ (Fiji) and reconstructed by NeuronStudio (0.9.92), and then cells were traced by ImageJ with the Neuron J plugin. A series of concentric circles centered on the cell soma (starting radius 10  $\mu\text{m}$  and increasing by 10- $\mu\text{m}$  steps) completely encompassed all branches. The number of dendritic intersections at each concentric circle was counted and analyzed.

## **Molecular Biological Analyses**

### *Protein Extraction and Preparation*

For tissue, mice were sacrificed after behavior tests by cervical dislocation, and the hippocampi were quickly separated on ice and cleaned with pre-cooled PBS. Each sample was used to extract total protein and membrane/cytoplasm components. Total protein was extracted with lysis buffer (#P0013, Beyotime Biotechnology) containing protease inhibitor (5 mg/mL; Roche). Membrane and cytoplasm fractions were extracted with the membrane and cytoplasm extraction reagent (#P0033, Beyotime Biotechnology) containing protease inhibitor according to the instructions. The protein concentration was determined by a BCA protein assay kit (#P0010, Beyotime Biotechnology). Protein extraction was the same for the cultured cells.

### *Immunoprecipitation (IP) and Immunoblot (IB) Analysis*

Eight hundred micrograms of extracted lysate was pre-incubated with protein A+G agarose beads (#P2028, Beyotime Biotechnology) for 1 h at 4°C and centrifuged at 2,500 rpm for 5 min. The supernatant was co-incubated with specific antibodies (Table S1) and rotated overnight at 4°C. Protein A+G agarose beads were added and gently rotated for another 3 h. After centrifugation at 2,500 rpm for 5 min, the precipitate was thoroughly washed four times in cold IP lysate, and 2  $\times$  SDS-PAGE loading buffer was added and boiled at 98°C for 6 min. For IB, 5  $\times$  loading buffer was added to the extract and boiled at 98°C for 6 min. Protein samples were separated by SDS-PAGE and transferred to PVDF membranes (#3010040001, Roche). The membranes were blocked with 5% skim milk at RT for 1 h and incubated with specific primary antibodies (Table S1) at 4°C overnight. The membranes were gently rinsed three times in fresh TBST (Tris-buffered saline with Tween 20), then incubated with the HRP-conjugated corresponding secondary antibodies (Table S1) at RT for 1 h. Immunoassays were performed and evaluated with ECL chemiluminescent substrate (#32106, Thermo Pierce).

### *Immunofluorescence (IF)*

After TIA and 35 days of MMS, mice were deeply anesthetized and perfused intracardially with warm saline, followed by 4% cold paraformaldehyde. The brains were carefully removed into 4% paraformaldehyde, left for 24 h at 4°C, and dehydrated in graded sucrose solutions for cryoprotection. The brains were embedded in OCT compound (#4583, Sakura Tissue-Tek) and cut into coronal sections (20  $\mu\text{m}$ ) on a cryostat microtome (Leica CM1850, Leica Instruments). Sodium citrate buffer was used for antigen retrieval at 98°C for 40 min and allowed to naturally cool to RT. Then, the non-specific proteins were blocked with 10% donkey serum and 0.3% Triton X-100 in PBS for 1 h at RT and the tissue was rinsed with PBS. The sections were incubated with specific primary antibodies (Table S1) overnight at 4°C. Then they were rinsed three times in PBS and incubated with fluorochrome-conjugated secondary antibodies for 60 min in the dark at RT and the nuclei were counterstained with DAPI (10 mg/mL; Sigma-Aldrich). Cultured cells were grown on gelatin-coated coverslips and then fixed in 4% paraformaldehyde for 15 min and permeabilized with 0.3% Triton X-100 for 15 min. The rest was the same as for the brain sections. Images were captured under a fluorescence microscope (IX-73, Olympus) and a laser scanning confocal microscope (Carl Zeiss LSM780, Zeiss Microsystems). ImageJ software (Fiji) was used to analyze the fluorescence intensity and location of target proteins.

## Cell Culture and Infection

### Primary Hippocampal Neuronal Cell Culture

Neonatal mice at postnatal P1 were quickly decapitated, and the brains were gently transferred into cold D-Hank's solution. The hippocampus was separated and chopped up, followed by 0.25% trypsin-EDTA (Sigma-Aldrich) incubation at 37°C for 10 min. Then DMEM-F12 containing 10% fetal bovine serum (FBS, Gibco) was used to stop the digestion, and the tissue was made into a single-cell suspension with a smooth glass pipette. Neurons were seeded on poly-L-lysine-coated (50 mg/mL, Sigma-Aldrich) culture dishes or coverslips at  $1 \times 10^6$  cells/cm<sup>2</sup> and then cultured in an incubator containing 5% CO<sub>2</sub> and 95% O<sub>2</sub> at 37°C. Twenty-four hours later, the culture medium was replaced with Neurobasal (Gibco) supplemented with 2% B27 (Gibco), 1% glutamine (Gibco), and 1% penicillin-streptomycin (Thermo Fisher), and half of the medium was changed twice a week. Cytarabine (200 mmol/L, Sigma-Aldrich) was added to purify neurons on the second day. Neurons cultured for 7–10 days were used for adenovirus infection or co-culture with microglia.

### Primary Microglial Cell Culture

As described previously [28], mixed glial cells were prepared from P1–P3 mice. The whole brain was separated into a cell suspension and planted in a culture flask. The glia cells were cultured with high-glucose DMEM (Gibco) supplemented with 20% FBS and 1% penicillin-streptomycin in an incubator. After microglia adhered to the bottom for 7–10 days, the medium was replaced every 3 days until ~15 days in culture. After that, microglia were shaken to separate from the mixed glial culture on a 37°C horizontal shaker at 200 rpm for 6 h. Microglia were obtained from the medium and then seeded on culture dishes at  $1 \times 10^6$  cells/cm<sup>2</sup>. Two days after infection by adenoviruses, microglia were collected for experiments or inoculated to co-culture with primary cultured neurons after washing three times in fresh culture medium.

### Viral Vector Infection

Adenoviruses encompassing GFP, full-length ANXA1, and blank vector were constructed by Vigene Biosciences (China). Cells were infected for 6 h and cultured with fresh medium for another 48 h.

## Statistics

Mice were randomly assigned to the various treatment groups, and measurements were made blind to group

assignment. Data are shown as the mean  $\pm$  SEM, and statistical analysis was performed using GraphPad Prism 9.0.0. Statistical significance was assessed using Student's *t*-test or ANOVA, as shown in Table S2.

## Results

### MMS Attenuates Excessive Dendritic Spine Pruning and Enhances Learning and Memory in TIA-treated Mice

The main clinical interventions of TIA recurrence are managing risk factors such as diabetes, hyperlipidemia, and cardiopathy. In addition to routine medications, moderate exercise and diet are also effective supplementary measures to reduce the incidence of TIA. We integrated and adapted animal experiments for the technically feasible paradigm named MMS. To identify the effects of MMS on learning and memory after TIA, 8-week-old C57 male mice underwent bilateral common carotid artery occlusion/reperfusion (TIA and TIA+MMS) or sham-operation (Ctrl). Then mice were treated with MMS (TIA+MMS) or control (Ctrl and TIA) for 5 weeks, followed by behavioral tests and sacrificed for subsequent synaptic and histological analyses (Fig. 1A).

We first conducted MWM tests to confirm the animals' spatial reference learning and memory. TIA-treated mice exhibited cognitive impairment indicated by the escape latency to search for the withdrawn platform on the first probe test. In contrast, MMS remarkably improved the cognitive function, including the escape latency, the times crossing the platform, swimming time in the target quadrant on the first probe test, and the time spent in the new quadrant on the reversed probe test (Figs 1B–G, and S1). In comparison, the swimming time in the previous target quadrant on the reversed probe test showed no difference among the three groups (Fig. S1C). NOR tasks were used to evaluate hippocampus-dependent memory in TIA and MMS mice. During the training session, mice explored two identical objects for a similar time among the three groups (Fig. 1H). In the test session, we found that the TIA+MMS group had a stronger predilection for the novel object than the TIA group, indicating that they had better recognition than the TIA-treated mice (Fig. 1I). In addition, TIA mice showed an impaired trend but not significantly different from Ctrl. Collectively, these results reveal that TIA mice display a slight cognitive dysfunction, and MMS enormously improves learning and memory in TIA-treated mice.

We further examined the synapses in TIA and MMS-treated mice. The electrophysiological results indicated that TIA inhibited the facilitation of LTP induction



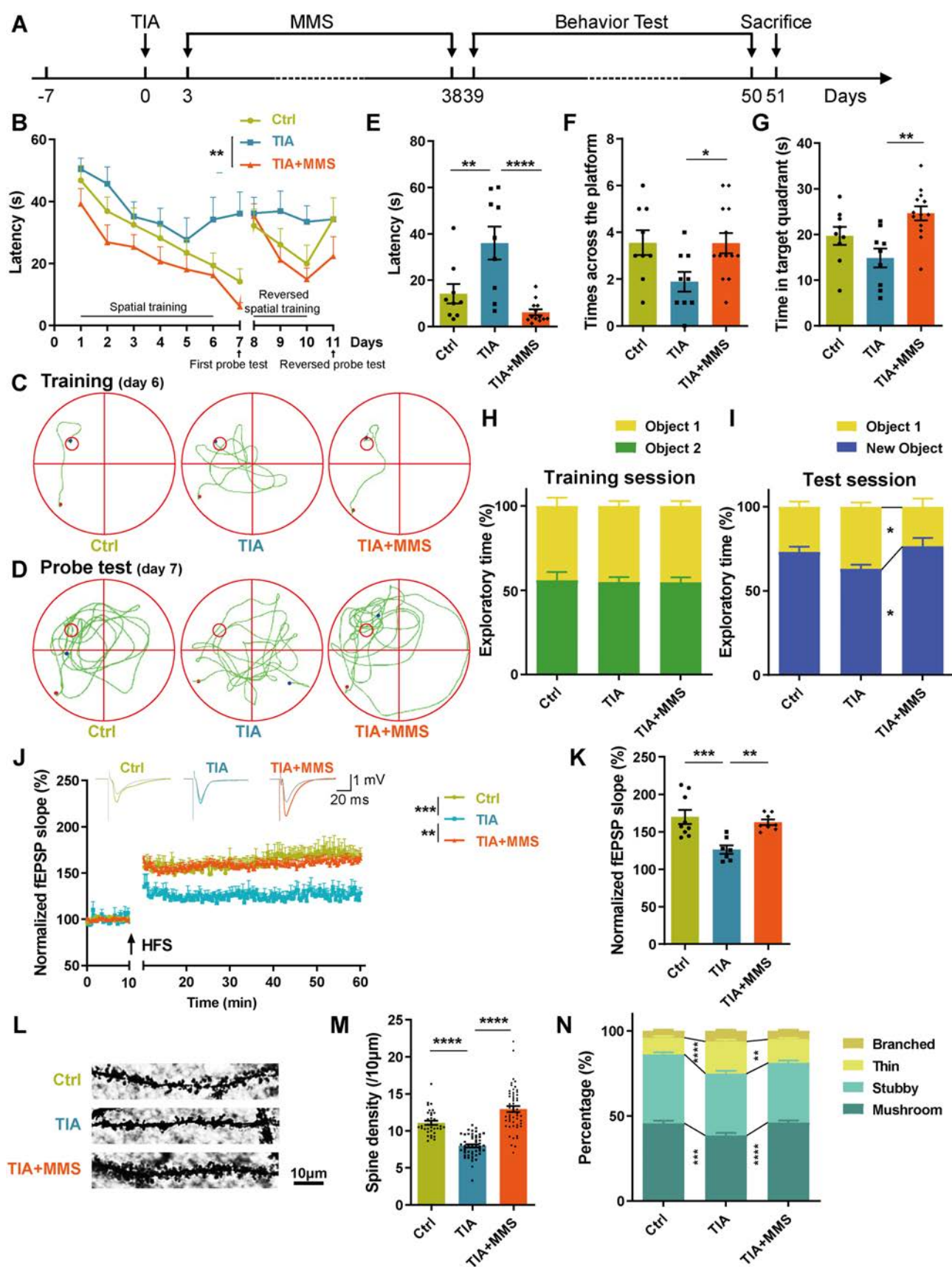


**Fig. 1** MMS attenuates excessive dendritic spine pruning and enhances learning and memory in TIA-treated mice. **A** Experiment schedule. Adult male mice were subjected to transient global cerebral ischemia surgery (sham for Ctrl) after habituation for 7 days. After 3 days of recovery, mice underwent MMS treatments (handled-only for Ctrl and TIA) for 35 days. On day 39, learning and memory were evaluated by MWM and NOR, and the synaptic plasticity was measured by long-term potentiation (LTP) and Golgi-Cox staining. **B**, **C** Average escape latency to find the hidden platform (**B**) and representative swimming tracings on day 6 (**C**). **D–G** In the first probe test, tracings (**D**), escaped latency (**E**), times passing the platform (**F**), and swimming time in the target quadrant (**G**). **H**, **I** Relative time to explore two identical objects during the training session (**H**) and explore the novel and familiar objects during NOR tasks (**I**). **J**, **K** LTP is impaired after TIA and then rescued by MMS in male mouse hippocampus slices. The average normalized slope and quantitative statistics of the fEPSPs 40–50 min after HFS induction (**K**) are shown. HFS, high-frequency stimulation; gray, before HFS induction; colored, after HFS induction. **L–N** The dendritic spines of hippocampal neurons reflected by Golgi-Cox staining (**L**), quantification of spine density (**M**), and classification by appearance (**N**). Data are presented for three independent experiments and shown as the mean  $\pm$  SEM. \* $P < 0.05$ , \*\* $P < 0.01$ , \*\*\* $P < 0.001$ , and \*\*\*\* $P < 0.0001$ .

compared with Ctrl, and the normalized slope of fEPSPs was significantly attenuated, and this was reversed by MMS (Fig. 1J–K). Moreover, the Golgi-Cox staining and the Sholl analysis showed that TIA significantly decreased the average branch number (especially in the proximal arbor) and the dendritic spine density of hippocampal neurons compared with Ctrl, indicating a deficit of synaptic structure in TIA-treated mice (Figs 1L–M and S2). By contrast, an elevation of the branch number, dendritic length in the distal arbor, and the spine density (even more abundant than Ctrl) indicated an increased number of synaptic contacts in TIA+MMS compared with TIA (Figs 1L–M and S2B–C). It is thought that mushroom and stubby spines are stable and mature for communication, whereas thin and branched spines appear to act as immature spines [29]. Based on their appearance, we grouped the dendritic spines and found that TIA impeded synaptic function while MMS ameliorated it (Fig. 1N). Our data indicate that TIA leads to morphological and functional deficiencies in hippocampal neuronal synapses, which are rescued by MMS.

In short, MMS contributes to the attenuation of excessive spine pruning and enhances cognitive performance in TIA-treated mice.

#### The CX3CR1 Level on Membrane is Reduced by MMS via ANXA1 in Microglia of TIA-Treated Mice

To confirm that ANXA1 is associated with synapses and behavior after TIA and MMS, we measured the protein level of ANXA1 in the hippocampus after such treatment.

IF and IB revealed that TIA upregulated hippocampal ANXA1, especially in Iba1-positive cells. On the other hand, the hippocampal ANXA1 protein level with TIA+MMS was comparable to Ctrl (Fig. 2A–D). Since the action of ANXA1 depends on its subcellular distribution, we further measured the ANXA1 levels in cytoplasm and membrane fractions. Using IB, we confirmed that MMS reduced the ANXA1 level on the membrane of TIA-treated mice, while the cytoplasmic level was not affected (Fig. 2E–F). It is worth noting that the increase in ANXA1 on membrane was without statistical significance after TIA, in keeping with the behavioral impairment. Interestingly, IB analysis of cellular components indicated that the levels and distributions of proteins were similar for CX3CR1 and ANXA1 (Fig. 2G–H).

We further explored the interaction between CX3CR1 and ANXA1. IF and IP assays revealed that more ANXA1 bound to CX3CR1 in the hippocampus after TIA, and this was reversed by MMS (Fig. 3A–D). Given the reduction of membranous ANXA1 and CX3CR1 after MMS, IP assays were performed with membrane protein-enriched fractions of hippocampal tissue lysates. We found that the binding of CX3CR1 and ANXA1 on the membrane was similar to that in the total cell lysates, showing no significant difference, indicating that the increase of CX3CR1–ANXA1 binding after TIA not only occurs on the membrane but also in the cytoplasm (Fig. 3E–F).

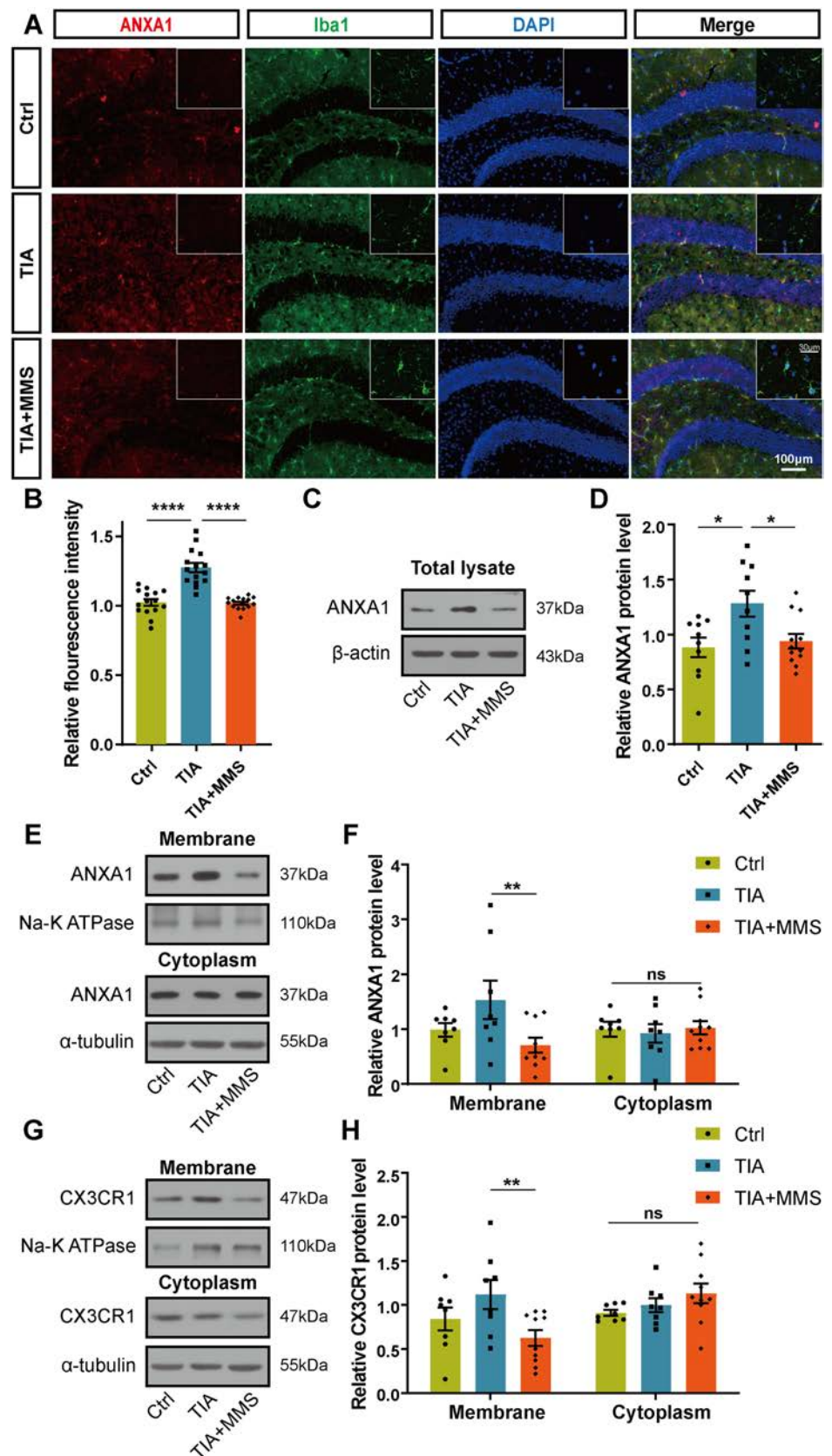
In order to investigate the effect of ANXA1 on CX3CR1, we further infected primary cultured microglia with adenovirus to overexpress ANXA1. As shown in Fig. 3G, the intensity of CX3CR1 on the microglial membrane increased after overexpression of ANXA1 (Fig. 3H). Similar results were confirmed by IB (Fig. 3J–K). In addition, the co-localization of CX3CR1 and ANXA1 was also enhanced, as evaluated by Pearson's coefficient (Fig. 3I).

In summary, our results indicate that TIA increases ANXA1 expression in the hippocampus and promotes the membrane distribution of CX3CR1 through an interaction between ANXA1 and CX3CR1. On the contrary, MMS treatment reduces ANXA1 and the combination of ANXA1 and CX3CR1 on the membrane after TIA.

#### MMS Reduces the Combination of CX3CR1 and CX3CL1 Promoted by ANXA1 in Microglia of TIA-Treated Mice

CX3CR1 and CX3CL1 are the bridge molecules for the interaction between microglia and neurons. In this part, we examined the CX3CR1–CX3CL1 combination in the hippocampus after TIA and MMS. Co-IP experiments revealed that the interaction of CX3CR1 and CX3CL1 was enhanced in TIA-treated mice, and this was inhibited by

**Fig. 2** The ANXA1 and CX3CR1 levels on membrane are reduced by MMS in microglia of TIA-treated mice. Male mice were subjected to TIA or sham surgery followed by 35 days of MMS and a series of behavior tests, then sacrificed for IB and IF analysis. **A**, **B** Fluorescence images of ANXA1 (red) and Iba1 (green) co-labeled with DAPI (blue) in hippocampal DG (**A**) and fluorescence intensity of ANXA1 (**B**). **C**, **D** Expression of ANXA1 in hippocampus by IB. **E–H** ANXA1 (**E**, **F**) and CX3CR1 (**G**, **H**) protein levels in cytoplasm and membrane of hippocampus by IB. Data are presented for three independent experiments and shown as the mean  $\pm$  SEM. ns for  $P > 0.05$ , \* $P < 0.05$ , \*\* $P < 0.01$ , and \*\*\*\* $P < 0.0001$ .





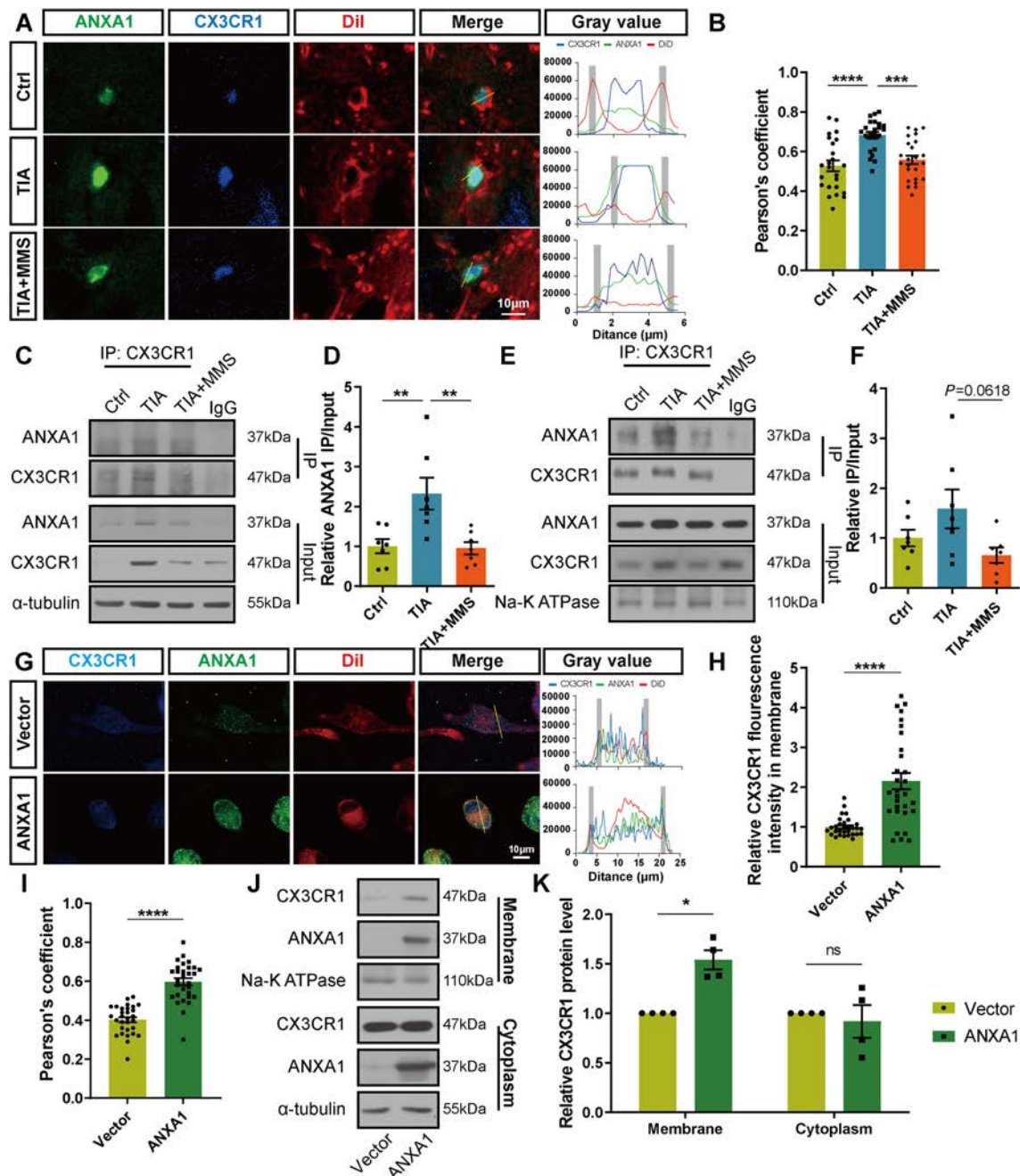


**Fig. 3** The level of CX3CR1 on membrane is promoted by ANXA1 in microglia of TIA-treated mice. **A, B** Fluorescence images and co-localization of ANXA1 (red) and CX3CR1 (green) in hippocampal DG after TIA and MMS treatments by IF. DiI is used as a membrane stain to label the membrane location. Merged profiles of the fluorescent intensity of ANXA1, CX3CR1, and DiI signals along the lines crossing cells as indicated. Gray columns indicate the cellular membrane location (**A**). Quantitative analysis is shown in (**B**). **C–F** The interaction and quantitative analysis of ANXA1 with CX3CR1 in total lysates (**C, D**) and membrane (**E, F**) of hippocampus after TIA and MMS treatments by co-IP. **G–I** Representative images

(**G**), fluorescence intensity of membranous CX3CR1 (**H**), and quantitative analysis of the co-localization of CX3CR1 (green) and ANXA1 (red) (**I**) in control and ANXA1-overexpressing primary microglia by IF. DiI marks the membrane location shown as the gray columns in the plot profiles. **J, K** Representative images (**J**) and quantitative analysis (**K**) of CX3CR1 in cytoplasm and membrane in control and ANXA1-overexpressing primary microglia by IB. Data represent at least three independent experiments and are shown as the mean  $\pm$  SEM. ns for  $P > 0.05$ , \* $P < 0.05$ , \*\* $P < 0.01$ , \*\*\* $P < 0.001$ , and \*\*\*\* $P < 0.0001$ .



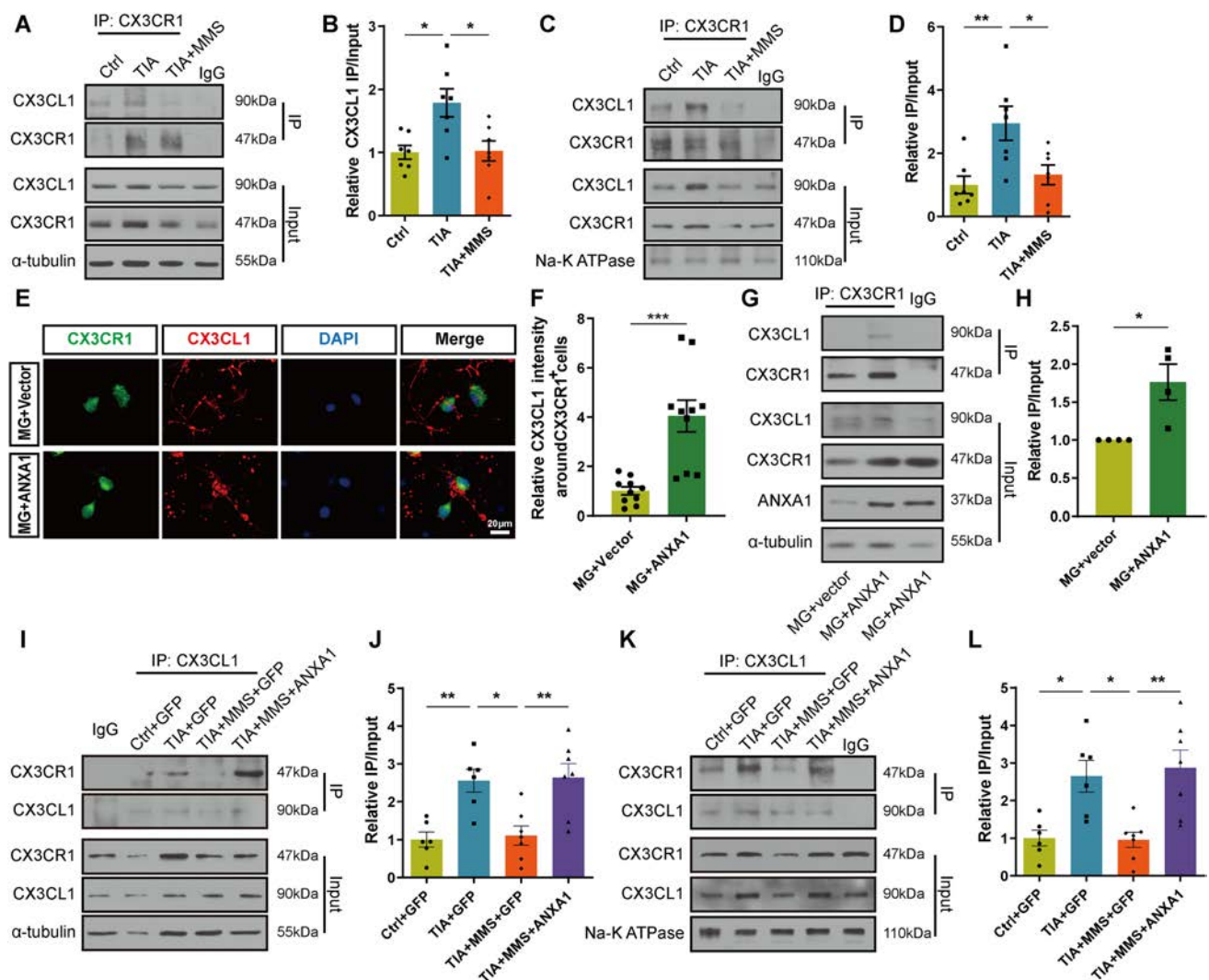


**Fig. 4** MMS reduces the combination of CX3CR1 and CX3CL1 promoted by ANXA1 in microglia of TIA-treated mice. **A–D** The interaction and quantitative analysis of CX3CL1 and CX3CR1 in total lysates (**A**, **B**) and membrane (**C**, **D**) of hippocampus after TIA and MMS by co-IP. **E–H** Primary cultured microglia infected with adenovirus encoding ANXA1 or control vector for 48 h, followed by co-culture with primary cultured neurons for another 24 h. Representative IF images (**E**, **F**) and co-IP analysis (**G**, **H**) of CX3CR1

(green) and CX3CL1 (red). **I–L** *Cx3cr1*-cre male mice injected with AAV-vector (GFP) or AAV-ANXA1 (ANXA1) in the bilateral hippocampus 10 days before TIA, followed by 35 days of MMS. The combination of CX3CL1 and CX3CR1 and quantitative analysis in total lysates (**I**, **J**) and membrane (**K**, **L**) of hippocampus by co-IP. Data represent at least three independent experiments and are shown as the mean  $\pm$  SEM. \* $P$  < 0.05, \*\* $P$  < 0.01.

MMS both in the total extracts (Fig. 4A, B) and the membrane fractions (Fig. 4C, D).

As described above, CX3CR1 was mostly expressed in microglia in the CNS, while CX3CL1 was mainly detected in neurons. Thus, we co-cultured primary microglia and neurons. We first generated microglia that overexpressed ANXA1 or blank vector and then transferred them to neurons. We found that the distribution ratio of CX3CR1 on the membrane was significantly increased in microglia overexpressing ANXA1 (Fig. 3G, H, J, K). Simultaneously, CX3CL1-positive staining close to microglia was significantly enhanced after overexpression of ANXA1 as well

(Fig. 4E, F). Meanwhile, IP analysis confirmed that the binding of CX3CR1 and CX3CL1 was enhanced after microglia overexpressed ANXA1 (Fig. 4G, H), suggesting that ANXA1 promotes the recruitment of microglia to neurons *via* a combination of CX3CR1 and neuron-derived CX3CL1.

Moreover, we injected adeno-associated virus (AAV2/6) expressing ANXA1 or control AAV (GFP) into the hippocampus DG of *Cx3cr1*-cre mice, this virus has been shown to target microglia/macrophages [28]. After modeling with TIA and MMS, we found that the TIA+MMS +ANXA1 group showed an enhanced combination of

CX3CR1 and CX3CL1 in hippocampus tissue compared with the TIA+MMS+GFP group (Fig. 4I–J). These results were further confirmed by IP analysis of hippocampal membrane-enriched components (Fig. 4K–L). Taken together, TIA promotes the combination of neuronal CX3CL1 and microglial CX3CR1 *via* ANXA1, while MMS reduces the CX3CL1–CX3CR1 combination by inhibition of ANXA1.

### **MMS Attenuates the Excessive Dendritic Spine Pruning Promoted by ANXA1 in the Microglia of TIA-Treated Mice**

In co-cultured primary microglia and neurons, we further investigated the effects of microglial ANXA1 on the synapses of neurons. We measured the levels of the presynaptic marker synaptophysin and the postsynaptic density protein PSD95, and found that PSD95 was significantly decreased after ANXA1 overexpression in microglia, while the presynaptic components were not affected (Fig. 5A–F), and this was further confirmed by *in vivo* experiments (Fig. 5G–I). These data reveal that microglial ANXA1 regulates the loss of postsynaptic elements but does not affect presynaptic components.

Next, we infected primary cultured neurons with GFP-labeled adenovirus and co-cultured them with microglia expressing ANXA1 or blank vector. Confocal analysis indicated that the neuronal synaptic density was reduced after overexpression of ANXA1 in microglia (Fig. 5J, K). Similar results were found in the hippocampus of mouse models with ANXA1 overexpression (Fig. 5L, M). In addition, Sholl analysis revealed that the effects of MMS on the dendritic branch number and the branching complexity of TIA-treated hippocampus were reversed after ANXA1 overexpression (Fig. S3).

In summary, we confirmed that overexpression of ANXA1 in microglia induces deficits of synaptic structure, especially the postsynaptic components, suggesting that ANXA1 is involved in the postsynaptic pruning by microglia.

### **The Protective Effects of MMS in Learning and Memory are Reversed by ANXA1 over-expression in the Microglia of TIA-Treated Mice**

Having shown that ANXA1 plays a vital role in synaptic structure, then we wondered whether ANXA1 participates in the process of learning and memory in mice after TIA and MMS. As shown in Fig. 6A, mice with microglia/macrophage-specific overexpression of ANXA1 in the hippocampus were created and treated with TIA and MMS. MWM tests suggested that overexpression of ANXA1 partially reversed the protective effects of MMS on TIA-

treated mice in the first probe test, in terms of escape latency, swimming distance in the target quadrant, and the number of platform crossings (Fig. 6B–G). Meanwhile, in the reversed probe test, the number of new target platform crossings was decreased after overexpression of ANXA1 (Fig. S4A, B). In contrast, the number of passes through the prior platform was not significantly changed (Fig. S4C). In brief, the spatial learning and memory were reduced after microglia/macrophage-specific overexpression of ANXA1 in the hippocampus, which may confer neurophysiological and neurobehavioral mechanism in TIA-treated mice. The NOR tasks further verified that MMS had protective effects on hippocampus-dependent recognition in TIA-treated mice, and these effects were blocked by overexpression of ANXA1 in microglia (Fig. 6H, I).

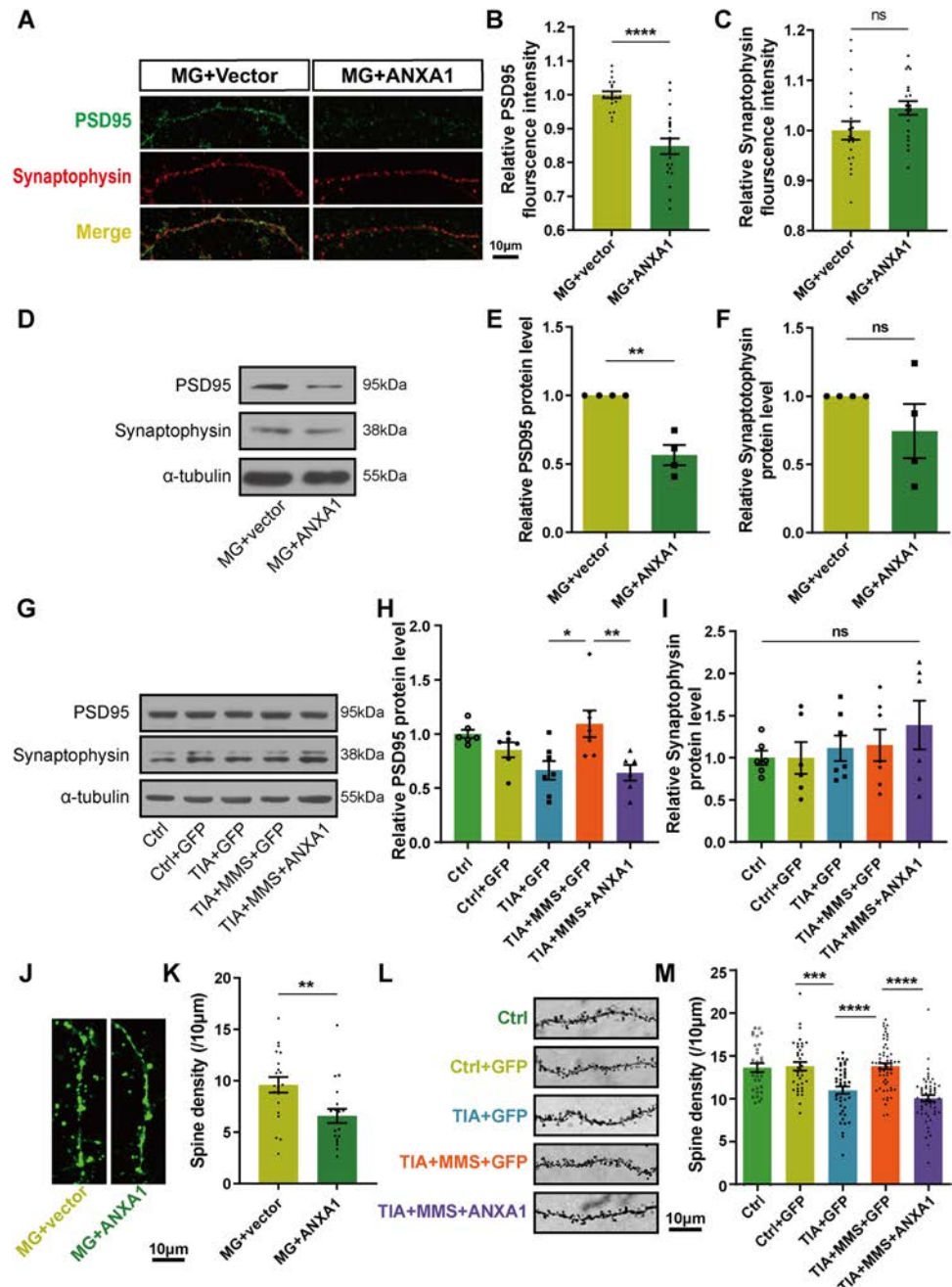
In all, we conclude that ANXA1 in hippocampal microglia participates in the processes of learning and memory after TIA and MMS. The overexpression of ANXA1 in microglia results in impaired cognition after TIA and MMS treatment, indicating that MMS-mediated neuroprotection may be ANXA1-dependent.

## **Discussion**

TIA significantly raises the risk of stroke and heart diseases that comprise the most common cause of morbidity and mortality in the world. However, only 5.02% of TIA patients receive treatment, in large part because many episodes of TIA are minimally symptomatic and usually last for a few minutes [31, 32]. As early as 15 years ago, targeting the risk factors of TIA, Hackam and Spence proposed that drugs combined with longer intervals of diet and exercise therapy may lead to further gains [33]. We wondered whether physical stimulation could alleviate TIA and what the mechanisms were. Although the mechanisms of neuronal death and behavioral deficits after ischemic stroke have been widely researched, the specific mechanisms of reversible and recrudescence impairments after TIA are still not fully clarified. In this study, we investigated the TIA mouse model and found that learning and memory were impaired. Following the effective preventions from the comprehensive and multifactorial approach to TIA, we generated an MMS paradigm involving physical and psychological aspects to intervene in TIA. Interestingly, we found that MMS remarkably rescues the cognitive function after TIA, which verified the supposition.

MMS was adapted from the CMS procedure that concentrates on diet and exercise to positively intervene in TIA. Considering that CMS is a paradigm to induce depression, we abandoned some of the stressors that can lead to a severe mood disorder such as restraint, white noise, and strobe light illumination, and found that the

**Fig. 5** MMS attenuate the excessive dendritic spine pruning promoted by ANXA1 in microglia of TIA-treated mice. **A–F** Primary cultured microglia infected with blank vector or ANXA1-overexpressing adenoviral for 48 h, then co-cultured with primary cultured neurons. Representative confocal images (**A**) and quantification of PSD95 (green, **B**) and synaptophysin (red, **C**) in co-cultured neurons and microglia. PSD95 and synaptophysin protein levels quantified by IB (**D–F**). **G–I** *Cx3cr1*-cre male mice injected with an AAV vector (GFP) or AAV-ANXA1 (ANXA1) in the bilateral hippocampus 10 days before TIA, followed by 35 days of MMS. PSD95 and synaptophysin protein levels in hippocampus measured by IB. **J, K** Neurons infected with GFP-tagged adenoviral vector and co-cultured with microglia. Representative images (**J**) and quantitative analysis (**K**) of spines. **L, M** Images and quantification of Golgi-Cox staining for analysis of hippocampal dendritic spines. Data represent at least three independent experiments and are shown as the mean  $\pm$  SEM. ns for  $P > 0.05$ , \* $P < 0.05$ , \*\* $P < 0.01$ , \*\*\* $P < 0.001$ , and \*\*\*\* $P < 0.0001$ .



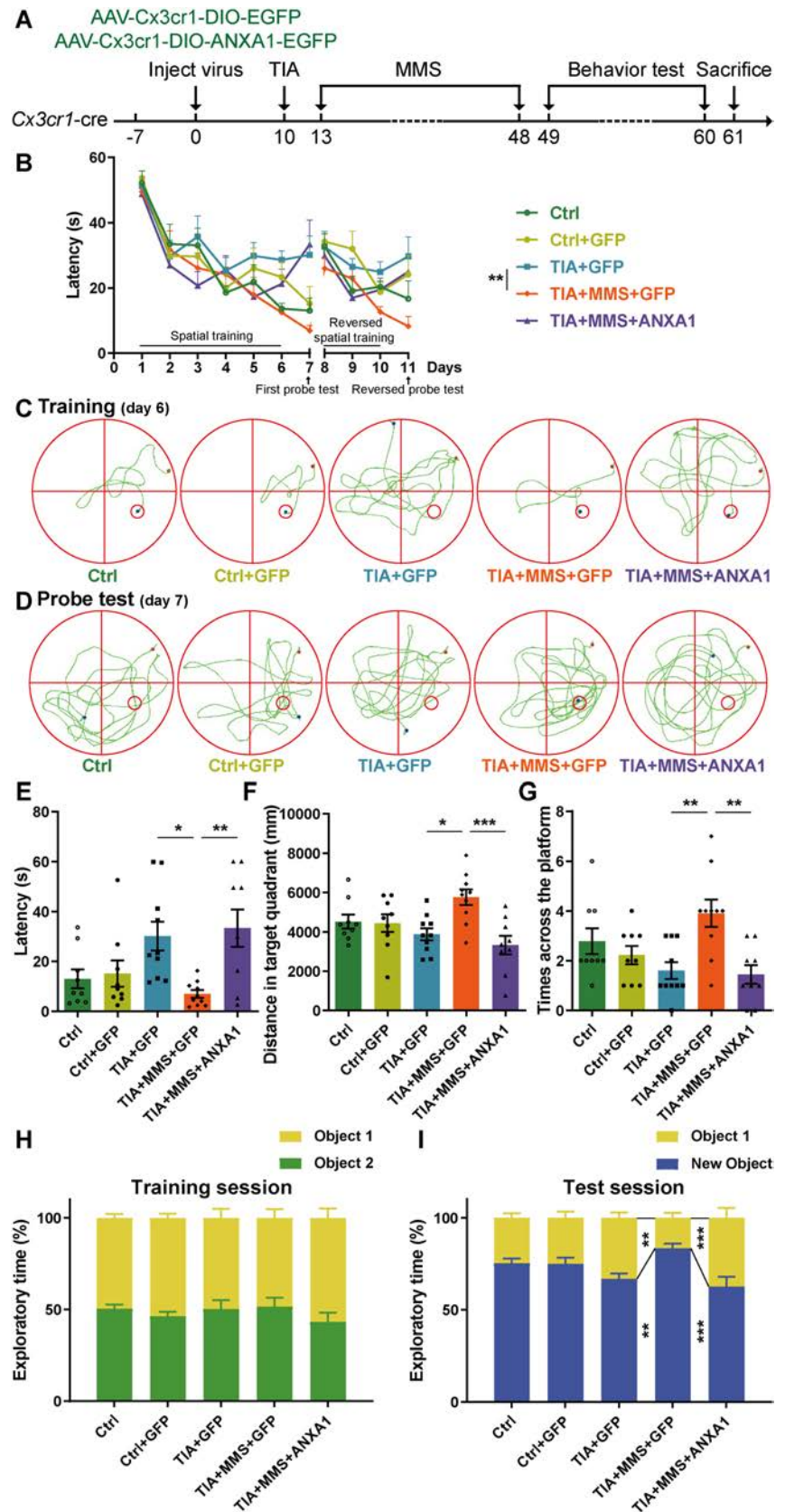
depressive disorder was alleviated in adult C57 male mice (data not shown). Next, we investigated how MMS rescued the cognitive deficits caused by TIA. Studies in elderly mice have shown that intermittent fasting and energy limitation might improve cognitive ability by increasing dendritic spines in the DG and decelerate brain aging [34]. On the other hand, the changeable environment and inappropriate bedding in MMS may increase the possibility of mice being forced to exercise, which could be related to hippocampal neurogenesis and the secretion of neurotrophic factors (such as brain-derived neurotrophic

factor) that improve the animal's cognition [35]. Besides, motor impairments increase the odds of subsequent stroke, further demonstrating the necessity of exercise [36]. In the present study, we found that damage to neuronal spines and synaptic function mainly caused the transient and reversible learning and memory impairments of TIA. Thus, it is crucial to determine whether MMS improve the neuronal tolerance to ischemia *via* neuronal branch spines.

Microglia have powerful phagocytic effects and play a vital role in the homeostasis of synapses and neural circuits through the CX3CR1–CX3CL1 signal. CX3CL1 is



**Fig. 6** The protective effects of MMS in learning and memory are reversed by ANXA1 over-expression in microglia of TIA-treated mice. **A** Experimental schedule: adeno-associated viruses are injected into the hippocampus of *Cx3cr1-cre* mice to overexpress ANXA1 in microglia/macrophages. Ten days later, mice are subjected to TIA and MMS and then learning and memory are evaluated by MWM and NOR. **B** Average escape latency to the hidden (days 1–6 and 8–10) and withdrawn (days 7 and 11) platform. **C** Representative tracings on day 6. **D–G** Representative tracings (**D**), escape latency (**E**), swimming distance in the target quadrant (**F**), and passes through the target platform (**G**) on day 7 (the first probe test). **H, I** Time spent exploring two identical objects (Objects 1 and 2) during the training session (**H**) as well as a novel (New object) and a familiar (Object 1) objects during the test session (**I**). Data represent three independent experiments and are shown as the mean  $\pm$  SEM. \* $P < 0.05$ , \*\* $P < 0.01$ , and \*\*\* $P < 0.001$ .





considered to be an “eat-me” signal released from neurons after ischemia and is specifically recognized by CX3CR1 on the microglial membrane. After that, the surplus synapses and the stressed neurons are engulfed by microglia [14]. We found that MMS reduced the CX3CR1 level on the membrane, corresponding with the attenuation of the CX3CR1–CX3CL1 interaction and the decreased deficits in postsynaptic elements, similar to Paolicelli’s research [14]. Nevertheless, no significant change was found for presynaptic substances. Probably because microglia-dependent dendritic spine turnover is associated with the formation of presynaptic filopodia [37], the presynaptic protein level we measured might be a dynamic balance between synaptic phagocytosis and synaptic remodeling. Generally, our results indicate that MMS protects neuronal function by inhibiting the over-pruning of synaptic spines *via* regulating the CX3CR1 level on the microglial membrane.

Our previous studies have focused a  $\text{Ca}^{2+}$ -dependent annexin protein, ANXA1, that is widely expressed in the immune system, especially in microglia of the CNS. We reported that ischemia caused by oxygen-glucose deprivation/reoxygenation (OGD/R) *in vitro* induces the elevation of ANXA1 expression in microglia [38]. Besides, microglial ANXA1 causes distinct neuronal fates after ischemia depending on its subcellular location. Phosphorylation of the serine 27 residue promotes the nuclear translocation of ANXA1 and increases pro-inflammatory cytokines [38]. Cytoplasmic ANXA1 regulates microglial polarization through selective autophagy [28, 39]. Secreted extracellular ANXA1 can bind to microglia-specific formyl peptide receptors to promote the activation and migration of microglia, thereby exerting powerful anti-inflammatory activity [40]. In addition to the above functions, we supposed that ANXA1 might play a key role in membrane translocation based on the membrane-binding property and wondered whether the elevated ANXA1 affected the membrane distribution of CX3CR1. For this reason, we overexpressed ANXA1 in primary cultured microglia. As we supposed, the membrane distribution of CX3CR1 was promoted by the enhanced interaction of ANXA1 and CX3CR1 in microglia, confirming the vital role of ANXA1 in the membrane distribution of CX3CR1. These results suggest that ANXA1 participates in the synaptic pruning of microglia *via* regulating CX3CR1 membrane translocation. Further study is still needed to identify the specific ANXA1–CX3CR1 interaction sites or other crosslinked proteins and the post-translational modifications of ANXA1, which regulate the combination with CX3CR1.

Next, we focused on the actions of ANXA1 in the process of synaptic pruning regulated by microglia under TIA. First, we found that TIA promoted the expression of ANXA1, similar to OGD/R [38]. Moreover, TIA

upregulated the interaction of ANXA1 and CX3CR1 and increased the membrane distribution of CX3CR1. Considering these results, we further confirmed that TIA upregulated the CX3CR1 level in the membrane fraction *via* the elevated expression of ANXA1. Thus, we further explored whether MMS could reverse the neurological deficits through downregulating ANXA1. As expected, MMS reduced the expression of ANXA1, the interaction of ANXA1 and CX3CR1, and the CX3CR1 level on the microglial membrane, further consistent with the marked protective effects on learning and memory. In addition, the protective effects of MMS on the synapses and cognition in TIA-treated mice were inhibited after specifically overexpressing ANXA1 in microglia, which further supported the hypothesis that elevated ANXA1 promotes the synaptic pruning by microglia after TIA, while MMS restores the synapses *via* ANXA1 downregulation. This indicates that appropriate dendritic spine pruning regulated by ANXA1 in microglia might be a potential treatment strategy for diseases with abnormal synapses and neuronal circuits in CNS maturation and homeostasis, such as enhancing the pruning of neuronal spines by overexpression of ANXA1 in Alzheimer’s disease and epilepsy, or decreasing it by downregulating ANXA1 in autism. In addition, whether ANXA1 in the CNS can pass the blood-brain barrier or indirectly change the peripheral protein level after ischemia to conveniently diagnose the synaptic dysfunction as an indicator is also a problem worthy of discussion.

From the present study, MMS provides a potential treatment strategy to ameliorate synaptic structure and cognitive function after TIA or other synaptic dysfunctions. However, further improvement is still needed. The degree of amelioration in TIA-treated mice depends on the intensity, frequency, and duration of the stimulations. Excessive stimulations could even aggravate the ischemic impairment and cause emotional disorders. Moreover, the detailed methods of MMS intervention still need to be refined for application to the clinic.

In conclusion, our findings confirm that MMS abolishes the upregulation of ANXA1 caused by TIA and then reduces the CX3CR1 level on the microglial membrane, followed by a decreased interaction between CX3CR1 and CX3CL1, and inhibits excessive synaptic pruning, which further results in the improvements of cognition after TIA. This study reveals the novel function of ANXA1 in dendritic spine pruning and tolerance to ischemia and suggests that microglial ANXA1 may be a promising therapeutic target for cerebral ischemia or other diseases with synaptic dysfunction.

**Acknowledgements** This work was supported by the National Natural Science Foundation of China (31771126).

**Conflict of interest** All authors declare that they have no interest conflict.

## References

- Easton JD, Saver JL, Albers GW, Alberts MJ, Chaturvedi S, Feldmann E, *et al.* Definition and evaluation of transient ischemic attack: A scientific statement for healthcare professionals from the American Heart Association/American Stroke Association Stroke Council; Council on Cardiovascular Surgery and Anesthesia; Council on Cardiovascular Radiology and Intervention; Council on Cardiovascular Nursing; and the Interdisciplinary Council on Peripheral Vascular Disease. The American Academy of Neurology affirms the value of this statement as an educational tool for neurologists. *Stroke* 2009, 40: 2276–2293.
- Luengo-Fernandez R, Gray AM, Rothwell PM. Effect of urgent treatment for transient ischaemic attack and minor stroke on disability and hospital costs (EXPRESS study): A prospective population-based sequential comparison. *Lancet Neurol* 2009, 8: 235–243.
- Adams RJ, Chimowitz MI, Alpert JS, Awad IA, Cerqueria MD, Fayad P. Coronary risk evaluation in patients with transient ischemic attack and ischemic stroke: A scientific statement for healthcare professionals from the Stroke Council and the Council on Clinical Cardiology of the American Heart Association/American Stroke Association. *Circulation* 2003, 108: 1278–1290.
- Epsztein J, Ben-Ari Y, Represa A, Crépel V. Late-onset epileptogenesis and seizure genesis: Lessons from models of cerebral ischemia. *Neuroscientist* 2008, 14: 78–90.
- Powers WJ, Rabinstein AA, Ackerson T, Adeoye OM, Bambakidis NC, Becker K, *et al.* Guidelines for the early management of patients with acute ischemic stroke: 2019 update to the 2018 guidelines for the early management of acute ischemic stroke: A guideline for healthcare professionals from the American heart association/American stroke association. *Stroke* 2019, 50: e344–e418.
- Qin C, Zhou LQ, Ma XT, Hu ZW, Yang S, Chen M, *et al.* Dual functions of microglia in ischemic stroke. *Neurosci Bull* 2019, 35: 921–933.
- Wright-Jin EC, Gutmann DH. Microglia as dynamic cellular mediators of brain function. *Trends Mol Med* 2019, 25: 967–979.
- Wang YJ, Huang ZH. Microglia interact with neurons by forming somatic junctions. *Neurosci Bull* 2020, 36: 1085–1088.
- Otto G. Synaptic nibbling. *Nat Rev Neurosci* 2018, 19: 322.
- Ozdinler PH, Macklis JD. IGF-I specifically enhances axon outgrowth of corticospinal motor neurons. *Nat Neurosci* 2006, 9: 1371–1381.
- Sellgren CM, Gracias J, Watmuff B, Biag JD, Thanos JM, Whittredge PB, *et al.* Increased synapse elimination by microglia in schizophrenia patient-derived models of synaptic pruning. *Nat Neurosci* 2019, 22: 374–385.
- Brown GC, Neher JJ. Microglial phagocytosis of live neurons. *Nat Rev Neurosci* 2014, 15: 209–216.
- Sekar A, Bialas AR, de Rivera H, Davis A, Hammond TR, Kamitaki N, *et al.* Schizophrenia risk from complex variation of complement component 4. *Nature* 2016, 530: 177–183.
- Paolicelli RC, Bolasco G, Pagani F, Maggi L, Scianni M, Panzanelli P, *et al.* Synaptic pruning by microglia is necessary for normal brain development. *Science* 2011, 333: 1456–1458.
- Bolós M, Perea JR, Terreros-Roncá J, Pallas-Bazarra N, Jurado-Arjona J, Ávila J, *et al.* Absence of microglial CX3CR1 impairs the synaptic integration of adult-born hippocampal granule neurons. *Brain Behav Immun* 2018, 68: 76–89.
- Ransohoff RM. Chemokines and chemokine receptors: Standing at the crossroads of immunobiology and neurobiology. *Immunity* 2009, 31: 711–721.
- Harrison JK, Jiang Y, Chen S, Xia Y, Maciejewski D, McNamara RK, *et al.* Role for neuronally derived fractalkine in mediating interactions between neurons and CX3CR1-expressing microglia. *Proc Natl Acad Sci U S A* 1998, 95: 10896–10901.
- Moss SE, Morgan RO. The annexins. *Genome Biol* 2004, 5: 219.
- Lim LH, Solito E, Russo-Marie F, Flower RJ, Perretti M. Promoting detachment of neutrophils adherent to murine post-capillary venules to control inflammation: Effect of lipocortin 1. *Proc Natl Acad Sci U S A* 1998, 95: 14535–14539.
- Tabe Y, Jin L, Contractor R, Gold D, Ruvolo P, Radke S, *et al.* Novel role of HDAC inhibitors in AML1/ETO AML cells: Activation of apoptosis and phagocytosis through induction of annexin A1. *Cell Death Differ* 2007, 14: 1443–1456.
- Flower RJ. Lipocortin and the mechanism of action of the glucocorticoids. *Br J Pharmacol* 1988, 94: 987–1015.
- Gerke V, Creutz CE, Moss SE. Annexins: linking  $Ca^{2+}$  signalling to membrane dynamics. *Nat Rev Mol Cell Biol* 2005, 6: 449–461.
- Kwon JH, Lee JH, Kim KS, Chung YW, Kim IY. Regulation of cytosolic phospholipase A2 phosphorylation by proteolytic cleavage of annexin A1 in activated mast cells. *J Immunol* 2012, 188: 5665–5673.
- Jiwa NS, Garrard P, Hainsworth AH. Experimental models of vascular dementia and vascular cognitive impairment: A systematic review. *J Neurochem* 2010, 115: 814–828.
- Kirino T, Tamura A, Sano K. Delayed neuronal death in the rat *Hippocampus* following transient forebrain ischemia. *Acta Neuropathol* 1984, 64: 139–147.
- Tye KM, Mirzabekov JJ, Warden MR, Ferenczi EA, Tsai HC, Finkelstein J, *et al.* Dopamine neurons modulate neural encoding and expression of depression-related behaviour. *Nature* 2013, 493: 537–541.
- Vorhees CV, Williams MT. Morris water maze: Procedures for assessing spatial and related forms of learning and memory. *Nat Protoc* 2006, 1: 848–858.
- Li X, Xia Q, Mao M, Zhou HJ, Zheng L, Wang Y, *et al.* Annexin-A1 SUMOylation regulates microglial polarization after cerebral ischemia by modulating IKK $\alpha$  stability *via* selective autophagy. *Sci Adv* 2021, 7: eabc5539.
- Bian WJ, Miao WY, He SJ, Qiu ZL, Yu X. Coordinated spine pruning and maturation mediated by inter-spine competition for cadherin/catenin complexes. *Cell* 2015, 162: 808–822.
- Sholl DA. Dendritic organization in the neurons of the visual and motor cortices of the cat. *J Anat* 1953, 87: 387–406.
- Wang YL, Zhao XQ, Jiang Y, Li H, Wang LM, Johnston SC, *et al.* Prevalence, knowledge, and treatment of transient ischemic attacks in China. *Neurology* 2015, 84: 2354–2361.
- Jiang B, Sun HX, Ru XJ, Sun DL, Chen ZH, Liu HM, *et al.* Prevalence, incidence, prognosis, early stroke risk, and stroke-related prognostic factors of definite or probable transient ischemic attacks in China, 2013. *Front Neurol* 2017, 8: 309.
- Hackam DG, Spence JD. Combining multiple approaches for the secondary prevention of vascular events after stroke: A quantitative modeling study. *Stroke* 2007, 38: 1881–1885.
- Wahl D, Cogger VC, Solon-Biet SM, Waern RVR, Gokarn R, Pulpitel T, *et al.* Nutritional strategies to optimise cognitive function in the aging brain. *Ageing Res Rev* 2016, 31: 80–92.
- Bekinschtein P, Oomen CA, Saksida LM, Bussey TJ. Effects of environmental enrichment and voluntary exercise on neurogenesis, learning and memory, and pattern separation: BDNF as a critical variable? *Semin Cell Dev Biol* 2011, 22: 536–542.
- Lodha N, Harrell J, Eisenschenk S, Christou EA. Motor impairments in transient ischemic attack increase the odds of a subsequent stroke: A meta-analysis. *Front Neurol* 2017, 8: 243.

37. Weinhard L, di Bartolomei G, Bolasco G, Machado P, Schieber NL, Neniskyte U, *et al.* Microglia remodel synapses by presynaptic trogocytosis and spine head filopodia induction. *Nat Commun* 2018, 9: 1228.
38. Zhao BM, Wang J, Liu L, Li X, Liu SX, Xia Q, *et al.* Annexin A1 translocates to nucleus and promotes the expression of pro-inflammatory cytokines in a PKC-dependent manner after OGD/R. *Sci Rep* 2016, 6: 27028.
39. Liu L, An DD, Xu JY, Shao B, Li X, Shi J. Ac2-26 induces IKK $\beta$  degradation through chaperone-mediated autophagy *via* HSPB<sub>1</sub> in NCM-treated microglia. *Front Mol Neurosci* 2018, 11: 76.
40. Luo ZZ, Gao Y, Sun N, Zhao Y, Wang J, Tian B, *et al.* Enhancing the interaction between annexin-1 and formyl peptide receptors regulates microglial activation to protect neurons from ischemia-like injury. *J Neuroimmunol* 2014, 276: 24–36.

# Prestin-Mediated Frequency Selectivity Does not Cover Ultrahigh Frequencies in Mice

Jie Li<sup>1,2</sup> · Shuang Liu<sup>1,2</sup> · Chenmeng Song<sup>1,2</sup> · Tong Zhu<sup>1,2</sup> · Zhikai Zhao<sup>1,2</sup> · Wenzhi Sun<sup>3,4</sup> · Yi Wang<sup>1,2</sup> · Lei Song<sup>5,6,7</sup> · Wei Xiong<sup>1,2</sup>

Received: 30 July 2021 / Accepted: 24 December 2021 / Published online: 12 March 2022

© Center for Excellence in Brain Science and Intelligence Technology, Chinese Academy of Sciences 2022

**Abstract** In mammals, the piezoelectric protein, Prestin, endows the outer hair cells (OHCs) with electromotility (eM), which confers the capacity to change cellular length in response to alterations in membrane potential. Together with basilar membrane resonance and possible stereociliary motility, Prestin-based OHC eM lays the foundation for enhancing cochlear sensitivity and frequency selectivity.

**Supplementary Information** The online version contains supplementary material available at <https://doi.org/10.1007/s12264-022-00839-4>.

Jie Li, Shuang Liu, and Chenmeng Song contributed equally to this work.

✉ Yi Wang  
yiwang2020@tsinghua.edu.cn

✉ Lei Song  
lei.song@yale.edu

✉ Wei Xiong  
wei\_xiong@tsinghua.edu.cn

<sup>1</sup> School of Life Sciences, Tsinghua University, Beijing 100084, China

<sup>2</sup> IDG/McGovern Institute for Brain Research at Tsinghua University, Tsinghua University, Beijing 100084, China

<sup>3</sup> Chinese Institute for Brain Research, Beijing 102206, China

<sup>4</sup> School of Basic Medical Sciences, Capital Medical University, Beijing 100069, China

<sup>5</sup> Department of Otolaryngology, Head and Neck Surgery, Shanghai Ninth People's Hospital, Shanghai Jiao Tong University School of Medicine, Shanghai 200011, China

<sup>6</sup> Ear Institute, Shanghai Jiao Tong University School of Medicine, Shanghai 200092, China

<sup>7</sup> Shanghai Key Laboratory of Translational Medicine on Ear and Nose Diseases, Shanghai 200011, China

However, it remains debatable whether Prestin contributes to ultrahigh-frequency hearing due to the intrinsic nature of the cell's low-pass features. The low-pass property of mouse OHC eM is based on the finding that eM magnitude dissipates within the frequency bandwidth of human speech. In this study, we examined the role of Prestin in sensing broad-range frequencies (4–80 kHz) in mice that use ultrasonic hearing and vocalization (to >100 kHz) for social communication. The audiometric measurements in mice showed that ablation of Prestin did not abolish hearing at frequencies >40 kHz. Acoustic associative behavior tests confirmed that *Prestin*-knockout mice can learn ultrahigh-frequency sound-coupled tasks, similar to control mice. *Ex vivo* cochlear  $\text{Ca}^{2+}$  imaging experiments demonstrated that without Prestin, the OHCs still exhibit ultrahigh-frequency transduction, which in contrast, can be abolished by a universal cation channel blocker, Gadolinium. *In vivo* salicylate treatment disrupts hearing at frequencies <40 kHz but not ultrahigh-frequency hearing. By pharmacogenetic manipulation, we showed that specific ablation of the OHCs largely abolished hearing at frequencies >40 kHz. These findings demonstrate that cochlear OHCs are the target cells that support ultrahigh-frequency transduction, which does not require Prestin.

**Keywords** Prestin · PIEZO2 · Ultrahigh-frequency hearing · Electromotility · Outer hair cells

## Introduction

Mammalian auditory function has ample capacity to discriminate sound frequencies ranging from several Hz to >100 kHz [1]. In large part, this functionality relies on the organ of Corti, a relatively newly-evolved organ

comparable to that found in lower vertebrates, which is comprised of three rows of outer hair cells (OHCs) and one row of inner hair cells (IHCs). The frequency-selectivity of hair cells is determined by their position along the cochlear coil. At the apex, the hair cells sense low frequencies; at the basal turn, they detect high frequencies [2, 3]. At each frequency, a travelling wave vibrates on the basilar membrane and finds its best matching position where OHCs actively and locally amplify the motion between the tectorial and basilar membranes [2, 4]. OHCs can change their length in response to fluctuations in receptor potential, a property also defined as electromotility (eM) [5–8]. OHC-based eM is believed to contribute to cochlear amplification, which significantly improves hearing sensitivity and frequency-selectivity in mammals [2, 3].

The somatic eM of the OHC is generated by the motor protein, Prestin [2, 9, 10]. As it is extensively expressed on the lateral membrane of OHCs, Prestin behaves as a biological piezoelectric element containing at least two functional domains: a voltage sensor, which detects fluctuations in membrane potential, and an actuator, which can undergo conformational change [10–12]. Recently, these component domains have been depicted by cryoelectron microscopy as discrete structures [13–15]. Prestin is the key protein enhancing the frequency-tuning process by providing OHCs with eM that is the basic mechanism driving cochlear amplification [10, 16, 17].

Although active cochlear amplification has been recorded both *in vivo* and *in vitro* at wide-ranging frequencies, the contribution of Prestin-based somatic eM at high frequencies remains elusive. In order to generate cochlear amplification, the OHC must change its length in a cycle-by-cycle manner, as reported at lower frequencies, such as 1 kHz [4, 9]. However, theoretically, Prestin-driven amplification is limited by two low-pass filters: one is formed by the resistance and capacitance of the cell membrane [18] and the other is due to the internal limitations in the velocity of conformational change of Prestin [19]. Using different recording configurations, the measured cut-off frequency of OHC eM varies considerably across several studies, in which the upper limit ranged from a few kHz [20] to at least 79 kHz [21–23]. Thus, whether Prestin-based OHC motility can power amplification through ultrahigh frequencies has not yet been established.

Interestingly, many animals, including mice, use ultrasonic hearing and vocalization (20 kHz to >100 kHz) for communication [24]. Previous phylogenetic and functional studies on Prestin have revealed trends in the distribution of genetic polymorphisms that appear to coincide with the ability of particular species to echolocate [25–29]. This suggests a co-evolution of Prestin eM with the ultrasonic vocalization of echolocating animals, such as cetaceans,

bats, and dolphins. Also noteworthy, *in vivo* approaches have shown that Prestin enhances hearing sensitivity across the whole frequency range [16, 30]. On the other hand, our recent study revealed that PIEZO2, a mechanically-activated channel, likely mediates ultrasonic hearing *via* OHCs [31]. Taken together, these data have motivated further study of the essential role Prestin plays in ultrasonic hearing.

## Materials and Methods

### Mouse Strains and Animal Care

*Prestin*-knockout (*Prestin*-KO) and *Prestin*-P2A-DTR (diphtheria toxin receptor) (*Prestin*-DTR) mouse lines were generated as described [32, 33]. Wild-type (WT) C57BL6 (B6) mice were used as controls for *Prestin*-KO mice. *Prestin*-DTR and littermate controls at the age of 3 weeks received a single intraperitoneal (i.p.) injection of diphtheria toxin (DT; Sigma, 2 µg/mL dissolved in saline) at a dose of 20 ng/g body weight. One week later, foot-shock behavior and audiometry were recorded in both DTR and littermate mice. The experimental procedures were approved by the Institutional Animal Care and Use Committee of Tsinghua University.

### Modified Auditory Brainstem Response (mABR)

Mice of either sex were anesthetized with 0.4% pentobarbital sodium in saline (0.2 mL/10 g, volume/body weight, i.p.). During the whole experiment, body temperature was maintained at 37 °C by a heating pad. After vertex skin removal, the skull was exposed and secured with a stainless-steel screw (M1.4 × 2.5). In contrast to the classical ABR configuration, a modified ABR (mABR) configuration was recorded to acquire better ABRs in response to ultrahigh-frequency stimuli. This was accomplished by connecting the electrode to a microscrew attached to the skull posterior to bregma (−7 mm AP, 0 mm ML), as previously described [31]. Precautions were taken not to puncture the dura. A recording electrode was connected to the screw by a silver wire with a diameter of 0.1 mm. Other operations were similar to regular ABR procedures. Reference and ground electrodes were inserted subcutaneously at the pinna and groin, respectively. The animals were overdosed with pentobarbital at the end of acute experiments. In survival experiments, the screw was secured with dental cement for later measurements. After surgery, lidocaine ointment was applied locally and Meloxicam (4 mg/kg i.p.) was injected for anesthesia, analgesia, and anti-inflammation.

mABR data were collected at ~200 kHz by an RZ6 workstation controlled by BioSig software (Tucker-Davis



Technologies, Alachua, FL). Clicks and 4–16 kHz pure-tone bursts were generated by a TDT MF1 closed-field magnetic speaker. A TDT EC1 (Coupler Model) electrostatic speaker was used to generate high frequencies (32–80 kHz). Prior to experiments, the two speakers were calibrated using 377C01 (free-field) or 377C10 (pressure) microphones with a 426B03 preamplifier and a 480C02 signal conditioner (PCB Piezotronics, Depew, NY). For sound stimulation, 0.1-ms clicks or 5-ms tone-bursts with a 0.5-ms rise/fall time were delivered at 21 Hz, with intensities ranging from 90 to 10 dB SPL in 10-dB steps. Responses to each acoustic stimulation with defined frequency and intensity levels were bandpass filtered (100 or 300 to 3000 Hz), amplified by RA4LI & RA4PA Medusa PreAmps (Tucker-Davis Technologies, Alachua, FL), repeatedly sampled 512 times, and then averaged. For lower frequencies, the lowest stimulus sound level at which a repeatable wave I could be identified was defined as the threshold [34]. Typically, frequencies >54 kHz in waveform were hard to identify due to the low signal-to-noise ratio. In most cases, wave I was missing in the waveform as reported by other groups [35]. However, one peak appeared at ~3 ms and its latency increased and amplitude decreased with stimulus levels. This peak was used to identify the threshold when wave I could not be detected. The responses disappeared postmortem, so the signals were biological.

Salicylate, a known competitor of intracellular chloride binding, was used to inhibit the functionality of Prestin. Specifically, 200 mg/kg sodium salicylate was applied i.p. to 1-month-old WT B6 mice. A higher salicylate dose was avoided since it can induce higher hearing-threshold elevation, making survival more difficult for mice during the 2-h measurement sessions. The 200 mg/kg limit introduced only mild hearing threshold elevation at lower frequencies by ~20 dB SPL. mABR thresholds were monitored every 10 min until 120 min post-injection and were measured again on day 2 to record the recovery. For finer time resolution, the responses were averaged 256 times, and only the EC1 speaker was used to deliver the pure tone stimuli (12–80 kHz) in a close-field configuration. Each measurement took ~8 min.

### Acoustic Cue-Associated Freezing Behavior

Male mice were used to investigate freezing behavior. Mouse locomotion in an operant (cubic, 30 × 30 × 30 cm<sup>3</sup>) or activity box (cylindrical, diameter of 35 cm and height 30 cm) was carried out in a soundproof chamber (Shino Acoustic Equipment Co., Ltd, Shanghai, China), and captured on camera with an infrared light source. Each mouse was allowed to freely explore the operant box for 30 min before the sound-associated foot-shock training.

During the training, an acoustic cue of 10 s containing a 50-ms pure tone (16 kHz or 63 kHz) at 50-ms intervals, was played. Electrical shocks of 1 s at 0.6 mA were given to the mouse at 5 s and 10 s. In the operant box, the electrical shocks were delivered by a metal grid floor powered by an electrical stimulator (YC-2, Chengdu Instrument Inc., Chengdu, China). Acoustic cues were generated by a free-field electrostatic speaker ES1 placed 15 cm above the floor and powered by an RZ6 workstation with BioSig software (Tucker-Davis Technologies, Alachua, FL). The cue was delivered every 3 min, and repeated 10 times before the trained mouse was placed into the home cage. After 24 h, the trained mouse was transferred to an activity box to test freezing behavior. In the activity box, the same ES1 speaker was placed 15 cm above the chamber floor to generate a 16 kHz or 63 kHz acoustic cue of 10 s duration (identical to the training cues). Cues were delivered at least 5 times during each test procedure. The sound intensity on the arena floor was calibrated from 70 dB SPL to 90 dB SPL, which is in the range of mouse hearing.

### Immunostaining

Mice were selected for immunostaining at the ages of 3 weeks, 1 month, 6 weeks, or 2 months. After anesthesia with Avertin (30 mg/mL in saline, 0.12–0.15 mL/10 g), mice were perfused with ice-cold phosphate-buffered saline (PBS), and then sacrificed by decapitation. The inner ears were dissected from the temporal bone, and fixed in fresh 4% paraformaldehyde (DF0135, Leagene, Anhui, China) in PBS for 12–24 h at 4 °C. After fixation, the inner ears were washed three times (10 min each) with PBS, and then immersed in 120 mM EDTA decalcifying solution (pH 7.5) for 24 h at room temperature (RT, 20–25 °C). This step was also followed by PBS washing.

The cochlear coils were finely dissected from the inner ears in PBS and blocked in 1% PBST [PBS + 1% Triton X-100 (T8787, Sigma-Aldrich, St. Louis, MO)] with 5% BSA (A3059, Sigma-Aldrich, St. Louis, MO) at room temperature for 1 h. The cochlear tissue was then incubated in 0.1% PBST/5% BSA solution with MYO7A antibody (1:1000, Cat.25-6790, Proteus Biosciences Inc., Ramona, CA) overnight at 4 °C and washed 3 times with 0.1% PBST at RT. The tissue was incubated with secondary antibody (Invitrogen anti-rabbit Alexa Fluor 647, 1:1000, A21244; Invitrogen Alexa Fluor 488 Phalloidin, 1:1000, Cat. A12379) and 1:1000 DAPI in 0.1% PBST/5% BSA solution at RT for 2–4 h. The tissue was washed 3 times with 0.1% PBST and mounted with ProLong Gold Antifade Mountant (Cat. P36930, Life Technology, Rockville, MD). Fluorescent immunostaining patterns were captured by an A1/SIM/STORM confocal microscope (A1

N-SIM STORM, Nikon, Japan). Whole-view images of cochlear tissue were composited using Photoshop software (Adobe, San Jose, CA).

### Cochlear $\text{Ca}^{2+}$ Imaging

A hemicochlear preparation [36, 37] was used for  $\text{Ca}^{2+}$  imaging of OHCs [31]. Mice at 1 month of age were anesthetized with isoflurane and sacrificed, and then the cochleae were dissected out using a dissection solution containing (in mmol/L): 5.36 KCl, 141.7 NaCl, 1  $\text{MgCl}_2$ , 0.5  $\text{MgSO}_4$ , 0.1  $\text{CaCl}_2$ , 10 H-HEPES, 3.4 L-glutamine, 10 D-glucose (pH 7.4, osmolality 290 mmol/kg). After immersion in cutting solution containing (in mmol/L) 145 NMDG-Cl, 0.1  $\text{CaCl}_2$ , 10 H-HEPES, 3.4 L-glutamine, 10 D-glucose (pH 7.4, osmolality 290 mmol/kg), cochleae were glued to a metal block with Loctite 401 and cut into 2 halves by a vibratome (VT1200S, Leica, Wetzlar, Germany; FREQ index at 7/Speed index at 50). The section plane was configured in parallel to the modiolus to minimize tissue damage. The hemicochleae were transferred into a recording dish, glued to the bottom, and loaded with 25  $\mu\text{g/mL}$  Fluo-8 AM (Invitrogen, Waltham, MA) in the recording solution. After 10-min incubation in a dark box at RT, the dye-loading solution was replaced by dye-free recording solution containing (in mmol/L): 144 NaCl, 0.7  $\text{Na}_2\text{PO}_4$ , 5.8 KCl, 1.3  $\text{CaCl}_2$ , 0.9  $\text{MgCl}_2$ , 10 H-HEPES, 5.6 D-glucose (pH 7.4, osmolality 310 mmol/kg).

An upright microscope (BX51WI, Olympus, Tokyo, Japan) equipped with a 60 $\times$  water immersion objective (LUMPlanFL, Olympus, Tokyo, Japan) and an sCMOS camera (ORCA Flash 4.0, Hamamatsu, Hamamatsu-Shi, Japan) was used for  $\text{Ca}^{2+}$  imaging, controlled by MicroManager 1.6 software [38] with a configuration of 4  $\times$  4 binning, 100-ms exposure time, and 2-s sampling interval. To maintain the best performance of the hemicochlea preparations, the whole procedure from cutting to imaging was finished within 15 min to ensure tissue sample integrity.

### Ultrasound Generation and Delivery *ex vivo*

A customized 80-kHz ultrasound transducer 27 mm in diameter was powered by a radio-frequency amplifier (Aigtek, ATA-4052, China) integrated with a high-frequency function generator (Rigol, DG1022U, China). An 80-kHz transducer was chosen because of its relatively small size (the lower the frequency, the larger the size) and its compatibility with physiological hearing frequencies in mice. For calibration, a high-sensitivity hydrophone (Precision Acoustics, UK) was positioned directly above the vibration surface. Transducer outputs were calibrated in a

tank filled with deionized, degassed water under free-field conditions. To stimulate the cochlea, the transducer was tightly fixed to the bottom of the recording dish with ultrasound gel. The distance between the tissue and ultrasound transducer was <5 mm. For the 80-kHz ultrasonic stimulation, a single pulse of 100 ms was applied, with a calibrated intensity at 8.91  $\text{W/cm}^2$   $I_{\text{SPTA}}$ .

### Low-frequency Fluid-jet Stimulation of Cochlea

The fluid-jet configuration was used as previously reported [39]. Briefly, a 27-mm diameter circular piezoelectric ceramic was sealed in a self-designed mineral oil tank. An electrode with a 5–10  $\mu\text{m}$  diameter tip filled with recording solution (in mmol/L: 144 NaCl, 0.7  $\text{Na}_2\text{PO}_4$ , 5.8 KCl, 1.3  $\text{CaCl}_2$ , 0.9  $\text{MgCl}_2$ , 10 H-HEPES, 5.6 D-glucose, pH 7.4, osmolality 310 mmol/kg) was mounted in the tank and transmitted the pressure wave to the hair bundle of an OHC in cochlea samples. The circular piezoelectric ceramic was driven by a sinusoidal voltage fluctuation generated from a patch-clamp amplifier (EPC10 USB, HEKA Elektronik, Lambrecht/Pfalz, Germany) and amplified 20-fold with a custom high-voltage amplifier. The 100-ms sinusoidal stimulation was delivered at a frequency of 2000 Hz and an amplitude of 130 V.

### Nonlinear Capacitance Recording

Neonatal mice at P7–P8 were used. Basilar membrane with hair cells was dissected and bathed in external solution containing (in mmol/L): 120 NaCl, 20 TEA-Cl, 2  $\text{MgCl}_2$ , 2  $\text{CoCl}_2$ , and 10 H-HEPES (pH 7.3 with NaOH, osmolality 300 mmol/kg with D-glucose). An internal solution at the same pH and osmolality contained (in mmol/L): 140 CsCl, 2  $\text{MgCl}_2$ , 10 EGTA, and 10 H-HEPES. Whole-cell patch clamping was done at a holding potential of 0 mV (Axon Axopatch 200B, Molecular Devices, Sunnyvale, CA). A continuous high-resolution two-sine stimulus (390.6 and 781.2 Hz) with 10 mV peak amplitude superimposed on a 250-ms voltage ramp (from +150 to –150 mV) was used. Data were acquired and analyzed using jClamp (Scisoft, New Haven, CT). Capacitance-voltage data were fit with a two-state Boltzmann function.

$$C_m = NLC + C_{\text{lin}} = Q_{\text{max}} \frac{ze}{k_B T} \frac{b}{(1+b)^2} + C_{\text{lin}}$$

where

$$b = \exp\left(-ze \frac{V_m - V_h}{k_B T}\right)$$

$C_{\text{lin}}$  is the linear membrane capacitance,  $Q_{\text{max}}$  is the maximum nonlinear charge,  $z$  is valence,  $e$  is electron

charge,  $K_B$  is the Boltzmann constant,  $T$  is absolute temperature,  $V_m$  is membrane potential, and  $V_h$  is voltage at peak capacitance.

### Experimental Design and Statistical Analysis

For animal tracing and locomotion evaluation, videos of mouse locomotion in foot-shock were analyzed using MatLab (MathWorks, Natick, MA) and EthoVision XT software (v11.5, Noldus, Wageningen, Netherland). The center of each mouse was used to draw the locomotion trace. To show speed, the locomotion trace was dotted every 0.5 s. To analyze foot-shock behavior, the percentage freezing time pre-cue (30 s before conditioned stimulus), and post-cue (30 s after conditioned stimulus), were calculated to compare the effect of sound-induced freezing.

For  $\text{Ca}^{2+}$  data analysis, to extract fluorescence signals we visually identified the regions of interest (ROIs) based on fluorescence intensity. To estimate fluorescence changes, the pixels in each specified ROI were averaged ( $F$ ). Relative fluorescence changes,  $DF/F_0 = (F - F_0)/F_0$ , were calculated as  $\text{Ca}^{2+}$  signals. The cochlear imaging data were analyzed offline using Micromanager software. An ROI was drawn to cover each hair cell. The fluorescence intensity of each ROI was normalized to its value in the frame immediately prior to each stimulation.

Data were managed and analyzed with MatLab 2014b (MathWorks, Natick, MA), Excel 2016 (Microsoft, Seattle, WA), Prism 6 (GraphPad Software, San Diego, CA), and Igor pro 6 (WaveMetrics, Lake Oswego, OR). N numbers are indicated in the figures or legends. For audiometry and behavioral experiments, N values present biological replicates of individual mice. For cochlear  $\text{Ca}^{2+}$  imaging experiments, N values indicate biological replicates of individual cells, which were collected from at least 3 mice. All data are shown as the mean  $\pm$  SD, as indicated in the figure legends. We used a two-tailed  $t$ -test for one-to-one comparison or one-way ANOVA for one-to-many comparisons to determine statistical significance ( $*P < 0.05$ ,  $**P < 0.01$ ,  $***P < 0.001$ , and  $****P < 0.0001$ ), which were compared by nonparametric tests if the data distribution was not Gaussian.

## Results

### Ultrahigh-frequency Hearing is Preserved in Mice with Prestin Knockout

In order to determine whether Prestin is crucial for ultrahigh-frequency hearing, the ABR thresholds were measured in both *Prestin*-KO and WT mice for hearing sensitivity at multiple frequencies (up to 80 kHz) (Fig. 1).

The *Prestin*-KO mouse was generated by a CRISPR/Cas9-mediated base editing approach, and showed a loss of OHC-eM [32] as previously described [17].

Consistent with previous studies [17], 2-month old *Prestin*-KO mice exhibited significantly elevated pure-tone mABR thresholds at 4–32 kHz cues; although these thresholds were relatively high ( $\sim 70$  dB SPL), they were still in the detectable range (Fig. 1A, E, dark purple). However, at frequencies  $>40$  kHz, the *Prestin*-KO mice at 2 months showed mABR thresholds  $>90$  dB SPL, the ceiling threshold indicative of profound deafness in general ABR testing (Fig. 1A, D, E, dark purple). One-month-old *Prestin*-KO mice showed mABR deficits similar to 2-month-old *Prestin*-KO mice at hearing frequencies ranging from 4 kHz to 32 kHz (Fig. 1B, E, light purple vs dark purple). However, hearing in the 40–80 kHz range was preserved with thresholds similar to control WT mice (Fig. 1C, D, E, light purple vs gray), distinct from that of 2-month-old *Prestin*-KO mice (Fig. 1D, E, light purple vs dark purple). The amplitude of P1–N1 of the mABR waveform in 1-month-old *Prestin*-KO mice was decreased by nearly half (Fig. S1). This implies that the *Prestin*-KO mice suffered some degree of neuronal loss prior to the elevation of mABR thresholds. Together, these results indicate that in mice, Prestin enhances hearing sensitivity primarily in an upper limit range of 40 kHz, but plays a less important role at frequencies above 40 kHz.

### Freezing Behavior Associated with Ultrahigh-frequency Hearing is Preserved in Prestin-KO Mice

To confirm that Prestin-driven OHC mechanics were not crucial for ultrahigh-frequency hearing, sound-associated fear conditioning experiments were performed for low- and high-frequency hearing in *Prestin*-KO mice (Fig. 2A). In the *Prestin*-KO mice and control cohorts, fear-conditioning tests were applied using an acoustic cue that was paired with electrical shocks to generate conditioned-freezing behaviors (Fig. 2A). On day 2, 1-month-, 2-month-old *Prestin*-KO, and 1-month-old WT mice were examined for sound cue-associated freezing behavior (Fig. 2B). The 1-month-old *Prestin*-KO mice were able to be trained to respond to the 16-kHz cue at 90 dB SPL but had a limited response to this cue at 60 dB SPL, while the control WT mice responded to the 16-kHz cue at both intensities (Fig. 2B–D). This demonstrates that the cochlear amplifier is intact in WT in the low-frequency range.

By comparison, both the 1-month-old *Prestin*-KO and WT mice acquired freezing behavior in response to the 63-kHz cue at 90 dB SPL (Fig. 2B, E). Consistent with the above mABR results, *Prestin*-KO mice showed associative freezing to the 63-kHz cue at 1 month but lost this

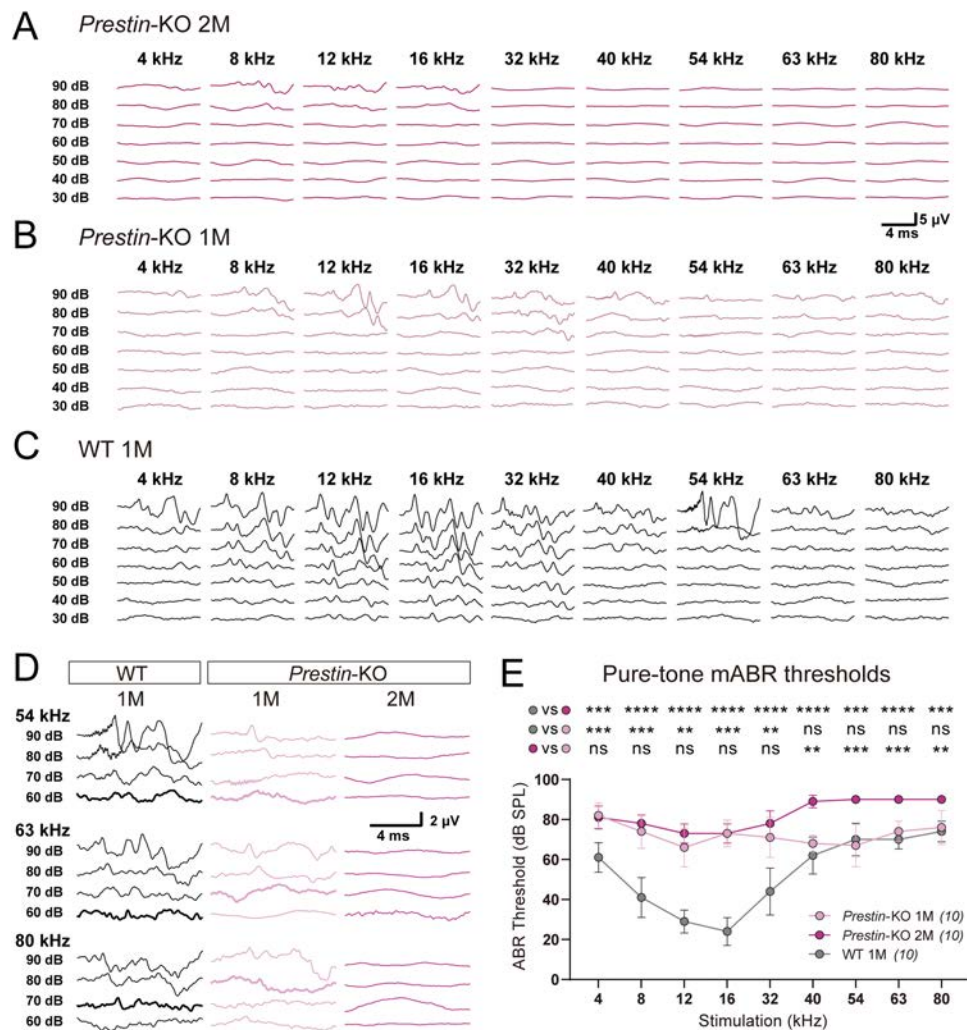


**Fig. 1** *Prestin*-knockout mice show distinct sensitivity at low and high frequencies. **A** Representative example of mABR signals in a 2-month-old (2M) *Prestin*-KO mouse. **B** Representative example of mABR signals in a 1-month (1M) *Prestin*-KO mouse. **C** Representative example of mABR signals in a 1-month (1M) WT C57BL/6 mouse. **D** Enlarged mABR traces with 54 kHz, 63 kHz, and 80 kHz sound stimuli in (A–C). Bold lines indicate visual thresholds. Peak at ~3 ms was used to identify the threshold for high frequencies. **E** Pure-tone mABR thresholds in *Prestin*-KO mice and control mice at designated ages. Note the distinct ABR thresholds to ultrasound frequencies between *Prestin*-KO mice at 1 month (1M, light purple) and *Prestin*-KO mice at 2 months (2M, purple). 1-month-old (1M)

sensitivity at 2 months of age (Fig. 2B–E). Freezing behavior in *Prestin*-KO mice was not as pronounced as that seen in WT mice when coupled with either 16 kHz or 63 kHz (Fig. 2C–E). This was thought to be the result of decreased freezing time potentially due to disrupted cochlear function [10, 16, 17]. These results suggest that Prestin and its eM may modestly contribute to, but are not essential for ultrahigh-frequency hearing.

*Prestin*-KO mice vs control mice, Kruskal-Wallis test, 4 kHz, \*\*\* $P = 0.0002$ ; 8 kHz, \*\*\* $P = 0.0006$ ; 12 kHz, \*\* $P = 0.0026$ ; 16 kHz, \*\*\* $P = 0.0002$ ; 32 kHz, \*\* $P = 0.0047$ ; 40 kHz,  $P = 0.7802$ ; 54 kHz,  $P > 0.9999$ ; 63 kHz,  $P = 0.9704$ ; 80 kHz,  $P > 0.9999$ . 2-month (2M) *Prestin*-KO mice vs control mice, Kruskal-Wallis test, 4 kHz, \*\*\* $P = 0.0005$ ; 54 kHz and 80 kHz, \*\*\* $P = 0.0003$ ; \*\*\*\* $P < 0.0001$  at other frequencies. 1-month-old (1M) *Prestin*-KO mice vs 2-month-old (2M) *Prestin*-KO mice, Kruskal-Wallis test, 4 kHz,  $P > 0.9999$ ; 8 kHz,  $P > 0.9999$ ; 12 kHz,  $P = 0.7182$ ; 16 kHz,  $P > 0.9999$ ; 32 kHz,  $P = 0.734$ ; 40 kHz, \*\* $P = 0.0016$ ; 54 kHz, \*\*\* $P = 0.0001$ ; 63 kHz, \*\*\* $P = 0.0009$ ; 80 kHz, \*\* $P = 0.0013$ . Data are presented as the mean  $\pm$  SD. N numbers are shown in panels.

### Progressive Loss of Cochlear Hair Cells in *Prestin*-KO Mice

It has been reported that ablation of Prestin induces the progressive loss of hair cells [40]. Therefore, we assessed the survival of hair cells in *Prestin*-KO mice at different ages. At 2 months of age, *Prestin*-KO mice lost the majority of OHCs and some basal IHCs (Fig. 3A, D). This may explain the abolished mABR signals at ultrahigh frequencies (Fig. 1E, dark purple). The absence of hair

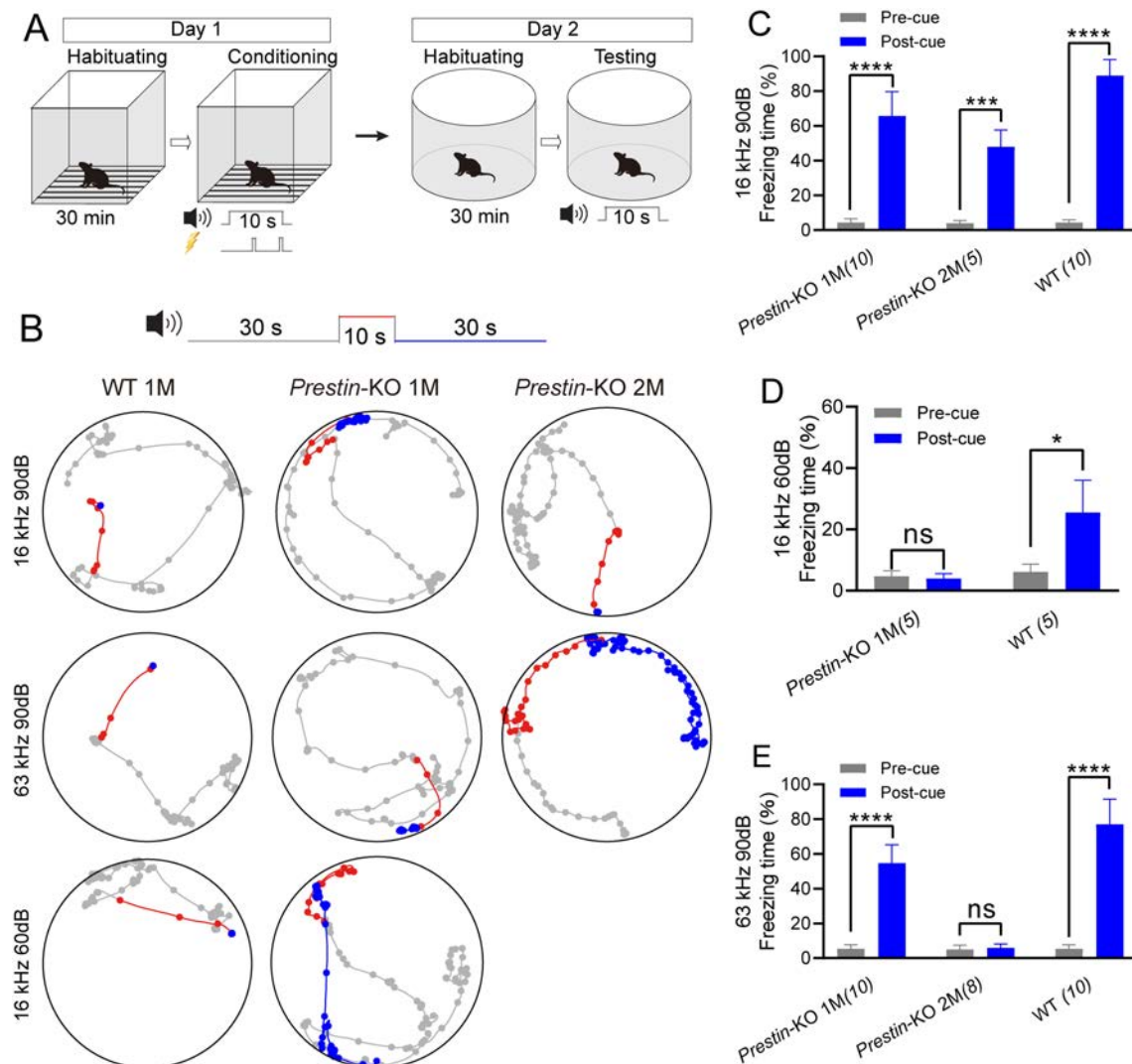


**Fig. 2** Ultrahigh-frequency hearing-associated freezing behavior is preserved in 1-month-old (1M) *Prestin-KO* mice. **A** Paradigm of sound-cue associated freezing behavior. Pure-tone sound at 16 kHz or 63 kHz played by a TDT ES1 (Free Field) electrostatic speaker is used as the conditioned stimulus, and foot-shock was used as the unconditioned stimulus. **B** Representative examples of locomotion of control mice, 1-month (1M), and 2-month (2M) *Prestin-KO* mice before (gray, 30 s), during (red, 10 s), and after (blue, 30 s) the pure-tone sound cue. The mice had been trained to pair either the 16-kHz or the 63-kHz cue with the foot-shock-induced freezing. Dots indicate the location of a mouse every 0.5 s. Note that the 2M *Prestin-KO* mouse reacts to the 16 kHz but not the 63 kHz cue at 90 dB SPL.

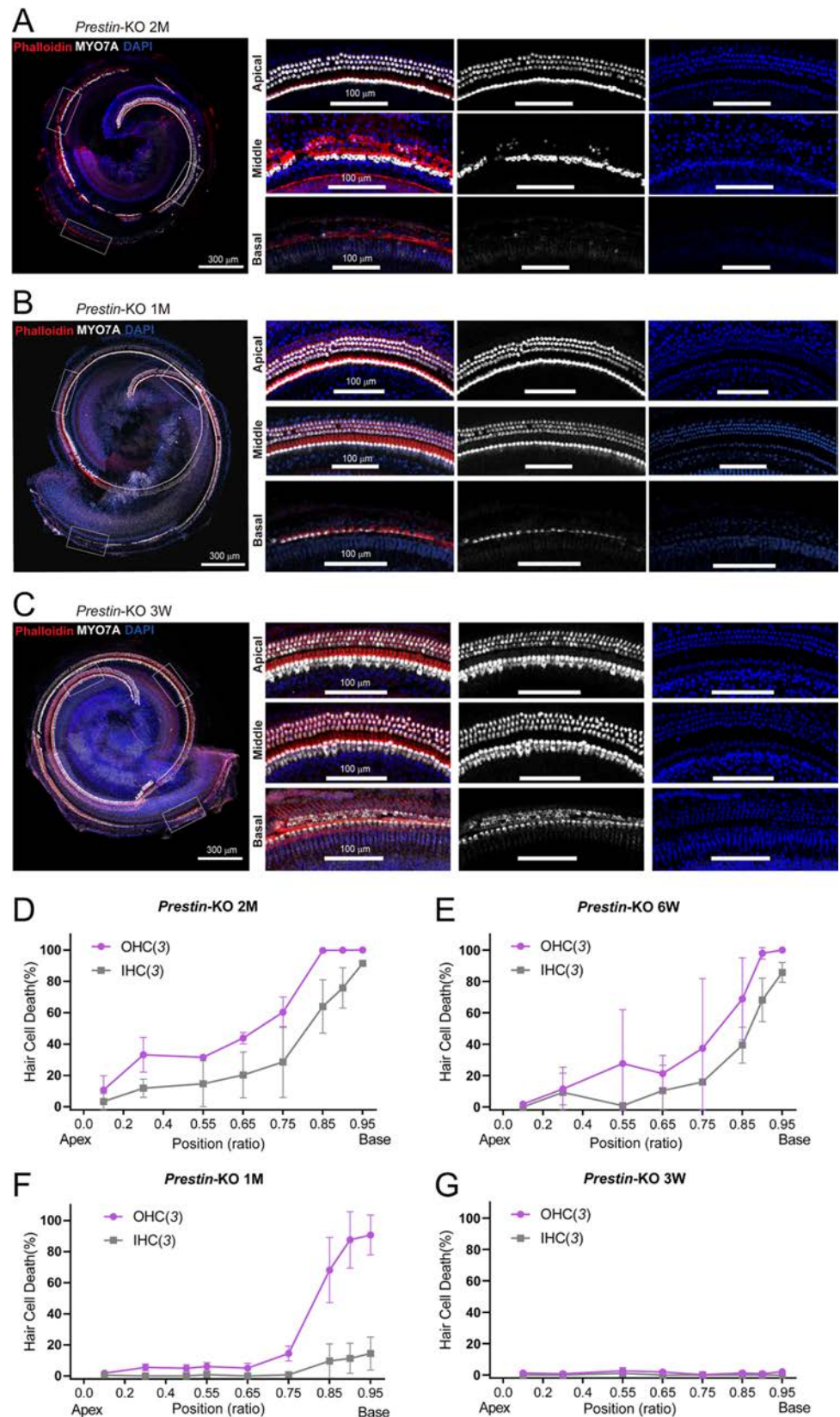
cells in 1.5-month *Prestin-KO* mice was not as profound as that in 2-month-old animals (Fig. 3E). *Prestin-KO* mice at the age of 1 month showed mostly preserved OHCs and IHCs, except for some OHC loss at very basal locations (Fig. 3B, F). Mechanistically, this may hinder the preservation of ultrahigh-frequency hearing (Fig. 1E). Further, we examined the cochleae from 3-week-old *Prestin-KO* mice and found that most of their hair cells were preserved (Fig. 3C, G). Thus, by measuring mABR thresholds in

3-week-old *Prestin-KO* mice (Fig. 4), we continued to show an obvious loss of hearing sensitivity at 4–32 kHz, as was seen in the 1-month-old *Prestin-KO* mice. Nevertheless, ultrasonic hearing in the range from 40 kHz to 80 kHz remained similar to the control cohort (Fig. 4C, D, gray vs yellow). These results from 3-week-old mice provide further confirmation that the Prestin defect disrupts lower frequency- but not ultrahigh-frequency hearing. The mABR thresholds of 3-week-old mice at ultrahigh



**Fig. 3** Progressive loss of hair cells in *Prestin*-KO mice.

**A** Reconstructed whole cochlear coil showing outer hair cell (OHC) survival from a 2-month-old (2M) *Prestin*-KO mouse. The cochlea is labeled with MYO7A antibody (white), phalloidin (red), and DAPI (blue). Left panels: scale bar, 300  $\mu$ m. Right panels: enlarged images of apical, middle, and basal fragments in the dashed-line frames in (A). Scale bar, 100  $\mu$ m. Note OHCs are only preserved in the apical coil. **B**, **C** Reconstructed whole cochlear coils showing OHC survival from a 1-month-old (1M) *Prestin*-KO mouse (**B**) and a 3-week-old (3W) *Prestin*-KO mouse (**C**). All the staining conditions are similar to (A). Note that most of the OHCs are present except in the basal part (**B**). **D–G** Loss of OHCs and IHCs in positions along the cochlear coil (as ratios) in 2M (**D**), 6W (**E**), 1M (**F**), and 3W (**G**) *Prestin*-KO mice. In (**D–G**), data are presented as the mean  $\pm$  SD, and N numbers are shown in panels.



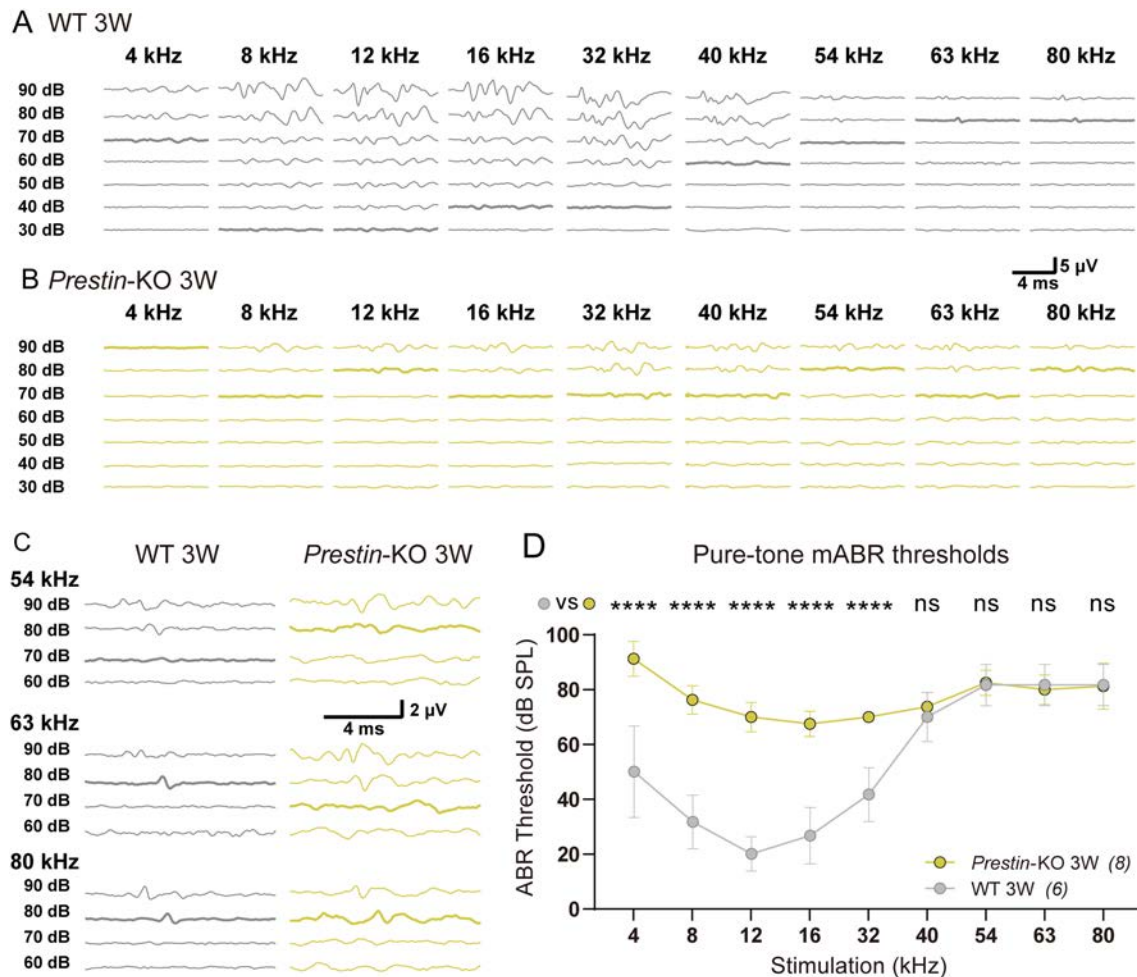


**Fig. 4** mABR measurements from 3-week-old (3W) *Prestin*-knock-out mice. **A** Representative example of mABR signals in a 3W WT mouse. **B** Representative example of mABR signals in a 3W *Prestin*-KO mouse. **C** Amplified representative examples of mABR signals in response to 54–80 kHz, 60–90 dB SPL stimuli (visual thresholds bolded). The peak at ~3 ms is used to identify the threshold. **D** Pure-tone mABR thresholds in *Prestin*-KO and control mice at 3W. Groups

are compared at each frequency. *Prestin*-KO mice vs control mice, Sidak's multiple comparisons test, 4 kHz, \*\*\*\* $P < 0.0001$ ; 8 kHz, \*\*\*\* $P < 0.0001$ ; 12 kHz, \*\*\*\* $P < 0.0001$ ; 16 kHz, \*\*\*\* $P < 0.0001$ ; 32 kHz, \*\*\*\* $P < 0.0001$ ; 40 kHz,  $P = 0.9824$ ; 54 kHz,  $P > 0.9999$ ; 63 kHz,  $P > 0.9999$ ; 80 kHz,  $P > 0.9999$ . Data are presented as the mean  $\pm$  SD. N numbers are shown in panels.

frequencies were slightly higher than those of 1-month-old animals (Fig. 1E vs Fig. 4D), probably because ultrasonic hearing was not fully mature at 3 weeks of age.

### Ultrahigh Frequency-induced Response in Cochlear OHCs After Prestin Deletion

As the cells responsible for cochlear amplification, OHCs possess mechano-electrical and electro-mechanical transducers (for functional forward and reverse transduction) at low frequencies, both of which are required for normal functionality. We examined both transductions, including ultrahigh-frequency transduction in *ex vivo* cochlea preparations. First, reverse transduction was tested with nonlinear capacitance (NLC) recordings, which showed complete

loss of motility in *Prestin*-KO OHCs, but not in the control cohort (Fig. 5A, B). Next, we tested whether Prestin contributes to ultrahigh-frequency forward transduction at the cellular level. The OHCs were stimulated by ultrahigh-frequency vibration while responses were monitored using  $\text{Ca}^{2+}$  imaging of the hemicochlea with an epifluorescence microscope [31]. A custom-made *ex vivo* stimulation stage delivered vibration of 80 kHz, which mimicked mechanical vibration in the cochlea driven by ultrahigh frequency (Fig. 5C). The cochlea preparation was loaded with Fluo-8 AM, a sensitive  $\text{Ca}^{2+}$  dye, to illuminate the vibration-evoked  $\text{Ca}^{2+}$  response of the hair cells.

The major cell type that takes up  $\text{Ca}^{2+}$  dye, the OHCs in 1-month-old WT mice showed a significant increase in fluorescence when subjected to 80 kHz vibration (Fig. 5D, E). A similar ultrahigh-frequency-elicited  $\text{Ca}^{2+}$  response

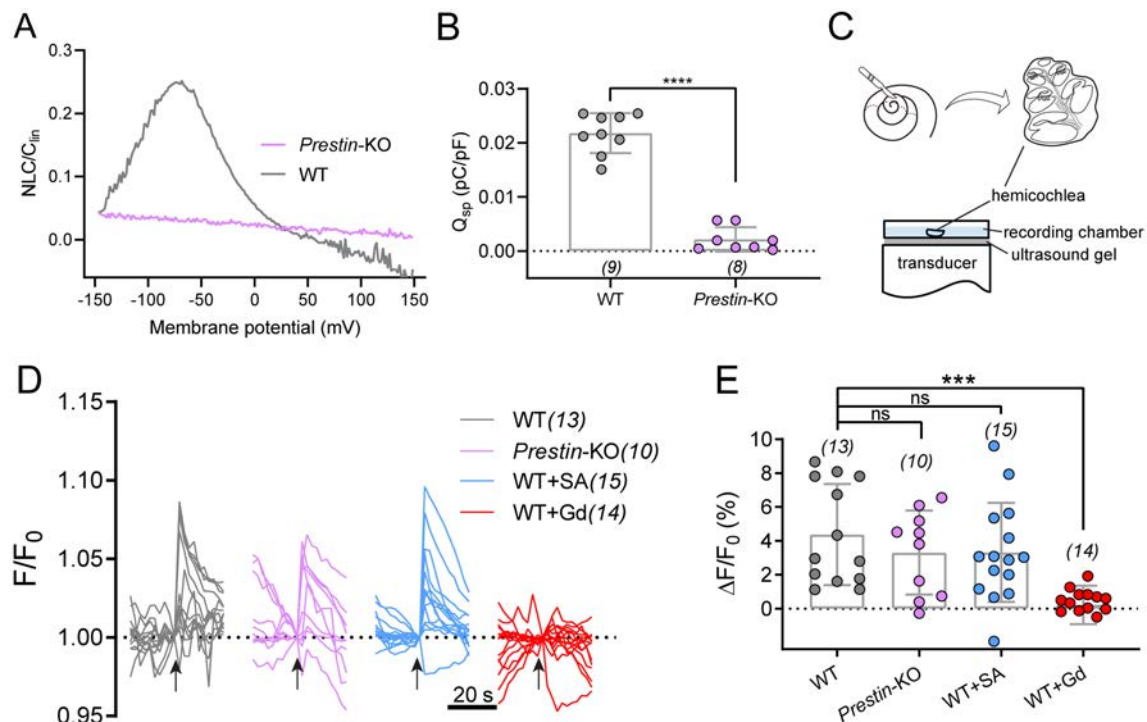


**Fig. 5** Ultrahigh-frequency-induced response in cochlear OHCs after Prestin deletion. **A** Nonlinear capacitance (NLC) in both *Prestin*-knockout and WT control OHCs. A representative example showing typical NLC pattern from a control OHC (gray). The NLC is absent in *Prestin*-knockout OHCs (purple). **B**  $Q_{sp}$  ( $Q_{max}/C_{lin}$ ) in *Prestin*-KO and WT OHCs. Unpaired *t*-test, \*\*\*\* $P < 0.0001$ . **C** Schematic showing preparation of hemicochlea and setup for ultrasonic transducer stimulation. An 80-kHz transducer is fixed underneath the recording dish with ultrasound gel. **D** Ultrasonic stimulation evokes  $Ca^{2+}$  responses in OHCs of cochlea preparations from control and *Prestin*-

KO mice. WT cochleae, *Prestin*-KO cochleae, WT cochleae treated with 10 mmol/L salicylic acid (WT+SA) were examined for the blockade of Prestin, and WT cochleae were treated with 10  $\mu$ mol/L  $Gd^{3+}$  (WT+Gd). Arrows indicate ultrasonic stimulation. The images were collected at 2-s intervals. **E** Quantification of the peak  $Ca^{2+}$  responses of OHCs calculated from recordings in (**D**). Kruskal-Wallis test: WT vs *Prestin*-KO,  $P > 0.9999$ ; WT vs WT+SA,  $P > 0.9999$ ; WT vs WT+Gd, \*\*\* $P = 0.0001$ . In (**B**) and (**E**), data are presented as the mean  $\pm$  SD, and N numbers are shown in panels.

was recorded in WT OHCs, *Prestin*-KO OHCs, and WT OHCs when exposed to salicylic acid perfusion (10 mmol/L), which blocks Prestin function (Fig. 5D, E) [41]. Furthermore, this response was abolished by treatment with the non-selective cation channel blocker,  $Gd^{3+}$  (10  $\mu$ mol/L) (Fig. 5D, E). In addition, low-frequency fluid-jet-induced hair-bundle mechanotransduction was preserved in *Prestin*-KO OHCs (Fig. S2). This result is similar to that seen in WT animals; inhibition by the mechanotransduction channel blocker dihydropyridine (Fig. S2). These results suggest that Prestin is not responsible for ultrahigh-frequency forward transduction.

### Salicylate Disrupts Low-frequency Hearing but not Ultrahigh-frequency Hearing

The OHC loss in *Prestin*-KO mice (Fig. 3) may compromise efforts to fully define the role of Prestin in ultrahigh-frequency hearing. To test this hypothesis more closely, we used pharmacological methods to acutely disrupt Prestin

function while maintaining OHC integrity. One-month-old WT mice were injected i.p. with salicylate to inhibit Prestin electromotility *in vivo* [42, 43]. The mABR thresholds were monitored every 10 min until 120 min after the thresholds stabilized, and were measured again on day 2 to test hearing recovery. Fig. 6A shows the mABR threshold-changes vs tone frequencies after salicylate injection. The threshold variation after salicylate injection is shown in Fig. 6B at a finer time resolution. Immediately after the injection, the 32–40 kHz thresholds were elevated. 70 min after injection, lower frequency thresholds (12–40 kHz) were elevated by  $\sim 20$  dB SPL and stabilized. In contrast, higher frequency thresholds (54–80 kHz) showed no significant change. The threshold elevation of 12–40 kHz recovered on the second day, indicating that the elevation was due to salicylate injection. These results indicate that the hearing sensitivity at lower frequencies (12–20 kHz) largely relies on Prestin electromotility, while sensitivity at higher frequencies (54–80 kHz) does not. It is interesting to note that 32–40 kHz thresholds showed different variation compared to lower and higher frequencies



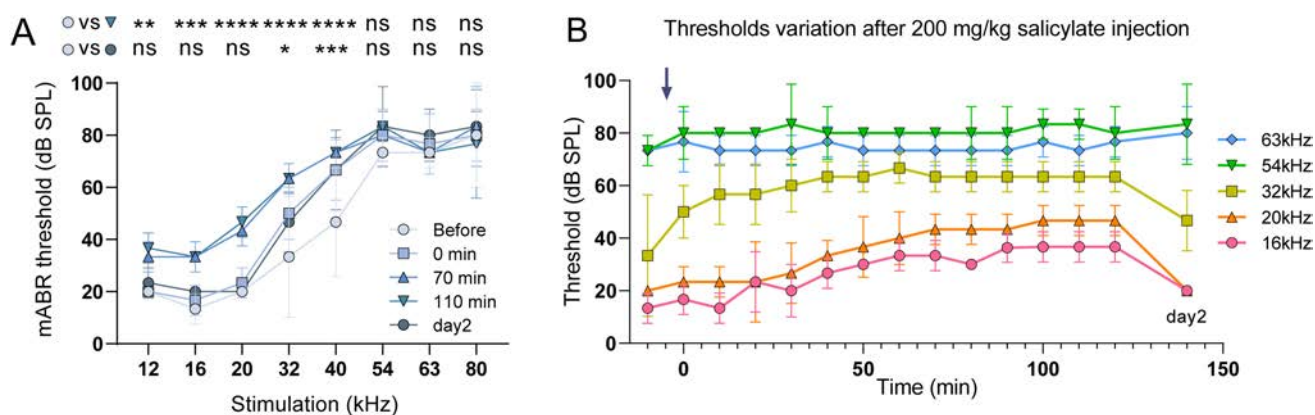


**Fig. 6** Salicylate disrupts low-frequency hearing but not ultrahigh-frequency hearing. **A** Pure-tone mABR thresholds change after 200 mg/kg salicylate i.p. injection in 1-month-old C57BL/6 mice. Thresholds before the injection, just after the injection (0 min), and at 70 min, 110 min, one day (day 2) post-injection are shown. Thresholds at 12–20 kHz show significant elevation after injection and stabilize at 70 min post-injection. This elevation recovered on the second day. In contrast, 54–80 kHz thresholds remained unchanged. Before vs 110 min, Dunnett test, 12 kHz,  $**P = 0.0041$ ; 16 kHz,

$***P = 0.0005$ ; 20 kHz,  $****P < 0.0001$ ; 32 kHz,  $****P < 0.0001$ ; 40 kHz,  $****P < 0.0001$ ; 54 kHz,  $P = 0.1380$ ; 63 kHz,  $P > 0.9999$ ; 80 kHz,  $P = 0.8995$ . Before vs day2, Dunnett test, 12 kHz,  $P = 0.8995$ ; 16 kHz,  $P = 0.4577$ ; 20 kHz,  $P > 0.9999$ ; 32 kHz,  $*P = 0.0280$ ; 40 kHz,  $***P = 0.0005$ ; 54 kHz,  $P = 0.1380$ ; 63 kHz,  $P = 0.4577$ ; 80 kHz,  $P = 0.8995$ . **B** Time-lapse mABR threshold variation after salicylate injection. The injection time was defined as 0 min (gray arrow). Data are presented as the mean  $\pm$  SD.  $n = 3$ .

(Fig. 6): the thresholds increased immediately after salicylate injection (0 min) and had not completely recovered to the untreated level by the second day. This may be due to salicylate-induced tinnitus, a known side-effect [44].

### Prestin-DTR Mice Used for Selective OHC Ablation

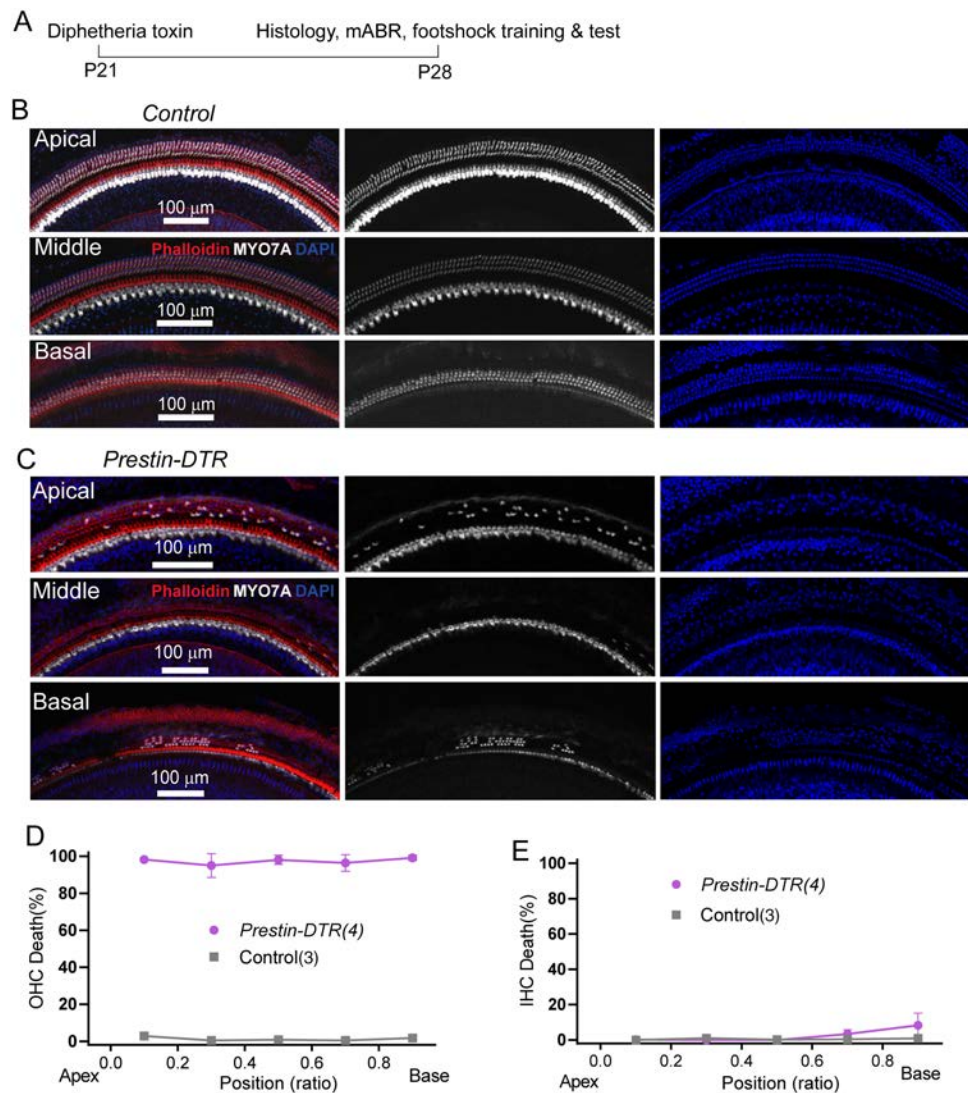
The previous experiments with *Prestin*-knockout mice exposed to salicylate were designed to examine *Prestin*'s role in ultrahigh-frequency hearing distinct from other OHC factors. Next, we investigated ultrahigh-frequency hearing in mice with OHC-specific ablation, using the DT/DTR system that has been applied successfully to kill cells of interest [45]. A *Prestin-P2A-DTR* knock-in mouse line was generated (*Prestin-DTR* mice), which exhibit *Prestin* promoter-driven DTR expression in its entirety, while preserving intact OHC *Prestin* expression [33]. After one injection of DT (20 ng/g) at postnatal day 21 (P21), the cochleae were dissected from heterozygous *Prestin-DTR*/+ and littermate (+/+) control mice, at P28 (Fig. 7A). Compared to the DT-injected controls in which all hair cells were intact (Fig. 7B, D, E), injected *Prestin-DTR*/+ mice showed OHC loss of  $\sim 90\%$  along the cochlear coils (Fig. 7C, D), in contrast to IHCs (Fig. 7C, E). This immunostaining result demonstrates the high efficiency of DT/DTR-driven OHC damage in *Prestin-DTR* mice.

### Ultrahigh-frequency Hearing Is Disrupted in *Prestin-DTR* Mice

Using a similar injection procedure (as in Fig. 7A), we measured the mABR thresholds in the two mouse groups. Compared with the control littermate mice in the 4–80 kHz frequency range (Fig. 8A, C), mice with DTR-induced OHC loss showed significant elevation of the mABR threshold (Fig. 8B, C). This suggested that reduction in OHCs resulted in severe hearing loss over the entire frequency range. mABR audiograms showed two kinds of threshold elevation profile (Fig. 8C). For 4–40 kHz, the experimental mice retained residual hearing with thresholds  $\sim 10$  dB below 90 dB SPL (Fig. 8C, green). In line with previous reports, residual hearing capacity in this frequency range relies on intact IHCs when amplification is uniquely disrupted by a lack of OHC-based eM [17]. On the other hand, for 40–80 kHz frequencies, there were no detectable mABR thresholds to 90 dB SPL in *Prestin-DTR*/+ mice (Fig. 8C, green). This indicates that there is more disrupted hearing sensitivity in ultrahigh frequencies. Moreover, it suggests that the loss of OHCs, rather than the lack of OHC eM, is the determining factor in abolishing ultrahigh-frequency sensitivity.

Next, sound-associated fear conditioning experiments were applied to assess hearing function in the *Prestin-DTR*/+ mice and controls. Figure 8D shows an example of locomotion in injected experimental mice and littermate controls. Freezing behavior was quantified as the percentage of time that the mice stopped moving as a function of the fright response (Fig. 8E, F). With 16-kHz 90-dB SPL

**Fig. 7** Cochlear OHC loss in DT-injected *Prestin-DTR* mice. **A** Schedule of DT injection and related tests. **B** Immunostaining image showing hair cell status in a control mouse at P28. Enlarged images show survival of OHCs in apical, middle, and basal locations. The cochlea is labeled with MYO7A antibody (white), phalloidin (red), and DAPI (blue). Note that most OHCs are lost but IHCs are not. Scale bar, 100  $\mu$ m. **C** Immunostaining image showing hair cell status in a *Prestin-DTR* mouse at P28. The staining protocol and display conditions are as in (B). Scale bar, 100  $\mu$ m. **D**, **E** Percentage loss of OHCs (D) and IHCs (E) at locations along the cochlea coil of P28 *Prestin-DTR* and control mice. N numbers are shown in panels.



cues, control mice exhibited significantly different freezing times pre- and post-cue (Fig. 8E, right). However, *Prestin-DTR* mice showed no learning deficits with 16-kHz 90-dB SPL cues since freezing was preserved after DTR-induced OHC knockout (Fig. 8E, left). The stimulus at 90 dB SPL was used because it was higher than the hearing threshold at 16 kHz as demonstrated by mABR testing (Fig. 8E). Freezing time was slightly reduced in DTR-induced OHC-knockout mice due to hearing loss. The freezing behavior of control mice in response to 63-kHz 90-dB SPL cues was well preserved (Fig. 8F, right). In contrast, OHC-knockout mice lacked this behavior, as their freezing times for both pre- and post-sound cues were near 0% (Fig. 8F, left). These results, which complement the mABR data and behavioral data from *Prestin-KO* mice (Figs 1, 2, and), show that the presence and functionality of OHCs are essential for ultrahigh-frequency sound detection.

## Discussion

In summary, we found that OHCs are essential for sensitive ultrahigh-frequency hearing. When OHCs were killed, either by DT/DTR-mediated cell toxicity in 1-month-old *Prestin-DTR* mice (Fig. 7C, D), or by extensive degeneration due to removal of Prestin in 2-month-old *Prestin-KO* mice (Fig. 3A, D), ultrahigh-frequency hearing (>40 kHz) was completely abolished. Our data suggest that Prestin is not essential for ultrahigh-frequency hearing, since ultrahigh-frequency hearing in 3-week-old *Prestin-KO* mice was preserved when Prestin was absent but OHCs were still present. These conclusions were supported by mABR recordings (Figs 1, 4, and 8A–C) and freezing behavior tests (Figs 2 and 8D–F).

By providing locally enhanced amplification, Prestin appears to improve frequency tuning [10, 16, 30]. This raises the question of how wide a hearing frequency range



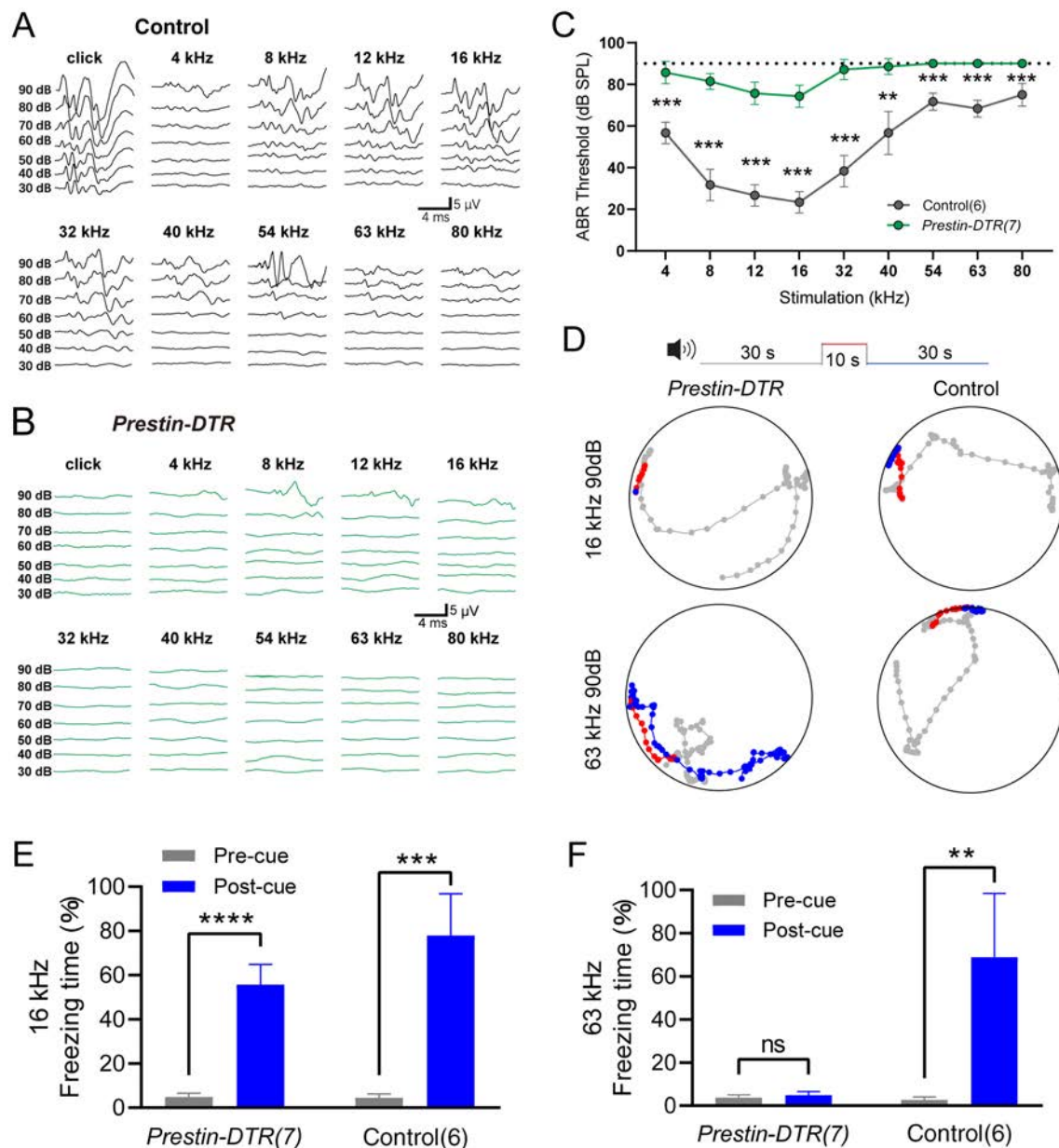


**Fig. 8** mABR measurements and acoustically-associative freezing behavior of DT-injected *Prestin-DTR* mice. **A** Representative example of mABR signals in an injected littermate control mouse. **B** Representative example of mABR signals in an injected *Prestin-DTR* mouse. **C** mABR thresholds in the *Prestin-DTR* mice (green) and control littermate mice (without *Prestin-DTR* expression, dark gray). All mice were injected with DT. Note that the injected *Prestin-DTR* mice show no detectable mABR response at 90 dB SPL at frequencies from 54 kHz to 80 kHz. Control vs injected *Prestin-DTR*, Mann-Whitney test,  $**P = 0.0012$  at 40 kHz,  $***P = 0.0006$  at other frequencies. **D** Representative examples of locomotion of control and *Prestin-DTR* mice before (gray, 30 s), during

(red, 10 s), and after (blue, 30 s) the pure-tone sound cue at 90 dB SPL. The mice had been trained to pair either the 16-kHz or the 63-kHz cue with the foot-shock-induced freezing. Dots indicate the location of a mouse every 0.5 s. Injected littermate mice were used as controls. **E**, **F** Percentage freezing time with the 16-kHz cue (**E**) or the 63-kHz cue (**F**). Pre-cue vs Post-cue, paired *t*-test, *Prestin-DTR* mice at 16 kHz,  $t_6 = 13.81$ ,  $****P < 0.0001$ ; Control mice at 16 kHz,  $t_5 = 9.774$ ,  $***P = 0.0002$ ; *Prestin-DTR* mice at 63 kHz,  $t_8 = 0.1187$ ,  $P = 0.9094$ ; Control mice at 63 kHz,  $t_5 = 5.386$ ,  $**P = 0.003$ . In (**C**), (**E**), and (**F**), data are presented as the mean  $\pm$  SD. N numbers are shown in panels. All the mice were  $\sim 1$  month old.

*Prestin* supports. Compound action potential (CAP) recordings have been used to probe the frequency-sensitivity in *Prestin*-KO mice [10, 46]. However, in these experiments, older mice (30–58 days) were used, and demonstrated a

complete CAP threshold shift from a low- to higher-frequency (45 kHz) boundary of recordings. There is extensive OHC loss in mice older than 1 month [40], and two studies have shown further evidence of hearing

sensitivity and frequency selectivity in *Prestin*-KO mice (17–21 days old) [16, 30]. Interestingly, in *Prestin*-KO mice, the CAP thresholds were elevated at all frequencies from low to high (up to 70 kHz) [30], and basilar membrane displacement measured by interferometry showed that the tuning characteristic frequency shifted from 60 kHz to 45 kHz [16, 30]. Subsequently, data from *Prestin-499* mice that carry a motility-defect V499G point mutation, showed that *Prestin-499* mice completely lost sharp frequency tuning. This effect is similar to that reported in post-mortem studies [30], which argue that knockout of Prestin affects both the stiffness of OHCs and organ of Corti mechanics.

Furthermore, with phylogenetic analysis, Prestin shows an evolutionary correlation with echolocation [25–27, 29, 47]. The resulting membrane-conformation of prestin appears to be linked to its NLC function, which may participate in high-frequency hearing. In contrast, the combined experimental data from our investigations of *Prestin-DTR* mice and *Prestin*-KO mice provided evidence that distinguishes the role of Prestin from that of OHCs in frequency selectivity. For frequencies between 4 kHz and 32 kHz, 3-week- and 1-month-old *Prestin*-KO mice had audiometric thresholds and behavioral test results similar to 2-month-old *Prestin*-KO mice. This suggests that Prestin is essential for low-frequency hearing. However, at frequency ranges beyond 32 kHz, 3-week- and 1-month-old *Prestin*-KO mice showed hearing sensitivity similar to control mice, and this disappeared 2 months after OHCs died, indicating that OHC maintenance, not Prestin, is key to ultrahigh-frequency hearing.

*In vivo* recordings measuring the motion of the organ of Corti have provided insight into frequency selectivity in mice. However, due to *in vivo* experimental limitations, the cycle-by-cycle response of OHCs to high-frequency stimuli is hard to determine. Some authors have proposed that this is not a necessary requirement for the cochlear amplifier to operate [48]. A more recent study of organ of Corti motion patterns from the apical cochlea in mice show that the cycle-by-cycle response is enhanced by OHCs at frequencies <10 kHz, while this enhancement is reduced in *Prestin 499* mice [49]. Yet, it is still questionable how high the cut-off frequency of Prestin-based eM is supported by its molecular properties. Before Prestin was cloned [9], eM in guinea-pig OHCs was found to be responsive to stimulus frequencies beyond 79 kHz [23], or limited to the 22-kHz boundary [21]. However, these results were made in microchamber preparations that bypassed membrane filtering problems [50–52]. A whole-cell patch capacitance measurement approach revealed that the limiting frequency is near 25 kHz [22].

*In vitro* measurements of OHC electromotility and membrane filtering properties were made to bridge the gap

between the experimental findings and the presumed theoretical barrier. By introducing the intrinsic piezoelectric property, it has been shown that the resistance–capacitance (RC) time constant is not a problem for high-frequency performance [53]. The RC time constant has been probed by assays ranging from an extracellularly-based cross-membrane voltage stimulus [21], to a robust  $K^+$  current that drops membrane resistance,  $R_m$  [54], and subsurface cisternae resistance [55, 56]. It has been suggested that OHCs exhibiting a lower *in vivo* resting  $R_m$  and activating more ion channels, could, in theory, improve the RC time constant of the cell membrane [57]. However, NLC, the signature property of Prestin, seems to inhibit facilitation of the high-frequency eM response because peak NLC (nearly double the linear capacitance) slows the membrane time constant [56, 58, 59]. Recently, the membrane filtering issue has been revisited by simultaneous measurement of motility and NLC using both microchamber and whole-cell patch clamping techniques [19, 20]. With appropriate compensation of significant series resistance, the most optimistic estimation of the frequency-following capability for OHC electromotility does not exceed 16 kHz [60]. This is far below the known high-frequency hearing range in mammals, including humans. Due to the capacitive nature of the Prestin response, in order for eM to follow the cycle-by-cycle motion of the basilar membrane, the operation of Prestin needs to shift off the peak of the NLC curve. This shift is necessary to gain a slightly faster time constant at the expense of a lower contribution to mechanical input to organ of Corti movement [60, 61].

It should be noted that receptor potentials are driven by the opening and closing of the mechano-electrical transduction (MET) channels located at the tips of the stereocilia [62, 63]. Although MET channels have a super-fast activation time constant that is shorter than 10  $\mu$ s (>100 kHz) [64], whether the bundle as a whole can overcome mechanical obstacles such as the viscoelastic drag of the fluid, and whether tectorial membrane coupling allows high-speed cyclical motion, remains an open question. These factors alone may exclude the possibility of Prestin-based eM in a cycle-by-cycle manner during ultrahigh-frequency stimulation. Thus, while benefiting from position-derived frequency selectivity, high-frequency OHCs may not require cycle-by-cycle motility. Rather, by using mechanics-based OHC-DC (Dieter's Cell) movement, or the mechanical properties inferred from the *in vivo* measurements taken by Vavakou *et al.*, high-frequency OHCs may serve as modulators for sound-evoked vibration [48].

In conclusion, our study has revealed that Prestin may not be an essential element for hearing at ultrahigh frequencies, the major frequency range for auditory

communication in mice. Prestin enhances the hearing sensitivity at low frequencies but is less likely to be an important biological factor in high-frequency hearing. Combined with our previous work [31], we speculate that the mechanosensitive channel PIEZO2 may acquire the ultrasonic energy and vibrate the cuticular plate, which further orchestrates the MET channel opening in hair bundles. Thus, Prestin enhances the sensitivity to low-to-middle-high frequencies by endowing OHCs with somatic motility, while PIEZO2 contributes to the detection of ultrahigh frequencies by vibrating stereocilia. Future work should recruit *in vivo* approaches, such as interferometry, to study organ of Corti motion patterns in more basal coil locations. This configuration would directly interrogate OHC motility across the cochlear coil upon hearing ultrahigh frequencies. Other genetically-engineered mouse models may be used, such as *Prestin-499* and conditional knockout of *Prestin*. For example, conditional knockout mice provide an excellent opportunity to examine the effect of Prestin deletion in adult animals that are known to have well-developed cochlear structure and the associated mechanical properties.

**Acknowledgements** We thank Drs. Wendol Williams, Joseph Santos-Sacchi, and Dhasakumar Navaratnam for critical reading and comments, and Dr. Wendol Williams for editing the manuscript, the Imaging Core Facility, Technology Center for Protein Sciences at Tsinghua University for assistance using imaging instruments and software, Dr. Qiuying Chen of Dr. Guoxuan Lian's laboratory at the Institute of Acoustics, Chinese Academy of Sciences for manufacturing the ultrasonic transducers, and Dr. Guangzhen Xing at the National Institute of Metrology for calibrating the ultrasonic transducers and the high-frequency amplifier. This work was supported by the National Natural Science Foundation of China (31522025, 31571080, 81873703, 81770995, and 31861163003), Beijing Municipal Science and Technology Commission (Z181100001518001), and a startup fund from the Tsinghua-Peking Center for Life Sciences to W.X.. W.X. is a CIBR cooperative investigator (2020-NKX-XM-04) funded by the Open Collaborative Research Program of Chinese Institute for Brain Research; National Key Research and Development Project (2018YFC1003003); The Postdoctoral International Exchange Program (Talent-Introduction Program); and the Shanghai Key Laboratory of Translational Medicine on Ear and Nose Diseases (14DZ2260300).

**Conflict of interests** The authors declare no competing interest.

## References

- Hopp SL, Owren MJ, Evans CS. Animal Acoustic Communication[M]. Berlin, Heidelberg: Springer Berlin Heidelberg, 1998.
- Fettiplace R, Hackney CM. The sensory and motor roles of auditory hair cells. *Nat Rev Neurosci* 2006, 7: 19–29.
- Ashmore J, Avan P, Brownell WE, Dallos P, Dierkes K, Fettiplace R. The remarkable cochlear amplifier. *Hear Res* 2010, 266: 1–17.
- Hudspeth AJ. Integrating the active process of hair cells with cochlear function. *Nat Rev Neurosci* 2014, 15: 600–614.
- Robles L, Ruggero MA. Mechanics of the mammalian cochlea. *Physiol Rev* 2001, 81: 1305–1352.
- Ashmore J. Outer hair cells and electromotility. *Cold Spring Harb Perspect Med* 2019, 9: a033522.
- Brownell WE, Bader CR, Bertrand D, de Ribaupierre Y. Evoked mechanical responses of isolated cochlear outer hair cells. *Science* 1985, 227: 194–196.
- Ashmore JF. A fast motile response in guinea-pig outer hair cells: The cellular basis of the cochlear amplifier. *J Physiol* 1987, 388: 323–347.
- Zheng J, Shen WX, He DZZ, Long KB, Madison LD, Dallos P. Prestin is the motor protein of cochlear outer hair cells. *Nature* 2000, 405: 149–155.
- Dallos P, Wu XD, Cheatham MA, Gao JG, Zheng J, Anderson CT, *et al.* Prestin-based outer hair cell motility is necessary for mammalian cochlear amplification. *Neuron* 2008, 58: 333–339.
- Schaechinger TJ, Gorbunov D, Halaszovich CR, Moser T, Kügler S, Fakler B, *et al.* A synthetic prestin reveals protein domains and molecular operation of outer hair cell piezoelectricity. *EMBO J* 2011, 30: 2793–2804.
- Yamashita T, Hakizimana P, Wu S, Hassan A, Jacob S, Temirov J, *et al.* Outer hair cell lateral wall structure constrains the mobility of plasma membrane proteins. *PLoS Genet* 2015, 11: e1005500.
- Bavi N, Clark MD, Contreras GF, Shen R, Reddy BG, Milewski W, *et al.* The conformational cycle of prestin underlies outer-hair cell electromotility. *Nature* 2021, 600: 553–558.
- Butan C, Song Q, Bai J-P, Tan WJT, Navaratnam D, Santos-Sacchi J. 2021.
- Ge JP, Elferich J, Dehghani-Ghahnaviye S, Zhao ZY, Meadows M, von Gersdorff H, *et al.* Molecular mechanism of prestin electromotive signal amplification. *Cell* 2021, 184: 4669–4679.e13.
- Mellado Lagarde MM, Drexel M, Lukashkin AN, Zuo J, Russell IJ. Prestin's role in cochlear frequency tuning and transmission of mechanical responses to neural excitation. *Curr Biol* 2008, 18: 200–202.
- Liberman MC, Gao JG, He DZZ, Wu XD, Jia SP, Zuo J. Prestin is required for electromotility of the outer hair cell and for the cochlear amplifier. *Nature* 2002, 419: 300–304.
- Santos-Sacchi J. Reversible inhibition of voltage-dependent outer hair cell motility and capacitance. *J Neurosci* 1991, 11: 3096–3110.
- Santos-Sacchi J. The speed limit of outer hair cell electromechanical activity. *HNO* 2019, 67: 159–164.
- Santos-Sacchi J, Tan W. The frequency response of outer hair cell voltage-dependent motility is limited by kinetics of prestin. *J Neurosci* 2018, 38: 5495–5506.
- Dallos P, Evans BN. High-frequency motility of outer hair cells and the cochlear amplifier. *Science* 1995, 267: 2006–2009.
- Gale JE, Ashmore JF. An intrinsic frequency limit to the cochlear amplifier. *Nature* 1997, 389: 63–66.
- Frank G, Hemmert W, Gummer AW. Limiting dynamics of high-frequency electromechanical transduction of outer hair cells. *Proc Natl Acad Sci USA* 1999, 96: 4420–4425.
- Portfors CV, Perkel DJ. The role of ultrasonic vocalizations in mouse communication. *Curr Opin Neurobiol* 2014, 28: 115–120.
- Li Y, Liu Z, Shi P, Zhang JZ. The hearing gene Prestin unites echolocating bats and whales. *Curr Biol* 2010, 20: R55–R56.
- Liu Y, Rossiter SJ, Han XQ, Cotton JA, Zhang SY. Cetaceans on a molecular fast track to ultrasonic hearing. *Curr Biol* 2010, 20: 1834–1839.
- Liu Z, Qi FY, Xu DM, Zhou X, Shi P. Genomic and functional evidence reveals molecular insights into the origin of echolocation in whales. *Sci Adv* 2018, 4: eaat8821.

28. Li G, Wang JH, Rossiter SJ, Jones G, Cotton JA, Zhang SY. The hearing gene Prestin reunites echolocating bats. *Proc Natl Acad Sci U S A* 2008, 105: 13959–13964.
29. Parker J, Tsagkogeorga G, Cotton JA, Liu Y, Provero P, Stupka E, *et al.* Genome-wide signatures of convergent evolution in echolocating mammals. *Nature* 2013, 502: 228–231.
30. Weddell TD, Mellado-Lagarde M, Lukashkina VA, Lukashkin AN, Zuo J, Russell IJ. Prestin links extrinsic tuning to neural excitation in the mammalian cochlea. *Curr Biol* 2011, 21: R682–R683.
31. Li J, Liu S, Song CM, Hu Q, Zhao ZK, Deng TT, *et al.* PIEZO2 mediates ultrasonic hearing *via* cochlear outer hair cells in mice. *Proc Natl Acad Sci U S A* 2021, 118: e2101207118.
32. Zhang H, Pan H, Zhou CY, Wei Y, Ying WQ, Li ST, *et al.* Simultaneous zygotic inactivation of multiple genes in mouse through CRISPR/Cas9-mediated base editing. *Development* 2018, 145: dev168906.
33. Sun SH, Li ST, Luo ZN, Ren MH, He SJ, Wang GQ, *et al.* Dual expression of Atoh1 and Ikzf2 promotes transformation of adult cochlear supporting cells into outer hair cells. *Elife* 2021, 10: e66547.
34. Romero S, Hight AE, Clayton KK, Resnik J, Williamson RS, Hancock KE, *et al.* Cellular and widefield imaging of sound frequency organization in primary and higher order fields of the mouse auditory cortex. *Cereb Cortex* 2020, 30: 1603–1622.
35. Garcia-Lazaro JA, Shepard KN, Miranda JA, Liu RC, Lesica NA. An overrepresentation of high frequencies in the mouse inferior colliculus supports the processing of ultrasonic vocalizations. *PLoS One* 2015, 10: e0133251.
36. Edge RM, Evans BN, Pearce M, Richter CP, Hu X, Dallos P. Morphology of the unfixed cochlea. *Hear Res* 1998, 124: 1–16.
37. Hu X, Evans BN, Dallos P. Direct visualization of organ of corti kinematics in a hemicochlea. *J Neurophysiol* 1999, 82: 2798–2807.
38. Edelstein A, Amodaj N, Hoover K, Vale R, Stuurman N. Computer control of microscopes using µManager. *Curr Protoc Mol Biol* 2010, Chapter 14: Unit14.20.
39. Liu S, Wang SF, Zou LZ, Li J, Song CM, Chen JF, *et al.* TMC1 is an essential component of a leak channel that modulates tonotopy and excitability of auditory hair cells in mice. *Elife* 2019, 8: e47441.
40. Wu XD, Gao JG, Guo YK, Zuo J. Hearing threshold elevation precedes hair-cell loss in prestin knockout mice. *Mol Brain Res* 2004, 126: 30–37.
41. Santos-Sacchi J. Control of mammalian cochlear amplification by chloride anions. *J Neurosci* 2006, 26: 3992–3998.
42. Oliver D, He DZ, Klöcker N, Ludwig J, Schulte U, Waldegger S, *et al.* Intracellular anions as the voltage sensor of prestin, the outer hair cell motor protein. *Science* 2001, 292: 2340–2343.
43. Stypulkowski PH. Mechanisms of salicylate ototoxicity. *Hear Res* 1990, 46: 113–145.
44. Lobarinas E, Sun W, Cushing R, Salvi R. A novel behavioral paradigm for assessing tinnitus using schedule-induced polydipsia avoidance conditioning (SIP-AC). *Hear Res* 2004, 190: 109–114.
45. Golub JS, Tong L, Nguyen TB, Hume CR, Palmiter RD, Rubel EW, *et al.* Hair cell replacement in adult mouse utricles after targeted ablation of hair cells with diphtheria toxin. *J Neurosci* 2012, 32: 15093–15105.
46. Cheatham MA, Huynh KH, Gao J, Zuo J, Dallos P. Cochlear function in Prestin knockout mice. *J Physiol* 2004, 560: 821–830.
47. Marcovitz A, Turakhia Y, Chen HI, Gloudemans M, Braun BA, Wang HQ, *et al.* A functional enrichment test for molecular convergent evolution finds a clear protein-coding signal in echolocating bats and whales. *Proc Natl Acad Sci U S A* 2019, 116: 21094–21103.
48. Vavakou A, Cooper NP, van der Heijden M. The frequency limit of outer hair cell motility measured *in vivo*. *Elife* 2019, 8: e47667.
49. Dewey JB, Altoè A, Shera CA, Applegate BE, Oghalai JS. Cochlear outer hair cell electromotility enhances organ of Corti motion on a cycle-by-cycle basis at high frequencies *in vivo*. *Proc Natl Acad Sci U S A* 2021, 118: e2025206118.
50. Santos-Sacchi J. On the frequency limit and phase of outer hair cell motility: Effects of the membrane filter. *J Neurosci* 1992, 12: 1906–1916.
51. Housley GD, Ashmore JF. Ionic currents of outer hair cells isolated from the Guinea-pig cochlea. *J Physiol* 1992, 448: 73–98.
52. Ashmore J. Pushing the envelope of sound. *Neuron* 2011, 70: 1021–1022.
53. Spector AA, Brownell WE, Popel AS. Effect of outer hair cell piezoelectricity on high-frequency receptor potentials. *J Acoust Soc Am* 2003, 113: 453–461.
54. Ospeck M, Dong XX, Iwasa KH. Limiting frequency of the cochlear amplifier based on electromotility of outer hair cells. *Biophys J* 2003, 84: 739–749.
55. Halter JA, Kruger RP, Yium MJ, Brownell WE. The influence of the subsurface cisterna on the electrical properties of the outer hair cell. *Neuroreport* 1997, 8: 2517–2521.
56. Song L, Santos-Sacchi J. An electrical inspection of the subsurface cisternae of the outer hair cell. *Biophys J* 2015, 108: 568–577.
57. Johnson SL, Beurg M, Marcotti W, Fettiplace R. Prestin-driven cochlear amplification is not limited by the outer hair cell membrane time constant. *Neuron* 2011, 70: 1143–1154.
58. Song L, Santos-Sacchi J. Disparities in voltage-sensor charge and electromotility imply slow chloride-driven state transitions in the solute carrier SLC26a5. *Proc Natl Acad Sci U S A* 2013, 110: 3883–3888.
59. Santos-Sacchi J, Iwasa KH, Tan W. Outer hair cell electromotility is low-pass filtered relative to the molecular conformational changes that produce nonlinear capacitance. *J Gen Physiol* 2019, 151: 1369–1385.
60. Santos-Sacchi J, Tan W. Voltage does not drive prestin (SLC26a5) electro-mechanical activity at high frequencies where cochlear amplification is best. *iScience* 2019, 22: 392–399.
61. Santos-Sacchi J, Tan W. Complex nonlinear capacitance in outer hair cell macro-patches: effects of membrane tension. *Sci Rep* 2020, 10: 6222.
62. Beurg M, Fettiplace R, Nam JH, Ricci AJ. Localization of inner hair cell mechanotransducer channels using high-speed calcium imaging. *Nat Neurosci* 2009, 12: 553–558.
63. Russell IJ, Sellick PM. Tuning properties of cochlear hair cells. *Nature* 1977, 267: 858–860.
64. Peng AW, Ricci AJ. Glass probe stimulation of hair cell stereocilia. *Methods Mol Biol* 2016, 1427: 487–500.

# Cross-Modal Interaction and Integration Through Stimulus-Specific Adaptation in the Thalamic Reticular Nucleus of Rats

Yumei Gong<sup>1,2,3</sup> · Yuying Zhai<sup>1</sup> · Xinyu Du<sup>1</sup> · Peirun Song<sup>1,2</sup> · Haoxuan Xu<sup>1,2</sup> · Qichen Zhang<sup>1,2</sup> · Xiongjie Yu<sup>1,2,3</sup>

Received: 21 August 2021 / Accepted: 11 November 2021 / Published online: 25 February 2022  
© Center for Excellence in Brain Science and Intelligence Technology, Chinese Academy of Sciences 2022

**Abstract** Stimulus-specific adaptation (SSA), defined as a decrease in responses to a common stimulus that only partially generalizes to other rare stimuli, is a widespread phenomenon in the brain that is believed to be related to novelty detection. Although cross-modal sensory processing is also a widespread phenomenon, the interaction between the two phenomena is not well understood. In this study, the thalamic reticular nucleus (TRN), which is regarded as a hub of the attentional system that contains multi-modal neurons, was investigated. The results showed that SSA existed in an interactive oddball stimulation, which mimics stimulation changes from one modality to another. In the bimodal integration, SSA to bimodal stimulation was stronger than to visual stimulation alone but similar to auditory stimulation alone, which indicated a limited integrative effect. Collectively, the present results provide evidence for independent cross-modal processing in bimodal TRN neurons.

**Keywords** Stimulus-specific adaptation · Regularity · Novelty detection · Thalamic reticular nucleus · Cross-modal

## Introduction

Stimulus-specific adaptation (SSA) is the process whereby a neuron responds better to a rare stimulus than to the same stimulus presented frequently; this is regarded as one of the mechanisms behind novelty and change detection [1–3]. SSA is common in the brain and has also been investigated in the auditory [4–7], visual [8], and somatosensory [9] pathways. However, only a few studies have included more than one modality [10, 11]. Cross-modal interaction and integration are common in daily life, since the everyday environment has auditory and visual information that appears alternately or synchronously. However, it is unclear how the brain interacts with alternating bimodal stimulation or integrates synchronous bimodal stimulation through SSA. Besides, no study has assessed the cross-modal interactive effect in SSA when the auditory or visual stimulation is separately presented, and thus it is unknown how the brain responds to the modal stimulation change. Visual and auditory information is usually integrated in the brain of humans and other animals to form the perception of unitary cross-modal events when the auditory and visual stimulations are synchronously presented [12, 13]. However, it is also unclear whether the cross-modal integration benefits novelty detection.

Reches *et al.* explored the modulatory effect of SSA in the forebrain of the barn owl [10], where neurons respond to visual rather than auditory stimulation, and found that bimodal (visual and auditory together) deviant stimuli evoke more robust responses than visual stimuli alone,

Yumei Gong and Yuying Zhai contributed equally to this work.

✉ Xiongjie Yu  
yuxiongji@zju.edu.cn

<sup>1</sup> Department of Neurology of the Second Affiliated Hospital of Zhejiang University School of Medicine, Interdisciplinary Institute of Neuroscience and Technology, College of Biomedical Engineering and Instrument Science, Zhejiang University, Hangzhou 310029, China

<sup>2</sup> Key Laboratory for Biomedical Engineering of Ministry of Education, Zhejiang University, Hangzhou 310027, China

<sup>3</sup> Zhejiang Provincial Key Laboratory of Cardio-Cerebral Vascular Detection Technology and Medicinal Effectiveness Appraisal, Zhejiang University, Hangzhou 310027, China



suggesting a cross-modal modulatory effect in SSA. Therefore, it is important to investigate truly bimodal neurons that respond to each mode of stimulation, to better understand the cross-modal effect during interaction and integration in SSA. However, such research is extremely limited. Unlike neurons in the forebrain of the barn owl, the multisensory neurons in the thalamic reticular nucleus (TRN) respond robustly to visual and auditory stimuli [14].

In this study, we used the TRN to investigate the cross-modal effect in SSA for the following reasons. First, the TRN is a good candidate to investigate the relationship between attention and novelty detection since it is strategically located between the thalamus and cortex, and both thalamocortical and corticothalamic projections pass through to give collateral branches to the TRN [15]. The TRN consists of GABAergic neurons, which project back only to the dorsal thalamus [16]. The TRN is the gatekeeper for information flow from the thalamus to the cortex, and it plays a crucial role in attention due to its anatomical location [17, 18]. Therefore, the relationship between attention and novelty detection deserves exploration. Second, multimodal neurons may play roles in the TRN. A mapping study of sensory responses in the TRN has shown that a subset of TRN cells contains multimodal sensory neurons [14]. However, the functional significance of these neurons is unknown. Third, neurophysiological properties suggest that SSA exists in multimodal TRN neurons. TRN neurons in the auditory sector have slow recovery and strong adaptation to repetitive identical stimuli [19]. Moreover, the adaptation is stimulus-specific in the frequency [20] and spatial domains [21], and thus a strong SSA may be present in multimodal TRN neurons. Taken together, the TRN provides an exciting opportunity to investigate the cross-modal effect in SSA.

## Materials and Methods

### Animals

We used young adult male Wistar rats (260–330 g; 6–8 weeks old) with clean external ears. Electrophysiological data were collected from ~40 rats. Animals were housed three per cage in a temperature- ( $24 \pm 1^\circ\text{C}$ ) and humidity- (40%–60%) controlled facility with a 12-h light/12-h dark cycle (lights on from 08:00 to 20:00). They had free access to food and water. All procedures were approved by the Animal Care and Use Committee of Zhejiang University and were performed according to the National Institutes of Health Guide for the Care and Use of Laboratory Animals.

The rats were anesthetized with urethane (1.35 g/kg body weight; 20% solution, i.p.). The anesthesia level was monitored through pedal-withdrawal and corneal reflexes,

and the rats were kept stable using supplementary doses of urethane (0.5 g/kg body weight, per hour) as needed. Atropine sulfate (0.05 mg/kg body weight, s.c.) was administered 15 min before anesthesia to suppress tracheal secretions. A local anesthetic (xylocaine, 2%) was liberally applied to reduce the pain during surgery. The body temperature was maintained at  $37\text{--}38^\circ\text{C}$  using a closed-loop heating system controlled by a rectal probe (FHC, Bowdoin, USA) throughout the experiments.

The rats underwent surgery as previously described [19, 20, 22, 23]. Briefly, the rat was mounted on a stereotaxic apparatus (Narishige SR-6R, Tokyo, Japan) after anesthesia induction. Then the dorsal surface of the skull was exposed. The connective tissue was removed and the bone surface was cleaned with saline and alcohol. A metal head-post was then implanted in the skull, and the rat was removed from the stereotaxic device. The rat was then held by the head post and exposed to a free-field acoustic environment. A craniotomy was made over the left hemisphere during each experiment to give dorsoventral access to the auditory sector of the TRN.

### Recording

Recordings were obtained using 2–7 M $\Omega$  tungsten micro-electrodes (Frederick Haer & Co., Bowdoinham, USA) in anesthetized rats in a sound-proof room. The electrode was inserted into TRN based on a rat brain atlas [24] and remotely controlled using a microdrive (Narishige MO-10, Tokyo, Japan) located outside the sound-proof chamber. A Tucker–Davis Technologies (TDT, Alachua, USA) OpenEx system was used to record the signal (sampling rate, 25 kHz, bandpass filter, 300–5000 Hz), then stored for further offline analysis in MatLab (MathWorks, Natick, USA).

### Anatomical Confirmation

An electrolytic lesion was made at the end of each experiment to verify coordinate accuracy. The rats were given an overdose of sodium pentobarbital (150 mg per rat i.p.; 30 mg/mL), then were transcardially perfused using 0.9% saline and 4% paraformaldehyde in 0.1 mol/L phosphate buffer (pH 7.3). The brain was removed after perfusion, then placed in 30% sucrose in 0.1 mol/L phosphate buffer. Consecutive coronal sections were cut at 50  $\mu\text{m}$  around the recording location, then Nissl stained. The Nissl image was overlaid with electrode tracks using the electrolytic lesions for guidance.

## Stimulus Presentation

A computer-controlled TDT Auditory Workstation (System 3) was used to generate digital acoustic stimuli (100 kHz sampling rate) and to deliver the sound through magnetic speakers (MF1, TDT, Alachua, USA). The sound pressure of the speaker was calibrated with a 1/4" condenser microphone (Brüel & Kjær 4954, Nærum, Denmark) and a PHOTON/RT analyzer (Brüel & Kjær), then set to 65 dB. Visual stimuli were generated using a single white LED (diameter: 4 mm) triggered by the TDT system. The following stimuli were used when a single bimodal TRN neuron was isolated.

### Single-Modal Stimulation

The noise burst or light stimulation was generated using a speaker or LED, both of which were located at the same site, 45° from the midline of the rat and contralateral to the recording side in the rat horizontal plane. The 100 ms noise burst (or light) was generated at a 1.2 s interstimulus interval (ISI) with 30 repetitions. A TRN neuron was defined as bimodal when it showed a significant response to both noise burst and light stimulation (200 ms response window before *vs* after stimulus onset; Wilcoxon's matched-pairs test,  $P < 0.01$ ).

### Interactive Cross-Modal Oddball

The interactive cross-modal oddball paradigm was presented after the neuronal responses to the noise and light of single-modal stimulation were recorded. The interactive cross-modal oddball had two sets of stimuli. In one set, the noise was presented five times as the standard stimulus followed by a single light stimulus as a deviant stimulus (Fig. 1A). This block (five standard stimuli followed by one deviant stimulus) was repeated 16 times at 200 ms ISI. In the other set, the standard and the deviant stimuli were reversed. These two sets were randomly presented five times each. The interactive cross-modal oddball was designed to investigate the interactive effect in SSA when the stimulation switches from one mode to the other.

### Integrative Cross-Modal Oddball

Two auditory, two visual, and two bimodal stimuli were used. The two visual stimuli only had a different azimuth of the horizontal position, 45° from the midline of the rat in the horizontal plane. The two auditory stimuli were set to match the locations of the visual stimuli. The visual and auditory stimuli at the same location were simultaneously presented in the bimodal condition. The oddball had six sets: two auditory, two visual, and two congruent bimodal

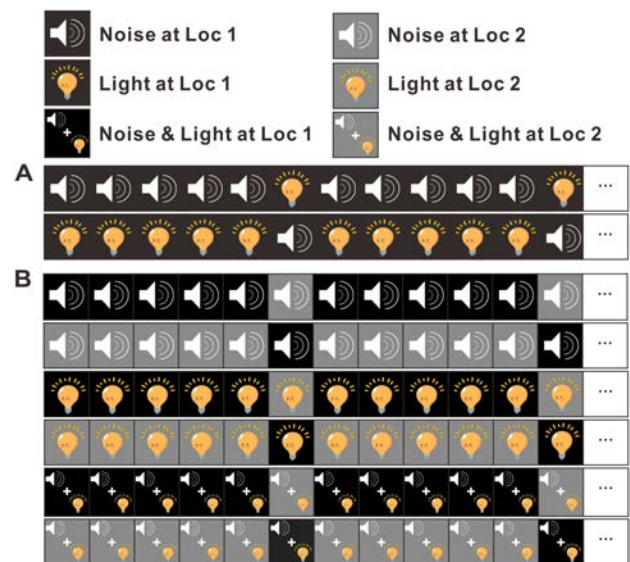


**Fig. 1** Experimental setup. **A** Each row represents a sample sequence from a single oddball block. The background color of the box represents location of the stimulus [black: location 1 (contralateral site, Loc 1); grey: location 2 (ipsilateral site, Loc 2)]. The two blocks show the interactive cross-modal oddball and are randomly presented; the sound and light stimuli are only presented at Loc 1. **B** The six rows represent the integrative cross-modal oddball and are randomly presented. Each block contains 96 successive stimuli with a 200-ms interstimulus interval and a 4.8 s period of silence after the last stimulus.

sets (Fig. 1B). Each set consisted of a sequence of 96 stimuli [(5 standard stimuli + 1 deviant stimulus)  $\times$  16] with a stimulus duration of 100 ms and an ISI of 200 ms. The standard stimulus in each block was presented five times followed by a single deviant stimulus. Six sets were randomly presented during the experiments. The integrative cross-modal oddball was designed to investigate the integrative effect in SSA when the bimodal stimulations were synchronously presented instead of only one modal stimulation in the interactive cross-modal oddball. Here, the integration and interaction during bimodal processing indicated two different scenarios, one corresponding to alternation of the presentation of each stimulation while the other corresponded to the synchronous presentation of both stimulations.

## Data Analysis

We used two SSA indexes, the stimulus index (SI) and common-stimulus-specific index (CSI) [20, 25, 26]. The SI was used to assess the normalized difference between the response to the rare appearance and the response to the common appearance of the same stimulus and was defined as follows:  $SI_i = (d_i - s_i)/(d_i + s_i)$  ( $i = 1, 2$ ), where  $s_i$  and  $d_i$  represent neuronal firing rate (0–200 ms window relative to the stimulus onset) induced by the standard and deviant

stimulation, respectively, and  $i$  represents each of two stimuli in the oddball paradigm. The CSI was used to quantify the tendency of the neuron to respond to a rare stimulus, independent of the stimulus, and was defined as follows:  $CSI = [d_1 + d_2 - s_1 - s_2] / [d_1 + s_1 + d_2 + s_2]$ . The CSI describes the degree of SSA for the neuron. The possible SI and CSI values range from  $-1$  to  $+1$ , where positive values indicate that the response to the deviant stimulus is greater and negative values show that the response to the standard stimulus is greater.

The firing rate of the deviant and standard responses was calculated using a 200-ms response window starting from the stimulus onset. Peristimulus time histograms (PSTHs; 8-ms binwidth) were computed from 400 and 80 trials for the standard and deviant stimuli, respectively. MatLab software was used for statistical analyses. Statistical test was performed through a paired  $t$ -test between the set of single-trial responses and the corresponding pre-stimulus activity levels, and between the different deviant responses (e.g. the bimodal deviant responses *vs* the auditory deviant responses) of the same neurons. We used the ANOVA *post hoc* test to compare deviant responses and standard responses for a single neuron.  $P < 0.01$  was considered statistically significant.

## Results

### SSA in the Cross-Modal Interaction

The auditory TRN neurons had strong SSA in the frequency and spatial domains [20, 21]. Here we examined whether the TRN neurons have cross-modal SSA. An essential screening of the responses was conducted for single-modal stimulation. TRN neurons (Fig. 2A; arrow) responded significantly to both sound and visual stimulation (Fig. 2B, 200 ms response window before *vs* after stimulus onset; Wilcoxon's matched-pairs test,  $P < 0.001$ ).

We used an interactive oddball paradigm (Fig. 1A) with one auditory stimulus and one visual stimulus presented at the same location in front of the rat. The raster plots showed responses to the sound and the light when the stimulus was deviant (Fig. 2C, top row) and standard (Fig. 2C, bottom row): the representative neuron had a stronger response to the deviant stimuli than to the standard stimuli for both modalities, and the PSTHs (Fig. 2D) demonstrated a significant difference between deviant and standard responses for both sound and light stimulations ( $P < 0.001$  for both modalities, ANOVA *post hoc* test).

The population-level analysis, including 68 neurons, is shown in Fig. 3. The mean firing rate in the 200-ms window after the stimulus onset increased from 25.2 Hz (standard sound) to 43.6 Hz (deviant sound) (Fig. 3A left,  $P < 0.001$ ,

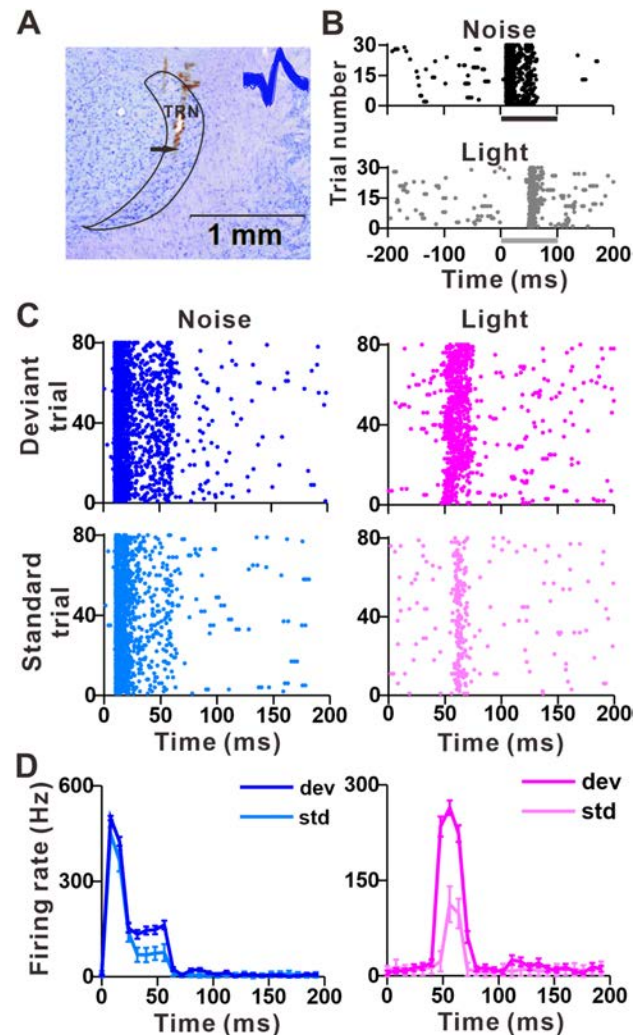


**Fig. 2** Responses of a TRN neuron to interactive oddball stimulation. **A** Nissl stain showing the track of a recording electrode (arrow, recording location; scale bar, 1 mm). Inset, spikes of all responses during the recording. **B** Raster plots showing the responses to the sound alone and light stimulation alone. The bars below the plots indicate the stimuli. **C** Raster plots corresponding to noise (left, blue) and light stimulation (right, pink) as the deviant (upper panels) and standard (lower panels) stimuli in the interactive oddball paradigm. The plots show the last 80 trials for standard responses, and all 80 trials for deviant responses. **D** PSTHs showing the deviant (dev; 80 trials) and standard responses (std; 400 trials). Error bars, SEM.

ANOVA *post hoc* test), and from 28.3 Hz (standard light) to 46.5 Hz (deviant light) (Fig. 3A right,  $P < 0.001$ , ANOVA *post hoc* test), suggesting a strong SSA in cross-modal interaction. Scatter-plots of the stimulus-specific index  $SI_{\text{sound}}$  *versus*  $SI_{\text{light}}$ , revealed that most points (64/68) fell within the first quadrant (Fig. 3B), similar to previous reports [20, 25, 27, 28]. The CSI, describing the strength of SSA, was  $\sim 0.28$  (Fig. 3C), which was significantly greater than 0 ( $P < 0.001$ ,  $t$ -test), indicating that SSA existed at the population level for cross-modal interaction.



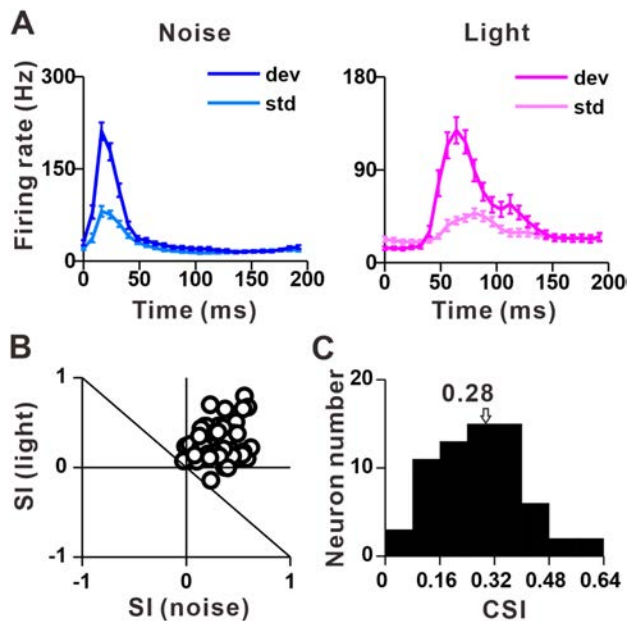


**Fig. 3** Responses to interactive oddball stimulation in the TRN neuronal population. **A** PSTHs of 68 neurons showing responses to noise (left) and light (right) stimulation. Error bars, SEM. **B** Scatterplots of SI (noise) (SI: stimulus-specific index) versus SI (light). **C** Distribution of common stimulus-specific index (CSI) for interactive oddball stimulation (arrow indicates the mean).

We directly compared the deviant response in the interactive cross-modal oddball and the response in the single-modal stimulation paradigms to explore whether the deviant response in one modality is affected by the background stimulation of the other modality. All the dots were close to the unitary line and were not significantly different for sound ( $P = 0.11$ , deviant responses vs alone responses, paired  $t$ -test, Fig. 4A) and light ( $P = 0.27$ , paired  $t$ -test, Fig. 4B) stimuli. These results suggest that the responses to one modality of stimuli are not affected by the preceding stimulation of the other modality in bimodal TRN neurons.

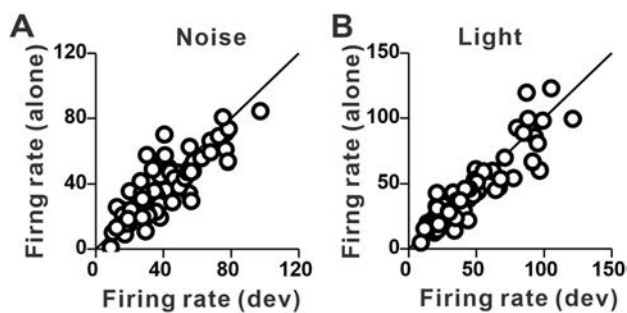


**Fig. 4** Similar responses to deviant and alone stimuli. Scatterplots displaying the comparisons among deviant responses in the interactive cross-modal oddball and those in the single modal paradigm for the sound (A) and light (B) stimuli.

## SSA in Cross-Modal Integration

After characterizing the SSA response in the cross-modal interaction, we explored whether TRN neurons integrate the synchronous bimodal stimulation through SSA. The congruent bimodal stimulation was presented at two oddball paradigm locations and single-mode stimulation at the same locations in the oddball paradigm was presented as the control (Fig. 1B). TRN neurons (Fig. 5A, left panel) showed robust responses to sound alone and light alone (Fig. 5B). Here, one visual stimulus

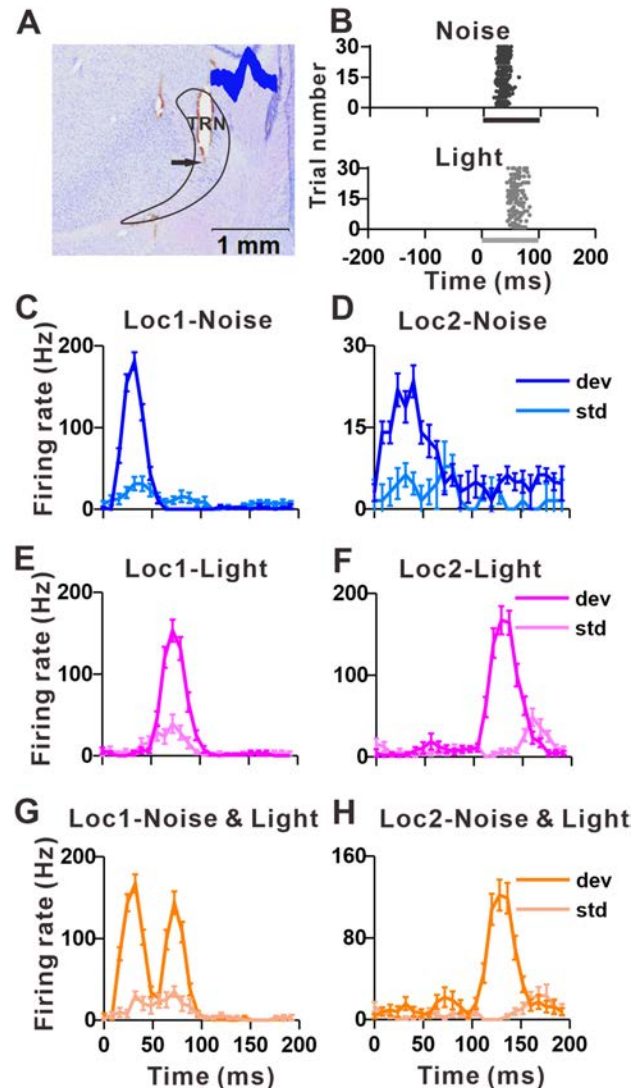


**Fig. 5** Response of a TRN neuron to integrative oddball stimulation. **A** Nissl staining showing the track of the recording electrode (arrow, recording location; scale bar, 1 mm). Inset, spikes of all responses to different stimulations. **B** Raster plots showing the responses to the sound and light stimulation alone. Bars below the plots indicate the stimuli. **C–H** PSTHs showing the deviant (dev; 80 trials) and standard responses (std; 400 trials) for the noise stimuli (C, D), light stimuli (E, F), and bimodal stimuli (G, H) in the integrative oddball. Error bars, SEM.

was positioned on the right at 45° (Loc 1, contralateral stimulus) and the other on the left at 45° (Loc 2, ipsilateral stimulus), and the two speakers were set to match the locations of the two visual stimuli. The bimodal stimuli had matching pairs of auditory and visual stimuli spatially. The auditory responses at the rare location were significantly stronger than the responses at the same location as the standard site (heavy blue *versus* light blue. Figure 5C:  $P < 0.001$ , Loc 1; Fig. 5D:  $P = 0.02$ , Loc 2, ANOVA *post hoc* test), suggesting the presence of auditory spatial SSA in the TRN, consistent with the previous results [21]. SSA to the location of the visual stimuli was also apparent (deviant stimuli *versus* standard stimuli. Fig. 5E:  $P < 0.001$ ; Fig. 5F:  $P < 0.001$ , ANOVA *post hoc* test). The results from the bimodal oddball blocks showed significant differences at both locations (Fig. 5G, H:  $P < 0.001$ , ANOVA *post hoc* test). The CSIs were 0.44, 0.38, and 0.44 for auditory, visual, and bimodal stimulations, respectively.

We compared the deviant responses among the three conditions to explore an integrative effect. The population PSTH from 25 single units (SUs) is shown in Fig. 6A, B. The auditory and visual deviant responses at location 1 (Fig. 6A) peaked at 16.5 ms and 80.5 ms, respectively. Bimodal deviant responses had two peaks, which were close to the peaks of the single modal responses. Bimodal responses at location 2 (Fig. 6B) also had two peaks, which were close to those of single modal responses. These results suggest that the bimodal responses are the summation of independent inputs from single-mode stimulation. We further compared the responses between the bimodal and single-mode conditions in two windows (0–50 ms and 50–200 ms) to test the above hypothesis. The first window was chosen as the auditory response while the second as the visual response. For the first window (Fig. 6C, D), the bimodal deviant responses were marginally stronger than the auditory deviant responses (Fig. 6C:  $P = 0.02$ ; Fig. 6D:  $P = 0.01$ , paired *t*-test) at both locations, but all the dots were very close to the unitary line (Fig. 6C, D). Consistently, the bimodal and visual deviant responses in the second window were not different (Fig. 6E:  $P = 0.57$ ; Fig. 6F:  $P = 0.69$ , paired *t*-test), and all the dots lay along the unitary line. These results suggest that bimodal stimulation has a very limited integrative effect.

We then explored the SSA property of the integrative oddball. Most values in the scatter plots for  $SI_{Loc1}$  (location 1) *versus*  $SI_{Loc2}$  (location 2), were in the first quadrant, implying the presence of SSA in these recorded neurons for all three conditions. The further the dots deviated from the diagonal, the more the SSA. However, the dots in the bimodal condition did not show any more deviation than single-mode conditions. The CSI averages were  $0.22 \pm 0.029$  (SEM),  $0.13 \pm 0.025$ , and  $0.21 \pm 0.027$  for auditory, visual, and bimodal conditions, respectively (Fig. 7D–F).

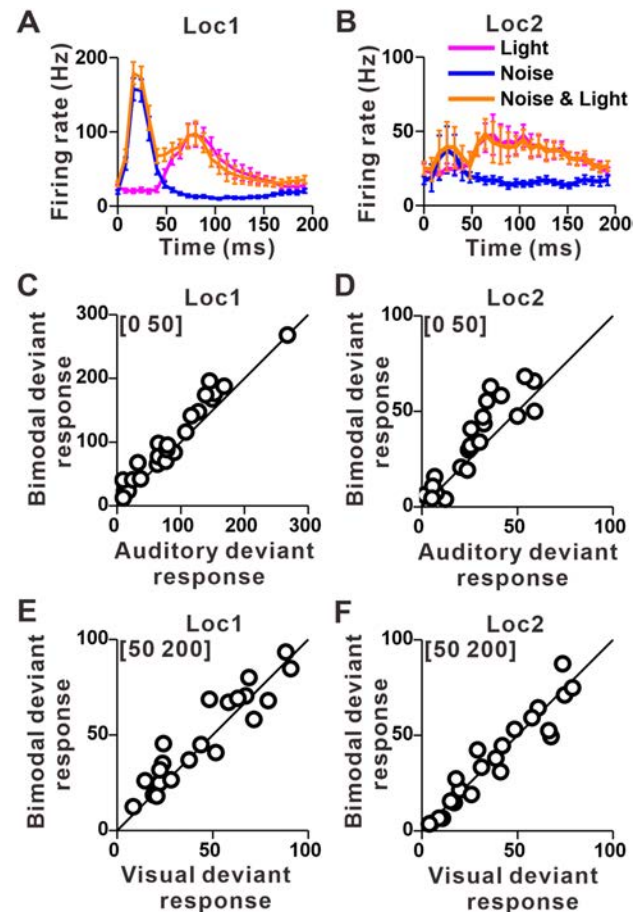


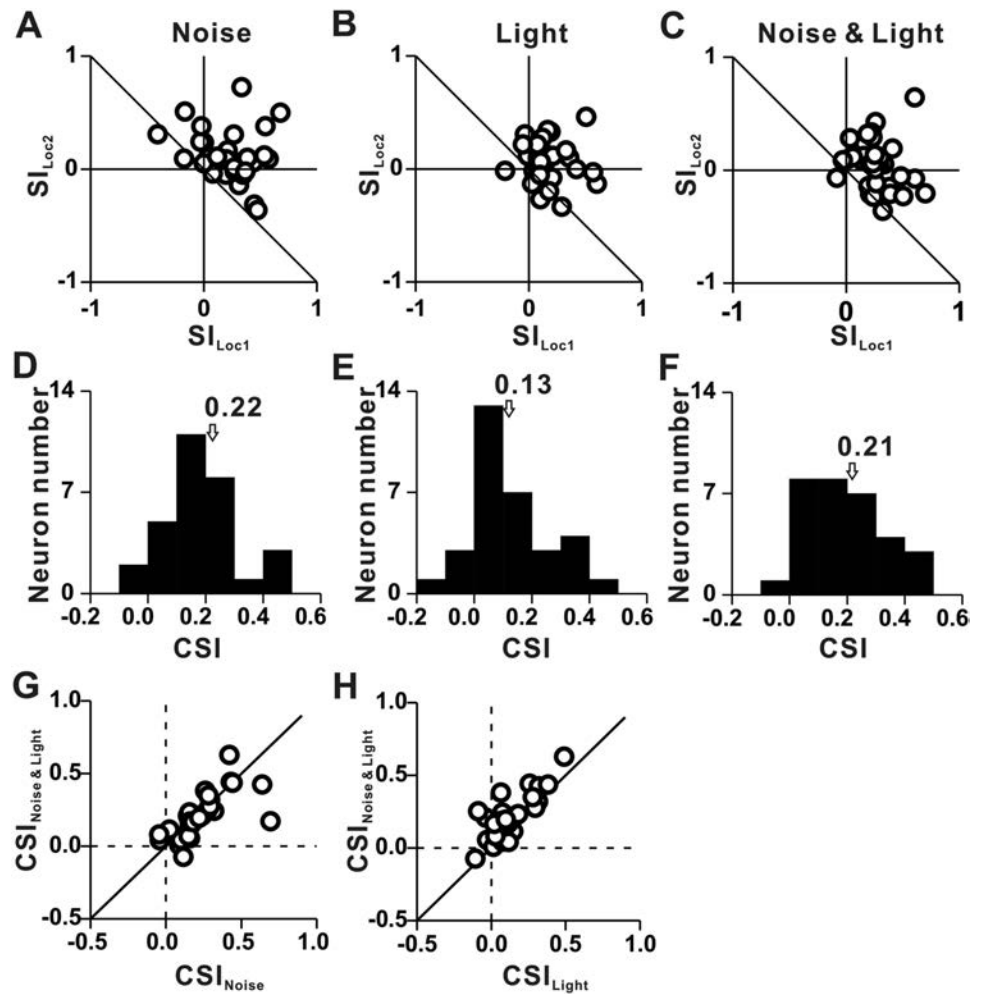
**Fig. 6** Responses to the deviant stimuli of the integrative oddball. **A**, **B** PSTHs showing the deviant response (80 trials) for the noise stimuli (blue color), light stimuli (pink color), and bimodal stimuli (yellow color) at the two locations (**A**: Loc 1; **B**: Loc 2). Error bars, SEM. **C–F** Scatterplots illustrating the comparison between the bimodal deviant response and single-mode deviant response (auditory: **C**, **D**; visual: **E**, **F**) for two windows: 0–50 ms (**C**, **D**) and 50–200 ms (**E**–**F**).

These values were significantly greater than 0 ( $P < 0.001$  for all the three conditions, *t*-test), indicating spatial SSA for auditory, visual, and bimodal stimuli. The CSI was greater in the bimodal condition than in the visual condition. However, CSI in the bimodal and auditory conditions were comparable ( $P = 0.03$ , bimodal *vs* visual conditions;  $P = 0.67$ ; bimodal *vs* auditory conditions, one-way ANOVA with *post hoc* test).

We further plotted the CSI of the bimodal condition against a single-mode condition to explore the relationship among the SSA strength of the different conditions (Fig. 7G, H). The CSIs were greater in the bimodal condition than in the visual condition (Fig. 7H,  $P < 0.001$ , paired *t*-test) but were similar to those in the auditory condition (Fig. 7G,  $P = 0.46$ , paired *t*-test). Furthermore, the CSIs of different combinations were positively correlated (Pearson correlation; Fig. 7H,  $r = 0.78$ ,  $P < 0.001$ ; Fig. 7G,  $r = 0.68$ ,  $P < 0.001$ ), indicating that the CSI



**Fig. 7** Responses to the integrative oddball stimulation in the TRN neuronal population. **A–C** Scatterplots of  $SI_{Loc2}$  versus  $SI_{Loc1}$  for noise (**A**), light (**B**), and bimodal (**C**) stimuli. **D–F** Distribution of the common stimulus-specific index (CSI) for noise (**D**), light (**E**), and bimodal (**F**) stimuli. Arrows indicate the mean. **G, H** Scatterplots showing the relationship among CSI for the noise, light, and bimodal stimuli. **G**, bimodal vs noise; **H**, bimodal vs light.



reflects some intrinsic neuronal property regardless of the stimulus type.

### Time Course of Cross-Modal Interaction and Integration

We first examined the response dynamic in the 96 stimulations in the block of the interactive oddball to assess the time course of the oddball paradigms in the recorded neuronal population (Fig. 1A). The neuronal response to sound continuously decreased from the first to the fifth stimulus, while it significantly increased to the sixth stimulus (light stimulation) (Fig. 8A, left panel). The response then successively decreased in the next five sound stimuli (from the seventh to the eleventh stimulus) and then increased again to the second light stimulation (the twelfth stimulus). This response pattern was repeated during the whole block, and thus the amplitude of the neuronal response formed a saw-tooth shape, with the deviant response to the light stimulation at the tip of the saw-tooth (Fig. 8A, left panel). The saw-tooth response pattern was

still evident when the standard and deviant stimuli were swapped (Fig. 8A, right panel), and the deviant response to the noise stimulation was also at the tip of the saw-tooth.

We then examined the response change over the 96 stimulations in the block of the integrative oddball (Fig. 8B). The neuronal response to sound at Loc 2 decreased with repetition and significantly increased to the sixth stimulus, sound at Loc 1 (Fig. 8B, left panel, upper row). The response then successively decreased for the next five sound stimuli (from the seventh to the eleventh stimulus), then increased to the deviant sound stimulation (the twelfth stimulus). This response pattern was repeated during the whole block, resembling the pattern of the time course of the interactive oddball (Fig. 8A). Moreover, the response significantly decreased from the first to the twelfth stimulation, then peaked when the standard and deviant locations were swapped (Fig. 8B, right panel, upper row). The response profile after the light stimulation (Fig. 8B, left panel, middle row) was similar to that of the sound stimulation with the deviant response (Loc 1) at the peak of the saw-tooth. The response decreased from the

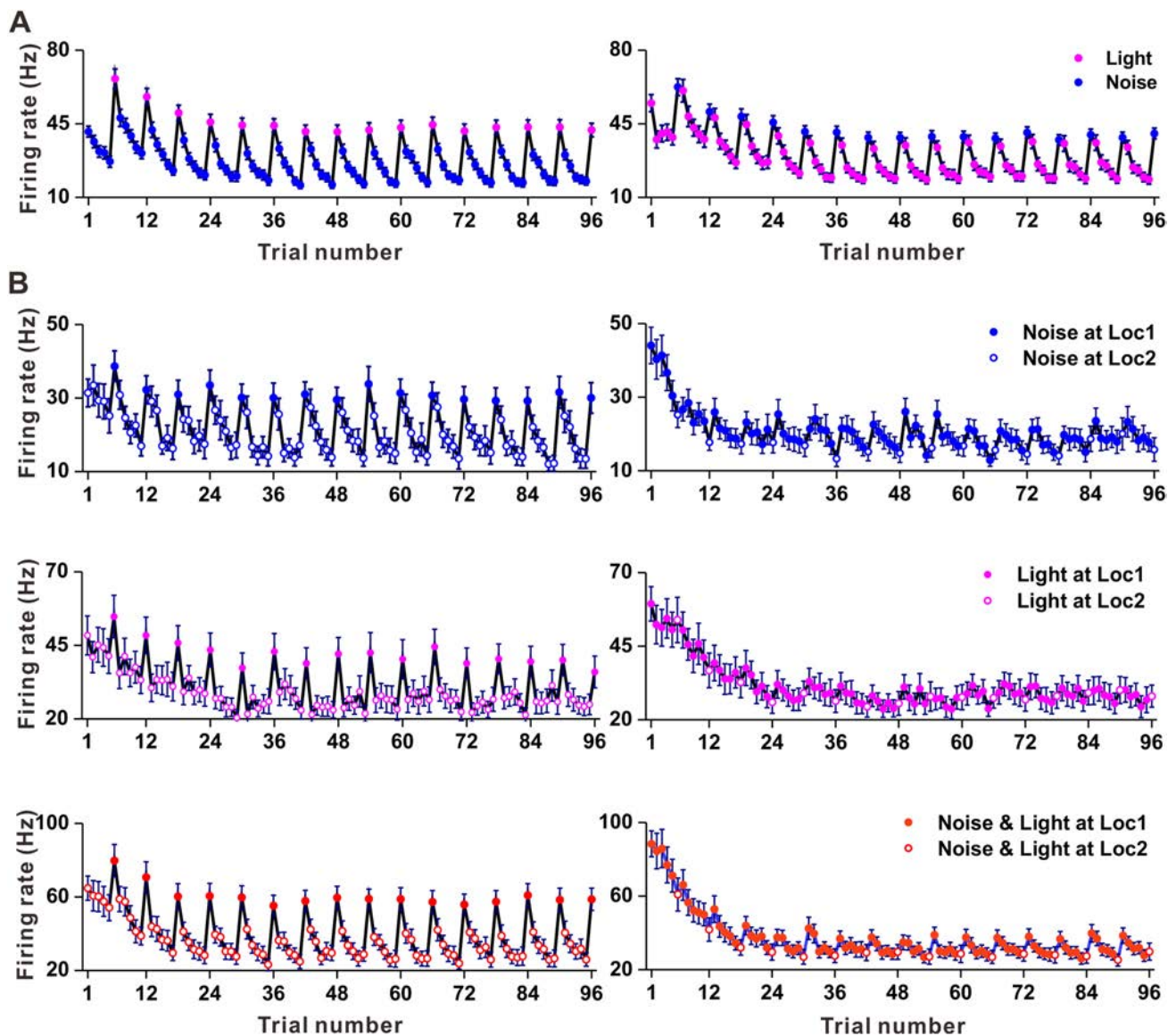


**Fig. 8** Time course of the responses in the interactive and integrative oddballs. **A** Response as a function of stimulus number in a block of interactive oddball (pink, light; blue, noise). **B** Response as a function

of stimulus number in a block of the integrative oddball for noise stimuli (upper panels), light stimuli (middle panels), and bimodal stimuli (lower panels).

first to the twenty-fourth stimulation, then peaked when the standard and deviant locations were swapped (Fig. 8B, right panel, middle row). The response profiles of the bimodal stimulation were similar to those of the sound stimulation for both locations (Fig. 8B, lower row).

## Discussion

We explored the cross-modal effect through interaction and integration in SSA. The TRN neurons showed robust SSA in the alternating bimodal oddball stimulation. For the synchronous bimodal stimulation, the strength of SSA in

the bimodal condition was comparable to that in the auditory condition.

## SSA in the Cross-Modal Interaction

SSA has been found and studied in almost all sensory modalities such as the visual [8], auditory [4–6], and somatosensory [9] systems. These studies have been conducted within the same sensory modality; to the best of our knowledge, no study has assessed the cross-modal interaction through SSA. The first part of the current study was designed to show how the one modal information pops out among the other modal background.

We formed an interactive oddball paradigm with auditory and visual stimuli at the same location to investigate the nature of cross-modal SSA through interaction (Fig. 1A). The interactive oddball paradigm (Figs. 2, 3) showed significant SSA, suggesting that the bimodal TRN neurons adapt to the high-probability occurrence of one modality while providing a robust response to the low-probability occurrence of another modality. The time-course analysis of the response during the interactive oddball stimulation showed that the deviant responses lay at the peak for both modalities (Fig. 8A), indicating the presence of SSA in the cross-modal interaction. Moreover, whether SSA reflects true deviance detection or simply adaptation has recently attracted much attention [28–30]. As a result, researchers have developed new sets of control experiments, including “deviant alone” and “many standards” to assess the above [28–30]. “Deviant alone” sequences consist only of the deviant stimulus, with the standard presentations replaced by non-stimulation. The temporal setting in the single-mode stimulation is exactly the same as the “deviant alone”. Here, the deviant responses were similar to the firing in single-mode stimulation (Fig. 4), suggesting novelty detection in the TRN in the cross-modal interactive environment. Therefore, the interactive cross-modal SSA described here provides a neural mechanism for novelty detection across sensory modalities.

### SSA in Cross-Modal Integration

Besides the cross-modal interaction, cross-modal integration is ubiquitous in everyday life. The integration of information from different sensory modalities has many advantages for human observers, including enhanced salience, resolution of perceptual ambiguities, and unified perception of objects and surroundings [31, 32]. The advantage of the cross-modal integration through SSA was first investigated in the entopallium [10]. Although neurons in the entopallium have weak or no response to the auditory stimuli, congruent auditory stimuli substantially enhance the visual SSA. The modulation effect of auditory stimulation on the visual SSA suggests that cross-modal integration can improve visual change detection when additional auditory information is available.

We also explored the cross-modal integration in the TRN in a similar experiment setting. For unimodal stimulation, the TRN neurons showed robust spatial SSA (Figs. 5C, D and 7A, D) for auditory stimulation, consistent with previous research [21]. Moreover, we also showed that the TRN neurons had strong spatial SSA for visual stimulation (Figs. 5E, F and 7B, E), suggesting that TRN neurons play a crucial role in spatial saliency for both auditory and visual modalities. In bimodal stimulation, the

SSA was stronger in the bimodal condition than in the visual condition (Fig. 7H), but similar to the auditory condition (Fig. 7G), suggesting a limited integrative effect in the TRN. Notably, there could be an integrative solid effect in the other scenario such as unsynchronous presentation of the two modal stimulations since the cross-modal effect may depend on the relative timing of the two modal stimulations.

### Multiple Sensory Processing in the TRN

The TRN is composed of sensory sectors, and each primarily controls the sensory processing of a given modality. A small subset of TRN cells contains multimodal sensory neurons, which lie near the border of sectors [15]. Anatomically, a single auditory neuron may receive inputs from visual cortical or thalamic inputs [22, 33]. Subthreshold sound or light stimuli modulate the responses of the unisensory visual or auditory neurons [34, 35]. These TRN cells sent axonal projections to first-order or higher-order thalamic nuclei, probably leading to cross-modal sensory influence in the thalamus [36, 37]. These results raise the possibility that the TRN constitutes neural pathways involved in cross-modal sensory gating. However, the nature of cross-modal sensory processing of multimodal sensory neurons in the TRN is unknown. We selectively recorded bimodal TRN neurons with two oddball stimulations (Fig. 1). The TRN neurons could rapidly switch to a response from the background mode of stimulation to the other mode of stimulation (Fig. 8). The TRN neurons specifically adapted to one modality but robustly responded to the other modality, enhancing modality-specific adaptation (Fig. 8). These results can be explained using the widely-accepted model “adaptation in narrowly-tuned modules” (ANTM) [38]. The ANTM model postulates that SSA in widely-tuned neurons reflects adaptation specific to inputs from neurons narrowly tuned to a repetitive frequency [39], enhancing frequency-specific adaptation. These results can also apply to awake subjects since the ANTM model can be operated through synaptic adaptation [39], which exists in both anesthetized and awake subjects.

The mode-specific adaptation in bimodal TRN neurons was also demonstrated in the integrative oddball experiment (Fig. 7). Besides, the strength of SSA in the bimodal and unimodal conditions was comparable, indicating that bimodal TRN neurons can process cross-modal information in a distributed and independent manner. Meanwhile, the deviant responses in the interactive oddball were similar to the responses to the same stimuli but without the other modality of background stimulation (Fig. 4). The bimodal deviant responses in the integrative oddball were also similar to the unimodal deviant responses in their

corresponding windows (Fig. 6). These results show that cross-modal processing in a single bimodal TRN neuron is independent, and this provides a neuronal mechanism for switching attention among different sensory modalities since the TRN plays a crucial role in attention [17, 18].

**Acknowledgements** We are grateful to Yale E. Cohen for editing the manuscript and Xiaokai Kou for his help with the experiments. This work was supported by the National Natural Science Foundation of China (31872768, 32171044, and 32100827), and Zhejiang University K.P. Chao's High Technology Development Foundation.

**Conflict of interest** The authors claim that there are no conflicts of interest.

## References

- Khoury L, Nelken I. Detecting the unexpected. *Curr Opin Neurobiol* 2015, 35: 142–147.
- Malmierca MS, Sanchez-Vives MV, Escera C, Bendixen A. Neuronal adaptation, novelty detection and regularity encoding in audition. *Front Syst Neurosci* 2014, 8: 111.
- Duque D, Ayala YA, Malmierca MS. Deviance detection in auditory subcortical structures: What can we learn from neurochemistry and neural connectivity? *Cell Tissue Res* 2015, 361: 215–232.
- Zhai YY, Sun ZH, Gong YM, Tang Y, Yu XJ. Integrative stimulus-specific adaptation of the natural sounds in the auditory cortex of the awake rat. *Brain Struct Funct* 2019, 224: 1753–1766.
- Rui YY, He J, Zhai YY, Sun ZH, Yu X. Frequency-dependent stimulus-specific adaptation and regularity sensitivity in the rat auditory thalamus. *Neuroscience* 2018, 392: 13–24.
- Carbajal GV, Malmierca MS. The neuronal basis of predictive coding along the auditory pathway: From the subcortical roots to cortical deviance detection. *Trends Hear* 2018, 22: 2331216518784822.
- Malmierca MS, Anderson LA, Antunes FM. The cortical modulation of stimulus-specific adaptation in the auditory midbrain and thalamus: A potential neuronal correlate for predictive coding. *Front Syst Neurosci* 2015, 9: 19.
- Müller JR, Metha AB, Krauskopf J, Lennie P. Rapid adaptation in visual cortex to the structure of images. *Science* 1999, 285: 1405–1408.
- Musall S, Haiss F, Weber B, von der Behrens W. Deviant processing in the primary somatosensory cortex. *Cereb Cortex* 2017, 27: 863–876.
- Reches A, Netser S, Gutfreund Y. Interactions between stimulus-specific adaptation and visual auditory integration in the forebrain of the barn owl. *J Neurosci* 2010, 30: 6991–6998.
- Wang WY, Hu L, Cui HY, Xie XB, Hu Y. Spatio-temporal measures of electrophysiological correlates for behavioral multisensory enhancement during visual, auditory and somatosensory stimulation: A behavioral and ERP study. *Neurosci Bull* 2013, 29: 715–724.
- Whitchurch EA, Takahashi TT. Combined auditory and visual stimuli facilitate head saccades in the barn owl (*Tyto alba*). *J Neurophysiol* 2006, 96: 730–745.
- Narins PM, Grabul DS, Soma KK, Gaucher P, Hödl W. Cross-modal integration in a dart-poison frog. *Proc Natl Acad Sci U S A* 2005, 102: 2425–2429.
- Shosaku A, Sumitomo I. Auditory neurons in the rat thalamic reticular nucleus. *Exp Brain Res* 1983, 49: 432–442.
- Pinaut D. The thalamic reticular nucleus: Structure, function and concept. *Brain Res Brain Res Rev* 2004, 46: 1–31.
- Jones EG. *The Thalamus*. 2nd ed. Cambridge; New York: Cambridge University Press, 2007: 218–224.
- Crick F. Function of the thalamic reticular complex: The searchlight hypothesis. *Proc Natl Acad Sci U S A* 1984, 81: 4586–4590.
- McAlonan K, Cavanaugh J, Wurtz RH. Guarding the gateway to cortex with attention in visual thalamus. *Nature* 2008, 456: 391–394.
- Yu XJ, Xu XX, Chen X, He SG, He JF. Slow recovery from excitation of thalamic reticular nucleus neurons. *J Neurophysiol* 2009, 101: 980–987.
- Yu XJ, Xu XX, He SG, He JF. Change detection by thalamic reticular neurons. *Nat Neurosci* 2009, 12: 1165–1170.
- Xu XX, Zhai YY, Kou XK, Yu XJ. Adaptation facilitates spatial discrimination for deviant locations in the thalamic reticular nucleus of the rat. *Neuroscience* 2017, 365: 1–11.
- Yu XJ, Meng XK, Xu XX, He J. Individual auditory thalamic reticular neurons have large and cross-modal sources of cortical and thalamic inputs. *Neuroscience* 2011, 193: 122–131.
- Song PR, Zhai YY, Gong YM, Du XY, He J, Zhang QC. Adaptation in the dorsal belt and core regions of the auditory cortex in the awake rat. *Neuroscience* 2021, 455: 79–88.
- Paxinos G, Watson C. *The Rat Brain in Stereotaxic Coordinates*, Elsevier Academic Press, Amsterdam, 2005, pp 86–111.
- Antunes FM, Nelken I, Covey E, Malmierca MS. Stimulus-specific adaptation in the auditory thalamus of the anesthetized rat. *PLoS One* 2010, 5: e14071.
- Ulanovsky N, Las L, Nelken I. Processing of low-probability sounds by cortical neurons. *Nat Neurosci* 2003, 6: 391–398.
- Malmierca MS, Cristaudo S, Pérez-González D, Covey E. Stimulus-specific adaptation in the inferior colliculus of the anesthetized rat. *J Neurosci* 2009, 29: 5483–5493.
- Farley BJ, Quirk MC, Doherty JJ, Christian EP. Stimulus-specific adaptation in auditory cortex is an NMDA-independent process distinct from the sensory novelty encoded by the mismatch negativity. *J Neurosci* 2010, 30: 16475–16484.
- Taaseh N, Yaron A, Nelken I. Stimulus-specific adaptation and deviance detection in the rat auditory cortex. *PLoS One* 2011, 6: e23369.
- Fishman YI, Steinschneider M. Searching for the mismatch negativity in primary auditory cortex of the awake monkey: Deviance detection or stimulus specific adaptation? *J Neurosci* 2012, 32: 15747–15758.
- Driver J, Spence C. Multisensory perception: Beyond modularity and convergence. *Curr Biol* 2000, 10: R731–R735.
- Shimojo S, Shams L. Sensory modalities are not separate modalities: Plasticity and interactions. *Curr Opin Neurobiol* 2001, 11: 505–509.
- Gutfreund Y. Stimulus-specific adaptation, habituation and change detection in the gaze control system. *Biol Cybern* 2012, 106: 657–668.
- Kimura A. Diverse subthreshold cross-modal sensory interactions in the thalamic reticular nucleus: Implications for new pathways of cross-modal attentional gating function. *Eur J Neurosci* 2014, 39: 1405–1418.
- Kimura A, Yokoi I, Imbe H, Donishi T, Kaneoke Y. Auditory thalamic reticular nucleus of the rat: Anatomical nodes for modulation of auditory and cross-modal sensory processing in the loop connectivity between the cortex and thalamus. *J Comp Neurol* 2012, 520: 1457–1480.
- Donishi T, Kimura A, Imbe H, Yokoi I, Kaneoke Y. Sub-threshold cross-modal sensory interaction in the thalamus:

- Lemniscal auditory response in the medial geniculate nucleus is modulated by somatosensory stimulation. *Neuroscience* 2011, 174: 200–215.
37. Noesselt T, Tyll S, Boehler CN, Budinger E, Heinze HJ, Driver J. Sound-induced enhancement of low-intensity vision: Multisensory influences on human sensory-specific cortices and thalamic bodies relate to perceptual enhancement of visual detection sensitivity. *J Neurosci* 2010, 30: 13609–13623.
38. Mill R, Coath M, Wennekers T, Denham SL. A neurocomputational model of stimulus-specific adaptation to oddball and Markov sequences. *PLoS Comput Biol* 2011, 7: e1002117.
39. Zhai YY, Auksztulewicz R, Song PR, Sun ZH, Gong YM, Du XY, *et al.* Synaptic adaptation contributes to stimulus-specific adaptation in the thalamic reticular nucleus. *Neurosci Bull* 2020, 36: 1538–1541.



REVIEW

# From Parametric Representation to Dynamical System: Shifting Views of the Motor Cortex in Motor Control

Tianwei Wang<sup>1,2,3</sup>  · Yun Chen<sup>1,2,3</sup>  · He Cui<sup>1,2,3</sup> 

Received: 12 September 2021 / Accepted: 29 November 2021 / Published online: 17 March 2022  
© The Author(s) 2022

**Abstract** In contrast to traditional representational perspectives in which the motor cortex is involved in motor control *via* neuronal preference for kinetics and kinematics, a dynamical system perspective emerging in the last decade views the motor cortex as a dynamical machine that generates motor commands by autonomous temporal evolution. In this review, we first look back at the history of the representational and dynamical perspectives and discuss their explanatory power and controversy from both empirical and computational points of view. Here, we aim to reconcile the above perspectives, and evaluate their theoretical impact, future direction, and potential applications in brain-machine interfaces.

**Keywords** Dimensionality reduction · Neural network · Machine learning · Population decoding · Brain-machine interface

## Introduction

The ultimate purpose of the nervous system is to produce appropriate action, and the motor cortex has long been thought to play a crucial role in planning and generating movement. Since the motor cortex was identified by Fritsch and Hitzig through surface electrical stimulation in the 1870s, several dogmas have been proposed to describe how it controls our musculoskeletal system. Anatomically, the motor cortex innervates the motoneuron pool in the spinal cord to drive skeletal muscles, and its neurons are clustered in accordance with the musculature following a somatotopic map [1]. Neurophysiological studies in non-human primates revealed that neuronal activity in the motor cortex is tuned to single-joint movements [2] and isometric force [3]. Since the 1980s, further studies of whole-arm movements have demonstrated that activity in the motor cortex represents a variety of motor parameters, such as direction [4], speed [5, 6], trajectory [7], and posture [8, 9].

Although the above representational perspective that directly maps neuronal activity to movement parameters is straightforward and has fostered brain-machine interfaces (BMIs), it still cannot explain the heterogeneous, complex, and time-varying firing patterns exhibited by many neurons in the motor cortex [10]. Since the 2000s, advances in neural interface and data science have enabled us to record and analyze large-scale neural signals. Recent studies have progressed from analyzing individual neurons to a systems approach, to the collective operation of neuronal populations. In line with this progression, Shenoy and colleagues proposed a dynamical system perspective [11, 12] which views the motor cortex as a dynamical machine that autonomously evolves during execution to issue descending motor commands. Based on the evaluation of neural data with a complex spatiotemporal structure, the

---

Tianwei Wang and Yun Chen contributed equally to this work.

---

✉ He Cui  
cuihe@ion.ac.cn

<sup>1</sup> Center for Excellence in Brain Science and Intelligent Technology, Institute of Neuroscience, Chinese Academy of Sciences, Shanghai 200031, China

<sup>2</sup> Shanghai Center for Brain and Brain-inspired Intelligence Technology, Shanghai 200031, China

<sup>3</sup> University of Chinese Academy of Sciences, Beijing 100049, China

dynamical system perspective has provided a deeper insight into high-dimensional neural trajectories in relation to motor planning and execution.

In this review, we not only summarize the paradigm shift from parametric representation to a dynamical system perspective, but also aim to reconcile these two viewpoints, which seem contradictory at first glance. Moreover, we present a global view of the integration of neural dynamics in the motor cortex with empirical studies on cortico-subcortical motor circuitry, theoretical work on the internal model, and BMI applications.

## Representation of Movement Parameters in the Motor Cortex

A fundamental doctrine of neuroscience is that brain structure and connectivity determine functionality. A central goal of neurophysiology has long been to determine where the function is implemented, and how the information is represented in various brain areas. Following this principle, Fritsch and Hitzig identified the motor cortex by determining an area of the cerebral cortex from which movements were evoked by the application of electrical stimulation (for review, see [13]). Now we know that both the primary motor cortex (M1) and premotor cortex send descending projections to the spinal cord *via* the corticospinal (CS) tract [14, 15]. The descending CS influence on muscles is indirectly mediated by spinal interneuronal circuits (Fig. 1A). From monkeys to apes to humans, an increasing number of CS axons directly innervate motoneurons in the spinal ventral horn [15, 16], forming the cortico-motoneuronal projection. These anatomical findings provide a solid support for a causal role for the motor cortex in muscle control. Moreover, the motor cortex also receives projections from the visual and somatosensory cortices [17], which provide information about the external environment and internal body status essential for motor control. Taken together, the motor cortex receives information about sensory input, motor intention, decisions, and body status, and generates motor commands that descend to the spinal cord and other subcortical areas [18]. Beyond the corticocortical and corticospinal connections, the basal ganglia-thalamocortical circuitry and corticocerebellar circuits also play important roles in motor initiation, termination, sensorimotor representation, and motor learning [19, 20]. Their outputs are delivered to the motor areas through the ventrolateral thalamus, while the motor areas project to the basal ganglia *via* the striatum, and to the cerebellum *via* the pontine nuclei [19, 21, 22]. Nonetheless, how the motor program is accomplished and its underlying computational mechanisms are still elusive.

Inspired by the visual system, where neuronal responses encode the properties of visual stimuli, neuroscientists initially investigated the motor cortex by determining how its activity represents motor variables. Influenced by the somatotopic anatomical organization of the motor cortex, Evarts utilized single-joint movements to determine how M1 activity varies with certain joint parameters, such as force, joint angle, and speed [2, 23]. Fetz and colleagues [3] simultaneously recorded electromyography (EMG) and neuronal activity in the motor cortex, and found that the facilitation of specific muscles can be induced by sub-threshold intracortical microstimulation (ICMS). These studies suggested that M1 neurons encode detailed information regarding intrinsic skeletomuscular parameters and help drive the effectors to accomplish the desired movement. For whole-arm reaching movements, neural activity in M1 is tuned to the directions of the endpoint movements (Fig. 1B) [4], and the firing rate (or discharge,  $D$ ) is related to movement direction *via* a cosine function (Fig. 1C):

$$D = b + a \cos(\theta - \text{PD})$$

where  $a$  is modulation depth,  $b$  is baseline,  $\theta$  is the movement direction, and PD is the preferred direction. Single-neuron activity in the motor cortex can be represented as a vector component projecting to the neuronal PD in accordance with the current firing rate, though the PDs might shift during motor adaptation [24, 25]. If a large population of neurons is recorded (Fig. 1D), a population vector algorithm [26, 27] is applied for BMIs [28] by using neuronal PDs and their instantaneous firing rates to decode the actual movement direction. First, the weight of each neuron in a time bin is calculated as the baseline-subtracted firing rate. Then, the resulting vector sum of all neurons' weights, multiplied by the unit vector along their PDs, is defined as the instantaneous population vector, which closely points to the actual movement direction. The whole-arm reach movement seems a good task for examining the correlation between high-level extrinsic information and neuronal activity in the motor cortex.

Due to the degrees of freedom problem in multi-joint movements, it is easier to study motor planning at the kinematic level, and directional tuning becomes a prominent feature for evaluating the impacts of other factors. Hence, it is unclear how M1 neurons represent high-level parameters like hand path. Because the high-level parameters are usually correlated with low-level muscle responses, a substantial effort has been made to dissociate them. Kakei *et al.* trained monkeys to perform step-tracking movements while gripping a handle with three different postures [29] to distinguish extrinsic (movement direction) from intrinsic (joint/muscle contraction) coordinates. About half of their recorded neurons displayed a stable PD in the various intrinsic coordinates, suggesting

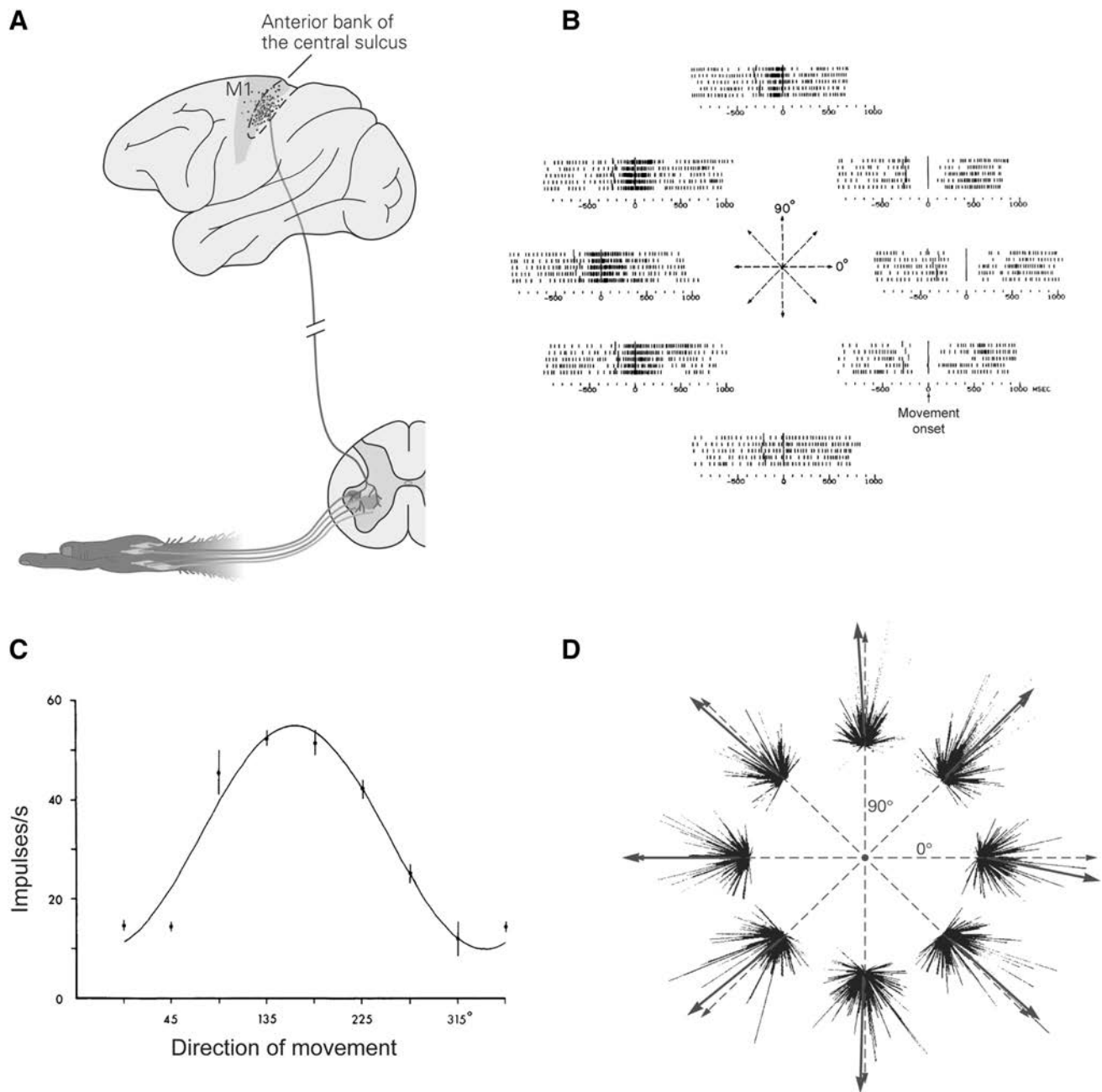


**Fig. 1** Illustration of the representational perspective. **A** M1 neurons mainly project to interneurons in the spinal cord *via* the corticospinal tract. Specifically, in primates, the corticomotoneurons are mainly located in the M1 sulcus, project monosynaptically to the motoneuron pool in the ventral horn. **B** Neuronal activity varies when monkeys push the manipulandum in different directions in the center-out task, which indicates selectivity for movement direction. **C** Firing rate of M1 neurons can be regressed with movement directions as a cosine

function. The direction with the highest firing rate is called the preferred direction (PD). **D** Single neurons are represented as vectors with PDs whose length is the firing rate. The summation of these vectors is congruent with the actual movement direction. **A** and **D** adapted from Principles of Neural Science, fifth edition, 2013: 835–864 [128] with permission from McGraw Hill; **B** and **C** adapted with permission from Georgopoulos *et al.*, 1982 [4].

that both “muscles” and “movements” are equally represented in M1. However, for most neurons the load applied during movement induced PD changes in M1 [30] within different 3D workspaces [31], which might have resulted from the task involving different covariates. Even for

unconstrained arm movements, directional tuning is also time-varying and segmented into two or three tuning components, and varies with other parameters [10, 32].

Hatsopoulos argued that single neurons are tuned to a direction at both lead and lag times, thus resulting in

temporally-evolving movement trajectories, rather than simply instantaneous movement parameters [7]. In this view, the PD shift in the center-out task could be induced by the mismatch between the preferred trajectory and the constant target directions.

In principle, the motor cortex performs not as a parametric representation to describe movement but as a repertoire to produce it. Soon after Fritsch and Hitzig found that brief electrical stimuli evoked twitches, Ferrier showed that longer electrical stimulation evoked complex movements [33, 34]. Graziano and coworkers refined this experiment using a behaviorally relevant duration of ICMS, and found that the evoked behaviors of monkeys were complex, coordinated, and “purposive” [35, 36]. Moreover, the stimulation sites in the macaque motor cortex are clustered according to categories of evoked actions, so it is difficult to build an explanatory model following the repertoire hypothesis. The potential dimensionality of movement categories makes it a non-deterministic polynomial problem, and the continuity and flexibility of natural movements are challenging for data collection and analysis.

An alternative approach to refining the representational model is to introduce more parameters. For instance, movement speed is also conveyed in the motor cortex, and a gain-offset modulation model can fit this correlation well [5, 37]. Like the aforementioned posture effect, the PD shift was believed to be the result of sensorimotor transformations [38]; this is accomplished by posture-related gain modulation in a recurrent network of extrinsic-like units with different preferences [39–41].

## Heterogeneity and Complexity of Firing Patterns in the Motor Cortex

The representational perspective is more focused on the “encoding-decoding” problem. Especially for movement kinematics and kinetics, it attempts to build the representational function in the generalized form:

$$r_n(t - \tau_n) = f_n[param_1(t), param_2(t), param_3(t) \dots]$$

where neuronal activity  $r_n$  is jointly tuned to movement parameters  $param_i$  and time lag  $\tau_n$  is used to cover the neuron-specific latency between cortical activity and parameters; neuronal conjunctive tuning to several variables is called mixed selectivity. If the tuning functions for each parameter are independent,  $f_n$  is a linear function [5, 7, 12, 28].

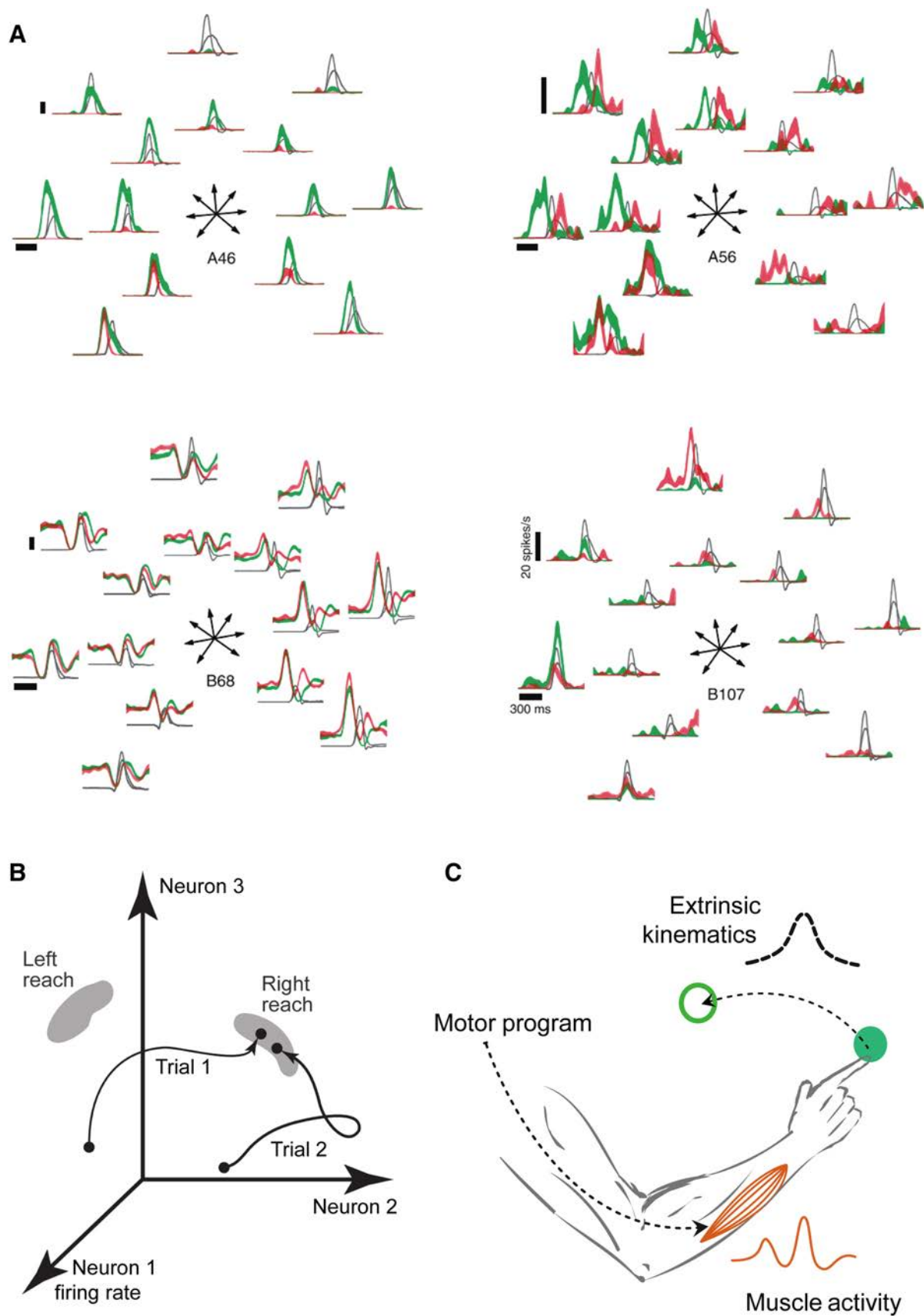
Another problem is the heterogeneity of neuronal activity in the motor cortex. As noted above, further studies on the tuning properties revealed that the temporal pattern does not always follow the representational model.

**Fig. 2** Illustration of the dynamical systems perspective. **A** In this task, the monkey performs a center-out reach with two distances and two hand speeds (gray, averaged hand velocity; red and green, mean firing rates fast and slow reaches, respectively). For neuron A46, tuning width varies with hand speed; for A56, the neural response leads the velocity profile in slow reach, while lagging in some directions of fast reach; B68 shows a multiphasic pattern with a different directional preference between preparatory and execution periods; and B107 presents a neuron that is excited only for long-distance reaches with speed-varied PD (adapted with permission from Churchland and Shenoy, 2007 [10]). **B** Neurons form a high-dimensional state space where the brain state evolves towards the optimal preparatory region to accomplish motor preparation (adapted with permission from Churchland *et al.*, 2006 [80]). **C** The efferent descending motor program from neural dynamics leads the temporal sequence of muscle activation and holistic movement.

In contrast to responses in the visual system that are triggered by the stimulus and maintained with stable preference, many neurons in the motor cortex exhibit ramping activity before movement onset, so-called preparatory activity, and a rapid bell-shaped peri-movement activity, although some neurons exhibit execution activity only, and others may show opposite tuning between preparation and execution. In addition, movement speed might not only reflect the change of firing rate and PD, but also the temporal relation between the neuronal response and the movement (Fig. 2A, [10, 32]). Even though some of the above findings might be explained by better behavioral measurements and by introducing more parameters into the representational model, they cast doubt on the model’s reliability. Following the doctrine that individual neurons are the basic computational units that represent information during each epoch in motor generation, such as the translation from extrinsic to intrinsic, from high-level to low-level, or formation and adjustment of the internal model, every stage and intermediate variable should be represented by the corresponding neuron, and all neurons together should formulate the movement command like the population vector. However, to compensate for the heterogeneous and time-varying tuning properties in the framework of representational perspective, nonlinear functions, and temporal profiles must be introduced, leading to increasingly complicated descriptive models without generalization.

## Neural Population Dynamics in the Motor Cortex

Interestingly, although single neurons show great heterogeneity, the linear decoding algorithms maintain stability and efficiency, indicating a robust linear readout at the population level, although there is a heterogeneous nonlinear response at the single-neuron level [26, 42, 43]. Several hypotheses have been proposed to explain this





phenomenon. The reliability of linear decoding algorithms such as population vectors may be due to the existence of a large population of neurons related to hand directions with uniformly distributed PDs [44]. The mixed selectivity produces high-dimensional neural representations, and enables a linear readout for every task-relevant parameter [45, 46]. In a neural network, it is granted that the neuronal connectivity preserves a coordinating functional organization with intrinsic dynamical evolution. Noise correlation and preference distribution somehow may reflect this dynamic procedure [47–49]. This neural constraint by connectivity is also related to population plasticity in motor learning [50–53]. On the other hand, both kinematic and kinetic spaces cannot explain as much neural population variance as the peri-movement space [11], indicating that neural activity contains task-irrelevant elements. Churchland *et al.* tried to interpret the neural population in the motor cortex as a dynamical system and applied jointed principal component analysis (jPCA) to extract components of evolution that form a temporally oscillating structure. Because the oscillation emerged from not only a rhythmic movement, but also from a single reach, they claimed the rotations of the populational state are a prominent feature of the motor cortex. This simple and consistent feature challenges the framework of representational perspective by emphasizing the population state evolution which can be described with ordinary differential equations as the dynamical system (Fig. 2B, C) [54]. It has been recently revealed that the “hand knob” area in the human premotor cortex is indeed tuned to the entire body; following the dynamical system view, its control is supposed to be accomplished through limb-specific parts and general movement dynamics rather than the motor homunculus [55].

However, Lebedev *et al.* argued that the oscillation structure is only a byproduct of jPCA, by which any neural population with temporal shifts of individual neurons’ firing rates, and a condition-specific temporal sequence, would result in such an oscillation structure. Therefore, it is an exaggeration to claim that the structure is related to “an unexpected yet surprisingly simple structure in the population response” which “explains many of the confusing features of individual neural responses.” [56]. Later studies further addressed the “epiphenomenon” problem and tended to agree with both of the opinions that the oscillation structure is a byproduct, while the population dynamics during reach is better explained by a dynamical system than representational framework [57]. The significant difference is possibly embedded in the covariance across time, neurons, and conditions [58].

Although the dynamical perspective inspired a new direction for understanding population activity and improved comprehension of the motor cortex, it seems to

dwelling in the qualitative description and visualization of high-dimensional data, but to lack a tight link to the behavior as the representational perspective. Understanding the encoding of the population dynamics, and the triggering and control of temporal evolution will require further quantitative approaches.

## Dimensionality Reduction and Neural Manifold

A variety of dimensionality reduction methods have emerged, enabling selective extraction of information from high-dimensional neural data. The resulting principal components are believed to be the epitome of complex neuronal activity, as they are chosen to preserve or highlight some instructive characteristics in the data [59].

In practice, components acquired with different dimensionality reduction methods reveal different structural features of the data. For example, the most widely used method, principal component analysis (PCA) can identify components capturing the largest variance, and meanwhile orthogonal to each other, making it efficient for separating the dominant dynamics linearly. In contrast, factor analysis (FA) leads to components regarding shared variance. In addition to these two methods based on the covariance of trial-averaged neural data, there are also unsupervised methods to depict the temporal dynamics of single-trial population activity in time-series data, such as hidden Markov models (HMM), Gaussian process factor analysis (GPFA), latent linear dynamical systems (LDS), and latent nonlinear dynamical systems (NLDS). Methods to preserve dependent variables have been developed as well: linear discrimination analysis (LDA) can maximize cross-group variance compared to the within-group variance if given the number of separate groups, while demixed PCA (dPCA) gives principal components according to discrete task-relevant parameters and their possible combinations (for review, see [59–61]).

Dimensionality reduction facilitates observation and understanding by realizing the visualization of data in a low-dimensional space, for the time-varying neural activity can be represented as continuous neural trajectories or the instantaneous neural states in the space defined by principal components. For instance, the fact that the largest component detected by dPCA was nearly condition-invariant, but time-varying, suggests the apportion for neural encoding in the motor cortex [62]. In addition, the clustering and separating of neural states corresponding to different task variables in a low-dimensional space implicate distinct neural encoding rules, and thus help to distinguish different cortical regions [63].

More importantly, given that they are not actual neuronal activities, what is the connotation or essence of

these principal components? It has been speculated that these components are key elements underlying behavior-relevant firing patterns that generate motor commands. This idea is embodied in a “manifold” theory, in which a manifold appears as a stable space restricted by some potent neural activity patterns called “neural modes” (Fig. 3A) [64]. It has been reported that a consistent neural manifold serves as the base for multiple motor behaviors [65], implying the possibility of a few basic sets of neural modes shared by the neural population.

Moreover, the finding that long-term learning would induce novel neural response patterns [52], shows the flexibility of such movement-relevant manifolds. On the other hand, the perturbation on manifold or off manifold are both favored to correlational studies, as they raise mechanistic hypotheses related to behavior [66].

Furthermore, principal components suggest functional partition in high-dimensional neural dynamics. It has been reported that subspaces captured by low-dimensional neural responses in different epochs, like preparatory and movement subspaces, are nearly orthogonal to each other, demonstrating their distinguishing functions [67, 68]. Beyond these period-relevant subspaces, a new method called preferential subspace identification (PSID) has lately been developed to model the neural dynamics relevant to behavior [69]. The transitions between subspaces and their relationships are expected to promote the understanding of the neural mechanism for motor control.

## Computational Models of Neural Dynamics for Movement Generation

With the observation of common tracks for neural trajectories from single trials in the same task, the temporal evolution of the neural population is deemed to generate movement itself, other than its parametric representation. In this sense, the framework of neural dynamics, which is a subject that studies those systems evolving with time [70], has been introduced.

In fact, it is not novel to view the cortex as a dynamical system: Decades ago the dynamical systems perspective nourished central pattern generator theories for the spinal cord and an equilibrium point hypothesis for motor control [71]. However, just as the analogy between a dynamical system and mind was controversial in the 1990s [72, 73], it is intriguing today to consider the motor cortex from a dynamical system perspective.

An approach to casting the motor cortex as a dynamical system is to regard the nervous system as a machine that generates an appropriate neural response pattern to trigger the holistic movement [12]. In this framework, time-varying neuronal activities contribute to motor control as

drivers, and the temporal evolution can be independent of the kinematic or kinetic parameters. In general, the temporal pattern of neuronal activities  $r(t)$  can be described with a differential equation,

$$\tau \dot{r}(t) = h[r(t)] + u(t)$$

where the temporal derivative of neural activity  $\dot{r}$ , is modulated by a time constant  $\tau$  and impacted by the local interactions in the motor cortex  $h(\cdot)$  and the input from other brain areas  $u(t)$   $\dot{r}(t) = h[r(t)] + u(t)$  [12]. In such a system, the initial states, the synaptic inputs due to connectivity among local circuits, the external inputs, and even the time constant, all have a considerable influence on neural activities.

Nevertheless, it has not been without confusion to verify the existence of such a dynamic system. For this purpose, surrogate datasets designed randomly, but sharing certain features of the original data were built with the “corrected Fisher randomization” (CFR) and “tensor maximum entropy” (TME) methods. As a result, preserved features alone cannot reproduce the dynamical structure in real neural data [58]. Thus, although this did not directly unveil the neural dynamical system, it indicated that the neural dynamics changed with an intrinsic logic.

To uncover a neural dynamical system, one cannot avoid depicting it. For this purpose, the neural trajectories now take on new values, since they not only exhibit the real-time neural states, but also indicate trends in the phase space. Measurements of condition-varying trajectories thus offer insights into neural mechanisms. The length, speed, and curvature of single trajectories, along with the angle between them, can be calculated to test hypotheses in a differential geometric way [74, 75]. While neural trajectories from data show the actual situations, “fixed points”, as one of the most salient features of phase portraits, can be even more significant because of their ability to predict situations starting from new initial states [70]. In neuroscience, stable fixed points or attractors, corresponding to steady states or equilibria of the system, can be regarded as stable response patterns such as memory [76, 77] or appropriate states necessary for movement [78].

Finding specific neural states that reflect the dynamical system is promising, but just the beginning. It is more important, but difficult, to figure out how the system is related to the behavior. In other words, how to explain the neural mechanism with the structure of the proposed dynamical system. It has been shown that one-dimensional dynamics are enough to model the transition from spontaneous activity to delay activity in the macaque lateral intraparietal area for spatial attention diversion [79], but things get more complicated for motor control. For a specific example of arm movement, the preparatory activity has been proposed to act as the initial state of a

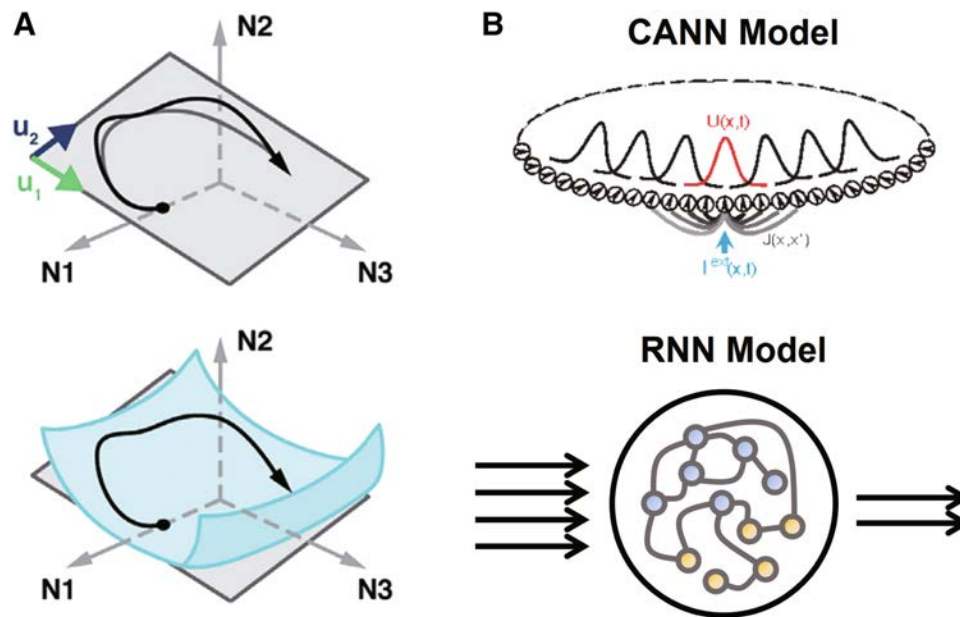


**Fig. 3** Illustration of neural manifolds and two kinds of recurrent network models. **A** Neural manifolds. The activity of three neurons (N1, N2, and N3) can be captured by a manifold spanned by two neural modes ( $u_1$  and  $u_2$ , as basic vectors). As a specific space defined by latent and shared neural activity patterns, a neural manifold can be approached by linearization despite its curvature in higher dimensions (adapted with permission from Gallego *et al.*, 2017 [64]). It is implied that the manifold underlies movement preparation and generation, because the necessary neural activity is expected to evolve on it. **B** Diagram of Continuous Attractor Neural Networks (CANNs). A CANN receives the external input  $I^{ext}(x, t)$  and the synaptic input  $U(x, t)$  at time  $t$  for neurons with preferred stimulus at  $x$ . All the model neurons are connected with each other, in a way that the difference between their preference for a stimulus determines the

strength of connectivity,  $J(x, x')$  denoting the interaction from the neuron at  $x$  to the neuron at  $x'$ , (adapted with permission from Wu S *et al.*, 2016 [88]). Therefore, this kind of recurrent network is highly structural and analytical. **C** Diagram of Recurrent Neural Networks (RNNs). The RNNs in modeling motor control now are usually based on dynamic nodes. That is, the neural nodes evolve following a differential equation, rather than being filtered by simple activation functions. The yellow dots denote the nodes with only inhibitory (negative) connections while the purple dots denote the others, as a possibility. The inputs for these networks can be external signals in step form, while the outputs so far have been EMG, velocity, and hand trajectories.

dynamical system for action [11]. In neural space, the population dynamical states converge to “a relatively tight set” after the appearance of targets (Fig. 2B). This set, called the “optimal subspace”, is supposed to benefit evolution to the desired motor command. According to the optimal subspace hypothesis, the goal of motor preparation is to set the population dynamical state into this optimal preparatory subspace [12, 80]. In fact, it is impractical to build a unified dynamical system for the entire movement generation process, for it has been demonstrated that different motor areas contain distinct neural dynamics [81]. Like the optimal subspace hypothesis, period- or location-specific dynamical systems may have more practical value at present.

Meanwhile, modeling efforts under the dynamical system perspective have been emerging [82–85]. Take the classical model of two-interval discrimination as an example. It is a simple mutual-inhibition network model that captures all task phases within a single framework. In this model, the population of neurons is simplified as an excitatory and an inhibitory node. Then the phase-plane

plot of input/output functions of these two nodes is sufficient to reveal the dynamics in each phase, including the shift of stable fixed points as well as the appearance and disappearance of line attractors [82].

While discrete attractor dynamics have recently been shown to support short-term memory associated with motor planning in mice [86], continuous attractor dynamics seem to have entered the field earlier. An early form of continuous attractor neural network (CANN) was a neural field consisting of several types of neurons as homogeneous subnets. This network could obtain equilibrium solutions without input, and react to a stimulus of stationary patterns [87]. Now CANNs (Fig. 3B, top) can be regarded as a kind of recurrent network adept at information representation, for stimuli can be encoded as their stable activity patterns (attractors). The translation-invariant connection determines this kind of network and becomes the most prominent feature [88]. In the field of motor control, CANNs have been applied to explain the encoding of continuous changing direction [89] and anticipative tracking [90].

Recurrent network models are established under the dynamical system perspective as well. Recurrent neural networks (RNNs, Fig. 3B lower), whose neurons evolve according to a group of ordinary differential equations, can generate desired EMG signal patterns after training. Moreover, the dynamics of either single neurons or the population of the model are comparable to real data [91]. In many applications, RNNs show eminent flexibility that is attributable to the adjustable connection structure [57, 92–96]. This plasticity, along with their temporal extensibility, makes RNNs the first choice for studies on the emergent property and behavior-relevant neuronal activities. Nonetheless, RNNs with fixed structural connectivity have recently been built. In an excitation-inhibition balanced recurrent network, which can generate complex movements, the neural dynamics also largely agree with experimental findings. The optimization for the stability of the connectivity in this network was guided by dynamics theory [97]. Except for being applied to build network models, mathematical knowledge and techniques in dynamics have also been introduced to open the “black box” of high-dimensional RNNs. In a theoretical study, the effect of linearization in realms of phase space around fixed points or points with very slow movements was explored. In the example cases provided, the mechanisms of networks could be deduced from linearized dynamics around these important points [98].

## Perspectives

Emerging as a new framework for understanding the neural basis of motor control, the dynamical systems perspective indeed is a complement or extension of the representational perspective, rather than a firm refutation. It emphasizes that the autonomous dynamical evolution is predominately determined by preparatory activity, consistent with the central concept in the prevalent theory of motor control, the internal model [99, 100]. Numerous behavioral and computational studies suggest that the motor program is inversely preplanned (inverse model) based on the forward model of future states, rather than adjusted online relying on continuous sensorimotor transformation during execution [101, 102]. From our point of view, dynamical evolution from initial neural states set by preparatory activity provides a plausible neural mechanism underpinning the internal model.

In principle, if the neural dynamical machine in the motor cortex autonomously generates motor commands, a cohesive motor program could be decoded from preparatory activity to rapidly drive an external actuator to implement BMIs. Although some models aimed to link neural dynamics and the muscle/arm [91, 97, 103],

remarkable advances in BMIs over the past two decades largely relied on a representational perspective [104–110]. In the current BMI framework, a decoder first is trained to find a parametric mapping between recorded neural activity and movement covariates, and then it continuously converts neural activity to control variables guiding external objects (see review, [111]). For this representative mapping, the population vector algorithm, as noted before, makes use of clear analytical relations which are intuitive and interpretable. In fact, the essence of decoders based on representational perspectives does not go beyond the population vector algorithm. Putting aside cosine tuning and Cartesian coordination, Sanger showed that the population vector can be found with the simple assumptions that neurons respond to behavior in a predictable way, and that neuronal preferences are approximately uniformly distributed in task space [112]. However, this frame is static, essentially depending on the previously-recorded fluctuating neural responses. Consequentially, movement of the actuator requires the continuous adjustment of brain-controlled signals without prior trajectory formation, unlike naturalistic movements planned in a feedforward manner, leading to unsatisfactory performance of BMIs for viable clinical applicability in terms of motion speed and smoothness (Fig. 4A, [113]).

In contrast to discriminative decoding algorithms fostered by representational perspectives that continuously translate neural signals into movement parameters, the decoders inspired by the dynamical systems perspective should be temporally generative to yield an integrative control program based on preparatory activity (Fig. 4B). Ideally, clinically feasible BMIs should be able to interact with dynamic environments in realtime, demanding a feedforward controller to produce ballistic movements [114–116]. Recently, in nonhuman primates, we tested a BMI with a generative model to intercept moving objects indicating potential advantages of feedforward control in dynamic BMI design for more biomimetic and flexible neuroprosthetics [117, 118].

So far, BMIs have distinguished themselves from a static decoder in various aspects. The good performance of current static decoders based on discriminative models may be due to neural redundancy and low task dimensionality [46, 64, 119, 120]. However, considering the limited, biased, and unstable sampling of daily neural recordings, a generative model would be preferred for a more naturalistic prosthesis.

Moreover, while a static decoder is not suitable for dynamic sensorimotor contingencies [121], novel BMIs based on neural dynamical systems enable the sophisticated integration of feedforward control and multi-modal feedback (e.g., *via* ICMS) [116, 122]. While the external device is controlled by only cortical signals, the control and

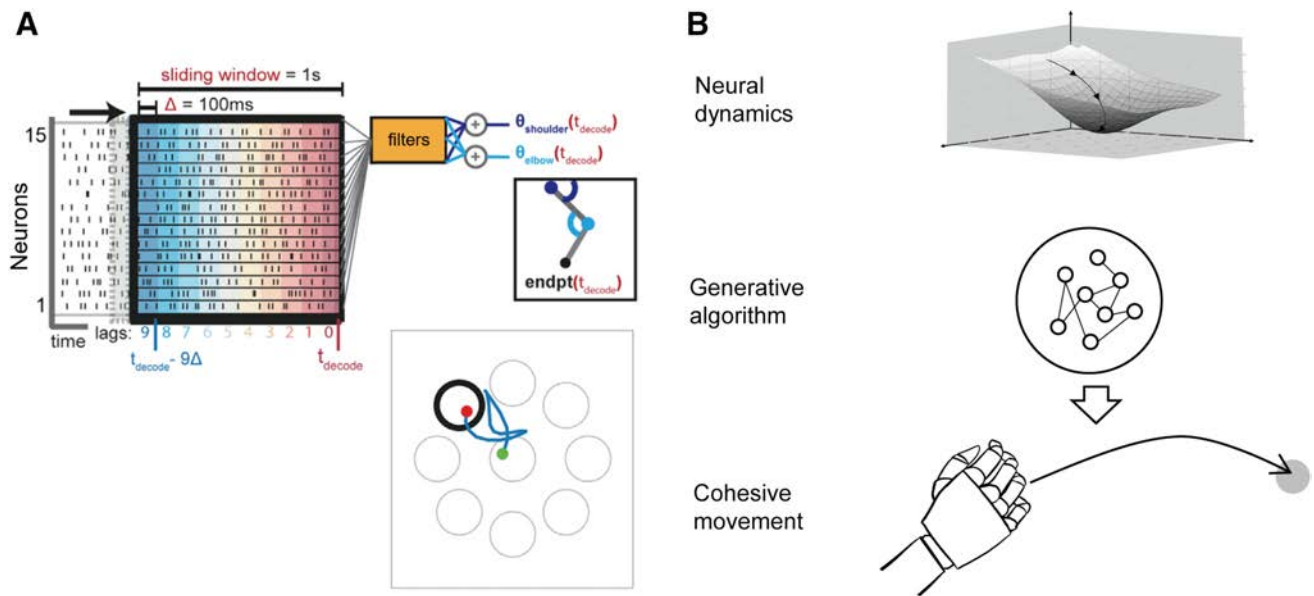


**Fig. 4** Decoding frameworks of BMIs based on representational (A) and dynamical systems (B) perspectives. **A** Neural activities within a certain sliding window ahead of the decode time  $t_{\text{decode}}$  are binned with 100 ms to form a high-dimensional matrix. BMIs based on representational perspectives usually use fixed decoders like the Wiener filter to map high-dimensional neural activities into low-dimensional control signals. From the start (green point) to the end (red point), the endpoint (endpt) trajectory (blue line) is segmented due to feedback adjustment (modified with permission from Athalye

*et al.*, 2017 [113]). **B** Schematic for BMIs from the dynamical systems perspective. This regards the motor cortex as a machine to generate proper neural activity patterns for the desired movement, and thus the movement can be implemented once the mapping between neural dynamics and concrete muscle activity is defined. In this situation, it is essential to first figure out stable neural states, for they function as attractors, and then design reliable generative algorithms (e.g. RNNs) for efficient neuron-to-muscle signal transition.

feedback of brain-controlled neuroprosthetics are different from natural movements, leading to novel neural responses [51–53, 123], suggesting an inherent difference between BMI control and neural decoding.

Furthermore, an optimistic dynamical perspective emphasizes the importance of initial state and temporal dynamics within the cortex, which subsequently triggers the detailed control program in subcortical and spinal circuitry [12, 124, 125], demanding hierarchical decoding algorithms for next-generation BMI control.

From our viewpoint, neural population dynamics and single-neuron characteristics complement each other. Neural population dynamics rely on the coordinated tuning of individual neurons, whereas single neurons must be spatiotemporally orchestrated to generate motor commands. On the other hand, the parametric representation and the dynamical systems perspectives are two sides of a coin. It is fair to suggest that the representation perspective asks, “what motor parameters are involved?”, while the dynamical system perspective focuses on “how does function evolve in time?”. Since the dynamical states can be representational [126], it is reasonable to hope that these two perspectives can be incorporated into one framework, though this will demand great effort. In the future, it will be helpful to quantitatively link neural population dynamics and holistic physical movement, as well as to identify the

recurrent neural circuitry underlying dynamical rules and external triggers for the transition from preparation to execution [127]. Studies on the initial state, local dynamics, and external inputs of a dynamical system could provide inspiration. Nevertheless, it is still unclear if neural dynamics emerge from the motor cortex alone or a larger brain network. Thus, it is important to identify the specific roles of multiple brain areas in future studies.

**Acknowledgments** We thank Q. Wang, Y. Zhang, C. Zheng, and R. Zheng for helpful comments on the manuscript. This review was supported by the National Key R&D Program (2017YFA0701102), the National Natural Science Foundation of China (31871047 and 31671075), Shanghai Municipal Science and Technology (18JC1415100 and 2018SHZDZX05), and the Strategic Priority Research Program of the Chinese Academy of Sciences (XDB32040100).

**Conflict of interest** The authors claim that there are no conflicts of interest.

**Open Access** This article is licensed under a Creative Commons Attribution 4.0 International License, which permits use, sharing, adaptation, distribution and reproduction in any medium or format, as long as you give appropriate credit to the original author(s) and the source, provide a link to the Creative Commons licence, and indicate if changes were made. The images or other third party material in this article are included in the article’s Creative Commons licence, unless indicated otherwise in a credit line to the material. If material is not included in the article’s Creative Commons licence and your intended



use is not permitted by statutory regulation or exceeds the permitted use, you will need to obtain permission directly from the copyright holder. To view a copy of this licence, visit <http://creativecommons.org/licenses/by/4.0/>.

## References

1. Penfield W. Some observations on the functional organization of the human brain. *Ideggyogy Sz* 1957, 10: 138–141.
2. Evarts EV. Relation of pyramidal tract activity to force exerted during voluntary movement. *J Neurophysiol* 1968, 31: 14–27.
3. Fetz EE, Cheney PD, German DC. Corticomotoneuronal connections of precentral cells detected by postspike averages of EMG activity in behaving monkeys. *Brain Res* 1976, 114: 505–510.
4. Georgopoulos AP, Kalaska JF, Caminiti R, Massey JT. On the relations between the direction of two-dimensional arm movements and cell discharge in primate motor cortex. *J Neurosci* 1982, 2: 1527–1537.
5. Inoue Y, Mao HW, Suway SB, Orellana J, Schwartz AB. Decoding arm speed during reaching. *Nat Commun* 2018, 9: 5243.
6. Churchland MM, Santhanam G, Shenoy KV. Preparatory activity in premotor and motor cortex reflects the speed of the upcoming reach. *J Neurophysiol* 2006, 96: 3130–3146.
7. Hatsopoulos NG, Xu QQ, Amit Y. Encoding of movement fragments in the motor cortex. *J Neurosci* 2007, 27: 5105–5114.
8. Schaffelhofer S, Scherberger H. Object vision to hand action in macaque parietal, premotor, and motor cortices. *Elife* 2016, 5: e15278.
9. Kettner RE, Marcario JK, Port NL. Control of remembered reaching sequences in monkey. II. Storage and preparation before movement in motor and premotor cortex. *Exp Brain Res* 1996, 112: 347–358.
10. Churchland MM, Shenoy KV. Temporal complexity and heterogeneity of single-neuron activity in premotor and motor cortex. *J Neurophysiol* 2007, 97: 4235–4257.
11. Churchland MM, Cunningham JP, Kaufman MT, Ryu SI, Shenoy KV. Cortical preparatory activity: Representation of movement or first cog in a dynamical machine? *Neuron* 2010, 68: 387–400.
12. Shenoy KV, Sahani M, Churchland MM. Cortical control of arm movements: A dynamical systems perspective. *Annu Rev Neurosci* 2013, 36: 337–359.
13. Gross CG. The discovery of motor cortex and its background. *J Hist Neurosci* 2007, 16: 320–331.
14. Dum RP, Strick PL. The origin of corticospinal projections from the premotor areas in the frontal lobe. *J Neurosci* 1991, 11: 667–689.
15. Picard N, Strick PL. Imaging the premotor areas. *Curr Opin Neurobiol* 2001, 11: 663–672.
16. Shinoda Y, Yokota J, Futami T. Divergent projection of individual corticospinal axons to motoneurons of multiple muscles in the monkey. *Neurosci Lett* 1981, 23: 7–12.
17. Wise SP, Boussaoud D, Johnson PB, Caminiti R. Premotor and parietal cortex: Corticocortical connectivity and combinatorial computations. *Annu Rev Neurosci* 1997, 20: 25–42.
18. Riehle A, Vaadia E (2005) Motor Cortex in Voluntary Movements: A Distributed System for Distributed Functions. CRC Press, Boca Raton.
19. Schmammann JD, Guell X, Stoodley CJ, Halko MA. The theory and neuroscience of cerebellar cognition. *Annu Rev Neurosci* 2019, 42: 337–364.
20. Dacre J, Colligan M, Clarke T, Ammer JJ, Schiemann J, Chamosa-Pino V. A cerebellar-thalamocortical pathway drives behavioral context-dependent movement initiation. *Neuron* 2021, 109: 2326–2338.e8.
21. Percheron G, François C, Talbi B, Yelnik J, Fénelon G. The primate motor thalamus. *Brain Res Brain Res Rev* 1996, 22: 93–181.
22. Ilinsky IA, Kultas-Ilinsky K. Sagittal cytoarchitectonic maps of the *Macaca mulatta* thalamus with a revised nomenclature of the motor-related nuclei validated by observations on their connectivity. *J Comp Neurol* 1987, 262: 331–364.
23. Evarts EV. Activity of pyramidal tract neurons during postural fixation. *J Neurophysiol* 1969, 32: 375–385.
24. Li CS, Padoa-Schioppa C, Bizzi E. Neuronal correlates of motor performance and motor learning in the primary motor cortex of monkeys adapting to an external force field. *Neuron* 2001, 30: 593–607.
25. Rokni U, Richardson AG, Bizzi E, Seung HS. Motor learning with unstable neural representations. *Neuron* 2007, 54: 653–666.
26. Georgopoulos AP, Schwartz AB, Kettner RE. Neuronal population coding of movement direction. *Science* 1986, 233: 1416–1419.
27. Georgopoulos AP, Kettner RE, Schwartz AB. Primate motor cortex and free arm movements to visual targets in three-dimensional space. II. Coding of the direction of movement by a neuronal population. *J Neurosci* 1988, 8: 2928–2937.
28. Schwartz AB, Moran DW. Motor cortical activity during drawing movements: Population representation during lemniscate tracing. *J Neurophysiol* 1999, 82: 2705–2718.
29. Kakei S, Hoffman DS, Strick PL. Muscle and movement representations in the primary motor cortex. *Science* 1999, 285: 2136–2139.
30. Kalaska JF, Crammond DJ. Cerebral cortical mechanisms of reaching movements. *Science* 1992, 255: 1517–1523.
31. Caminiti R, Johnson PB, Galli C, Ferraina S, Burnod Y. Making arm movements within different parts of space: The premotor and motor cortical representation of a coordinate system for reaching to visual targets. *J Neurosci* 1991, 11: 1182–1197.
32. Suway SB, Orellana J, McMorland AJC, Fraser GW, Liu Z, Velliste M, *et al.* Temporally segmented directionality in the motor cortex. *Cereb Cortex* 2018, 28: 2326–2339.
33. Ferrier D, Burdon-Sanderson JS. Experiments on the brain of monkeys. *Proc R Soc Lond* 1875, 23: 409–430.
34. Ferrier D. Experimental researches in cerebral physiology and pathology. *J Anat Physiol* 1873, 8: 152–155.
35. Graziano MSA, Taylor CSR, Moore T. Complex movements evoked by microstimulation of precentral cortex. *Neuron* 2002, 34: 841–851.
36. Graziano M. The organization of behavioral repertoire in motor cortex. *Annu Rev Neurosci* 2006, 29: 105–134.
37. Moran DW, Schwartz AB. Motor cortical representation of speed and direction during reaching. *J Neurophysiol* 1999, 82: 2676–2692.
38. Kakei S, Hoffman DS, Strick PL. Sensorimotor transformations in cortical motor areas. *Neurosci Res* 2003, 46: 1–10.
39. Salinas E, Abbott LF. Vector reconstruction from firing rates. *J Comput Neurosci* 1994, 1: 89–107.
40. Ajemian R, Bullock D, Grossberg S. A model of movement coordinates in the motor cortex: Posture-dependent changes in the gain and direction of single cell tuning curves. *Cereb Cortex* 2001, 11: 1124–1135.
41. Baraduc P, Guigon E, Burnod Y. Recoding arm position to learn visuomotor transformations. *Cereb Cortex* 2001, 11: 906–917.
42. Schwartz AB. Motor cortical activity during drawing movements: Population representation during sinusoid tracing. *J Neurophysiol* 1993, 70: 28–36.
43. Rossi-Pool R, Zainos A, Alvarez M, Zizumbo J, Vergara J, Romo R. Decoding a decision process in the neuronal population of dorsal premotor cortex. *Neuron* 2017, 96: 1432–1446.e7.

44. Sanger TD. Optimal unsupervised motor learning for dimensionality reduction of nonlinear control systems. *IEEE Trans Neural Netw* 1994, 5: 965–973.
45. Rigotti M, Barak O, Warden MR, Wang XJ, Daw ND, Miller EK, *et al.* The importance of mixed selectivity in complex cognitive tasks. *Nature* 2013, 497: 585–590.
46. Fusi S, Miller EK, Rigotti M. Why neurons mix: High dimensionality for higher cognition. *Curr Opin Neurobiol* 2016, 37: 66–74.
47. Eyherabide HG, Samengo I. When and why noise correlations are important in neural decoding. *J Neurosci* 2013, 33: 17921–17936.
48. Kanitscheider I, Coen-Cagli R, Pouget A. Origin of information-limiting noise correlations. *Proc Natl Acad Sci U S A* 2015, 112: E6973–E6982.
49. Scott SH, Gribble PL, Graham KM, Cabel DW. Dissociation between hand motion and population vectors from neural activity in motor cortex. *Nature* 2001, 413: 161–165.
50. Sadtler PT, Quick KM, Golub MD, Chase SM, Ryu SI, Tyler-Kabara EC, *et al.* Neural constraints on learning. *Nature* 2014, 512: 423–426.
51. Hennig JA, Golub MD, Lund PJ, Sadtler PT, Oby ER, Quick KM, *et al.* Constraints on neural redundancy. *Elife* 2018, 7: e36774.
52. Oby ER, Golub MD, Hennig JA, Degenhart AD, Tyler-Kabara EC, Yu BM, *et al.* New neural activity patterns emerge with long-term learning. *Proc Natl Acad Sci U S A* 2019, 116: 15210–15215.
53. Golub MD, Sadtler PT, Oby ER, Quick KM, Ryu SI, Tyler-Kabara EC, *et al.* Learning by neural reassociation. *Nat Neurosci* 2018, 21: 607–616.
54. Churchland MM, Cunningham JP, Kaufman MT, Foster JD, Nuyujukian P, Ryu SI, *et al.* Neural population dynamics during reaching. *Nature* 2012, 487: 51–56.
55. Willett FR, Deo DR, Avansino DT, Rezaii P, Hochberg LR, Henderson JM, *et al.* Hand knob area of premotor cortex represents the whole body in a compositional way. *Cell* 2020, 181: 396–409.e26.
56. Lebedev MA, Ossadtchi A, Mill NA, Urpí NA, Cervera MR, Nicolelis MAL. Analysis of neuronal ensemble activity reveals the pitfalls and shortcomings of rotation dynamics. *Sci Rep* 2019, 9: 18978.
57. Michaels JA, Dann B, Scherberger H. Neural population dynamics during reaching are better explained by a dynamical system than representational tuning. *PLoS Comput Biol* 2016, 12: e1005175.
58. Elsayed GF, Cunningham JP. Structure in neural population recordings: An expected byproduct of simpler phenomena? *Nat Neurosci* 2017, 20: 1310–1318.
59. Cunningham JP, Yu BM. Dimensionality reduction for large-scale neural recordings. *Nat Neurosci* 2014, 17: 1500–1509.
60. Cunningham JP, Ghahramani Z. Linear dimensionality reduction: Survey, insights, and generalizations. *J Mach Learn Res* 2015, 16: 2859–2900.
61. Kobak D, Brendel W, Constantinidis C, Feierstein CE, Kepecs A, Mainen ZF, *et al.* Demixed principal component analysis of neural population data. *Elife* 2016, 5: e10989.
62. Kaufman MT, Seely JS, Sussillo D, Ryu SI, Shenoy KV, Churchland MM. The largest response component in the motor cortex reflects movement timing but not movement type. *eNeuro* 2016, 3: ENEURO.0085-16.2016.
63. Parthasarathy A, Herikstad R, Bong JH, Medina FS, Libedinsky C, Yen SC. Mixed selectivity morphs population codes in prefrontal cortex. *Nat Neurosci* 2017, 20: 1770–1779.
64. Gallego JA, Perich MG, Miller LE, Solla SA. Neural manifolds for the control of movement. *Neuron* 2017, 94: 978–984.
65. Gallego JA, Perich MG, Naufel SN, Ethier C, Solla SA, Miller LE. Cortical population activity within a preserved neural manifold underlies multiple motor behaviors. *Nat Commun* 2018, 9: 4233.
66. Jazayeri M, Afraz A. Navigating the neural space in search of the neural code. *Neuron* 2017, 93: 1003–1014.
67. Kaufman MT, Churchland MM, Ryu SI, Shenoy KV. Cortical activity in the null space: Permitting preparation without movement. *Nat Neurosci* 2014, 17: 440–448.
68. Elsayed GF, Lara AH, Kaufman MT, Churchland MM, Cunningham JP. Reorganization between preparatory and movement population responses in motor cortex. *Nat Commun* 2016, 7: 13239.
69. Sani OG, Abbaspourazad H, Wong YT, Pesaran B, Shanechi MM. Modeling behaviorally relevant neural dynamics enabled by preferential subspace identification. *Nat Neurosci* 2021, 24: 140–149.
70. Strogatz SH. *Nonlinear Dynamics and Chaos: with Applications to Physics, Biology, Chemistry, and Engineering*. 2nd ed., CRC Press, 2018.
71. Sternad D. Debates in dynamics: A dynamical systems perspective on action and perception. *Hum Mov Sci* 2000, 19: 407–423.
72. van Gelder T. What might cognition Be, if not computation? *J Philos* 1995, 92: 345–381.
73. Eliasmith C. Computation and dynamical models of mind. *Minds Mach* 1997, 7: 531–541.
74. Remington ED, Narain D, Hosseini EA, Jazayeri M. Flexible sensorimotor computations through rapid reconfiguration of cortical dynamics. *Neuron* 2018, 98: 1005–1019.e5.
75. Wang J, Narain D, Hosseini EA, Jazayeri M. Flexible timing by temporal scaling of cortical responses. *Nat Neurosci* 2018, 21: 102–110.
76. Hopfield JJ. Neural networks and physical systems with emergent collective computational abilities. *Proc Natl Acad Sci U S A* 1982, 79: 2554–2558.
77. Wimmer K, Nykamp DQ, Constantinidis C, Compte A. Bump attractor dynamics in prefrontal cortex explains behavioral precision in spatial working memory. *Nat Neurosci* 2014, 17: 431–439.
78. Churchland MM, Yu BM, Cunningham JP, Sugrue LP, Cohen MR, Corrado GS, *et al.* Stimulus onset quenches neural variability: A widespread cortical phenomenon. *Nat Neurosci* 2010, 13: 369–378.
79. Ganguli S, Bisley JW, Roitman JD, Shadlen MN, Goldberg ME, Miller KD. One-dimensional dynamics of attention and decision making in LIP. *Neuron* 2008, 58: 15–25.
80. Churchland MM, Yu BM, Ryu SI, Santhanam G, Shenoy KV. Neural variability in premotor cortex provides a signature of motor preparation. *J Neurosci* 2006, 26: 3697–3712.
81. Lara AH, Cunningham JP, Churchland MM. Different population dynamics in the supplementary motor area and motor cortex during reaching. *Nat Commun* 2018, 9: 2754.
82. Machens CK, Romo R, Brody CD. Flexible control of mutual inhibition: A neural model of two-interval discrimination. *Science* 2005, 307: 1121–1124.
83. Wong KF, Huk AC, Shadlen MN, Wang XJ. Neural circuit dynamics underlying accumulation of time-varying evidence during perceptual decision making. *Front Comput Neurosci* 2007, 1: 6.
84. Barak O, Sussillo D, Romo R, Tsodyks M, Abbott LF. From fixed points to chaos: Three models of delayed discrimination. *Prog Neurobiol* 2013, 103: 214–222.
85. Hennequin G, Ahmadian Y, Rubin DB, Lengyel M, Miller KD. The dynamical regime of sensory cortex: Stable dynamics around a single stimulus-tuned attractor account for patterns of noise variability. *Neuron* 2018, 98: 846–860.e5.

86. Inagaki HK, Fontolan L, Romani S, Svoboda K. Discrete attractor dynamics underlies persistent activity in the frontal cortex. *Nature* 2019, 566: 212–217.
87. Amari SI. Dynamics of pattern formation in lateral-inhibition type neural fields. *Biol Cybern* 1977, 27: 77–87.
88. Wu S, Wong KYM, Fung CCA, Mi YY, Zhang WH. Continuous attractor neural networks: Candidate of a canonical model for neural information representation. *F1000Res* 2016, 5.
89. Georgopoulos AP, Taira M, Lukashin A. Cognitive neurophysiology of the motor cortex. *Science* 1993, 260: 47–52.
90. Mi Y, Fung CCA, Wong KYM, Wu S. Spike frequency adaptation implements anticipative tracking in continuous attractor neural networks. *Front Comput Neurosci* 2014, 1: 505–513.
91. Sussillo D, Churchland MM, Kaufman MT, Shenoy KV. A neural network that finds a naturalistic solution for the production of muscle activity. *Nat Neurosci* 2015, 18: 1025–1033.
92. Hardy NF, Goudar V, Romero-Sosa JL, Buonomano DV. A model of temporal scaling correctly predicts that motor timing improves with speed. *Nat Commun* 2018, 9: 4732.
93. Goudar V, Buonomano DV. Encoding sensory and motor patterns as time-invariant trajectories in recurrent neural networks. *Elife* 2018, 7: e31134.
94. Russo AA, Bittner SR, Perkins SM, Seely JS, London BM, Lara AH, *et al.* Motor cortex embeds muscle-like commands in an untangled population response. *Neuron* 2018, 97: 953–966.e8.
95. Zimnik AJ, Churchland MM. Independent generation of sequence elements by motor cortex. *Nat Neurosci* 2021, 24: 412–424.
96. Song HF, Yang GR, Wang XJ. Reward-based training of recurrent neural networks for cognitive and value-based tasks. *Elife* 2017, 6: e21492.
97. Hennequin G, Vogels TP, Gerstner W. Optimal control of transient dynamics in balanced networks supports generation of complex movements. *Neuron* 2014, 82: 1394–1406.
98. Sussillo D, Barak O. Opening the black box: Low-dimensional dynamics in high-dimensional recurrent neural networks. *Neural Comput* 2013, 25: 626–649.
99. Wolpert DM, Ghahramani Z, Jordan MI. An internal model for sensorimotor integration. *Science* 1995, 269: 1880–1882.
100. Shadmehr R, Mussa-Ivaldi FA. Adaptive representation of dynamics during learning of a motor task. *J Neurosci* 1994, 14: 3208–3224.
101. Sheahan HR, Franklin DW, Wolpert DM. Motor planning, not execution, separates motor memories. *Neuron* 2016, 92: 773–779.
102. McNamee D, Wolpert DM. Internal models in biological control. *Annu Rev Control Robot Auton Syst* 2019, 2: 339–364.
103. Stroud JP, Porter MA, Hennequin G, Vogels TP. Motor primitives in space and time *via* targeted gain modulation in cortical networks. *Nat Neurosci* 2018, 21: 1774–1783.
104. Serruya MD, Hatsopoulos NG, Paninski L, Fellows MR, Donoghue JP. Instant neural control of a movement signal. *Nature* 2002, 416: 141–142.
105. Musallam S, Corneil BD, Greger B, Scherberger H, Andersen RA. Cognitive control signals for neural prosthetics. *Science* 2004, 305: 258–262.
106. Carmena JM, Lebedev MA, Crist RE, O'Doherty JE, Santucci DM, Dimitrov DF, *et al.* Learning to control a brain-machine interface for reaching and grasping by Primates. *PLoS Biol* 2003, 1: E42.
107. Hochberg LR, Serruya MD, Friehs GM, Mukand JA, Saleh M, Caplan AH, *et al.* Neuronal ensemble control of prosthetic devices by a human with tetraplegia. *Nature* 2006, 442: 164–171.
108. Santhanam G, Ryu SI, Yu BM, Afshar A, Shenoy KV. A high-performance brain-computer interface. *Nature* 2006, 442: 195–198.
109. Velliste M, Perel S, Spalding MC, Whitford AS, Schwartz AB. Cortical control of a prosthetic arm for self-feeding. *Nature* 2008, 453: 1098–1101.
110. Aflalo T, Kellis S, Klaes C, Lee B, Shi Y, Pejsa K, *et al.* Neurophysiology. Decoding motor imagery from the posterior parietal cortex of a tetraplegic human. *Science* 2015, 348: 906–910.
111. Lebedev MA, Nicolelis MAL. Brain-machine interfaces: From basic science to neuroprostheses and neurorehabilitation. *Physiol Rev* 2017, 97: 767–837.
112. Sanger TD. Theoretical considerations for the analysis of population coding in motor cortex. *Neural Comput* 1994, 6: 29–37.
113. Athalye VR, Ganguly K, Costa RM, Carmena JM. Emergence of coordinated neural dynamics underlies neuroprosthetic learning and skillful control. *Neuron* 2017, 93: 955–970.e5.
114. Cui H. Forward prediction in the posterior parietal cortex and dynamic brain-machine interface. *Front Integr Neurosci* 2016, 10: 35.
115. Li YH, Wang Y, Cui H. Eye-hand coordination during flexible manual interception of an abruptly appearing, moving target. *J Neurophysiol* 2018, 119: 221–234.
116. Pandarinath C, Ames KC, Russo AA, Farshchian A, Miller LE, Dyer EL, *et al.* Latent factors and dynamics in motor cortex and their application to brain-machine interfaces. *J Neurosci* 2018, 38: 9390–9401.
117. Li CY, Zhang YH, Wang TW, Xu XX, Wang QF, Xu B, *et al.* Generative decoding of intracortical neuronal signals for online control of robotic arm to intercept moving objects. *J Phys: Conf Ser* 2020, 1576: 012057.
118. Lan N, Hao MZ, Niu CM, Cui H, Wang Y, Zhang T, *et al.* Next-generation prosthetic hand: From biomimetic to biorealistic. *Research (Wash D C)*, 2021: 4675326.
119. Braun DA, Wolpert DM. Optimal control: When redundancy matters. *Curr Biol* 2007, 17: R973–R975.
120. Franklin DW, Wolpert DM. Computational mechanisms of sensorimotor control. *Neuron* 2011, 72: 425–442.
121. Xu MP, Meng JY, Yu HQ, Jung TP, Ming D. Dynamic brain responses modulated by precise timing prediction in an opposing process. *Neurosci Bull* 2021, 37: 70–80.
122. Flesher SN, Downey JE, Weiss JM, Hughes CL, Herrera AJ, Tyler-Kabara EC, *et al.* A brain-computer interface that evokes tactile sensations improves robotic arm control. *Science* 2021, 372: 831–836.
123. Sakellari S, Christopoulos VN, Aflalo T, Pejsa KW, Rosario ER, Ouellette D, *et al.* Intrinsic variable learning for brain-machine interface control by human anterior intraparietal cortex. *Neuron* 2019, 102: 694–705.e3.
124. Wenger N, Moraud EM, Gandar J, Musienko P, Capogrosso M, Baud L, *et al.* Spatiotemporal neuromodulation therapies engaging muscle synergies improve motor control after spinal cord injury. *Nat Med* 2016, 22: 138–145.
125. Wagner FB, Mignardot JB, le Goff-Mignardot CG, Demesmaeker R, Komi S, Capogrosso M, *et al.* Targeted neurotechnology restores walking in humans with spinal cord injury. *Nature* 2018, 563: 65–71.
126. Bechtel W. Representing time of day in circadian clocks. *Knowledge and representation* 2011: 129–162.
127. Sauerbrei BA, Guo JZ, Cohen JD, Mischiati M, Guo W, Kabra M, *et al.* Cortical pattern generation during dexterous movement is input-driven. *Nature* 2020, 577: 386–391.
128. Kandel ER, Mack S, Jessell TM, Schwartz JH, Siegelbaum SA, Hudspeth AJ. *Principles of Neural Science*, 5th ed. McGraw-Hill Education, 2013.

REVIEW

# Factors Influencing Alzheimer's Disease Risk: Whether and How They are Related to the APOE Genotype

Rong Zhang<sup>1</sup> · Xiaojiao Xu<sup>1</sup> · Hang Yu<sup>1</sup> · Xiaolan Xu<sup>1</sup> · Manli Wang<sup>1</sup> · Weidong Le<sup>1</sup> 

Received: 18 October 2021 / Accepted: 25 November 2021 / Published online: 11 February 2022  
© The Author(s) 2022

**Abstract** Alzheimer's disease (AD) is the most prevalent neurodegenerative disease featuring progressive cognitive impairment. Although the etiology of late-onset AD remains unclear, the close association of AD with apolipoprotein E (APOE), a gene that mainly regulates lipid metabolism, has been firmly established and may shed light on the exploration of AD pathogenesis and therapy. However, various confounding factors interfere with the APOE-related AD risk, raising questions about our comprehension of the clinical findings concerning APOE. In this review, we summarize the most debated factors interacting with the APOE genotype and AD pathogenesis, depict the extent to which these factors relate to APOE-dependent AD risk, and discuss the possible underlying mechanisms.

**Keywords** Apolipoprotein E · Alzheimer's disease · Ethnicity · Diet · Geographic factor · Aging · Gender

## Background

Alzheimer's disease (AD) is one of the most prevalent and influential neurodegenerative diseases, characterized by typical pathological findings of beta-amyloid (A $\beta$ ) and tau plaques [1, 2]. Featuring irreversible and progressive deterioration of cognitive function and mainly affecting

the elderly, AD imposes an enormous burden on patients, communities, and healthcare systems. Unfortunately, as life expectancy increases, the population of AD patients is expanding rapidly. The number of AD patients in the USA is estimated to grow from 4.7 million to 13.8 million from 2010 to 2050 [3]. Other countries are believed to be confronted with a similar impact of AD.

Apolipoprotein E (APOE) is a multifunction protein that plays a crucial role in the intercellular and interstitial transport of lipid and the mediation of dynamic lipid levels and lipid metabolism [4]. APOE fulfills its function by forming a close connection with lipoproteins and their receptors. Besides, APOE is also involved in neurophysiological processes such as synapse development and remodeling. Two vital single nucleotide polymorphisms (SNPs) located in APOE coding regions, rs429358 (C>T) and rs7412 (C>T), define the three major subtypes of APOE allele,  $\epsilon$ 2,  $\epsilon$ 3, and  $\epsilon$ 4. Alteration of  $\epsilon$ 2,  $\epsilon$ 3, and  $\epsilon$ 4 confers crucial variation on the protein structure of APOE, its physiological function, and its effect on related diseases [5, 6]. Besides its crucial effect on lipid metabolism,  $\epsilon$ 4 is the first, by far the most relevant and the most intensively studied risk gene for late-onset AD [6, 7]. APOE  $\epsilon$ 4 carriers have a higher lifetime incidence of AD and an earlier onset. In rough estimation, Farrer *et al.* found that individuals who carry one  $\epsilon$ 4 allele bear a 2–4 fold AD risk, and those with two copies of  $\epsilon$ 4 have an 8–12 fold AD risk [8].

Since the close association of APOE and AD was explicitly established in 1993, many studies have explored the underlying mechanism. Although the exact mechanism remains obscure, it is widely acknowledged that APOE is extensively involved in various pathologic processes of AD. (1) A $\beta$ -dependent pathways: APOE-related AD risk can be largely attributed to an alteration of protein deposition, for the APOE genotype is no longer

✉ Weidong Le  
wdle@sibs.ac.cn

<sup>1</sup> Institute of Neurology, Sichuan Academy of Medical Sciences, Sichuan Provincial People's Hospital, University of Electronic Science and Technology of China, Chengdu 611731, China

significantly associated with the clinical phenotype after controlling for AD pathology [9]. *APOE*  $\epsilon 4$  carriers and  $\epsilon 4$  knock-in mice both manifest exacerbated A $\beta$  proteinopathy [10, 11]. Experiments showed that ApoE/APOE co-precipitates with A $\beta$  in mice and AD patients [12], APOE  $\epsilon 4$  may facilitate the aggregation both *in vitro* and *in vivo* [13, 14]. Researchers also reported the more rapid formation of A $\beta$  oligomer as well as slower clearance of A $\beta$  in  $\epsilon 4$  knock-in rats, which corresponds with the results from studies in APOE  $\epsilon 4$  cells [15–17]. (2) A $\beta$ -independent pathways: APOE  $\epsilon 4$  can up-regulate neuroinflammation, as reported in  $\epsilon 4$  carriers and knock-in mice [18, 19], possibly through regulation of glia [20–22]. APOE  $\epsilon 4$  is harmful to the integrity of the blood-brain barrier in mice [23], and blood-brain barrier impairment of the hippocampus and medial temporal lobe, correlated with cognitive dysfunction, has been reported in human  $\epsilon 4$  carriers. Besides, the APOE genotype may alter the production of brain-derived neurotrophic factor and neuroprotective sirtuin, as well as energy expenditure [24–26].

APOE-related AD risk can be influenced by various factors, such as ancestry, gender, environment, and diet. These factors may exert their influence through distinct mechanisms such as regulation of transcription or expression of APOE, alteration of lipid metabolism, impacting the AD pathological process in which APOE is deeply involved. Previous epidemiological research provides abundant evidence to understand how these factors interact with APOE-related AD risk and the possible physiological explanation of these interactions. Here, we provide an overall review of the most debated confounding factors and discuss how they are connected to APOE and the pathogenesis of AD (Fig. 1).

## Ethnicity and APOE

The rough frequency ranges of the APOE  $\epsilon 2/3/4$  alleles are (0–7%)/(69–85%)/(4–40%) across the world [7], but this ratio varies significantly among different ethnicities (Table 1). Generally, the frequency of the  $\epsilon 2$  allele is relatively constant, which leads to the negative correlation of the  $\epsilon 3$  and  $\epsilon 4$  alleles [27]. The APOE  $\epsilon 4$  allele comprises a larger proportion in Central Africa (40%), Oceania (37%), and Australia (26%), while in Europe and Asia, the  $\epsilon 4$  allele frequency ranges from 10% to 25%, roughly positively related to the latitude of residence [7].

The ethnic background has a certain impact on AD risk, based on numerous epidemiological studies (Table 1). A 7-year longitudinal study based on the multi-ethnic population in New York established that, compared with Caucasians, African-American people [hazard ratio (HR) = 2.6] and Caribbean Hispanic people (HR = 2.3) are

confronted with a significantly higher risk of AD [32]. Later, the cohort study conducted in Northern California included six ethnic groups further demonstrated that Asian Americans have the lowest incidence of AD, followed by Caucasians, Pacific Islanders, and Latin Americans (HR = 1.25–1.29), then American Indians (HR = 1.43), and the most affected African Americans (HR = 1.73) [33]. Kevin and his team summarized 28,027,071 beneficiaries of the Medicare Fee-for-Service to estimate the prevalence of AD and related dementias in different subgroups. The result showed that the order of ethnicities with prevalence from low to high is Asian and Pacific Islanders (8.4%), American Indians and Alaska Natives (9.1%), non-Hispanic Caucasians (10.3%), Hispanics (12.2%), and African Americans (13.8%) [34]. Since these studies included and analyzed several confounding factors such as educational level, vascular diseases, and other comorbidities, the authors made it clear that the inequalities in AD incidence most likely result from the diversity of ethnic genetic backgrounds.

The meta-analysis by Farrer and colleagues found that African and Hispanic  $\epsilon 4$  carriers, compared with Caucasian  $\epsilon 4$  carriers, have a lower APOE-related AD risk [8]. Meanwhile, Japanese  $\epsilon 4$  carriers have an even higher odds ratio than Caucasian Americans. The data roughly showed that, with respect to ancestry difference, APOE  $\epsilon 4$  frequency is inversely associated with the  $\epsilon 4$ -related AD risk, implying that the APOE gene polymorphism partially contributes to the vulnerability to diseases like AD. In two cohort studies by Tang *et al.* and Evans *et al.*, APOE  $\epsilon 4$  was found to cause a lower increase in AD incidence in Africans than in Caucasians, despite African Americans bearing higher basal AD incidence [32, 35].

The mechanisms underlying the distinct ancestry-specific  $\epsilon 4$ -related AD risk remains unclear, but genetic research has provided insightful explanations regarding this issue. By comparing the association between SNPs and odds ratios in respect of AD, researchers have found that variations in the region surrounding the APOE gene accounts for most of the ethnicity-specific APOE effect on AD. Blue *et al.* compared 3,067 Caribbean Hispanics with 3,028 Europeans concerning the APOE genotype, local ancestry, genome-wide ancestry, and AD risk [36]. They discovered that local ancestry shows the strongest association (odds ratio, OR = 0.61) with AD risk other than the  $\epsilon 4\epsilon 4$  genotype (OR = 8.59), while the impact of genome-wide ancestry is much less (OR = 1.004). Rajabli *et al.* used 5,496 African American and 389 Puerto Rican individuals to analyze the effect of local ancestry and global ancestry on APOE  $\epsilon 4$ -related AD risk. They found that only local ancestry has a significant influence ( $P$  = 0.019) [37]. Cornejo-Olivas *et al.* conducted genome-wide genotyping in the Peruvian population. They reported that



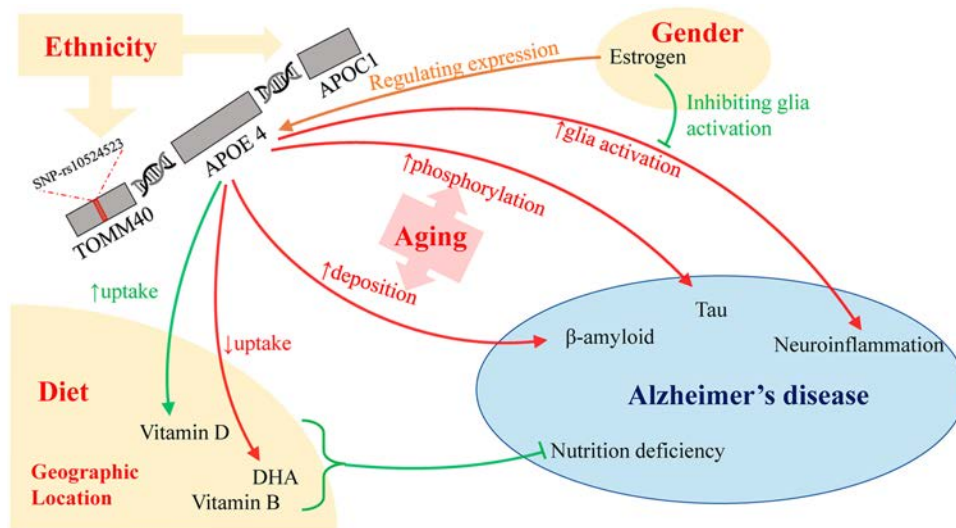


**Fig. 1** Interaction of confounding factors with the APOE  $\epsilon 4$  allele and Alzheimer's disease (AD). APOE  $\epsilon 4$  influences AD through regulation of  $\beta$ -amyloid and tau deposition, neuroinflammation, and neuronal nutrition. Confounding factors may influence the  $\epsilon 4$ -AD association through the following mechanisms: ethnicity impacts the local ancestry of the APOE gene and thus AD risk; gender acts with

the effects of hormones, mainly estrogen, to change APOE expression and neuroinflammation; aging directly enhances proteinopathy; diet and geographic location alter the nutritional status, jointly with APOE. APOE, apolipoprotein E; TOMM40, Translocase of the Outer Mitochondrial Membrane 40; APOC1, apolipoprotein C1; DHA, docosahexaenoic acid.

the ancestry local to the *APOE* gene, rather than the whole genome background, contributes to the  $\epsilon 4$ -related AD risk [38]. Conversely, a few studies have reported that the heterogeneous ancestry-specific *APOE*  $\epsilon 4$  effect may be derived from different genetic backgrounds or environments. Blue *et al.* noted that European carriers have a three times higher OR than the Hispanic population even when they share the same origin of  $\epsilon 4$  allele [36]. By genetic screening in specific Arabic populations with high AD incidence, Farrer and colleagues discovered that the elevated AD risk has little connection with  $\epsilon 4$  but plausible connections with other genetic or environmental factors [39].

To further understand why genetic polymorphisms local to the *APOE* gene cause ethnic differences, we might first turn to genome-wide association sequencing and phylogenetic research regarding the detection of AD risk factors. To date, the polymorphisms found most relevant to *APOE* and AD are in the sequences of Translocase of the Outer Mitochondrial Membrane 40 (TOMM40) and apolipoprotein C1 (APOC1), two flanking genes on each side of the *APOE* region. In 1998, Lai and colleagues finished mapping SNPs around *APOE* and established a 4-Mb high-density sequence containing 121 SNPs [40]. Later, their team tested these SNPs for their relevance to AD and identified 2 SNPs in the TOMM40 gene showing a strong association with both  $\epsilon 4$  allele and AD risk [41]. Roses *et al.* reported one polymorphism, rs10524523, located in intron 6 of TOMM40, defined by the length of its polyT tract, to be closely associated with the age at AD onset

[42]. After that, surging amounts of evidence showing the interaction between TOMM40 and AD have been published, suggesting that the TOMM40/*APOE* alleles are better predictors of disease onset than *APOE* alone [43]. Interestingly, the rs10524523 polymorphism is significantly distinct between different ethnicities, which might explain the inconsistent effect of *APOE* polymorphism on ethnicity [43]. Specifically, about half of the *APOE*  $\epsilon 4$  alleles of African Americans are linked with the S allele of TOMM40, which is associated with a lower risk or reduced onset of AD than its counterpart, the L allele. In contrast, only 2% of the *APOE*  $\epsilon 4$  alleles of Caucasians are linked with the S allele. However, whether the action of TOMM40 polymorphism depends on APOE remains obscure. Although Caselli *et al.* reported that TOMM40 influences the decline in cognitive performance in non-AD subjects in an *APOE*-independent manner [44], more evidence is required to verify the interaction between *APOE* and TOMM40. These two genes are in linkage disequilibrium. Zhou *et al.* reported that variation in APOC1 confers an  $\epsilon 4$ -independent risk of AD, and the distribution of the APOC1 polymorphism, not surprisingly, varies significantly in different ethnicities [45]. To sum up, polymorphisms in TOMM40 and APOC1 may explain ethnicity-related AD risks, but the underlying mechanisms need further studies.

**Table 1** Frequency of APOE  $\epsilon 4$  allele in different ethnic groups.

| Ethnicity     | Country       | APOE $\epsilon 4$ frequency in the entire population | AD risk OR ( $\epsilon 3\epsilon 4$ ) | AD risk OR ( $\epsilon 4\epsilon 4$ ) | References                           |
|---------------|---------------|--|---------------------------------------|---------------------------------------|--------------------------------------|
| African       | USA           | 19.0   | 1.1                                   | 5.7                                   | Farrer L.A. <i>et al.</i> , 1997 [8] |
| Caucasian     | Multinational | 13.7   | 2.7                                   | 12.5                                  | Farrer L.A. <i>et al.</i> , 1997 [8] |
| Hispanic      | Multinational | 11.0   | 2.2                                   | 2.2                                   | Farrer L.A. <i>et al.</i> , 1997 [8] |
| Japanese      | Japan         | 8.9  | 5.6                                   | 33.1                                  | Farrer L.A. <i>et al.</i> , 1997 [8] |
| Chinese (Han) | China         | 13.5   | 2.7                                   | 8.3                                   | Tan L. <i>et al.</i> , 2013 [28]     |
| Indian        | India         | 7.0–12.7   | 4.2                                   | 4.8                                   | Agarwal R. <i>et al.</i> , 2014 [29] |
| Chilean       | Chile         | 19   | 2.4                                   | 12.8                                  | Quiroga P. <i>et al.</i> , 1999 [30] |
| Iranian       | Iran          | 2.6–6.7  | 3.7                                   | 7.5                                   | Abyadeh M. <i>et al.</i> , 2019 [31] |

APOE, apolipoprotein E; AD, Alzheimer's disease; OR, odds ratio.

## Gender and APOE

In medical studies, gender represents the identity defined by the biological distinction between male and female, which results from differences in expression of gender-related genes, gonadal development, and hormone levels [46].

Tremendous efforts have been made to establish the correlation between gender and AD risk. A large population-based study in the USA reported that 2/3 of all AD patients are female, and the longer average life span of women is the most probable cause. In respect of age-stratified AD risk, the specific impact of gender remains debatable. In Europe, most researchers have reported that women suffer a higher incidence of AD, and this phenomenon is more evident in the oldest group (>75 years) [47–49]. Research conducted in Asian countries such as Japan [37] and China [38] found consistent result, while in the USA, most studies on this topic, including the MoVIES Project, the Framingham study, and the Baltimore Longitudinal Study, failed to reach the same conclusion [50–52].

Since the connection of the *APOE* gene and AD was established, researchers have focused on the gender-dependent effect on APOE function. Payami and colleagues first reported that the *APOE*  $\epsilon 4$  allele, especially in heterozygous carriers, confers more AD risk on female carriers than males [53]. After that, the meta-analysis by Farrer *et al.*, collecting data from >5,000 AD patients, concluded that female  $\epsilon 4$  carriers face a larger increase of AD risk than their male counterparts, as illustrated by the age-stratified OR curve [8]. Subsequent research confirmed this conclusion, and it has become clearer that male carriers with one copy of  $\epsilon 4$  have the same AD risk as non-carriers [54, 55]. Besides cross-sectional studies, a longitudinal study by Altmann *et al.*, which focused on the speed at

which healthy people convert to cognitive impairment during aging, also demonstrated a stronger effect of *APOE*  $\epsilon 4$  on women [56]. A recent study analyzing the chromatin accessibility landscape in 19 postmortem late-onset AD brains in comparison with 21 control brains reported that *APOE* loci have more pronounced differences in females than in males [57]. While all the donors in this study were homozygous for *APOE*  $\epsilon 3$ , it will be interesting to find out whether these gender-dependent differences in the chromatin accessibility landscape have any APOE isoform-specific characteristics.

The gender-dependent effect of *APOE* on AD-risk is evident, but the mechanism behind it remains vague. Fortunately, both clinical and animal studies have provided clues for a possible explanation. It has gradually become clear that the variation of cerebrospinal fluid (CSF) tau levels in patients according to *APOE* gene diversity also occur in a gender-dependent manner. Damoiseaux and colleagues reported a greater elevation of CSF tau, but not  $\beta$ -amyloid, in female  $\epsilon 4$  carriers, which coincided with the conclusion of Altmann *et al.* [56, 58]. Hohman *et al.* summarized the information from several large AD cohorts. They reported a stronger effect of *APOE*  $\epsilon 4$  in women to cause increased CSF tau, but they failed to find the same difference compared to pathological findings [59]. Later, the same team examined healthy cohorts with high A $\beta$  burden and found much earlier tau deposition in women than men. Still, this gender-related effect was found to be independent of *APOE* genotype [60]. Besides interaction with CSF tau, gender may influence AD pathogenesis by an estrogenic effect. Specifically, estrogen replacement treatment has been shown to be beneficial for non- $\epsilon 4$  female carriers while it is detrimental for carriers in terms of cognitive performance and AD risk [61, 62]. Estrogen may interact with *APOE* and AD risk by multiple

mechanisms. First, estrogen might directly regulate the expression of both *APOE* and APOE receptors. Stone *et al.* found that estrogen replacement treatment up-regulates the *APOE* mRNA level in brain tissue, and Wang *et al.* suggested that this specific regulation occurring in the brain results from the specific distribution of different estrogen receptors in glia [63, 64]. Second, the neurogenetic effect of estrogen is influenced by *APOE* polymorphism. Estrogen has been reported to promote neurite expansion, which only happens when *APOE*  $\epsilon 2$  or  $\epsilon 3$ , but not  $\epsilon 4$ , is present [65]. Third, estrogen might alleviate the inflammatory response, as NO and cytokine production by immune-activated microglia, and the *APOE*  $\epsilon 4$  genotype is reported to inhibit this anti-inflammatory effect [66]. In addition to the tau- and estrogen-related mechanisms discussed above,  $\text{Ca}^{2+}$  hyperactivity and the gut microbiome have also been reported to be affected by gender-*APOE* association in animal models [67, 68].

## Aging and APOE

Aging is one of the most established and crucial risk factors for AD. Epidemiological studies have found that AD risk increases with age, even in the oldest group (>80 years). The incidence of AD per year gradually grows from 0.6% in people aged 65 to 69 years, to 3.3% in persons aged 80 to 84 years, and even higher in persons aged 85 years and older [69].

*APOE*  $\epsilon 4$  acts synergistically with the process of aging, resulting in a distinctive pattern of AD. First, *APOE*  $\epsilon 4$  leads to a more severe phenotype of cognitive decline. A pattern of more cognitive decline, mimicking the process of AD, has been found in clinically normal *APOE*  $\epsilon 4$  carriers [70]. This cognitive decline was later reported to be strengthened by aging [71]. Second, *APOE*  $\epsilon 4$  is associated with accelerated augmentation of AD incidence with age. Qian *et al.* integrated four large cohorts, and their model showed the hazard ratio of AD per year is positively related to the  $\epsilon 4$  dose (1.08–1.16, 1.51–2.23, and 2.63–3.57 for 0, 1, and 2 copies) [72]. Third, *APOE*  $\epsilon 4$  may have an altered impact on different age groups. A longitudinal study by Bonham manifested a bell-curve association of  $\epsilon 4$ -related AD risk and age. The strongest effect of  $\epsilon 4$  was found in the 70–80 years group, with a peak hazard ratio of 1.8 [73]. However, the difference of  $\epsilon 4$ -related AD risk across groups failed to reach significance.

*APOE*  $\epsilon 4$ -related age-dependent AD risk may be partially explained by accelerated deposition of A $\beta$ . Morris *et al.* examined CSF biomarkers and cerebral A $\beta$  imaging in healthy subjects grouped by *APOE* genotype and demonstrated that  $\epsilon 4$  carriers show a heavier burden of A $\beta 42$  deposition [11]. Notably, in the 45–49 years age

group, the A $\beta$  imaging showed positive findings only in  $\epsilon 4$  carriers (10.7% vs 0%), indicating that  $\epsilon 4$  enhances preclinical AD pathogenesis in adults. Besides, the cortical binding potential of A $\beta$  markers rises with aging in association with the  $\epsilon 4$  dose (0.020, 0.013, and 0.003 per year in  $\epsilon 4$  homozygotes,  $\epsilon 4$  heterozygotes, and non-carriers, respectively), suggesting that  $\epsilon 4$  significantly aggravates the progress of AD pathology. Similar effects on other AD pathologies have also been reported in AD patients carrying the  $\epsilon 4$  allele [74]. Several studies have reported that a similar pattern of tau deposition is seen in  $\epsilon 4$  carriers [75, 76], but this has been challenged by other studies. Proteinopathy of tau and A $\beta$  is widely recognized to act in an age-dependent manner [77]; *APOE* seems to influence aging-related AD by regulating tau and A $\beta$  metabolism.

## Diet and APOE

Since no current medication can stop or reverse the progress of AD, an increasing number of studies (mainly cross-sectional) have been carried out to uncover the exact role of diet in modulating the course of the disease. Diverse nutrients such as vitamins, antioxidants, and lipids, generally recognized as necessities in brain development and regeneration, came first when searching for AD modifiers. Researchers found that specific types of nutrient impacted the risk of cognitive decline and AD risk. Vitamin B, especially folate and niacin, was reported to be protective against cognitive decline in two observational studies on young adults and older people [78, 79]. Randomized clinical trials testing folic acid supplementation in the elderly revealed the positive effect of maintaining cognitive ability [80]. Vitamin D deficiency, defined as serum vitamin D <10 ng/mL, was shown to be hazardous for AD according to several cohort studies [81], and Zhao *et al.* conducted a prospective cohort study that verified that high vitamin D supplementation is protective against dementia [82]. Omega-3 fatty acids from seafood is another component found to be beneficial by inhibiting cognitive decline. Zhang *et al.* summarized 21 cohorts to conclude that a diet with a higher intake of fish, omega-3 fatty acids, or docosahexaenoic acid (DHA, the major component of dietary omega-3 fatty acids) leads to a lower risk of AD [83], and clinical trials supported the mentally protective effect of DHA in DHA-deficient people [84]. Besides single nutrients, dietary patterns have also been frequently tested for their possible effect on cognitive function. The Mediterranean diet, the Dietary Approaches to Stop Hypertension (DASH) diet, and the Mediterranean-DASH Intervention for Neurodegenerative Delay (MIND) diet have been the major focus of research. Besides fruits,

vegetables, and whole-grains, the Mediterranean diet features the consumption of olive oil, plant protein, and seafood, and the DASH diet emphasizes a reduction of saturated and trans lipids, sodium, and sugar intake; whereas the MIND diet is a combination of the former two diets [85]. Numerous cross-sectional studies and several clinical trials have reported that adopting the Mediterranean diet reduces the risk of both cognitive decline and AD [86–88]. Studies focusing on the DASH diet reported that lower sodium intake is associated with better executive functions. Further studies have reported that MIND has a better protective effect against AD than the Mediterranean or DASH diet [89, 90]. Moreover, the ketogenic diet or supplementation with the ketogenic medium are associated with cognitive improvement and a lower risk of AD, with a deceleration of tau and A $\beta$  accumulation in the brain [91, 92].

The benefits gained from diets against AD seem to partially depend on *APOE* polymorphisms. Deficiency of vitamin B12 and vitamin D are both associated with weaker cognitive function based on observational studies, and this is more evident in *APOE*  $\epsilon$ 4 carriers [93, 94]. Notably, *APOE*  $\epsilon$ 4 is associated with a lower risk of vitamin D deficiency [95]. The majority of studies examining omega-3 fatty acid supplements reported that its benefits are restricted to only  $\epsilon$ 4 carriers. In a large longitudinal study of the elderly population conducted by Ondine van de Rest *et al.* [96], weekly seafood consumption with the optimal amount of omega-3 fatty acid intake from food was found to enhance global and several cognitive domains of cognitive function in  $\epsilon$ 4 carriers. Cross-sectional analyses of deceased subjects reported that weekly seafood consumption was associated with fewer pathological AD findings by autopsy only in  $\epsilon$ 4 carriers [97]. A randomized clinical trial in younger groups demonstrated that 6 months of DHA supplementation conferred better cognitive performance [98]. Carbohydrate intake could be another dietary factor involved in *APOE*-dependent AD risk. Gendreau *et al.* reported that the glycemic load in the afternoon (mostly representing afternoon snacks) had a synergic effect with  $\epsilon$ 4 to elevate AD risk [99]. In another recent report, both Mediterranean and MIND diet patterns are more beneficial to  $\epsilon$ 4 carriers, as was found by Debora *et al.* when examining the association between MIND diet score and cognitive assessment in the Framingham Heart Study [100].

The interaction of AD and diet might function in different manners. *APOE*  $\epsilon$ 4 has been reported to elevate the serum level of vitamin D [93], indicating a putative protective effect. We postulate that *APOE*  $\epsilon$ 4 regulates vitamin D transport, conferring resistance to vitamin D deficiency. Therefore, low serum vitamin D in *APOE*  $\epsilon$ 4 carriers might manifest a more severe undernutrition

condition. For saturated fatty acids, Hanson *et al.* reported that the CSF levels of lipids deplete A $\beta$ , which is hazardous for AD pathogenesis, and that this is closely associated with the *APOE* genotype and excessive intake of dietary saturated fatty acids [101]. They proposed that collaboration of the *APOE*  $\epsilon$ 4 allele and dietary saturated fatty acids leads to less lipidation of CSF A $\beta$ , which results in less A $\beta$  binding to *APOE* and more deposition of toxic A $\beta$  [101]. For unsaturated fatty acids, omega-3 fatty acids, Yassine and colleagues proposed that  $\epsilon$ 4 interferes with DHA metabolism, having a neurotoxic effect at an early stage of neurodegeneration [102]. Yassine *et al.* deduced that: (1) DHA is catabolized faster in  $\epsilon$ 4 carriers [103], possibly because very low-density lipoprotein is catabolized faster than high-density lipoprotein in the liver, and preferential binding with the very low-density lipoprotein of  $\epsilon$ 4 thus facilitates lipid transport and catabolism, including DHA consumption; (2)  $\epsilon$ 4 damages the blood-brain barrier integrity, which inhibits the cerebral uptake of DHA; and (3)  $\epsilon$ 4 is associated with less lipidation and decelerates the transfer of lipids in the central nervous system. The above led to the conclusion that *APOE*  $\epsilon$ 4 lowers CSF DHA, playing a crucial role in AD pathogenesis. In addition, DHA is widely known for its anti-inflammatory effect [104] and acts by mediating activated microglia [105]. Bos *et al.* demonstrated that supplementation with DHA through upregulation of peroxisome proliferator-activated receptor-gamma (PPAR- $\gamma$ ), mitigates inflammation in  $\epsilon$ 4 carriers [106]. For carbohydrates, Zhao *et al.* reported that *APOE*  $\epsilon$ 4 in mice impairs the insulin pathway by trapping the insulin receptors in endosomes [107], and hyperglycemia, in turn, facilitates the glycation of *APOE* and exacerbates AD pathogenesis [108], so that carbohydrate intake elevates AD risk synergistically with *APOE*  $\epsilon$ 4.

## Geographical Location and *APOE*

A limited number of studies indicate that geographical factors modify the pathogenesis or progress of AD. Most studies have reported a positive correlation of residential altitude with the severity of cognitive impairment. In the comparison of a population living at low altitude (500 m), Bolivians living at high altitude (3,700 m) have a slower processing speed and reduced attention, independent of age and ancestry [109]. Hota *et al.* reported that after living at high altitude for one year, acclimatized lowlanders are more susceptible to cognitive decline [110]. Conversely, Thielke *et al.* reported that, in California counties, the mortality rate attributed to AD is inversely associated with the altitude of residence, which fits their theory that long terms of hypoxia might slow the progress of AD [111]. Russ and colleagues explored dementia standardized

mortality ratios in Italy and New Zealand and concluded that living at higher latitudes is associated with higher mortality of dementia [112].

Since few studies have concentrated on the interaction between geographic location, *APOE*, and AD, the distribution of *APOE* polymorphisms might help us to deduce how the *APOE* effect is modified by altitude and latitude. Epidemiological data suggest that geographical factors distinctly shape the distribution of *APOE* polymorphisms. In Europe and Asia, the *APOE*  $\epsilon 4$  allele frequency is positively correlated with latitude [113, 114]: the lowest value is <10% in the Mediterranean area and South China, and gradually ascends to 25% in northern areas. This gradient suggests that a low latitude might enhance the pathogenic effect of  $\epsilon 4$ .

It is hard to explicitly determine how altitude or latitude factors affect *APOE*-related AD risk due to the many cofounders such as ethnicity, diet, and economy. However, the geographical distribution of *APOE* may shed light on the mechanism. Vitamin D production by ultraviolet light and temperature account for the major biological effect of latitude. As noted above, the  $\epsilon 4$  allele is associated with a higher level of serum vitamin D [115], which may explain why northern populations that receive less UV light exhibit a higher frequency of *APOE*  $\epsilon 4$ . Eisenberg proposed that temperature may also contribute to the geographic distribution of *APOE* in that people in tropical areas display faster lipid depletion, thus favoring *APOE*  $\epsilon 3$  [116]. Although little evidence supports the interaction of *APOE* and altitude, considering that hypoxia-induced cognitive impairment is regulated by the *APOE* genotype [117], *APOE*  $\epsilon 4$  may be less frequent in highland populations.

## Conclusions

In this review, we summarized the major confounding factors that might influence the *APOE* genotype-associated AD risk and discussed plausible mechanisms behind these factor-factor interactions. Ethnicity, gender, and age, as observational factors, clearly alter the *APOE*-dependent risk, mainly through variation in local ancestry, hormones, and aging-related proteinopathy, respectively. Diet and geographic location, as interventional factors, are complicated due to their interaction with other confounding factors. However, clinical trials provide evidence verifying that certain subfactors, such as vitamin D, DHA, latitude, and altitude, can influence  $\epsilon 4$ -related AD risk to some extent.

Since the last several decades have seen repetitive failures to develop  $A\beta$ - or tau-targeted therapies for AD, strategies besides decreasing fibril aggregation are gaining popularity, including *APOE*-targeted therapies. Based on

several putative roles that *APOE* plays in AD pathology, current research mainly focuses on the following strategies: increasing *APOE* levels and its lipidation [118], blocking *APOE* and  $A\beta$  interaction [119], and using *APOE* mimetics [120]. We hope the factors discussed in this review may serve to better evaluate *APOE*-targeted therapies or the grouping of subjects. On the other hand, *APOE* genotype has been applied in almost all AD risk-prediction models, and researchers are still searching for a better model to elaborate the effect of *APOE* [121], where stratification by the confounding factors discussed in our review should be the first consideration.

Limitations in this review should be noted. First, considering the wide range of potential factors involved in this topic, certain factors or their corresponding supportive evidence could be missed. Second, studies brought into our review are mostly cross-sectional, with extensively varied study designs and subject conditions, which may compromise our conclusion. Thirdly, as mentioned above, numerous *APOE*-modifying factors could interact with each other, making the epidemiological evidence less convincing, since the inclusion of all related factors seems impossible in clinical studies. Further clinical trials and meta-analyses are needed for better stratification and regression of numerous factors. Moreover, a surging number of studies concerning *APOE* and AD is in progress or in the planning stage, and when their results come out, we could have a more comprehensive understanding of this topic.

To sum up, several factors act as a modifier of  $\epsilon 4$ -related risk, and they deserve more attention for further studies focusing on *APOE*, from both the investigative and clinical aspects. Since a growing number of therapies targeting *APOE* are being developed and tested clinically [122], those *APOE*-modifying factors should serve as new targets for treatment or reference for population stratification.

**Acknowledgements** We thank Professor Hongmei Li from Department of Neuroscience, Mayo Clinic and Yingjun Zhao from Fujian Provincial Key Laboratory of Neurodegenerative Disease and Aging Research, Institute of Neuroscience, School of Medicine, Xiamen University for their critical review of this manuscript. This work was supported by the Chengdu Science and Technology Bureau (2019-YF05-00655-SN), Key Project of the Medical Science Department, University of Electronic Science and Technology of China (ZYGX2020ZB035) and Guangdong Provincial Key R&D Program (2018B030337001).

**Competing interests** The authors declare that they have no conflict of interest.

**Open Access** This article is licensed under a Creative Commons Attribution 4.0 International License, which permits use, sharing, adaptation, distribution and reproduction in any medium or format, as long as you give appropriate credit to the original author(s) and the source, provide a link to the Creative Commons licence, and indicate



if changes were made. The images or other third party material in this article are included in the article's Creative Commons licence, unless indicated otherwise in a credit line to the material. If material is not included in the article's Creative Commons licence and your intended use is not permitted by statutory regulation or exceeds the permitted use, you will need to obtain permission directly from the copyright holder. To view a copy of this licence, visit <http://creativecommons.org/licenses/by/4.0/>.

## References


1. Le WD. Inauguration of a unique journal Ageing and Neurodegenerative Diseases: A new beginning seeking cures for age-related neurodegenerative diseases. *Ageing Neurodegener Dis* 2021, <https://doi.org/10.20517/and.2021.01>.
2. DeTure MA, Dickson DW. The neuropathological diagnosis of Alzheimer's disease. *Mol Neurodegener* 2019, 14: 32.
3. Hebert LE, Weuve J, Scherr PA, Evans DA. Alzheimer disease in the United States (2010–2050) estimated using the 2010 census. *Neurology* 2013, 80: 1778–1783.
4. Hauser PS, Narayanaswami V, Ryan RO. Apolipoprotein E: From lipid transport to neurobiology. *Prog Lipid Res* 2011, 50: 62–74.
5. Li ZH, Shue F, Zhao N, Shinohara M, Bu GJ. APOE2: Protective mechanism and therapeutic implications for Alzheimer's disease. *Mol Neurodegener* 2020, 15: 63.
6. Najm R, Jones EA, Huang YD. Apolipoprotein E4, inhibitory network dysfunction, and Alzheimer's disease. *Mol Neurodegener* 2019, 14: 24.
7. Belloy ME, Napolioni V, Greicius MD. A quarter century of APOE and Alzheimer's disease: Progress to date and the path forward. *Neuron* 2019, 101: 820–838.
8. Farrer LA, Cupples LA, Haines JL, Hyman B, Kukull WA, Mayeux R. Effects of age, sex, and ethnicity on the association between apolipoprotein E genotype and Alzheimer disease. A meta-analysis. APOE and Alzheimer Disease Meta Analysis Consortium. *JAMA* 1997, 278: 1349–1356.
9. Rahman MM, Lendel C. Extracellular protein components of amyloid plaques and their roles in Alzheimer's disease pathology. *Mol Neurodegener* 2021, 16: 59.
10. Holtzman DM, Bales KR, Tenkova T, Fagan AM, Parsadanian M, Sartorius LJ, *et al.* Apolipoprotein E isoform-dependent amyloid deposition and neuritic degeneration in a mouse model of Alzheimer's disease. *Proc Natl Acad Sci U S A* 2000, 97: 2892–2897.
11. Morris JC, Roe CM, Xiong C, Fagan AM, Goate AM, Holtzman DM, *et al.* APOE predicts amyloid-beta but not tau Alzheimer pathology in cognitively normal aging. *Ann Neurol* 2010, 67: 122–131.
12. Rebeck GW, Reiter JS, Strickland DK, Hyman BT. Apolipoprotein E in sporadic Alzheimer's disease: Allelic variation and receptor interactions. *Neuron* 1993, 11: 575–580.
13. Cho HS, Hyman BT, Greenberg SM, Rebeck GW. Quantitation of apoE domains in Alzheimer disease brain suggests a role for apoE in Aβ aggregation. *J Neuropathol Exp Neurol* 2001, 60: 342–349.
14. Garai K, Verghese PB, Baban B, Holtzman DM, Frieden C. The binding of apolipoprotein E to oligomers and fibrils of amyloid-β alters the kinetics of amyloid aggregation. *Biochemistry* 2014, 53: 6323–6331.
15. Castellano JM, Kim J, Stewart FR, Jiang H, DeMattos RB, Patterson BW, *et al.* Human apoE isoforms differentially regulate brain amyloid-β peptide clearance. *Sci Transl Med* 2011, 3: 89ra57.
16. Hashimoto T, Serrano-Pozo A, Hori Y, Adams KW, Takeda S, Banerji AO, *et al.* Apolipoprotein E, especially apolipoprotein E4, increases the oligomerization of amyloid β peptide. *J Neurosci* 2012, 32: 15181–15192.
17. Ma QY, Zhao Z, Sagare AP, Wu YX, Wang M, Owens NC, *et al.* Blood-brain barrier-associated pericytes internalize and clear aggregated amyloid-β42 by LRP1-dependent apolipoprotein E isoform-specific mechanism. *Mol Neurodegener* 2018, 13: 57.
18. Zhao N, Ren YX, Yamazaki Y, Qiao WH, Li FY, Felton LM, *et al.* Alzheimer's risk factors age, APOE genotype, and sex drive distinct molecular pathways. *Neuron* 2020, 106: 727–742.e6.
19. Berger M, Cooter M, Roesler AS, Chung S, Park J, Modliszewski JL, *et al.* APOE4 copy number-dependent proteomic changes in the cerebrospinal fluid. *J Alzheimers Dis* 2021, 79: 511–530.
20. Main BS, Villapol S, Sloley SS, Barton DJ, Parsadanian M, Agbaegbu C, *et al.* Apolipoprotein E4 impairs spontaneous blood brain barrier repair following traumatic brain injury. *Mol Neurodegener* 2018, 13: 17.
21. Wang SW, Li BY, Solomon V, Fonteh A, Rapoport SI, Bennett DA, *et al.* Calcium-dependent cytosolic phospholipase A<sub>2</sub> activation is implicated in neuroinflammation and oxidative stress associated with ApoE4. *Mol Neurodegener* 2021, 16: 26.
22. Liu TF, Zhu B, Liu Y, Zhang XM, Yin J, Li XG, *et al.* Multi-omic comparison of Alzheimer's variants in human ESC-derived microglia reveals convergence at APOE. *J Exp Med* 2020, 217: e20200474.
23. Bell RD, Winkler EA, Singh I, Sagare AP, Deane R, Wu ZH, *et al.* Apolipoprotein E controls cerebrovascular integrity via cyclophilin A. *Nature* 2012, 485: 512–516.
24. Liu YH, Jiao SS, Wang YR, Bu XL, Yao XQ, Xiang Y, *et al.* Associations between ApoEε4 carrier status and serum BDNF levels—new insights into the molecular mechanism of ApoEε4 actions in Alzheimer's disease. *Mol Neurobiol* 2015, 51: 1271–1277.
25. Theendakara V, Patent A, Peters Libeu CA, Philpot BD, Flores S, Descamps O, *et al.* Neuroprotective Sirtuin ratio reversed by ApoE4. *Proc Natl Acad Sci U S A* 2013, 110: 18303–18308.
26. Farmer BC, Williams HC, Devanney NA, Piron MA, Nation GK, Carter DJ, *et al.* APOE4 lowers energy expenditure in females and impairs glucose oxidation by increasing flux through aerobic glycolysis. *Mol Neurodegener* 2021, 16: 1–18.
27. Corbo RM, Scacchi R. Apolipoprotein E (APOE) allele distribution in the world Is APOE\*4 a 'thrifty' allele? *Ann Hum Genet* 1999, 63: 301–310.
28. Tan L, Yu JT, Zhang W, Wu ZC, Zhang Q, Liu QY, *et al.* Association of GWAS-linked loci with late-onset Alzheimer's disease in a northern Han Chinese population. *Alzheimers Dement* 2013, 9: 546–553.
29. Agarwal R, Tripathi CB. Association of apolipoprotein E genetic variation in Alzheimer's disease in Indian population: A meta-analysis. *Am J Alzheimers Dis Other Dement* 2014, 29: 575–582.
30. Quiroga P, Calvo C, Albala C, Urquidí J, Santos JL, Pérez H, *et al.* Apolipoprotein E polymorphism in elderly Chilean people with Alzheimer's disease. *Neuroepidemiology* 1999, 18: 48–52.
31. Abyadeh M, Djafarian K, Heydarinejad F, Alizadeh S, Shab-Bidar S. Association between apolipoprotein E gene polymorphism and Alzheimer's disease in an Iranian population: A meta-analysis. *J Mol Neurosci* 2019, 69: 557–562.
32. Tang MX, Cross P, Andrews H, Jacobs DM, Small S, Bell K, *et al.* Incidence of AD in African-Americans, Caribbean hispanics, and caucasians in northern Manhattan. *Neurology* 2001, 56: 49–56.

33. Mayeda ER, Glymour MM, Quesenberry CP, Whitmer RA. Inequalities in dementia incidence between six racial and ethnic groups over 14 years. *Alzheimers Dement* 2016, 12: 216–224.
34. Matthews KA, Xu W, Gaglioti AH, Holt JB, Croft JB, Mack D, *et al.* Racial and ethnic estimates of Alzheimer's disease and related dementias in the United States (2015–2060) in adults aged  $\geq 65$  years. *Alzheimers Dement* 2019, 15: 17–24.
35. Evans DA, Bennett DA, Wilson RS, Bienias JL, Morris MC, Scherr PA, *et al.* Incidence of Alzheimer disease in a biracial urban community: Relation to apolipoprotein E allele status. *Arch Neurol* 2003, 60: 185–189.
36. Blue EE, Horimoto ARVR, Mukherjee S, Wijsman EM, Thornton TA. Local ancestry at APOE modifies Alzheimer's disease risk in Caribbean Hispanics. *Alzheimers Dement* 2019, 15: 1524–1532.
37. Rajabli F, Feliciano BE, Celis K, Hamilton-Nelson KL, Whitehead PL, Adams LD, *et al.* Ancestral origin of ApoE  $\epsilon 4$  Alzheimer disease risk in Puerto Rican and African American populations. *PLoS Genet* 2018, 14: e1007791. <https://doi.org/10.1371/journal.pgen.1007791>.
38. Marca-Ysabel MV, Rajabli F, Cornejo-Olivas M, Whitehead PG, Hofmann NK, Illanes Manrique MZ, *et al.* Dissecting the role of Amerindian genetic ancestry and the ApoE  $\epsilon 4$  allele on Alzheimer disease in an admixed Peruvian population. *Neurobiol Aging* 2021, 101: 298–315.
39. Farrer LA, Friedland RP, Bowirrat A, Waraska K, Korszyn A, Baldwin CT. Genetic and environmental epidemiology of Alzheimer's disease in arabs residing in Israel. *J Mol Neurosci* 2003, 20: 207–212.
40. Lai E, Riley J, Purvis I, Roses A. A 4-Mb high-density single nucleotide polymorphism-based map around human APOE. *Genomics* 1998, 54: 31–38.
41. Martin ER, Lai EH, Gilbert JR, Rogala AR, Afshari AJ, Riley J, *et al.* SNPing away at complex diseases: Analysis of single-nucleotide polymorphisms around APOE in Alzheimer disease. *Am J Hum Genet* 2000, 67: 383–394.
42. Roses AD, Lutz MW, Amrine-Madsen H, Saunders AM, Crenshaw DG, Sundseth SS, *et al.* A TOMM40 variable-length polymorphism predicts the age of late-onset Alzheimer's disease. *Pharmacogenomics J* 2010, 10: 375–384.
43. Crenshaw DG, Gottschalk WK, Lutz MW, Grossman I, Saunders AM, Burke JR, *et al.* Using genetics to enable studies on the prevention of Alzheimer's disease. *Clin Pharmacol Ther* 2013, 93: 177–185.
44. Caselli RJ, Dueck AC, Huentelman MJ, Lutz MW, Saunders AM, Reiman EM, *et al.* Longitudinal modeling of cognitive aging and the TOMM40 effect. *Alzheimers Dement* 2012, 8: 490–495.
45. Zhou XP, Chen Y, Mok KY, Kwok TCY, Mok VCT, Guo QH, *et al.* Non-coding variability at the APOE locus contributes to the Alzheimer's risk. *Nat Commun* 2019, 10: 3310.
46. Mielke MM, Vemuri P, Rocca WA. Clinical epidemiology of Alzheimer's disease: Assessing sex and gender differences. *Clin Epidemiol* 2014, 6: 37–48.
47. Fratiglioni L, Viitanen M, von Strauss E, Tontodonati V, Herlitz A, Winblad B. Very old women at highest risk of dementia and Alzheimer's disease: Incidence data from the Kungsholmen Project, Stockholm. *Neurology* 1997, 48: 132–138.
48. Ott A, Breteler MM, van Harskamp F, Stijnen T, Hofman A. Incidence and risk of dementia. The Rotterdam Study. *Am J Epidemiol* 1998, 147: 574–580.
49. Letenneur L, Gilleron V, Commenges D, Helmer C, Orgogozo JM, Dartigues JF. Are sex and educational level independent predictors of dementia and Alzheimer's disease? Incidence data from the PAQUID project. *J Neurol Neurosurg Psychiatry* 1999, 66: 177–183.
50. Ganguli M, Dodge HH, Chen P, Belle S, DeKosky ST. Ten-year incidence of dementia in a rural elderly US community population: The MoVIES Project. *Neurology* 2000, 54: 1109–1116.
51. Kawas C, Gray S, Brookmeyer R, Fozard J, Zonderman A. Age-specific incidence rates of Alzheimer's disease: The Baltimore Longitudinal Study of Aging. *Neurology* 2000, 54: 2072–2077.
52. Bachman DL, Wolf PA, Linn RT, Knoefel JE, Cobb JL, Belanger AJ, *et al.* Incidence of dementia and probable Alzheimer's disease in a general population: The Framingham Study. *Neurology* 1993, 43: 515–519.
53. Payami H, Montee KR, Kaye JA, Bird TD, Yu CE, Wijsman EM, *et al.* Alzheimer's disease, apolipoprotein E4, and gender. *JAMA* 1994, 271: 1316–1317.
54. Bretsky PM, Buckwalter JG, Seeman TE, Miller CA, Poirier J, Schellenberg GD, *et al.* Evidence for an interaction between apolipoprotein E genotype, gender, and Alzheimer disease. *Alzheimer Dis Assoc Disord* 1999, 13: 216–221.
55. Breitner JC, Wyse BW, Anthony JC, Welsh-Bohmer KA, Steffens DC, Norton MC, *et al.* APOE-epsilon4 count predicts age when prevalence of AD increases, then declines: The Cache County Study. *Neurology* 1999, 53: 321–331.
56. Altmann A, Tian L, Henderson VW, Greicius MD. Alzheimer's Disease Neuroimaging Initiative Investigators. Sex modifies the APOE-related risk of developing Alzheimer disease. *Ann Neurol* 2014, 75: 563–573.
57. Barrera J, Song LY, Gamache JE, Garrett ME, Safi A, Yun Y, *et al.* Sex dependent glial-specific changes in the chromatin accessibility landscape in late-onset Alzheimer's disease brains. *Mol Neurodegener* 2021, 16: 58.
58. Damoiseaux JS, Seeley WW, Zhou J, Shirer WR, Coppola G, Karydas A, *et al.* Gender modulates the APOE  $\epsilon 4$  effect in healthy older adults: Convergent evidence from functional brain connectivity and spinal fluid tau levels. *J Neurosci* 2012, 32: 8254–8262.
59. Hohman TJ, Dumitrescu L, Barnes LL, Thambisetty M, Beecham G, Kunkle B, *et al.* Sex-specific association of apolipoprotein E with cerebrospinal fluid levels of tau. *JAMA Neurol* 2018, 75: 989–998.
60. Buckley RF, Mormino EC, Rabin JS, Hohman TJ, Landau S, Hanseeuw BJ, *et al.* Sex differences in the association of global amyloid and regional tau deposition measured by positron emission tomography in clinically normal older adults. *JAMA Neurol* 2019, 76: 542–551.
61. Rippon GA, Tang MX, Lee JH, Lantigua R, Medrano M, Mayeux R. Familial Alzheimer disease in Latinos: Interaction between APOE, stroke, and estrogen replacement. *Neurology* 2006, 66: 35–40.
62. Kang JH, Grodstein F. Postmenopausal hormone therapy, timing of initiation, APOE and cognitive decline. *Neurobiol Aging* 2012, 33: 1129–1137.
63. Stone DJ, Rozovsky I, Morgan TE, Anderson CP, Hajian H, Finch CE. Astrocytes and microglia respond to estrogen with increased apoE mRNA *in vivo* and *in vitro*. *Exp Neurol* 1997, 143: 313–318.
64. Wang JM, Irwin RW, Brinton RD. Activation of estrogen receptor alpha increases and estrogen receptor beta decreases apolipoprotein E expression in *Hippocampus in vitro* and *in vivo*. *Proc Natl Acad Sci USA* 2006, 103: 16983–16988.
65. Nathan BP, Barsukova AG, Shen F, McAsey M, Struble RG. Estrogen facilitates neurite extension via apolipoprotein E in cultured adult mouse cortical neurons. *Endocrinology* 2004, 145: 3065–3073.
66. Brown CM, Choi E, Xu Q, Vitek MP, Colton CA. The APOE4 genotype alters the response of microglia and macrophages to 17beta-estradiol. *Neurobiol Aging* 2008, 29: 1783–1794.

67. Larramona-Arcas R, González-Arias C, Perea G, Gutiérrez A, Vitorica J, García-Barrera T, *et al.* Sex-dependent calcium hyperactivity due to lysosomal-related dysfunction in astrocytes from APOE4 versus APOE3 gene targeted replacement mice. *Mol Neurodegener* 2020, 15: 35.
68. Maldonado Weng J, Parikh I, Naqib A, York J, Green SJ, Estus S, *et al.* Synergistic effects of APOE and sex on the gut microbiome of young EFAD transgenic mice. *Mol Neurodegener* 2019, 14: 47.
69. Hebert LE, Scherr PA, Beckett LA, Albert MS, Pilgrim DM, Chown MJ, *et al.* Age-specific incidence of Alzheimer's disease in a community population. *JAMA* 1995, 273: 1354–1359.
70. Caselli RJ, Dueck AC, Osborne D, Sabbagh MN, Connor DJ, Ahern GL, *et al.* Longitudinal modeling of age-related memory decline and the APOE epsilon4 effect. *N Engl J Med* 2009, 361: 255–263.
71. Williams OA, An Y, Armstrong N, Shafer AT, Helpfrey J, Kitner-Triolo M, *et al.* O4–05-01: Apolipoprotein ε4 allele effects on longitudinal cognitive trajectories are sex- and age-dependent. *Alzheimer's Dement* 2019, 15: P1241–P1242.
72. Qian J, Wolters FJ, Beiser A, Haan M, Ikram MA, Karlawish J, *et al.* APOE-related risk of mild cognitive impairment and dementia for prevention trials: An analysis of four cohorts. *PLoS Med* 2017, 14: e1002254. <https://doi.org/10.1371/journal.pmed.1002254>.
73. Bonham LW, Geier EG, Fan CC, Leong JK, Besser L, Kukull WA, *et al.* Age-dependent effects of APOE ε4 in preclinical Alzheimer's disease. *Ann Clin Transl Neurol* 2016, 3: 668–677.
74. Drzezga A, Grimmer T, Henriksen G, Mühlau M, Perneczky R, Miederer I, *et al.* Effect of APOE genotype on amyloid plaque load and gray matter volume in Alzheimer disease. *Neurology* 2009, 72: 1487–1494.
75. Quevenco FC, van Bergen JM, Treyer V, Studer ST, Kagerer SM, Meyer R, *et al.* Functional brain network connectivity patterns associated with normal cognition at old-age, local β-amyloid, tau, and APOE4. *Front Aging Neurosci* 2020, 12: 46.
76. Wennberg AM, Tosakulwong N, Lesnick TG, Murray ME, Whitwell JL, Liesinger AM, *et al.* Association of apolipoprotein E ε4 with transactive response DNA-binding protein 43. *JAMA Neurol* 2018, 75: 1347–1354.
77. Lim YY, Ellis KA, Pietrzak RH, Ames D, Darby D, Harrington K, *et al.* Stronger effect of amyloid load than APOE genotype on cognitive decline in healthy older adults. *Neurology* 2012, 79: 1645–1652.
78. Qin B, Xun P, Jacobs DR, Zhu N, Daviglus ML, Reis JP, *et al.* Intake of niacin, folate, vitamin B-6, and vitamin B-12 through young adulthood and cognitive function in midlife: The Coronary Artery Risk Development in Young Adults (CARDIA) study. *Am J Clin Nutr* 2017, 106: 1032–1040.
79. Lefèvre-Arbogast S, Féart C, Dartigues JF, Helmer C, Letenneur L, Samieri C. Dietary B vitamins and a 10-year risk of dementia in older persons. *Nutrients* 2016, 8: E761.
80. Durga J, van Boxtel MP, Schouten EG, Kok FJ, Jolles J, Katan MB, *et al.* Effect of 3-year folic acid supplementation on cognitive function in older adults in the FACIT trial: A randomised, double blind, controlled trial. *Lancet* 2007, 369: 208–216.
81. Jayedi A, Rashidy-Pour A, Shab-Bidar S. Vitamin D status and risk of dementia and Alzheimer's disease: A meta-analysis of dose-response. *Nutr Neurosci* 2019, 22: 750–759.
82. Zhao C, Tsapanou A, Manly J, Schupf N, Brickman AM, Gu Y. Vitamin D intake is associated with dementia risk in the Washington Heights-Inwood Columbia Aging Project (WHI-CAP). *Alzheimers Dement* 2020, 16: 1393–1401.
83. Zhang Y, Chen JN, Qiu JN, Li YJ, Wang JB, Jiao JJ. Intakes of fish and polyunsaturated fatty acids and mild-to-severe cognitive impairment risks: A dose-response meta-analysis of 21 cohort studies. *Am J Clin Nutr* 2016, 103: 330–340.
84. Yurko-Mauro K, McCarthy D, Rom D, Nelson EB, Ryan AS, Blackwell A, *et al.* Beneficial effects of docosahexaenoic acid on cognition in age-related cognitive decline. *Alzheimers Dement* 2010, 6: 456–464.
85. Scarmeas N, Anastasiou CA, Yannakoulia M. Nutrition and prevention of cognitive impairment. *Lancet Neurol* 2018, 17: 1006–1015.
86. Wu L, Sun D. Adherence to Mediterranean diet and risk of developing cognitive disorders: An updated systematic review and meta-analysis of prospective cohort studies. *Sci Rep* 2017, 7: 41317.
87. Valls-Pedret C, Sala-Vila A, Serra-Mir M, Corella D, de la Torre R, Martínez-González MÁ, *et al.* Mediterranean diet and age-related cognitive decline: A randomized clinical trial. *JAMA Intern Med* 2015, 175: 1094–1103.
88. Martínez-Lapiscina EH, Clavero P, Toledo E, Estruch R, Salas-Salvado J, San Julián B, *et al.* Mediterranean diet improves cognition: The PREDIMED-NAVARRA randomised trial. *J Neurol Neurosurg Psychiatry* 2013, 84: 1318–1325.
89. Morris MC, Tangney CC, Wang YM, Sacks FM, Bennett DA, Aggarwal NT. MIND diet associated with reduced incidence of Alzheimer's disease. *Alzheimers Dement* 2015, 11: 1007–1014.
90. Hosking DE, Eramudugolla R, Cherbuin N, Anstey KJ. MIND not Mediterranean diet related to 12-year incidence of cognitive impairment in an Australian longitudinal cohort study. *Alzheimers Dement* 2019, 15: 581–589.
91. Fortier M, Castellano CA, Croteau E, Langlois F, Bocti C, St-Pierre V, *et al.* A ketogenic drink improves brain energy and some measures of cognition in mild cognitive impairment. *Alzheimers Dement* 2019, 15: 625–634.
92. Neth BJ, Mintz A, Whitlow C, Jung Y, Solingapuram Sai K, Register TC, *et al.* Modified ketogenic diet is associated with improved cerebrospinal fluid biomarker profile, cerebral perfusion, and cerebral ketone body uptake in older adults at risk for Alzheimer's disease: A pilot study. *Neurobiol Aging* 2020, 86: 54–63.
93. Maddock J, Cavadino A, Power C, Hyppönen E. 25-hydroxyvitamin D, APOE ε4 genotype and cognitive function: findings from the 1958 British birth cohort. *Eur J Clin Nutr* 2015, 69: 505–508.
94. Feng L, Li JL, Yap KB, Kua EH, Ng TP. Vitamin B-12, apolipoprotein E genotype, and cognitive performance in community-living older adults: Evidence of a gene-micronutrient interaction. *Am J Clin Nutr* 2009, 89: 1263–1268.
95. Dursun E, Alaylıoğlu M, Bilgiç B, Hanağası H, Lohmann E, Atasoy IL, *et al.* Vitamin D deficiency might pose a greater risk for ApoEε4 non-carrier Alzheimer's disease patients. *Neurol Sci* 2016, 37: 1633–1643.
96. van de Rest O, Wang YM, Barnes LL, Tangney C, Bennett DA, Morris MC. APOE ε4 and the associations of seafood and long-chain Omega-3 fatty acids with cognitive decline. *Neurology* 2016, 86: 2063–2070.
97. Morris MC, Brockman J, Schneider JA, Wang Y, Bennett DA, Tangney CC, *et al.* Association of seafood consumption, brain mercury level, and APOE ε4 status with brain neuropathology in older adults. *JAMA* 2016, 315: 489–497.
98. Stonehouse W, Conlon CA, Podd J, Hill SR, Minihane AM, Haskell C, *et al.* DHA supplementation improved both memory and reaction time in healthy young adults: A randomized controlled trial. *Am J Clin Nutr* 2013, 97: 1134–1143.
99. Gentreau M, Chuy V, Féart C, Samieri C, Ritchie K, Raymond M, *et al.* Refined carbohydrate-rich diet is associated with long-term risk of dementia and Alzheimer's disease in apolipoprotein E ε4 allele carriers. *Alzheimers Dement* 2020, 16: 1043–1053.

100. van Lent DM, O'Donnell A, Beiser AS, Vasan RS, DeCarli CS, Scarmeas N, *et al.* Mind diet adherence and cognitive performance in the Framingham heart study. *J Alzheimer's Dis* 2021, 82: 827–839.
101. Hanson AJ, Bayer-Carter JL, Green PS, Montine TJ, Wilkinson CW, Baker LD, *et al.* Effect of apolipoprotein E genotype and diet on apolipoprotein E lipidation and amyloid peptides: Randomized clinical trial. *JAMA Neurol* 2013, 70: 972–980.
102. Yassine HN, Braskie MN, Mack WJ, Castor KJ, Fonteh AN, Schneider LS, *et al.* Association of docosahexaenoic acid supplementation with alzheimer disease stage in apolipoprotein E  $\epsilon$ 4 carriers: A review. *JAMA Neurol* 2017, 74: 339–347.
103. Chouinard-Watkins R, Rioux-Perreault C, Fortier M, Tremblay-Mercier J, Zhang Y, Lawrence P, *et al.* Disturbance in uniformly  $^{13}\text{C}$ -labelled DHA metabolism in elderly human subjects carrying the apoE  $\epsilon$ 4 allele. *Br J Nutr* 2013, 110: 1751–1759.
104. Calder PC. *Omega*-3 fatty acids and inflammatory processes: From molecules to man. *Biochem Soc Trans* 2017, 45: 1105–1115.
105. Fourrier C, Remus-Borel J, Greenhalgh AD, Guichardant M, Bernoud-Hubac N, Lagarde M, *et al.* Docosahexaenoic acid-containing choline phospholipid modulates LPS-induced neuroinflammation *in vivo* and in microglia *in vitro*. *J Neuroinflammation* 2017, 14: 170.
106. Bos MM, Noordam R, Blauw GJ, Slagboom PE, Rensen PCN, van Heemst D. The ApoE  $\epsilon$ 4 isoform: Can the risk of diseases be reduced by environmental factors? *J Gerontol: Ser A* 2019, 74: 99–107.
107. Zhao N, Liu CC, van Ingelgom AJ, Martens YA, Linares C, Knight JA, *et al.* Apolipoprotein E4 impairs neuronal insulin signaling by trapping insulin receptor in the endosomes. *Neuron* 2017, 96: 115–129.e5.
108. Li YM, Dickson DW. Enhanced binding of advanced glycation endproducts (AGE) by the ApoE4 isoform links the mechanism of plaque deposition in Alzheimer's disease. *Neurosci Lett* 1997, 226: 155–158.
109. Hill CM, Dimitriou D, Baya WR, Gavlak-Dingle J, Lesperance V, *et al.* Cognitive performance in high-altitude Andean residents compared with low-altitude populations: From childhood to older age. *Neuropsychology* 2014, 28: 752–760.
110. Hota SK, Sharma VK, Hota K, Das S, Dhar P, Mahapatra BB, *et al.* Multi-domain cognitive screening test for neuropsychological assessment for cognitive decline in acclimatized lowlanders staying at high altitude. *Indian J Med Res* 2012, 136: 411–420.
111. Thielke S, Slatore CG, Banks WA. Association between alzheimer dementia mortality rate and altitude in California counties. *JAMA Psychiatry* 2015, 72: 1253–1254.
112. Russ TC, Murianni L, Icaza G, Slachevsky A, Starr JM. Geographical variation in dementia mortality in Italy, new Zealand, and Chile: The impact of latitude, vitamin D, and air pollution. *Dement Geriatr Cogn Disord* 2016, 42: 31–41.
113. Egert S, Rimbach G, Huebbe P. ApoE genotype: From geographic distribution to function and responsiveness to dietary factors. *Proc Nutr Soc* 2012, 71: 410–424.
114. Hu P, Qin YH, Jing CX, Lu L, Hu B, Du PF. Does the geographical gradient of ApoE4 allele exist in China? A systemic comparison among multiple Chinese populations. *Mol Biol Rep* 2011, 38: 489–494.
115. Huebbe P, Nebel A, Siegert S, Moehring J, Boesch-Saadatmandi C, Most E, *et al.* APOE  $\epsilon$ 4 is associated with higher vitamin D levels in targeted replacement mice and humans. *FASEB J* 2011, 25: 3262–3270.
116. Eisenberg DT, Kuzawa CW, Hayes MG. Worldwide allele frequencies of the human apolipoprotein E gene: Climate, local adaptations, and evolutionary history. *Am J Phys Anthropol* 2010, 143: 100–111.
117. Kaushal N, Ramesh V, Gozal D. Human apolipoprotein E4 targeted replacement in mice reveals increased susceptibility to sleep disruption and intermittent hypoxia. *Am J Physiol Regul Integr Comp Physiol* 2012, 303: R19–R29.
118. Cramer PE, Cirrito JR, Wesson DW, Lee CY, Karlo JC, Zinn AE, *et al.* ApoE-directed therapeutics rapidly clear  $\beta$ -amyloid and reverse deficits in AD mouse models. *Science* 2012, 335: 1503–1506.
119. Sawmiller D, Habib A, Hou HY, Mori T, Fan AR, Tian J, *et al.* A novel apolipoprotein E antagonist functionally blocks apolipoprotein E interaction with N-terminal amyloid precursor protein, reduces  $\beta$ -amyloid-associated pathology, and improves cognition. *Biol Psychiatry* 2019, 86: 208–220.
120. Wang LK, Hou HY, Zi D, Habib A, Tan J, Sawmiller D. Novel apoE receptor mimetics reduce LPS-induced microglial inflammation. *Am J Transl Res* 2019, 11: 5076–5085.
121. Ebenau JL, van der Lee SJ, Hulsman M, Tesi N, Jansen IE, Verberk IMW, *et al.* Risk of dementia in APOE  $\epsilon$ 4 carriers is mitigated by a polygenic risk score. *Alzheimers Dement (Amst)* 2021, 13: e12229. <https://doi.org/10.1002/dad2.12229>.
122. Yamazaki Y, Zhao N, Caulfield TR, Liu CC, Bu GJ. Apolipoprotein E and Alzheimer disease: Pathobiology and targeting strategies. *Nat Rev Neurol* 2019, 15: 501–518.

# Induced Dopaminergic Neurons for Parkinson's Disease Therapy: Targeting the Striatum or Midbrain/Substantia Nigra Pars Compacta?

Huadong Xu<sup>1</sup> · Xu Cheng<sup>1</sup> · Qian Song<sup>2,3</sup> · Yuxin Yang<sup>1,4</sup> · Changhe Wang<sup>1,2,3</sup>  · Xinjiang Kang<sup>1,4</sup>

Received: 3 September 2021 / Accepted: 11 December 2021 / Published online: 23 February 2022

© Center for Excellence in Brain Science and Intelligence Technology, Chinese Academy of Sciences 2022

Parkinson's disease (PD) is a common neurodegenerative disease among the elderly, characterized by the specific loss of dopaminergic (DAergic) neurons in the substantia nigra pars compacta (SNpc) and defects in dopamine (DA) release in the striatum. So far, enhancement of DA concentration or electrical stimulation of specific nuclei in basal ganglia circuits is effective for the clinical treatment of PD. DA can be enhanced by either systemic drug administration or by cell-replacement treatment (CRT), and the latter is assumed to be once for all the most promising strategy for PD therapy. The cell sources for CRT include fetal mesencephalic tissue, embryonic stem cells (ESCs), and induced pluripotent stem cells (iPSCs). The alleviation of motor syndromes in PD patients and animal models following cell transplantation has been

well-established [1]. We have shown that DA released by grafted cells contributes to the alleviation of motor defects in rat models of PD [2]. Although the effectiveness of CRT for PD therapy has been validated, the ethics of using fetal mesencephalic tissue and the potential tumorigenesis of ESCs and iPSCs are still practical barriers to clinical translation.

## Induced DAergic neurons (iDNs) from Non-Neuronal Cells *in vitro*

Neurons induced from non-neuronal cells through lineage conversion are termed induced neurons (iNs). Compared to ESCs and iPSCs, lineage conversion bypasses a proliferative progenitor state with minimal tumorigenesis risk [3]. iNs, exhibiting neuron-like features of firing action potentials and forming functional synapses with neighboring cells, were first generated by exogenous expression of lineage-specific transcriptional factors (TFs), including *Ascl1*, *Brn2*, and *Myt1l*, in fibroblasts *in vitro* [4]. Besides fibroblasts, other non-neural human somatic cells and pluripotent stem cells have been successfully converted into neurons by transfection with lineage-determining TFs *in vitro* [5]. Since loss of DAergic neurons is the etiology of PD, conversion of non-neuronal cells into DAergic neurons has naturally become an exciting therapeutic strategy for PD. By forced expression an array of neuron-determining TFs, such as *Ascl1*, *Brn2*, *Myt1l*, *Sox2*, *Ngn2*, and DAergic neuron fate-determining TFs, such as *Nurr1*, *Lmx1a*, *FoxA2*, and *Pitx3*, fibroblasts have been successfully converted into DA-like neurons *in vitro* [6, 7]. The iNs are capable of releasing DA and exhibit DAergic neuron-like electrophysiological profiles. Importantly,

Huadong Xu, Xu Cheng have contributed equally to this work.

✉ Changhe Wang  
changhewang@xjtu.edu.cn

✉ Xinjiang Kang  
kxj335@163.com

<sup>1</sup> Key Laboratory of Medical Electrophysiology, Ministry of Education of China, The Institute of Cardiovascular Research, Southwest Medical University, Luzhou 646000, China

<sup>2</sup> Neuroscience Research Center, Institute of Mitochondrial Biology and Medicine, Key Laboratory of Biomedical Information Engineering of Ministry of Education, School of Life Science and Technology, Xi'an Jiaotong University, Xi'an 710049, China

<sup>3</sup> Department of Neurology, The First Affiliated Hospital of Xi'an Jiaotong University, Xi'an 710061, China

<sup>4</sup> College of Life Science, Liaocheng University, Liaocheng 252059, China



transplantation of iNs into the striatum alleviates the motor defects in mouse [6] and rat [7] models of PD.

### iDNs from Glial Cells *In Situ*

Although the DAergic neurons derived from ESCs, iPSCs, or iNs *in vitro* can alleviate the PD motor defects by transplantation into the striatum or SNpc, the problems of ectopic cells grafted into the host brain still need to be overcome, including ethical issues, tumorigenesis, and immunological rejection. Thus, the concept of converting DAergic neurons from non-neuronal cells *in situ* becomes more attractive and encouraging.

There is a consensus that the same origin of neurons and glial cells from common progenitor radial glial cells confers the possibility of converting glial cells into neurons by lineage reprogramming [8]. Glial cells become reactive when the brain is damaged or under the neurodegenerative conditions, forming glial scars that initially restrict the spread of damage, but ultimately are harmful to axonal regeneration [9]. Reprogramming these cells into functional neurons not only reduces the detrimental effects of glial scars, but also re-establishes damaged neuronal circuits and facilitates functional recovery. The striatum and SNpc are the most seriously affected brain regions in PD patients and animal models, and converting the glial cells into functional DAergic neurons in these two regions is an appealing strategy for PD therapy.

But more recently, Zhang and colleagues reported that “the presumed astrocyte-converted neurons were not originated from the resident astrocytes but from the adeno-associated virus (AAV)-infected endogenous neurons” [10]. Intriguingly, there was a tit-for-tat report from Chen and colleagues showing that the astrocyte-converted neurons did indeed originate from the astrocytes through lineage tracing [11]. The possible explanations for this discrepancy are that the titers of AAV used in their studies and the number of tracing days for astrocyte-to-neuron conversion after virus injection were different. Application of a much lower titer of AAV with more tracing days enabled Chen and colleagues to detect the astrocyte-to-neuron conversion through lineage tracing. Therefore, this controversy alerts the field of lineage transdifferentiation that, to draw a stringent conclusion, the lineage-tracing strategy is essential for the determination of cell fate conversion *in vivo*.

### iDNs from Glial Cells in the Striatum?

The striatum is a hot-spot for cell-based PD therapy due to its large volume and its critical roles as a converging node in movement control. Whether glial cells in the striatum

can be converted into functional DAergic neurons is a hotly-debated issue (Fig. 1).

Glial cells can transdifferentiate into neurons efficiently in the striatum [12–20]. Astrocytes are non-neuronal glial cells that can be converted into neuroblasts by expressing the TF Sox2, and they further develop into mature neurons when treated with histone deacetylase inhibitor, BDNF, and noggin [14], and NG2 glial cells could be reprogrammed into neurons by expressing the TFs Ascl1, Lmx1a, and Nurr1 [17]. Furthermore, the iNs are functionally integrated into local neuronal circuits.

The subtypes and identities of iNs *in vivo* were determined by multiple factors [21]. Astrocytes can be converted into pyramidal neurons in stab-wounded cortex by expressing Ngn2 and Nurr1; these neurons develop lamina-specific hallmarks and molecular identities according to their laminar location [22], indicating the important roles of region-specificity, and even layer-specificity in determining the identity of iNs. Non-neuronal cells in the striatum and cortex can be converted into GABAergic and glutamatergic neurons by combined treatment with growth factors and the TF neurexigen2, respectively [12]. These findings imply that the intrinsic property of starter cells and microenvironmental cues impact the identity of iNs, and the non-neuronal cells are inclined to be converted into the intrinsic subtypes of neurons at different brain loci *in situ*.

GABAergic neurons are the dominant intrinsic neurons in the striatum, thus glial cells are apt to be converted into this subtype of neuron in this region. Indeed, that glial cells are mainly converted into GABAergic neurons in the striatum by expression of lineage-specific factors has been supported by a series of studies [13, 15, 18]. Astrocytes are converted into calretinin-positive interneurons by Sox2 expression [13], NG2 glial cells into fast-spiking parvalbumin neurons by the TFs Ascl1, Lmx1a, and Nurr1 expression in the striatum [15], and oligodendrocytes (another kind of glial cell) into GABAergic cells including DARPP32- and parvalbumin-positive neurons by knock-down of polypyrimidine tract-binding protein (PTB) [18]. However, several groups have reported that astrocytes can be converted into DA-like neurons by lineage reprogramming in the striatum of 6-OHDA induced PD models [16, 19, 20]. By application of the TFs Neurod1, Ascl1, and Lmx1A and the microRNA miR218 [16], or by application of the TFs Ascl1, Pitx3, Lmx1a, and Nurr1 and electro-magnetized gold nanoparticles (AuNPs) under EMFs [19], or by PTB knockdown with CRISPR-CasRx [20], astrocytes can be converted into DA-like neurons in the striatum. More importantly, the induced DA-like neurons alleviate the PD motor defects. How can this discrepancy be explained? One possible explanation is the presence of reactive gliosis in the striatum of the 6-OHDA-induced PD model, and reactive astrocytes are prone to be converted

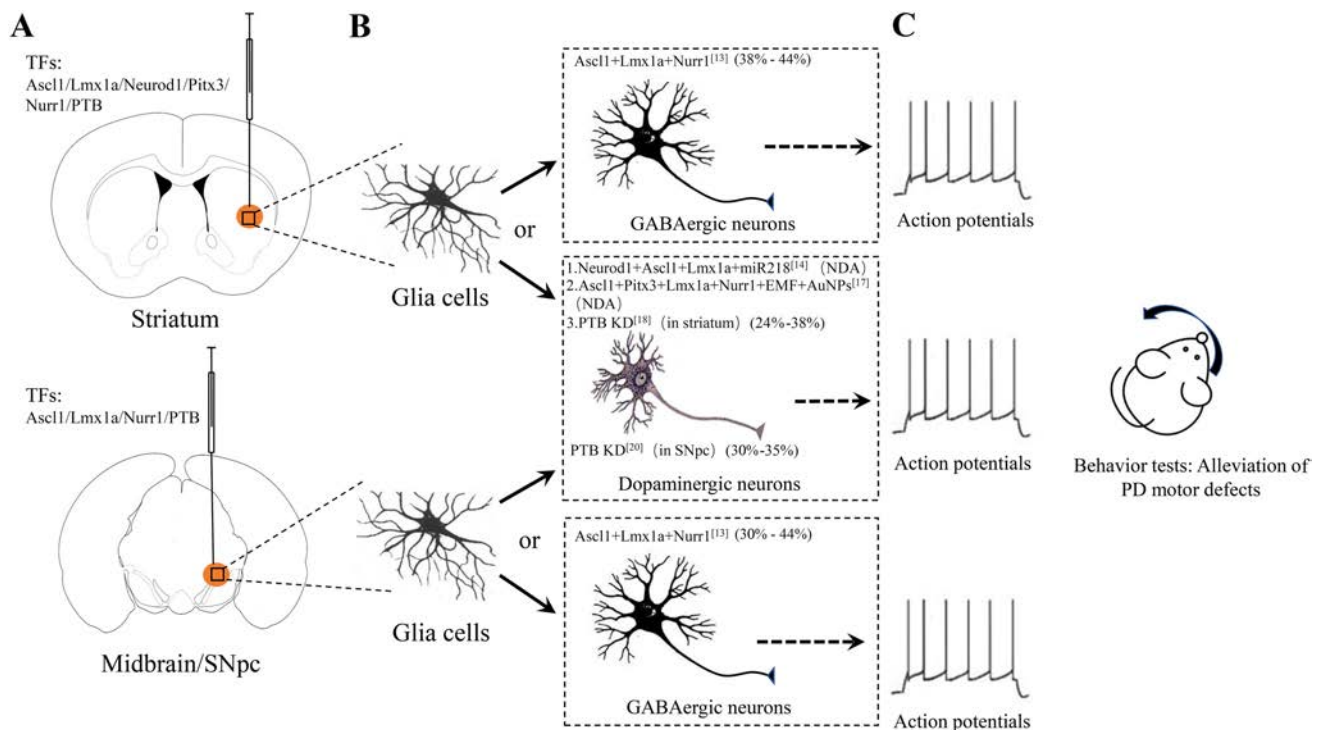


**Fig. 1** Glial cell-induced neurons (iNs) in the striatum and midbrain/SNpc in the PD mouse model. **A** Transcriptional factors (TFs) are delivered into the striatum (upper panel) or midbrain/SNpc (lower panel). **B** The subtypes of iNs are identified by both immunohistochemistry and electrophysiology, but the results are different in the striatum or midbrain/SNpc by application of different combinations

of TFs. Note the different combinations of TFs in the dashed rectangle. The values in parentheses are the conversion efficiency. **C** Functional analysis of iNs. The iNs, including DAergic and GABAergic neurons, are functionally mature; only DAergic neurons have a therapeutic effect in the PD mouse model. AuNPs, gold nanoparticles; EMF, electromagnetic field; NDA: no data available.

into DAergic neurons. However, Pereira *et al.* has reported that glial cells are converted into GABAergic interneurons, when transdifferentiated with the lineage conversion TFs Ascl1, Lmx1a, and Nurr1, in the striatum of the 6-OHDA-induced PD model [15], implying that reactive gliosis alone does not affect the subtypes of iNs, and other essential factors/conditions may be responsible for the discrepancy in the subtypes of iNs.

### iNs from Glial Cells in the Midbrain/SNpc?

The number of DAergic neurons is substantially reduced in the SNpc of PD patients and animal models. Theoretically, the SNpc should be the principal target for CRT. Considering the long projection from the SNpc to the striatum and lack of environmental cues to guide the grafted cells/transdifferentiated cells in the VTA projecting to the striatum in the adult brain, this region has not been considered as an ideal therapeutic target for cell-based PD therapy. However, recent research has shown that human ESC-derived midbrain DA neurons characterized by the A9 subtype reconstruct the nigrostriatal pathway and restore motor function in the PD mouse model after being grafted into the substantia nigra, implying that the identity of grafted

neurons determines the axonal pathfinding to the dorsal striatum [23]. We first reported that astrocytes can be converted into DAergic neurons by PTB knockdown in the SNpc, and the motor defects of the PD mouse model are completely reversed [24]. Unexpectedly, the iNs projected their axons to the dorsal striatum and reconstructed the nigrostriatal pathway, accompanied by the restoration of DA release in the striatum of PD mice. The behavioral tests showed the complete reversal of apomorph- and amphetamine-induced rotation, as well as motor defects in the cylinder test, indicating functional restoration. This opened a new avenue for PD therapy.

However, the subtypes of iNs in the midbrain/SNpc were also different (Fig. 1). Pereira *et al.* reported that glial cells in the midbrain transduced with the TFs Ascl1, Lmx1a, and Nurr1, were converted into interneurons, but not TH-positive neurons in PD models [15]. Thus, the findings that the mechanisms underlying DA-fate determinants such as Lmx1a and Nurr1 cannot convert glial cells into DAergic neurons, and only PTB downregulation can, needs further investigation before clinical trials.

## Strategy of Reprogramming Site-Selection for PD Therapy

Regarding reprogramming sites in the striatum and SNpc for PD therapy, the SNpc may be the better candidate. First, iDNs can be efficiently converted from astrocytes by PTB downregulation. Second the SNpc is where DA neurons reside, and the converted DAergic neurons are not alien to neighboring cells. The iDNs receive synaptic inputs from different upstream neurons, regulating the excitability of iDNs and ensuring proper DA release in the striatum. However, iDNs are ectopic to the striatum, and there are no proper circuits that control iDNs in the striatum, leading to random and irregular release of DA, which would lead to side-effects such as dyskinesia.

## Combination of TFs for the Induction of DA Neurons

The aim of combination of TFs in cell-lineage conversion is either to improve the conversion efficiency, or to obtain a specific subtype of cells, or both. *Ascl1*, *Brn2*, *Myt1l*, *Sox2*, *Ng2*, and *NeuroD1* play major roles in converting non-neuronal cells into neurons. The different combination of the above TFs contributes to the different efficiency of cell-lineage conversion. Vierbuchen *et al.* reported that the conversion rate of fibroblast-to-neuron under the combination of *Ascl1*, *Brn2*, and *Myt1l* is 2–3 fold higher than that of *Ascl1*, *Brn2*, *Myt1l*, *Zic1*, and *Olig2* *in vitro* [4].

Cell-lineage conversion is more complicated *in vivo* than *in vitro*. Besides the efficiency of conversion, the subtype of iDNs is another major challenge. It is conceivable that many neurological diseases preferentially affect a specific subtype of neurons over other types. For instance, since DAergic neurons are preferentially lost in PD, induction of DAergic neurons from glial cells *in situ* should be the ideal method for PD treatment. It is reasonable to suggest that the co-introduction of DAergic neuron fate-determining TFs, such as *Nurr1*, *Lmx1a*, *FoxA2*, and *Pitx3*, along with the neuron-determining TFs noted above, can convert glial cells into DAergic neurons. However, the expression of *Ascl1*, *Lmx1a*, and *Nurr1* in Ng2 cells in the striatum fails to generate DAergic neurons, but produces GABAergic neurons [15]. This is somewhat surprising, as *Nurr1* is critical for the differentiation of DAergic neurons, while under the condition of expressing *Ascl1*, *Lmx1a*, *Nurr1*, and *Pitx3*, astrocytes are successfully converted into DAergic neurons in the striatum of a PD mouse model [19]. The combination of *Pitx3*, a factor important for the early development and survival of midbrain DAergic neurons, with *Nurr1* may be crucial for the conversion of DAergic neurons from glial cells. Of

note, the intrinsic lineage of the glial cells and local environmental cues are also essential for the final fate of the converted cells *in vivo*.

To improve the efficiency of cell-lineage conversion *in vivo*, the combination of TFs with other assistant factors, such as small molecules (VPA, BDNF, noggin, FGF2, and EGF), microRNAs (*miR124* and *miR218*) and physical methods (AuNPs and EMF), have also been applied to cell-lineage reprogramming. For example, the conversion rate of DAergic neurons from astrocytes under the combination of TFs *Ascl1*, *Pitx3*, *Lmx1a*, and *Nurr1* with magnetized AuNPs under EMF conditions, which promotes histone acetylation and thereby increases the accessibility of neuronal loci to TFs, is 4–5 fold higher than that of the TFs alone [19].

Therefore, different combinations of TFs determine the conversion efficiency from glial cells to specific subtype of neurons to a large extent, and some assistant factors also play a synergistic role in the improvement of the conversion rate. Thus, further investigation of the underlying mechanism is necessary and important for the development of lineage transdifferentiation and the treatment of neurological diseases.

## Challenge of Treating PD with iDNs

Although some reports of glia-to-iDN conversion *in vivo* provide the proof-of-concept for PD treatment, some challenges still need to be overcome before clinical translation. The first challenge is how to convert glial cells into *bona fide* midbrain DA neurons. Some iDNs share certain markers identical to midbrain DA neurons, but they are not fully functional neurons. The second challenge is how to control the quantity of iDNs. A few iDNs is not sufficient to relieve the PD syndromes. However, excessive iDNs induce side-effects such as dyskinesia by releasing more than sufficient DA in the striatum. The third but not the last challenge is how to maintain the long-term survival of iDNs in brain. On one hand, the iDNs derived from PD patients commonly carry the genetic mutations associated with PD. On the other hand, the overall milieu/microenvironment of the PD brain is not iDN-friendly. Both of these quickly lead to iDN degeneration.

## Summary

Lineage reprogramming provides an alternative therapeutic strategy not only for PD, but also for other neurodegenerative diseases, such as Huntington disease and Alzheimer disease. Glia cells are ideal sources of starter cells for reprogramming, and the option of nuclei or brain regions

for reprogramming will be critical for the clinical translation of iDNs for PD therapy. The studies of iDNs *in situ* for PD therapy are at initial stage and many obstacles still have to be overcome before clinical translation.

**Acknowledgements** This insight was supported by the National Natural Science Foundation of China (32171233, 32000704, 81974203, 81901308, 31670843, 21790390, and 21790394), the Natural Science Foundation of Sichuan Province, China (2020YJ0337 and 2020YJ0378), the Natural Science Foundation of Shaanxi Province of China (2020JQ-029 and 2019JC-07), the Key Research and Development Program of Shaanxi Province, China (2017SF-113), the Science and Technology Innovation Projects of China (20-163-00-TS-009-035-01), China Postdoctoral Science Foundation (2018M640972), and the Innovation Capability Support Program of Shaanxi Province, China (2021TD-37).

**Conflict of interest** The authors declare that they have no conflict of interest.

## References

- Hargus G, Cooper O, Deleidi M, Levy A, Lee K, Marlow E. Differentiated Parkinson patient-derived induced pluripotent stem cells grow in the adult rodent brain and reduce motor asymmetry in Parkinsonian rats. *Proc Natl Acad Sci U S A* 2010, 107: 15921–15926.
- Kang XJ, Xu HD, Teng SS, Zhang XY, Deng ZJ, Zhou L, *et al.* Dopamine release from transplanted neural stem cells in Parkinsonian rat striatum *in vivo*. *Proc Natl Acad Sci U S A* 2014, 111: 15804–15809.
- Torper O, Pfisterer U, Wolf DA, Pereira M, Lau S, Jakobsson J, *et al.* Generation of induced neurons via direct conversion *in vivo*. *Proc Natl Acad Sci U S A* 2013, 110: 7038–7043.
- Vierbuchen T, Ostermeier A, Pang ZP, Kokubu Y, Südhof TC, Wernig M. Direct conversion of fibroblasts to functional neurons by defined factors. *Nature* 2010, 463: 1035–1041.
- Pang ZP, Yang N, Vierbuchen T, Ostermeier A, Fuentes DR, Yang TQ, *et al.* Induction of human neuronal cells by defined transcription factors. *Nature* 2011, 476: 220–223.
- Kim J, Su SC, Wang HY, Cheng AW, Cassady JP, Lodato MA, *et al.* Functional integration of dopaminergic neurons directly converted from mouse fibroblasts. *Cell Stem Cell* 2011, 9: 413–419.
- Liu XJ, Li F, Stubblefield EA, Blanchard B, Richards TL, Larson GA, *et al.* Direct reprogramming of human fibroblasts into dopaminergic neuron-like cells. *Cell Res* 2012, 22: 321–332.
- Dimou LD, Götz M. Glial cells as progenitors and stem cells: New roles in the healthy and diseased brain. *Physiol Rev* 2014, 94: 709–737.
- Karimi-Abdolrezaee S, Billakanti R. Reactive astrogliosis after spinal cord injury-beneficial and detrimental effects. *Mol Neurobiol* 2012, 46: 251–264.
- Wang LL, Serrano C, Zhong XL, Ma SP, Zou YH, Zhang CL. Revisiting astrocyte to neuron conversion with lineage tracing *in vivo*. *Cell* 2021, 184: 5465–5481.e16.
- Xiang ZQ, Xu L, Liu MH, Wang QS, Li W, Lei WL, *et al.* Lineage tracing of direct astrocyte-to-neuron conversion in the mouse cortex. *Neural Regen Res* 2021, 16: 750–756.
- Grande A, Sumiyoshi K, López-Juárez A, Howard J, Sakthivel B, Aronow B, *et al.* Environmental impact on direct neuronal reprogramming *in vivo* in the adult brain. *Nat Commun* 2013, 4: 2373.
- Niu WZ, Zang T, Smith DK, Vue TY, Zou YH, Bachoo R, *et al.* SOX2 reprograms resident astrocytes into neural progenitors in the adult brain. *Stem Cell Reports* 2015, 4: 780–794.
- Niu WZ, Zang T, Zou YH, Fang SH, Smith DK, Bachoo R, *et al.* *In vivo* reprogramming of astrocytes to neuroblasts in the adult brain. *Nat Cell Biol* 2013, 15: 1164–1175.
- Pereira M, Birtele M, Shrigley S, Benitez JA, Hedlund E, Parmar M, *et al.* Direct reprogramming of resident NG2 *Glia* into neurons with properties of fast-spiking parvalbumin-containing interneurons. *Stem Cell Reports* 2017, 9: 742–751.
- Rivetti di Val Cervo P, Romanov RA, Spigolon G, Masini D, Martín-Montañez E, Toledo EM, *et al.* Induction of functional dopamine neurons from human astrocytes *in vitro* and mouse astrocytes in a Parkinson's disease model. *Nat Biotechnol* 2017, 35: 444–452.
- Torper O, Ottosson DR, Pereira M, Lau S, Cardoso T, Grealish S, *et al.* *In vivo* reprogramming of striatal NG2 *Glia* into functional neurons that integrate into local host circuitry. *Cell Rep* 2015, 12: 474–481.
- Weinberg MS, Criswell HE, Powell SK, Bhatt AP, McCown TJ. Viral vector reprogramming of adult resident striatal oligodendrocytes into functional neurons. *Mol Ther* 2017, 25: 928–934.
- Yoo J, Lee E, Kim HY, Youn DH, Jung J, Kim H, *et al.* Electromagnetized gold nanoparticles mediate direct lineage reprogramming into induced dopamine neurons *in vivo* for Parkinson's disease therapy. *Nat Nanotechnol* 2017, 12: 1006–1014.
- Zhou HB, Su JL, Hu XD, Zhou CY, Li H, Chen ZR, *et al.* *Glia*-to-neuron conversion by CRISPR-CasRx alleviates symptoms of neurological disease in mice. *Cell* 2020, 181: 590–603.e16.
- Wang FC, Cheng LP, Zhang XH. Reprogramming glial cells into functional neurons for neuro-regeneration: Challenges and promise. *Neurosci Bull* 2021, 37: 1625–1636.
- Mattugini N, Bocchi R, Scheuss V, Russo GL, Torper O, Lao CL, *et al.* Inducing different neuronal subtypes from astrocytes in the injured mouse cerebral cortex. *Neuron* 2019, 103: 1086–1095.e5.
- Xiong M, Tao YZ, Gao QQ, Feng B, Yan W, Zhou YY, *et al.* Human stem cell-derived neurons repair circuits and restore neural function. *Cell Stem Cell* 2021, 28: 112–126.e6.
- Israel Z, Asch N. Reversing a model of Parkinson's disease with *in situ* converted nigral neurons. *Mov Disord* 1955, 2020: 35.

# Expanding Views of Mitochondria in Parkinson's Disease: Focusing on *PINK1* and *GBA1* Mutations

Yu Yuan<sup>1</sup> · Xizhen Ma<sup>1</sup> · Ning Song<sup>1</sup> · Junxia Xie<sup>1</sup>

Received: 31 December 2021 / Accepted: 6 March 2022 / Published online: 11 May 2022  
© Center for Excellence in Brain Science and Intelligence Technology, Chinese Academy of Sciences 2022

A new conceptual model has been proposed for Parkinson's disease (PD) pathogenesis, which can be divided into triggering, facilitating, and aggravating processes [1]. Mitochondria are believed to participate in all three phases: pesticides (one of the definite triggers in PD pathogenesis) inhibit mitochondrial complex I (MCI); mitochondrial dysfunction also comes into play as facilitator/aggravator *via* the chronic production of reactive oxygen species (ROS) or the link with impaired autophagy/neuroinflammation; and finally the neurodegeneration and the spread of  $\alpha$ -synuclein pathology [1].

Among several subpopulations of vulnerable neurons in PD, dopaminergic neurons are more susceptible because they have fewer mitochondria, while their extensive, branching axons place more bioenergetic demand on mitochondria [2]. The direct link between mitochondrial dysfunction and PD pathogenesis has been validated by a recent study showing that loss of *Ndufs2*, a vital subunit of the MCI catalytic core, is sufficient to cause the disruption of MCI and progressive parkinsonism [3]. In mice with *Ndufs2* deletion, the energy supply in dopaminergic neurons switches from mitochondrial ATP production to almost entirely glycolysis. This reveals the metabolic plasticity of dopaminergic neurons; however, this also leads to axon-first loss-of-function, and triggers a gradual,

levodopa-reactive parkinsonism ultimately as shown in humans [3]. More recently, strong evidence from gut microbiota studies further supports a role for mitochondrial dysfunction in PD pathogenesis. Both *in vitro* and *in vivo*, the microbial toxin  $\beta$ -N-methylamino-L-alanine (BMAA) specifically targets mitochondria thus inducing their fragmentation and decreased turnover. Although there is still no evidence that the gut microbiota can produce BMAA *in vivo*, foodborne (often detected in aquatic food products) BMAA is able to travel from the gut to the brain and target mesencephalic rather than cortical mitochondria. Together with the intestinal events such as gut dysbiosis, loss of barrier integrity, and the propagation of  $\alpha$ -synuclein aggregates, dysfunctional mitochondria drive innate immunity activation and neuroinflammation, which primes neurodegeneration and motor deficits [4].

The above evidence points to the importance of mitochondrial dysfunction in sporadic PD developing from environmental insults. Several monogenic mutations that encode proteins responsible for maintaining mitochondrial health have been implicated in early-onset PD, among which *PINK1* (*PARK6*) has been extensively investigated [5]. The *PINK1* gene encodes a mitochondrial serine/threonine protein kinase known as PTEN-induced kinase 1, which can phosphorylate the cytoplasmic E3 ubiquitin ligase Parkin and recruit the latter to damaged mitochondria. Mitochondrial proteins go through ubiquitination and then recruit autophagosomes for mitophagy; this helps to clear damaged mitochondria and protect cells from injury and stress. *PINK1* is believed to promote mitochondrial ubiquitination either dependent on PRKN or likely through other ubiquitin E3 ligases. There is also new evidence that *Pink1* is not necessary for mitochondrial ubiquitination in *Dnm1l/Drp1* (a dynamin-related GTPase) knockout mice, in which mitophagy is blocked. In the absence of *Pink1*,

✉ Ning Song  
ningsong@qdu.edu.cn

✉ Junxia Xie  
jxiexie@public.qd.sd.cn

<sup>1</sup> Institute of Brain Science and Disease, School of Basic Medicine, Shandong Provincial Key Laboratory of Pathogenesis and Prevention of Neurological Disorders, Qingdao University, Qingdao 266071, China



mitochondrial ubiquitination does not decline in the *dnm1*-knockout liver; instead, a new mechanism of SQSTM1-KEAP1-RBX1 complex-dependent ubiquitination occurs for mitophagy. It has been suggested that PINK1 controls the balance between mitochondrial fission and fusion, rather than globally controlling mitochondrial ubiquitination [6]. Actually, the PINK1–Parkin–ubiquitination signaling cascade is not the only pathway regulating mitophagy. A new kinase substrate of PINK1 has recently been reported to provide new mechanistic insights into PINK1-primed mitophagy. Mitochondrial Tu translation elongation factor (TUFm) can be phosphorylated at Ser222 in a PINK1-dependent manner. By interfering negatively with the conjugation of Atg5–Atg12, the autophagy-related proteins in *Drosophila* and human, phosphorylation of TUFm-S222 is then sufficient to interact with PINK1 genetically and negatively regulate mitophagy. This study concluded a dual role of PINK1 in regulating mitophagy, either activating mitophagy as previously reported or suppressing mitophagy *via* the phosphorylation of TUFm. Notably, the self-antagonizing feature of PINK1–TUFm in mitophagy is evolutionarily conserved across species [7].

Interestingly, PINK1 protein is selectively more abundant in primate brains than in rodent brains. However, in a new *PINK1*-knockout monkey model using CRISPR/Cas9, there is no alteration in the morphology and number of mitochondria assessed by electron microscopy in surviving/degenerated neurons in the substantia nigra. Consistent with the *in vivo* findings, mitochondrial proteins (VDAC1, TOM20, Complex-II, -III, -V) in cultured primary monkey neurons with *PINK1* deletion and mitochondrial dynamics (size, length, and motility) in *PINK1*-deleted astrocytes are not significantly different. Meanwhile, *PINK1* deficiency reduces the phosphorylation of several proteins important for neuronal function and survival. Therefore, neurodegeneration caused by *PINK1* mutation/deletion might be attributable to the PINK1 kinase activity rather than its mitochondrial function, thus updating the current understanding of *PINK1* contributions to the pathogenesis of PD [8].

More recently, *PINK1* deficiency has first been reported to be associated with ceramide accumulation in mitochondria *via* a defective electron transport chain. An accumulation of ceramide was observed in mitochondria isolated from *Pink1*-knockout mouse embryonic fibroblasts and *Pink1*-deficient flies, as well as patient-derived fibroblasts endogenously carrying homozygous *PINK1* mutations, suggesting that the aberrant ceramide homeostasis associated with *PINK1* is evolutionarily conserved. Importantly, increased ceramide accumulation in *PINK1*-deficient mitochondria are proposed to serve as a signal for ceramide-induced mitophagy. This might be in an attempt to meet the requirements for mitochondrial clearance when impaired

mitophagy is caused by *PINK1* mutations, although it is still not consistent whether *PINK1* deficiency severally affects mitochondrial function in different models [9]. We speculated that, in spite of the dispensable role in mitochondrial ubiquitination and even mitochondrial function, *PINK1* does not appear to be exclusively related to mitochondrial dysfunction. Considering that *PINK1* is a clear monogenic factor in familial PD, unveiling the contributions of *PINK1* in the mitochondria-associated neurodegeneration of PD is worthy of further investigation, especially in unique models such as *Drosophila*, rodents, and human beings.

As for ceramide (lipid) homeostasis, recent findings have demonstrated that lipids surrounded by defective mitochondria are present in the Lewy body cores of postmortem brains from PD patients [10]. Accumulation of lipids within cells induces cellular stress in which lysosomes play a pivotal role. *GBA1* encodes glucocerebrosidase (GCase), a lysosomal enzyme involved in ceramide synthesis, known to be the most common risk factor in PD pathogenesis. *GBA1* mutations cause lysosomal dysfunction, as well as the accumulation of glucosylceramide and  $\alpha$ -synuclein, which contribute to a toxic cascade. Wild-type GCase activation by small-molecule modulators is able to rescue pathogenic phenotypes in induced pluripotent stem cells (iPSC)-derived dopaminergic neurons or mice with *GBA1* mutants [11]. Apart from the well-accepted lysosomal contributions in *GBA1*-related neurodegeneration [12], recent findings support the role of mitochondrial dysfunction. Impaired mitophagy has been reported in postmortem brains from PD patients carrying heterozygous *GBA* mutations [13]. In mice with the L444P knock-in mutation, mitochondrial fission in the hippocampus decreases and fewer impaired mitochondria are recruited to phagophores in hippocampal neurons, which specifically inhibits mitophagy due to the mutant GCase protein. Meanwhile, the absence of GCase activity hinders the lysosomal clearance of autophagosomes. Therefore, a dual mechanism of both the mutant protein and the loss of GCase activity disrupt both an initial step of recruitment and a subsequent step of lysosomal degradation, eventually the mitochondrial dysfunction and mitophagy defect triggered by *GBA1* mutations [13].

Recently, mitochondrial-lysosomal (M–L) contact has been shown to mediate and bilaterally control the cross-talk between the two organelles in human neurons. Visualized by confocal live-cell microscopy, the duration of M–L contact tethering is prolonged in PD patient-derived mutant *GBA1* dopaminergic neurons, indicative of inefficient untethering events, that is, decreased levels of the untethering protein TBC1D15. The prolonged tethering is caused by the selective loss of GCase activity rather than global lysosomal enzyme dysfunction, and this can be restored by

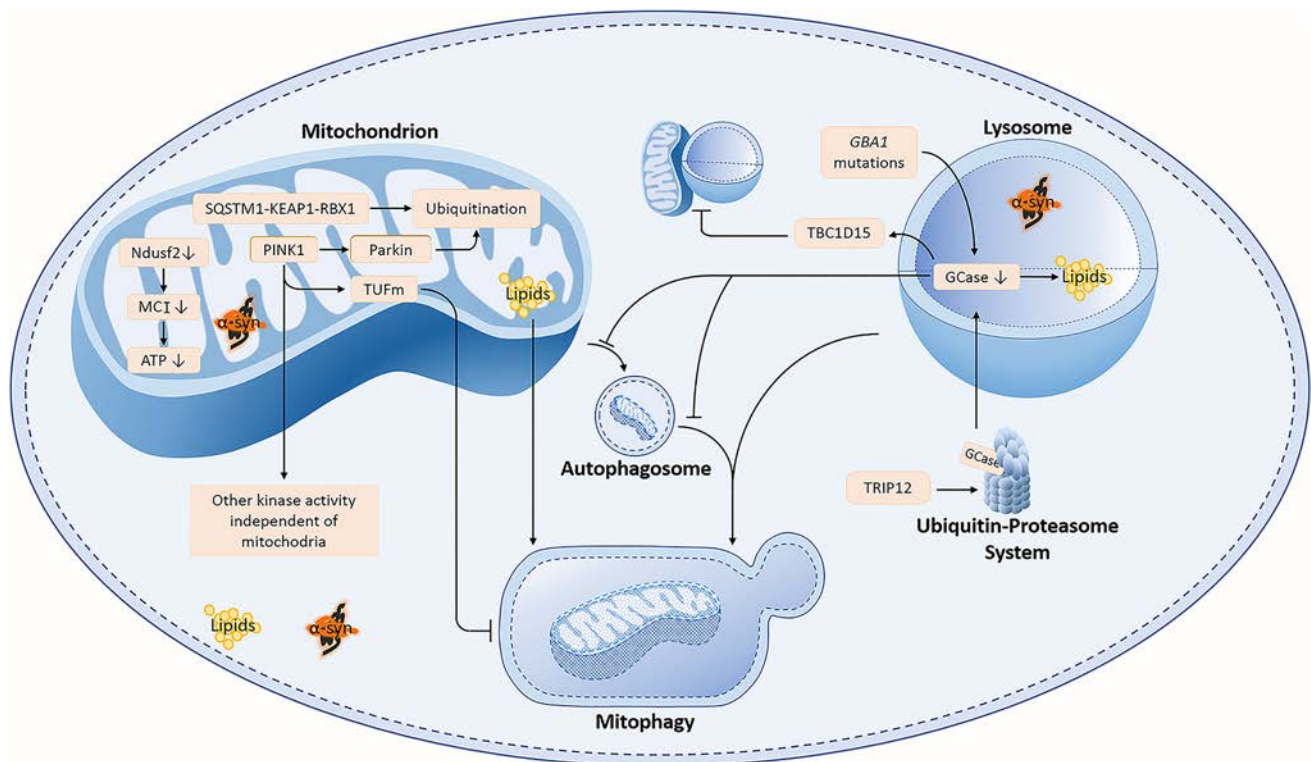


**Fig. 1** Under physiological conditions, PINK1 phosphorylates and recruits the cytoplasmic E3 ubiquitin ligase Parkin, the latter mediating the ubiquitination of mitochondrial protein and then recruiting autophagosomes for mitophagy. PINK1 also phosphorylates TUFm and suppresses mitophagy, suggesting a dual role of PINK1 in regulating mitophagy. Other kinase activity independent of mitochondria might exist for PINK1. Under the condition of PINK1 deficiency, mitophagy can be blocked. Meanwhile, a new mechanism of SQSTM1-KEAP1-RBX1 complex-dependent ubiquitination occurs for mitophagy. PINK1 deficiency linked with ceramide accumulation might also trigger ceramide-induced mitophagy to

meet the requirements for mitochondrial clearance. In addition to *GBA1* mutations resulting in GCase dysfunction, TRIP12-mediated GCase ubiquitination causes premature GCase degradation *via* the ubiquitin-proteasome system. The loss of GCase activity causes the accumulation of lipids and  $\alpha$ -synuclein in lysosomes. This also causes prolonged mitochondria-lysosome contact *via* down-regulating the untethering protein TBC1D15, or disrupts autophagosome recruitment and lysosomal degradation. Although GCase functional impairment is associated with mitochondrial dysfunctions, the direct link between GCase and mitochondria needs to be further elucidated.

increasing GCase activity [14]. The E3 ligase thyroid hormone receptor interacting protein 12 (TRIP12) has been identified as a major regulator of GCase. TRIP12-mediated ubiquitination of GCase at lysine 293 strictly controls GCase levels *via* the ubiquitin-proteasome system. The level of TRIP12 is significantly inversely correlated with GCase in the SN of PD patients. Both *in vivo* and *in vitro* evidence has suggested that increased TRIP12 causes premature GCase degradation, leading to mitochondrial dysfunction and thus  $\alpha$ -syn aggregation. GCase is required in TRIP12-triggered mitochondrial dysfunction since TRIP12 overexpression does not worsen the mitochondrial dysfunction in *GBA1*-knockout SH-SY5Y cells, while GCase overexpression fully rescues the reduction of mitochondrial length and the decreased MCI enzyme activity [15]. In *GBA1*-knockout SH-SY5Y cells, reduced GCase activity is accompanied by reduced mitochondrial length and increased ROS, although a previous study reported that cells with *GBA* deletion (loss of GCase

enzyme activity) do not show mitochondrial defects [16]. Therefore, we conclude that GCase functional impairment is strongly associated with mitochondrial dysfunctions; however, the direct link between GCase and mitochondria needs to be further elucidated.

Last but not least, as the key contributor to PD pathogenesis,  $\alpha$ -synuclein, either under physiological or pathological conditions, is closely linked to mitochondrial function. Oligomeric  $\alpha$ -synuclein has been delivered to localize to the mitochondria and interact with ATP synthase. Generating ROS is thought to be an intrinsic property of the oligomers, which induces lipid peroxidation in particular at the inner mitochondrial membrane [17]. Given the interrelated nature of lipid homeostasis, mitochondrial, and lysosomal function in  $\alpha$ -synuclein pathology [18–20] (Fig. 1), we highlight the influence of mitochondrial dysfunction in PD pathogenesis, with an emphasis on the *PINK1* and *GBA1* mutations in familial PD and *PINK1* and GCase dysfunction in sporadic PD.

**Acknowledgements** This insight article was supported by the National Natural Science Foundation of China (32170984 and 31871049), the Excellent Innovative Team of Shandong Province, and the Taishan Scholars Construction Project.

**Conflict of interest** All authors claim that there are no conflicts of interest.

## References

- Johnson ME, Stecher B, Labrie V, Brundin L, Brundin P. Triggers, facilitators, and aggravators: Redefining Parkinson's disease pathogenesis. *Trends Neurosci* 2019, 42: 4–13.
- Trinh D, Israwi AR, Arathoon LR, Gleave JA, Nash JE. The multi-faceted role of mitochondria in the pathology of Parkinson's disease. *J Neurochem* 2021, 156: 715–752.
- González-Rodríguez P, Zampese E, Stout KA, Guzman JN, Ilijic E, Yang B. Disruption of mitochondrial complex I induces progressive Parkinsonism. *Nature* 2021, 599: 650–656.
- Esteves AR, Munoz-Pinto MF, Nunes-Costa D, Candeias E, Silva DF, Magalhães JD, *et al.* Footprints of a microbial toxin from the gut microbiome to mesencephalic mitochondria. *Gut* 2021. <https://doi.org/10.1136/gutjnl-2021-326023>.
- Li H, Wu SH, Ma X, Li X, Cheng TL, Chen ZF, *et al.* Co-editing PINK<sub>1</sub> and DJ-1 genes via adeno-associated virus-delivered CRISPR/Cas9 system in adult monkey brain elicits classical parkinsonian phenotype. *Neurosci Bull* 2021, 37: 1271–1288.
- Yamada T, Dawson TM, Yanagawa T, Iijima M, Sesaki H. SQSTM1/p62 promotes mitochondrial ubiquitination independently of PINK<sub>1</sub> and PRKN/parkin in mitophagy. *Autophagy* 2019, 15: 2012–2018.
- Lin JJ, Chen K, Chen WF, Yao YZ, Ni SW, Ye MN, *et al.* Paradoxical mitophagy regulation by PINK<sub>1</sub> and TUFm. *Mol Cell* 2020, 80: 607–620.e12.
- Yang WL, Guo XY, Tu ZC, Chen XS, Han R, Liu YT, *et al.* PINK<sub>1</sub> kinase dysfunction triggers neurodegeneration in the primate brain without impacting mitochondrial homeostasis. *Protein Cell* 2022, 13: 26–46.
- Vos M, Dulovic-Mahlow M, Mandik F, Frese L, Kanana Y, Haissatou Diaw S, *et al.* Ceramide accumulation induces mitophagy and impairs  $\beta$ -oxidation in PINK<sub>1</sub> deficiency. *Proc Natl Acad Sci U S A* 2021, 118. e2025347118.
- Shahmoradian SH, Lewis AJ, Genoud C, Hench J, Moors TE, Navarro PP, *et al.* Lewy pathology in Parkinson's disease consists of crowded organelles and lipid membranes. *Nat Neurosci* 2019, 22: 1099–1109.
- Burbulla LF, Jeon S, Zheng JB, Song PP, Silverman RB, Krainc D. A modulator of wild-type glucocerebrosidase improves pathogenic phenotypes in dopaminergic neuronal models of Parkinson's disease. *Sci Transl Med* 2019, 11: eaa6870.
- Behl T, Kaur G, Fratila O, Buhas C, Judea-Pusta CT, Negrut N, *et al.* Cross-talks among GBA mutations, glucocerebrosidase, and  $\alpha$ -synuclein in GBA-associated Parkinson's disease and their targeted therapeutic approaches: A comprehensive review. *Transl Neurodegener* 2021, 10: 4.
- Li HY, Ham A, Ma TC, Kuo SH, Kanter E, Kim D, *et al.* Mitochondrial dysfunction and mitophagy defect triggered by heterozygous GBA mutations. *Autophagy* 2019, 15: 113–130.
- Kim S, Wong YC, Gao FD, Krainc D. Dysregulation of mitochondria-lysosome contacts by GBA1 dysfunction in dopaminergic neuronal models of Parkinson's disease. *Nat Commun* 1807, 2021: 12.
- Seo BA, Kim D, Hwang H, Kim MS, Ma SX, Kwon SH, *et al.* TRIP12 ubiquitination of glucocerebrosidase contributes to neurodegeneration in Parkinson's disease. *Neuron* 2021, 109: 3758–3774.e11.
- Osellame LD, Rahim AA, Hargreaves IP, Gegg ME, Richard-Londt A, Brandner S, *et al.* Mitochondria and quality control defects in a mouse model of Gaucher disease—links to Parkinson's disease. *Cell Metab* 2013, 17: 941–953.
- Ludtmann MHR, Angelova PR, Horrocks MH, Choi ML, Rodrigues M, Baev AY, *et al.* A-synuclein oligomers interact with ATP synthase and open the permeability transition pore in Parkinson's disease. *Nat Commun* 2018, 9: 2293.
- Erskine D, Koss D, Korolchuk VI, Outeiro TF, Attems J, McKeith I. Lipids, lysosomes and mitochondria: Insights into Lewy body formation from rare monogenic disorders. *Acta Neuropathol* 2021, 141: 511–526.
- Wang R, Sun HY, Ren HG, Wang GH. A-Synuclein aggregation and transmission in Parkinson's disease: A link to mitochondria and lysosome. *Sci China Life Sci* 2020, 63: 1850–1859.
- Wang CJ, Yang TT, Liang MY, Xie JX, Song N. Astrocyte dysfunction in Parkinson's disease: From the perspectives of transmitted  $\alpha$ -synuclein and genetic modulation. *Transl Neurodegener* 2021, 10: 39.

# The Mechanism for Allocating Limited Working Memory Resources in Multitasking

Lu Gan<sup>1</sup> · Jinglong Wu<sup>1</sup> · Ji Dai<sup>2,3,4</sup>  · Shintaro Funahashi<sup>1</sup>

Received: 13 October 2021 / Accepted: 19 January 2022 / Published online: 11 April 2022

© Center for Excellence in Brain Science and Intelligence Technology, Chinese Academy of Sciences 2022

## Visual Working Memory and Capacity Limitation

Working memory plays an important role in many complex cognitive activities such as thinking, reasoning, decision-making, and language comprehension. Working memory refers to a mechanism involving both the temporary storage and the manipulation of information. As an important approach toward understanding the mechanisms of working memory, visual working memory has attracted attention since the 1990s. Visual working memory plays an essential role in the perception and cognition of visual information and simultaneously maintains information about multiple attributes of a visual object (e.g., colors, shapes, texture, motion direction, and spatial position) in different dimensions [1–3].

Visual working memory is one of the essential functions in daily life. To accomplish a particular goal (e.g., driving a car to a specific destination), it is usually necessary to perform multiple visual tasks and handle various types of

information simultaneously (e.g., checking traffic lights and signs and watching other cars' movements). In this situation, the cognitive system for each task must prepare a necessary amount of memory. As the number of tasks increases, the total amount of memory necessary for all tasks increases. However, the capacity of working memory is limited. A series of human behavioral studies have shown that the capacity of visual working memory is only 3–4 items [4]. Therefore, under multitasking conditions, the total amount of resources needed for all component tasks often exceeds the currently available capacity. As a result, the performance of one or more component tasks is impaired. This phenomenon is called dual-task interference. To focus discussion more on the current context, dual-task interference is confined to cognitive processes involving working memory. To understand the neural mechanisms of visual working memory and its management, it is important to understand why dual-task interference happens and how available memory is allocated to each component task depending on its demand.

✉ Ji Dai  
ji.dai@siat.ac.cn

✉ Shintaro Funahashi  
funahashi.shintaro.35e@kyoto-u.jp

<sup>1</sup> Research Center for Medical Artificial Intelligence, Shenzhen Institute of Advanced Technology, Chinese Academy of Sciences, Shenzhen 518055, China

<sup>2</sup> CAS Key Laboratory of Brain Connectome and Manipulation, the Brain Cognition and Brain Disease Institute, Shenzhen Institute of Advanced Technology, Chinese Academy of Sciences, Shenzhen 518055, China

<sup>3</sup> Shenzhen-Hong Kong Institute of Brain Science-Shenzhen Fundamental Research Institutions, Shenzhen 518055, China

<sup>4</sup> University of The Chinese Academy of Sciences, Beijing 100049, China

## Models for Flexible Allocation of Memory Resources

Based on the results of behavioral and neuroimaging studies, two models have been proposed to understand the cause of dual-task interference, namely the slot-based model and the flexible resource model. The slot-based model supposes that each item is stored in a “memory slot” and that only three or four such slots are available at one time [4, 5]. When all slots are taken by one task, additional items for other tasks cannot be stored, causing dual-task interference. Luck and Vogel (1997) used a change detection task to explore the capacity of visual working

memory, in which the participants were required to answer whether two successively presented objects were the same or not [4]. They found that the participants exhibited 100% correct performance when the number of items was  $<3$  and that their performances became significantly worse when the number of items was  $>4$ . Changing the duration of stimulus presentation did not affect these percentages. These results support the slot-based model and suggest that working memory capacity does not affect information processing.

However, the slot-based model has been challenged by studies examining how accurately memorized items are recalled. Behavioral experiments have shown that the accuracy of behavioral performance gradually decreases even if the number of objects simultaneously stored is within the capacity limit [6–8]. In addition to the number, the features binding to the stored objects such as location and orientation also affect the behavioral performance [8]. Therefore, the simple slot-based model cannot fully explain such complex behavioral effects. Thus, the flexible resource model was proposed, in which memory resources are allocated for each item flexibly depending on the importance and complexity of the items or the number of simultaneously stored items. This model has been supported by recent behavioral and neurophysiological studies [9, 10].

### Baddeley's Model of Working Memory and the Central Executive

The mechanism for allocating a limited capacity of working memory remains to be solved. Among theoretical models of working memory, Baddeley's 4-component model is well known [11]; this is composed of one master component and three slave components including the phonological loop, the visuospatial sketchpad, and the episodic buffer. Specifically, the phonological loop stores speech-based information for speech perception and language comprehension; the visuospatial sketchpad stores information for visuospatial processing and other information that cannot be processed by language; and the episodic buffer stores integrated episodes or chunks and not only acts as a buffer between the phonological loop and the visuospatial sketchpad but also links working memory with perception and long-term memory. The master component, namely the central executive, coordinates and integrates the operations of the three slave components to achieve the current goal. The central executive is thought to be a system for allocating limited memory resources to each of the slave components depending on their demands. For example, if visuospatial processing becomes more demanding than language processing, the central executive

allocates more memory to visuospatial processing. Accordingly, an appropriate control process or strategy would eventually be selected to accomplish the current goal. The functions of the central executive can be best understood using the dual-task paradigm. In a dual-task condition in which the participant is required to remember the locations and physical features of the objects simultaneously, spatial and visual working memory processes can function either independently or interactively depending on different contexts within a limited memory capacity [12]. Therefore, a system allocating memory resources to each of two processes, which corresponds to the central executive, is inevitable.

### The Overlap Hypothesis and Possible Mechanism of Dual-task Interference

As Baddeley suggested, the dual-task paradigm has been thought to be an appropriate and effective method to study the mechanism for allocating working memory resources based on the demand. The memory demand for performing each task is not always fixed but changes in a flexible manner depending on the circumstances and the memory demands of other tasks. Therefore, the flexible resource model would be appropriate to explain how limited working memory resources are allocated to each task in the dual-task condition. To explain the mechanism of the flexible resource model, an "overlap hypothesis" (Fig. 1) has been proposed [13]. When two working memory tasks (A and B) are performed independently (Fig. 1A, B), electrophysiological studies show that each neuron in the prefrontal cortex, for example, usually exhibits specific stimulus or action selectivity, or exhibits a specific temporal pattern of activity, which is referred to as task-specific or task-related activity. Since each task evokes specific groups of task-related activities, the different populations of neurons would participate in the performance of each task, although some groups of neurons would participate in both tasks (shared group). When both tasks are performed simultaneously (dual-task condition, Fig. 1C), each task not only recruits its own population of neurons (task A or B specific population, Fig. 1D, E) but also tries to recruit as many neurons as possible from the shared group (Fig. 1F) by competition with the other task. This hypothesis assumes that the strength of the interference effect depends on the "functional brain distance" between the regions each of which participates in each task. If the functional distance is short for tasks A and B, both tasks A and B would have a greater degree of common functions for performing both tasks and hence have a larger population of shared group neurons. Therefore, in dual-task conditions, a strong competition would occur between two



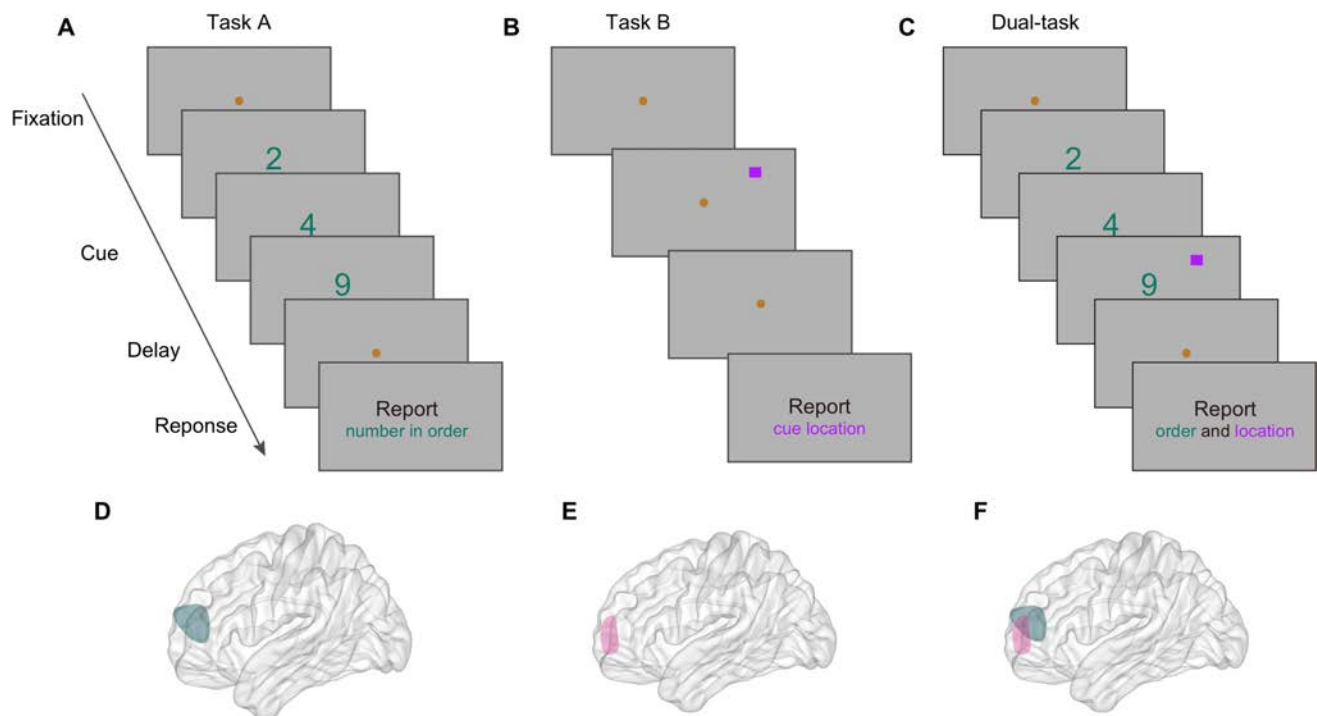


**Fig. 1** An example of the dual-task and an illustration of the overlap hypothesis. **A** A digit recall task (non-spatial visual working memory task), in which the participant has to remember the numbers during the delay period. **B** A visuospatial task (spatial working memory task), in which the participant has to remember the location of a visual cue during the delay period. **C** The dual-task condition, in which the participant performs both tasks A and B simultaneously. **D**, **E** Schematic activation area of the prefrontal cortex in the single-task

condition. Dark green and magenta indicate activation areas during the performance of task A and task B, respectively. Note that each task activates not only its own cortical region but also a region shared with another task. **F** Schematic activation area of the prefrontal cortex in the dual-task condition. Since each task tries to recruit as much area as possible from the shared region, competition occurs between the two tasks, causing dual-task interference.

tasks to recruit as many neurons as possible from the shared group.

This hypothesis is supported by several imaging studies. Early studies using positron emission tomography (PET) technology indicated that while a dual-task involving both auditory and visual working memory does not activate any dual-task specific region, independent performance of each task activates largely overlapping areas in the prefrontal, parietal, and cingulate cortex [14, 15]. In a human functional magnetic resonance imaging (fMRI) study using a dual-task (auditory comprehension and visual rotation), activation in the temporal and parietal cortices during the dual-task was substantially less than the sum of the activation when the two tasks were performed independently, indicating the presence of an interference effect in the dual-task condition [16]. The degree of overlap of activated brain areas in single-task conditions correlated with the degree of the decline in dual-task performance. In neurophysiological studies using monkeys, since the dorsolateral prefrontal cortex is thought to be responsible for dual-task interference, Watanabe and Funahashi recorded prefrontal activity while the monkeys performed spatial attention and memory tasks in the dual-task condition [17].

They found that the ability of prefrontal neurons to represent task-relevant information decreased to a degree proportional to the increased demand of the counterpart task. They further proposed that the dual-task interference is caused by simultaneous and overloaded recruitment of the common neural population by the two tasks simultaneously. Thus, the overlap hypothesis considers that the memory resource for task A corresponds to a whole population of neurons that exhibit task-related activity during the performance of task A. Since the neural population for task A overlaps the population for task B, simultaneous performance of both tasks causes competition between tasks to recruit as many neurons as possible for each task, which causes normal performance for one task (winner) and impaired performance for the other task (loser), or impaired performance of both tasks, because the size of the shared neuron group is limited. Thus, the overlap hypothesis would explain how the available memory resources are flexibly and adaptively allocated to each component task in multitasking conditions and why dual-task interference occurs.

## Conclusion and Perspective

Research on the neural mechanisms of dual-task interference has revealed that the memory resource corresponds to the computational capacity of a neural population associated with a particular information process and that dual-task interference is caused by simultaneous recruitment of the common neural population by concurrently performing two tasks. By a competition between two tasks to recruit as many neural populations as possible, a winner and a loser are determined. However, it is not yet clear how a winner and a loser are determined and what factor determines a winner. How much memory is allocated to each of two tasks is affected by not only the strength of memory demand of each task but also the order of the task priority or the significance of the task, or the order of task performance. It is not known which factor is most effective for determining the winner. To clarify these unsolved problems, further studies are needed, probably in non-human primates, because a variety of neuroscience methods including invasive approaches (e.g., extracellular recording, chemical/electrical stimulation, and viral-based neural tracing) are available in animal studies to understand the mechanisms of the management of working memory [18, 19].

In addition, dual-task interference can occur not only during working memory but also during other phases of perception and behavioral execution. It is not yet clear which stage of the cognitive process is more affected by dual-task interference, and how the similarity between tasks affects the interference. Using extracellular recording to reveal function-related activity (e.g. sensory-related, memory-related, and action-related) and compare the activity features between single-task and dual-task conditions, and between different pairs of dual-tasks (e.g. a pair of visual-related tasks and a pair of visual-auditory tasks), it is possible to address these questions.

On the other hand, the phenomenon that neurons exhibiting complex response profiles to different tasks can also be interpreted as “mixed selectivity” [20]. Mixed selectivity neurons encode distributed information about all task-relevant aspects. It is not clear how many kinds of information each or a population of mixed selective neurons can encode and whether the population activity of mixed selective neurons recorded during dual-task performance can decode the information necessary to perform each component task. Therefore, the capacity of information that mixed selectivity neurons can encode is not infinite but is also limited. In that sense, the concept of the overlap hypothesis seems to be similar to the concept of mixed selectivity. However, the theory of mixed selectivity focuses more on the neural dynamics in coding different

features, while the overlap hypothesis talks more about neuron populations and their brain regions. Even so, there is potential that these two theories inspire each other and develop together.

Lastly, understanding how the nervous system performs memory management efficiently and in a coordinated manner to operate multiple cognitive processes may contribute to the development of a new generation of artificial intelligence (AI) [21]. To perform multiple tasks simultaneously without any disturbance from any task, AI systems must install appropriate memory management mechanisms. Understanding how a winning task is determined, what factor determines a winning task, and how the task priority, the task significance, or the order of the task performance affect which task becomes a winner in behavioral and neurophysiological studies would provide important information to avoid interference effects in multitasking conditions and contribute significantly to develop a new generation of AI systems.

**Acknowledgements** This insight was supported by the Shenzhen Oversea Innovation Team Project (KQTD20180413181834876), the National Natural Science Foundation of China (U20A2017), the Strategic Priority Research Program of the Chinese Academy of Science (XDBS01030100), and the Shenzhen-Hong Kong Institute of Brain Science–Shenzhen Fundamental Research Institutions (NYKFKT2019009), China.

**Conflict of interest** The authors declare no conflict of interest.

## References

1. Wheeler ME, Treisman AM. Binding in short-term visual memory. *J Exp Psychol Gen* 2002, 131: 48–64.
2. Luria R, Vogel EK. Shape and color conjunction stimuli are represented as bound objects in visual working memory. *Neuropsychologia* 2011, 49: 1632–1639.
3. Ku YX, Yuan TF. “transient” or “persistent” coding for working memory. *Neurosci Bull* 2020, 36: 1233–1235.
4. Luck SJ, Vogel EK. The capacity of visual working memory for features and conjunctions. *Nature* 1997, 390: 279–281.
5. Vogel EK, Woodman GF, Luck SJ. Storage of features, conjunctions, and objects in visual working memory. *J Exp Psychol Hum Percept Perform* 2001, 27: 92–114.
6. Alvarez GA, Cavanagh P. The capacity of visual short-term memory is set both by visual information load and by number of objects. *Psychol Sci* 2004, 15: 106–111.
7. Awh E, Barton B, Vogel EK. Visual working memory represents a fixed number of items regardless of complexity. *Psychol Sci* 2007, 18: 622–628.
8. Bays PM, Husain M. Dynamic shifts of limited working memory resources in human vision. *Science* 2008, 321: 851–854.
9. Markov YA, Utochkin IS, Brady TF. Real-world objects are not stored in holistic representations in visual working memory. *J Vis* 2021, 21: 18.
10. Anderson DE, Vogel EK, Awh E. Precision in visual working memory reaches a stable plateau when individual item limits are exceeded. *J Neurosci* 2011, 31: 1128–1138.

11. Baddeley A. Working memory: Theories, models, and controversies. *Annu Rev Psychol* 2012, 63: 1–29.
12. Wood JN. When do spatial and visual working memory interact? *Atten Percept Psychophys* 2011, 73: 420–439.
13. Roland PE. Cortical organization of voluntary behavior in man. *Hum Neurobiol* 1985, 4: 155–167.
14. Klingberg T. Concurrent performance of two working memory tasks: Potential mechanisms of interference. *Cereb Cortex* 1998, 8: 593–601.
15. Klingberg T, Roland PE. Interference between two concurrent tasks is associated with activation of overlapping fields in the cortex. *Brain Res Cogn Brain Res* 1997, 6: 1–8.
16. Just MA, Carpenter PA, Keller TA, Emery L, Zajac H, Thulborn KR. Interdependence of nonoverlapping cortical systems in dual cognitive tasks. *NeuroImage* 2001, 14: 417–426.
17. Watanabe K, Funahashi S. Neural mechanisms of dual-task interference and cognitive capacity limitation in the prefrontal cortex. *Nat Neurosci* 2014, 17: 601–611.
18. Dai J, Brooks DI, Sheinberg DL. Optogenetic and electrical microstimulation systematically bias visuospatial choice in primates. *Curr Biol* 2014, 24: 63–69.
19. Funahashi S, Bruce CJ, Goldman-Rakic PS. Visuospatial coding in primate prefrontal neurons revealed by oculomotor paradigms. *J Neurophysiol* 1990, 63: 814–831.
20. Rigotti M, Barak O, Warden MR, Wang XJ, Daw ND, Miller EK. The importance of mixed selectivity in complex cognitive tasks. *Nature* 2013, 497: 585–590.
21. Xu YJ, Liu X, Cao X, Huang CP, Liu EK, Qian S, *et al.* Artificial intelligence: A powerful paradigm for scientific research. *Innovation (N Y)* 2021, 2: 100179.

RESEARCH HIGHLIGHT

# Getting a Sense of ATP in Real Time

Anthony D. Umpierre<sup>1</sup> · Koichiro Haruwaka<sup>1</sup> · Long-Jun Wu<sup>1,2,3</sup> 

Received: 2 January 2022 / Accepted: 23 January 2022 / Published online: 30 March 2022

© Center for Excellence in Brain Science and Intelligence Technology, Chinese Academy of Sciences 2022

Adenosine 5'-triphosphate (ATP) is a purinergic signal that can be sensed by all major cell classes in the brain. ATP is a key signal released during periods of physical damage/injury, inflammation, and neurological events, such as seizures. Understanding ATP signaling in the living brain is complicated by its fast enzymatic degradation, its action at multiple receptors, and its somewhat elusive mechanism of release across cell classes. Luckily, the Li lab has recently developed a highly optimized, genetically encoded ATP sensor with the potential to greatly improve our understanding of ATP signaling mechanisms and dynamics [1] (Fig. 1).

Termed GRAB<sub>ATP1.0</sub>, the sensor developed by Wu *et al.* is based upon the circularly-permuted GFP concept underlying GCaMP sensors. However, GRAB<sub>ATP1.0</sub> is fused to the ATP- and ADP-sensing G-protein coupled receptor, P2Y1 (Fig. 1). This ~1.9 kb construct has been successfully packaged into a number of plasmids and can be selectively expressed in neurons and astrocytes through AAV transfection. What makes GRAB<sub>ATP1.0</sub> a particularly excellent resource is its selectivity for ATP and ADP over all other purines and neurotransmitters. In addition, GRAB<sub>ATP1.0</sub> senses ATP in a dynamic range spanning 1 nmol/L to 1 mmol/L, matching the extracellular concentrations of ATP expected during physiology and

pathophysiology [2]. Finally, upon ATP stimulation, GRAB<sub>ATP1.0</sub> demonstrates a 5- to 10-fold fluorescent response in culture or zebrafish, with responses reaching 3-fold in the mouse cortex. Based upon its dynamic range, fluorescent signal, and reliable expression, GRAB<sub>ATP1.0</sub> exhibits ideal qualities for a robust *in vivo* sensor for ATP and ADP (Fig. 1).

One of the major questions surrounding ATP signaling is how it is released by different cell classes. In the spinal cord, ATP can be released through a vesicular mechanism to influence chronic pain conditions [3]. However, in the brain, the ATP release mechanism is largely obscure. In zebrafish, ATP can be released through the hemichannel Pannexin-1 [4]. In mouse, neuronal hyperactivity can induce ATP release through a hemichannel of as yet unknown identity [5]. Using the newly developed GRAB<sub>ATP1.0</sub> sensor, Wu *et al.* demonstrate that extracellular ATP responses induced by swelling in neuronal culture are not impacted by tetanus toxin light chain, a synaptic release inhibitor. Thus, swelling-induced ATP release is likely non-vesicular. Moving forward, GRAB<sub>ATP1.0</sub> should allow for robust, high-throughput pharmacological screening of hemichannels and volume-sensitive channels to identify the major mediator(s) of neuronal or glial ATP release.

The second major question surrounding ATP signaling is the timing of its extracellular actions. As a small molecule with endonucleases for its extracellular degradation [2], ATP is expected to be a relatively short-lived signal. Previously, the timing of ATP signaling has been studied using microdialysis, which does not allow for real-time measurements or high sensitivity. In characterizing their new ATP sensor, Wu *et al.* provide some intriguing insights into the signaling time of ATP [1]. In culture, a transient ATP application evokes relatively rapid

✉ Long-Jun Wu  
wu.longjun@mayo.edu

<sup>1</sup> Department of Neurology, Mayo Clinic, Rochester, MN 55905, USA

<sup>2</sup> Department of Neuroscience, Mayo Clinic, Jacksonville, FL 32224, USA

<sup>3</sup> Department of Immunology, Mayo Clinic, Rochester, MN 55905, USA

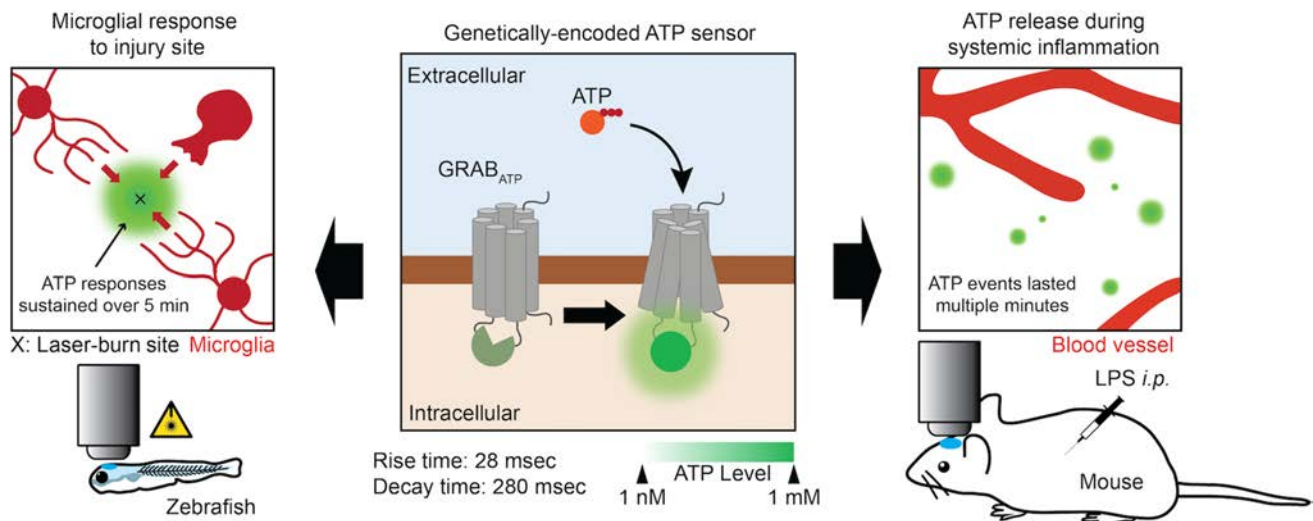


**Fig. 1** Development of the genetically-encoded ATP sensor (GRAB<sub>ATP1.0</sub>) and its responses to ATP release through *in vivo* imaging. GRAB<sub>ATP1.0</sub> is an ATP (and ADP)-specific sensor that increases green fluorescence upon extracellular ATP binding.

fluorescent sensor dynamics, including an activation time in the tens of milliseconds, with a deactivation time in the hundreds of milliseconds. The inactivation likely reflects a dispersion or degradation of ATP, because the fused P2Y1 construct does not appear to desensitize, even with 2 hours of continued ATP exposure. Thus, GRAB<sub>ATP1.0</sub> can rapidly sense ATP and inactivate upon its loss/dispersion. However, ATP events reported in zebrafish and mouse can be exceptionally long-lasting. Local, transient application of ATP to the zebrafish optic tectum can produce a signal lasting 30–40 s, while laser-burn injury can induce a sustained and spreading ATP response for >5 min (Fig. 1). In mouse cortex, systemic inflammation by LPS injection can evoke ATP events lasting several minutes (Fig. 1). The impetus for such long-lived events likely reflects sustained ATP release, but the cell classes involved and the potential for feed-forward signaling are all worthy of study. These key aspects of sustained ATP signaling could be dissected thanks to the robust nature of the Li lab's new sensor. Sustained purine signals are known triggers of pro-inflammatory cytokines and many neurological disorders [6], positioning this construct as an informative tool for future *in vivo* longitudinal studies of brain and spinal cord diseases.

Signals like ATP are still incompletely understood when it comes to their downstream signaling impact on complex biology. ATP can evoke neuronal and glial Ca<sup>2+</sup> activity, microglial process motility, and ionic flux at the receptor level [6]. Thereafter, there is a somewhat incomplete picture of how these receptor-mediated responses impact biology at the circuit or systems level. Recent studies have demonstrated that local degradation of ATP into adenosine

GRAB<sub>ATP1.0</sub> is validated *in vivo* in zebrafish and mouse brain. In zebrafish, microglia respond to radially spreading ATP release from the site of injury. In mouse cortex, ATP release events occur during LPS-induced systemic inflammation.

during seizure activity provides an important negative feedback loop that reduces pre-synaptic release and seizure severity [7]. This is a positive first step in understanding how purines regulate the local environment, beyond their known roles in cytokine production. The fact that purines are such a ubiquitous damage and danger signal, potentially sensed across all brain cell classes, suggests that they play a key role in coordinating complex brain responses to disease, injury, and infection. Wu *et al.* provide an early example of how to harness an ATP sensor in this domain, by showing the coordinated motility of dsRed-labeled microglia towards an ATP-rich injury site. Thus, the GRAB<sub>ATP1.0</sub> sensor would be extremely useful in studying microglial process convergence towards neurons during periods of heightened or lowered brain activity [5, 8, 9]. In addition, understanding how ATP and other signals, such as glutamate, interact and potentially reinforce each other could have great benefits in understanding hypersynchronous disorders such as epilepsy, stroke, migraine, and chronic pain. The unique pattern of ATP fluorescence, including its radial spread over many microns has interesting parallels to the glutamate plumes recently described during migraine [10]. At the same time, it will be interesting to know which aspects of basal physiology involve elevated ATP signaling. In particular, it will be intriguing to study if certain aspects of cognition involve ATP signaling in the learning, consolidation, or retrieval phases of task performance.

At this stage, GRAB<sub>ATP1.0</sub> has a few minor limitations. First, the high end of the dynamic range (1 mmol/L extracellular ATP) could represent a saturated signal during pathological events such as stroke or seizure.



Towards this end, the authors have also developed a lower affinity variant with faster off-time kinetics, called ATP1.0-L, which should help in detecting faster ATP events during pathology. The second limitation of any extracellular ATP sensor is its inability to pinpoint the cellular source(s) of ATP release without additional pharmacological or genetic approaches. This would be particularly important to determine in their studies of ATP release in LPS-induced systemic inflammation. The third limitation of GRAB<sub>ATP1.0</sub>, as noted by the authors, is its inability to distinguish between ATP and ADP in real time. The final limitation of GRAB<sub>ATP1.0</sub> is its current AAV packaging under hSyn and GFAP promoters. In future, a Cre-dependent viral construct (*i.e.*, “FLEX”) would allow for a greater range of expression, while a knock-in mouse is currently needed to study microglia. Nevertheless, having a robust ATP sensor opens up countless possibilities to better understand an elusive signaling molecule noted for its roles in disease and injury. The GRAB<sub>ATP1.0</sub> sensor and its potential combination with red-shifted sensors and pharmacology should allow researchers to uncover new mechanisms governing ATP release and regulation, as well as its impact on acute or chronic disease progression.

**Acknowledgements** This Research Highlight was supported by grants from the NIH, USA (F32NS114040 and R01NS088627).

## References

1. Wu Z, He K, Chen Y, Li H, Pan S, Li B. A sensitive GRAB sensor for detecting extracellular ATP *in vitro* and *in vivo*. *Neuron* 2022, 110: 770–782.
2. Yegutkin GG. Nucleotide- and nucleoside-converting ectoenzymes: Important modulators of purinergic signalling cascade. *Biochim Biophys Acta* 2008, 1783: 673–694.
3. Masuda T, Ozono Y, Mikuriya S, Kohro Y, Tozaki-Saitoh H, Iwatsuki K, *et al.* Dorsal horn neurons release extracellular ATP in a VNUT-dependent manner that underlies neuropathic pain. *Nat Commun* 2016, 7: 12529.
4. Li Y, Du XF, Liu CS, Wen ZL, Du JL. Reciprocal regulation between resting microglial dynamics and neuronal activity *in vivo*. *Dev Cell* 2012, 23: 1189–1202.
5. Eyo UB, Peng JY, Swiatkowski P, Mukherjee A, Bispo A, Wu LJ. Neuronal hyperactivity recruits microglial processes via neuronal NMDA receptors and microglial P2Y<sub>12</sub> receptors after status epilepticus. *J Neurosci* 2014, 34: 10528–10540.
6. Burnstock G, Krügel U, Abbracchio MP, Illes P. Purinergic signalling: From normal behaviour to pathological brain function. *Prog Neurobiol* 2011, 95: 229–274.
7. Badimon A, Strasburger HJ, Ayata P, Chen XH, Nair A, Ikegami A, *et al.* Negative feedback control of neuronal activity by microglia. *Nature* 2020, 586: 417–423.
8. Eyo UB, Gu N, De S, Dong HL, Richardson JR, Wu LJ. Modulation of microglial process convergence toward neuronal dendrites by extracellular calcium. *J Neurosci* 2015, 35: 2417–2422.
9. Cserép C, Pósfai B, Lénárt N, Fekete R, László ZI, Lele Z, *et al.* Microglia monitor and protect neuronal function through specialized somatic purinergic junctions. *Science* 2020, 367: 528–537.
10. Parker PD, Suryavanshi P, Melone M, Sawant-Pokam PA, Reinhart KM, Kaufmann D, *et al.* Non-canonical glutamate signaling in a genetic model of migraine with aura. *Neuron* 2021, 109: 611–628.e8.

RESEARCH HIGHLIGHT

# Fundamental Neurocircuit of Anti-inflammatory Effect by Electroacupuncture Stimulation Identified

Jiayu Hu<sup>1,2,3</sup> · Wanye Hu<sup>1,2,3</sup> · Lusheng Tang<sup>3</sup> · Ying Wang<sup>2</sup>

Received: 9 December 2021 / Accepted: 2 February 2022 / Published online: 18 April 2022

© Center for Excellence in Brain Science and Intelligence Technology, Chinese Academy of Sciences 2022

As an important part of Traditional Chinese Medicine, acupuncture has the history of several thousand years in China and has been widely applied and accepted in clinical practice all over the world. Modern randomized clinical trials have demonstrated the effectiveness of acupuncture in treating a range of ailments, including gastrointestinal disorders and stress urinary incontinence [1, 2]. The ancient ‘meridian-channel’ theory claimed that applying certain stimuli to specific somatic tissues (acupoints) can remotely regulate the physiology of internal organs [3]. However, the actual existence of such meridians has not been supported by modern anatomical studies, although acupoints appear to be located in fascial tissue rich in nerves, vascular/lymphatic vessels, and immune cells [4]. But a recent study published in *Nature* showed that some bodily physiology can be modulated by nerve reactions that are directly related to acupoint stimulation. The researchers found that a class of PROKR2<sup>Cre</sup>-labeled dorsal root ganglion (DRG) neurons is essential for low-intensity electroacupuncture stimulation (ES) to activate the pathway of the vagal-adrenal axis [5]. Notably, according to the physical distribution characteristics of such nerves, the anti-inflammatory effect of low-intensity ES at different parts can be predicted, providing strong evidence for the relative specificity of acupoints.

Since the 1970s, some studies have demonstrated that squeezing or ES can activate the peripheral branches of neurons from the DRG and trigeminal ganglion. Then the sensory information is transmitted from the spinal cord to the brain, ultimately modulating various aspects of physiology through the activation of peripheral autonomic neural pathways [6]. The autonomic nervous system is divided into parasympathetic and sympathetic branches. Strong extrusion or ES at abdominal acupoints such as Tianshu (ST25) can drive gastrointestinal sympathetic nerve pathways to restrain motility *via* both segmental spinal reflexes and supraspinal circuits. Meanwhile, the same stimulus at fore/lower limb acupoints such as the hindlimb Zusanli (ST36) acupoint drive a vagal reflex parasympathetic response and promote gastrointestinal motility. These results suggest that a certain level of stimulation is able to drive different autonomic neural pathways from diverse acupoints or body regions, leading to positive or negative regulation of visceral physiological processes.

ES can also drive the ability to regulate severe systemic inflammation or cytokine storms. Okusa *et al.* first pointed out that ES of cervical cholinergic vagal efferents inhibits systemic inflammation, which was further confirmed in subsequent studies [7, 8]. Some studies have also found that ES at acupoints in limb areas can activate vagal efferents, resulting in dopamine release and subsequent inhibition of systemic inflammation [8, 9]. In a recent study, Liu *et al.* found that the adrenal vagal reflexes can be driven by low-intensity ES at acupoints of the hind limbs, while driving the gastric vagal reflexes requires higher-intensity stimulation [3, 10]. Interestingly, these vagal reflexes in two different body regions are able to be activated by ES at hindlimb acupoints, but not at abdominal acupoints [2]. The different results for reflexes activation caused by distinct acupoint stimulation also occurs in the sympathetic reflexes. For

✉ Ying Wang  
nancywangying@163.com

<sup>1</sup> Bengbu Medical College, Bengbu 233030, China

<sup>2</sup> Clinical Research Center, Affiliated Hangzhou First People’s Hospital, Zhejiang University School of Medicine, Hangzhou 310006, China

<sup>3</sup> Laboratory Medicine Center, Department of Laboratory Medicine, Zhejiang Provincial People’s Hospital, Affiliated People’s Hospital, Hangzhou Medical College, Hangzhou 310014, China

example, the splenic sympathetic reflexes can be activated from almost all body regions, unlike the gastrointestinal sympathetic reflexes that are selectively activated by abdominal ES [6]. These phenomena provide an important direction for future research on the neuroanatomical basis of acupuncture, that is, how to explain the selective specificity and intensity dependence between acupoints that drive various autonomic nerve pathways.

In this study, the researchers hypothesized that the vagal-adrenal axis is driven by sensory pathways that innervate the specific tissues of the hind limbs, such as joints, bones, and skeletal muscles, rather than by other regional or superficial tissues. They first discussed the distribution of neurons marked by PROKR2<sup>Cre</sup>, a class of myelinated neurons that are mainly enriched and expressed in DRGs innervating limb segments. And made it clear that they specifically innervate the deep fascia tissue of limbs (such as periosteum, joint ligament, and myofascia), but not the epidermal tissue of skin and the main fascia tissue of the abdomen (such as the peritoneum). Based on this conclusion, the researchers specifically knocked out such DRG sensory neurons by cross genetic methods to study the role of PROKR2<sup>Cre</sup> DRG neurons in the acupuncture-induced vagal-adrenal anti-inflammatory pathway.

The ES test was performed on the hindlimb ST36 acupoint of PROKR2<sup>ADV</sup>-Abl mice (the PROKR2<sup>Cre</sup>-marked DRG neurons were ablated) and control mice (without ablation of PROKR2<sup>Cre</sup>-marked DRG neurons) by inserting bilateral electroacupuncture into the tibialis anterior muscle near the peroneal nerve. In control mice, low intensity (0.5 mA) ES was sufficient to induce the release of norepinephrine, epinephrine, and dopamine from the adrenal chromaffin cells dependent on the vagus nerve, resulting in a 50% reduction in tumor necrosis factor (TNF) and interleukin-6 (IL-6) induction and a 40% increase in survival rate. Meanwhile these effects were not found in PROKR2<sup>ADV</sup>-Abl mice. Referring to the previous research conclusion of the team on abdominal ST25 acupoint ES, 0.5 mA cannot drive the vagus nerve or sympathetic nerve reflex. And only high intensity ES can drive the sympathetic reflex, having an anti-inflammatory effect independent of vagus nerve effusion. No changes were found in PROKR2<sup>ADV</sup>-Abl mice; high-intensity ES at the ST36 acupoint on the hind limb also drove the spinal sympathetic reflex and had an anti-inflammatory effect (Fig. 1A). Therefore, it is reasonable to speculate that PROKR2<sup>ADV</sup> neurons are the only neurons required for low intensity ES to drive the vagus-adrenal anti-inflammatory axis from the hindlimb ST36 acupoint (Fig. 1B).

In a gain-of-function study, the researchers further investigated whether the intensity of laser acupuncture could substitute for low-intensity ES stimulation by triggering action potential discharges in PROKR2<sup>ADV</sup>-labeled DRG neuron subsets using blue-light pulses. Similar to the above

experimental results, the induction rate of Fos induced by spinal neurons of lamina I, retrogradely labeled Fos in output neurons of the vagus nerve, and ChAT+ efferent neurons increased significantly under bilateral light stimulation of the ST36 site, accompanied by increased levels of norepinephrine, adrenaline, and dopamine. The anti-inflammatory effect resulted in a 50% reduction in TNF and IL-6 production and a 50% increase in survival compared to the control group. Thus, optical activation of PROKR2<sup>ADV</sup> fibers can basically simulate 0.5-mA ES at the ST36 acupoint, and fully drive the vagus-adrenal anti-inflammatory axis. Laser acupuncture is a new method which uses a laser micro-beam to irradiate acupoints to treat diseases [11]. Compared with traditional acupuncture, it has a series of advantages such as simplicity, no pain, no infection, and no adverse reactions. The above results clearly provide a theoretical basis for the practical application of laser acupuncture.

PROKR2<sup>ADV</sup> neurons innervate different tissue areas: the *Nefn<sup>low</sup>Bmpr1b+* subgroup innervates hair follicles, while *Nefn<sup>high</sup>* neurons preferentially innervate deep fascia in the limbs. Is it possible that the vagal-adrenal axis could be driven both by neurons innervating the superficial skin of the hind limb and by neurons innervating the deep fascia? To rule out this possibility, the researchers created mice with selective transection of either the common peroneal nerve or the lateral cutaneous nerve and subjected them to electroacupuncture at the same ST36 point. Fos induction in spinal lamina I neurons that project to the nucleus tractus solitarius were eliminated in common peroneal nerve-transected mice, while anti-inflammatory effects were not affected in tibial or sural nerve-transected mice. Further intradermal 0.5-mA ES at the ST36 point did not induce any activation of the anti-inflammatory axis. It is clear that stimulation of neurons innervating the superficial skin cannot activate the vagal response, which reinforces the possibility that the vagal-adrenal anti-inflammatory axis is mediated by PROKR2<sup>ADV</sup> sensory neurons innervating the deep fascia of the limb.

In addition, they also tested whether the innervation pattern of PROKR2<sup>ADV</sup> sensory fibers can also produce anti-inflammatory response through low-intensity ES in other areas of the body. They performed 0.5-mA ES on the gastrocnemius muscle of the hindlimb with sparse distribution of PROKR2<sup>ADV</sup>, the semitendinosus muscle of the thigh region, and the forelimb deep branch of the radial nerve close to the shousanli (LI10) region enriched with PROKR2<sup>ADV</sup>. The experimental results clearly showed that the production of TNF and IL-6 was reduced remarkably after stimulating at the LI10 acupoint, while ES on the gastrocnemius muscle did not have the same effect. It is reasonable to speculate that the innervation pattern of PROKR2<sup>ADV</sup> sensory fibers could retrospectively predict, to some extent, the areas of the body where low-intensity ES drives anti-inflammatory effects, thus providing clues to other acupoints that can produce anti-

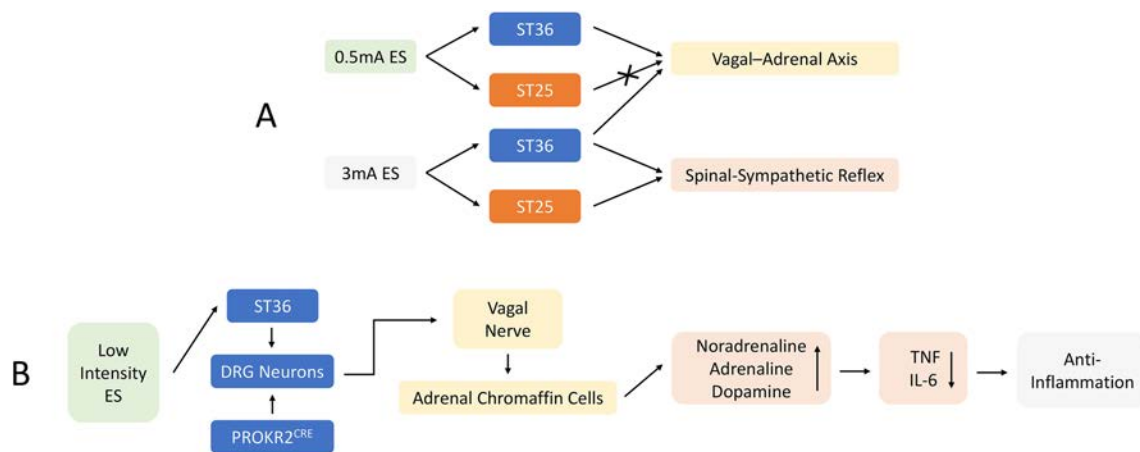


**Fig. 1** **A** Neural reflex pathways activated by different acupoints and ES intensity stimulation. **B** Neuroanatomical basis of low intensity ES stimulation driving the vagal-adrenal anti-inflammatory axis.

inflammatory responses through stimulation. What is more, it is remarkable that the gastrocnemius muscle and semitendinosus muscle, where PROKR2<sup>ADV</sup> nerve fibers rarely project, are the traditional acupoints rarely applied distributed in acupuncture therapy.

In summary, the research team fully authenticated that the vagal-adrenal axis can be driven by sensory channels that innervate specific tissues of the human hindlimbs. Furthermore, the experiments also demonstrated the existence of acupoint selectivity and specificity in driving particular autonomic nerve channels such as the vagal-adrenal axis, which retrospectively predict the areas of the body that can activate anti-inflammatory effects. In addition, the stimulation factors such as intensity [12] and the depth of needle placement have also been shown to significantly affect the results of the experiments. The above conclusion provides some inspiration for the study of driving different autonomic pathways by adjusting ES parameters. Predictably, similar studies in the future will help acupuncture researchers to optimize the stimulation parameters and design appropriate sham controls, so as to improve the effectiveness and safety of acupuncture therapy and solve the treatment and management problems of specific diseases. There is no doubt that this experimental result has achieved a historic breakthrough in acupuncture research. But more acupoints and corresponding autonomic nerve reflex pathways should be further explored and tested in follow-up research, so as to form a complete and systematic neuroanatomical basis of the meridian-channel theory.

**Acknowledgements** This Research Highlight was supported by National Natural Science Foundation of China (82102938), Zhejiang Public Welfare Technology Application Research Project (LGF19H080006, LGF21H010008, and LGF20H080005), Medical and Health Science and Technology Project of Zhejiang Province (2021KY842, 2021KY483, 2021KY077, 2022KY503, 2022KY046, 2022KY236, and 2022KY074), and Outstanding Youth Foundation of Zhejiang Provincial People's Hospital (ZRY2020B001).

**Conflict of interest** The authors declare that there is no conflict of interest.

## References

1. Lima FA, Ferreira LE, Pace FH. Acupuncture effectiveness as a complementary therapy in functional dyspepsia patients. *Arq Gastroenterol* 2013, 50: 202–207.
2. Ma QF. Somato-autonomic reflexes of acupuncture. *Med Acupunct* 2020, 32: 362–366.
3. Liu SB, Wang ZF, Su YS, Ray RS, Jing XH, Wang YQ. Somatotopic organization and intensity dependence in driving distinct NPY-expressing sympathetic pathways by electroacupuncture. *Neuron* 2020, 108: 436–450.e7.
4. Zhao ZQ. Neural mechanism underlying acupuncture analgesia. *Prog Neurobiol* 2008, 85: 355–375.
5. Liu SB, Wang ZF, Su YS, Qi L, Yang W, Fu MZ, *et al.* A neuroanatomical basis for electroacupuncture to drive the vagal-adrenal axis. *Nature* 2021, 598: 641–645.
6. Sato A. Neural mechanisms of autonomic responses elicited by somatic sensory stimulation. *Neurosci Behav Physiol* 1997, 27: 610–621.
7. Okusa MD, Rosin DL, Tracey KJ. Targeting neural reflex circuits in immunity to treat kidney disease. *Nat Rev Nephrol* 2017, 13: 669–680.
8. Ulloa L, Quiroz-Gonzalez S, Torres-Rosas R. Nerve stimulation: Immunomodulation and control of inflammation. *Trends Mol Med* 2017, 23: 1103–1120.
9. Lim HD, Kim MH, Lee CY, Namgung U. Anti-inflammatory effects of acupuncture stimulation via the vagus nerve. *PLoS One* 2016, 11: e0151882.
10. Su YS, He W, Wang C, Shi H, Zhao YF, Xin JJ, *et al.* “Intensity-response” effects of electroacupuncture on gastric motility and its underlying peripheral neural mechanism. *Evid Based Complement Alternat Med* 2013, 2013: 535742.
11. Chon TY, Mallory MJ, Yang J, Bubblitz SE, Do A, Dorsher PT. Laser acupuncture: A concise review. *Med Acupunct* 2019, 31: 164–168.
12. Huo R, Han SP, Liu FY, Shou XJ, Liu LY, Song TJ, *et al.* Responses of primary afferent fibers to acupuncture-like peripheral stimulation at different frequencies: Characterization by single-unit recording in rats. *Neurosci Bull* 2020, 36: 907–918.





## Brief Instructions to Authors

*Neuroscience Bulletin* (NB) aims to publish research advances in the field of neuroscience and promote exchange of scientific ideas within the community. The journal publishes original papers of various topics on neuroscience and focuses on potential disease implications on the nervous system. NB welcomes research contributions on molecular, cellular, or developmental neuroscience using multidisciplinary approaches and functional strategies.

### Manuscript Submission

Manuscripts should be submitted through our online submission system, ScholarOne Manuscripts, at <http://mc03.manuscriptcentral.com/nsb> or <http://www.neurosci.cn>.

Manuscript file types that we accept for online submission include Word and WordPerfect. For Figure submission, we accept JPEG, TIFF, or AI files. Required items differ for each article type and are specified during the submission process.

The submitted manuscript should be accompanied with a signed “*Neuroscience Bulletin* copyright transfer statement and submission form”.

### Manuscript Preparation

**Original Article:** An original article contains original research materials and presents compelling data on conceptual advances in any area of neuroscience. The total character count of all sections of the main text (including references and figure legends but excluding supplemental data) should not exceed 80,000, including spaces. Up to 8 figures and/or tables are allowed for the entire manuscript. The minimum requirement of a submitted research article is 40,000 characters in total (or 5000 words excluding the references) and at least 6 display items (figures and tables). The submitted manuscript should be a substantial novel research study in all aspects of neuroscience organizing a complete story with complex mechanisms elucidated using multiple techniques or approaches. NB also welcomes clinical research investigating the pathogenesis or diagnostic markers of a disease. Please note that for clinical trials, an Informed Consent should be provided as supplemental material and stated in the main text. NB no longer accepts clinical research that lack insightful mechanistic implications. References are limited to 100.

**Review:** Authoritative reviews contribute greatly to our journal and we are interested in comprehensive articles well-written to describe recent development in any field of neuroscience for a general audience. Authors are expected to cover controversies in the field and propose their own viewpoints in an unbiased and justifiable way. In particular, the scope of the review should not be dominated by the authors' own work. Review is usually 5,000 to 8,000 words in length (including an abstract of no more than 150 words, excluding the references and title) and 3–6 schematic illustrations are strongly encouraged. Reviews are often contributed by leaders in the field and solicited by the editors. The authors are encouraged to submit a letter of inquiry before the submission.

**Insight:** For Insight, the article should contain discussion on recent primary research literature similarly as Review. Yet, Insight is shorter in length (no more than 2,000 words, excluding the reference and title) and focuses on a narrower scope. It is possible

that in Insight authors advocate a position over a controversial issue or a speculative hypothesis. One schematic illustration is allowed to make the Insight more comprehensive. References are limited to 20.

**Method:** NB welcomes Method article on novel experimental techniques in any field of basic neuroscience. The Method can be written in the Research Article format yet the content should follow the criteria described below. The description of the method must be accompanied by its validation, its application to an important biological question, and results illustrating its performance in comparison to available approaches. The manuscript will be judged on its novelty, general interest, through assessments of methodological performance and comprehensive technical descriptions that facilitate immediate application. The detailed step-by-step procedure must be described in the form of flow charts for readers to comprehend easily. Additional annotation for key procedures and special treatments will be encouraged. In addition, please note that NB no longer accepts Method on neurosurgery pathway, surgical techniques, or any other clinical related technical studies.

**Letter to the Editor:** The Letter to the Editor reports a short but exciting finding in a particular field of neuroscience with high quality and of broad interest. The letter should be brief yet concise, and no specific subsections are required. No Materials and Methods section is needed, but any technical information which the authors think is important should be submitted as supplementary materials. The total words count should not exceed 2500 (exclude references and title) and the display items should be limited to 2. References are limited to 15. No abstract and subsections are needed.

**Research Highlight:** The Research Highlight describes recent research advances by articles published in NB or other journals. It highlights the main results of the research, emphasizes the significance and provides further discussion on the topic. The main text of a Research Highlight is up to 1,500 words (excluding references and title) with no more than 10 references and one or two figures. Research Highlights are usually by editor invitation, but submitted manuscript with high quality will also be considered. No abstract and subsections are needed.

Submitted manuscripts should be divided into the following sections:

(1) Title Page; (2) Abstract; (3) Introduction; (4) Materials and Methods; (5) Results; (6) Discussion; (7) Acknowledgements; (8) References; (9) Figures, legends, and tables; (10) Supplementary information.

### Manuscript Revision

Upon peer-reviews, the authors may be asked to revise the manuscript. If the authors have substantial reasons to believe that their manuscript was treated unfairly, they may appeal for reconsideration. Revision should be completed within four (minor revision) or eight weeks (major revision). The authors should provide a cover letter and a point-to-point response for addressing the reviewers' comments. The editor will notify the corresponding author upon the acceptance of the manuscript. Accepted papers will be processed to advanced online publication as soon as possible.

**Proofs**

A PDF proof will be sent to the authors for them to correct last minute errors on the manuscript.

**Page Charges**

Page charges for the printed form are as follows: 500 CNY (80 USD) for each text page, 800 CNY (120 USD) for each page containing black-and-white figures, 1500 CNY (250 USD) for each page containing color figures. The corresponding author will receive an invoice on all the publication-related charges once the manuscript is accepted for publication and enters the editing process.

**Make checks or money orders payable to:**

Center for Excellence in Brain Science and Intelligence  
Technology, Chinese Academy of Sciences  
(中国科学院脑科学与智能技术卓越创新中心)

The bank account number is 4585 4835 7666,  
Shanghai Jianguo West Road Subbranch, Bank of China  
(中国银行上海市建国西路支行).

Address of Editorial Office of Neuroscience Bulletin:

319 YueYang Road, Room 612, Building 8, Shanghai 200031,  
China.

Phone: +86-21-64032273; 64170853; 64032696;

E-mail: nsb@ion.ac.cn  
<http://www.neurosci.cn>

(Updated January 2021)

## Neuroscience Bulletin Copyright Transfer Statement and Submission Form

We submit this type of article (✓):

- Original Article
- Review
- Research Highlight
- Insight
- Letter to the Editor
- Method

**Title of article:**

Words:                      Figures:                      (Color figures:                      );                      Tables:

**A signature below certifies compliance with the following statements**

**Copyright Transfer Statement:** The copyright to this article is transferred to *Neuroscience Bulletin*, Center for Excellence in Brain Science and Intelligence Technology, CAS and Springer Nature (respective to owner if other than Center for Excellence in Brain Science and Intelligence Technology, CAS and Springer Nature and for U.S. government employees: to the extent transferable) effective if and when the article is accepted for publication. The author warrants that his/her contribution is original and that he/she has full power to make this grant. The author signs for and accepts responsibility for releasing this material on behalf of any and all co-authors. The copyright transfer covers the exclusive right and license to reproduce, publish, distribute and archive the article in all forms and media of expression now known or developed in the future, including reprints, translations, photographic reproductions, microform, electronic form (offline, online) or any other reproductions of similar nature. An author may self-archive an author-created version of his/her article on his/her own website. He/she may also deposit this version on his/her institution's and funder's (funder designated) repository at the funder's request or as a result of a legal obligation, including his/her final version, provided it is not made publicly available until after 12 months of official publication. He/she may not use the publisher's PDF version which is posted on [www.springerlink.com](http://www.springerlink.com) for the purpose of self-archiving or deposit. Furthermore, the author may only post his/her version provided acknowledgement is given to the original source of publication and a link is inserted to the published article on Springer's website. The link must be accompanied by the following text: "The original publication is available at [www.springerlink.com](http://www.springerlink.com)". The author is requested to use the appropriate DOI for the article. Articles disseminated via [www.springerlink.com](http://www.springerlink.com) are indexed, abstracted and referenced by many abstracting and information services, bibliographic networks, subscription agencies, library networks, and consortia.

After submission of this agreement signed by the corresponding author, changes of authorship or in the order of the authors listed will not be accepted by *Neuroscience Bulletin*, Center for Excellence in Brain Science and Intelligence Technology, CAS and Springer Nature.

### Authorship responsibilities

I/We confirm that:

- (1) The work described has not been published before in any language or in any journal or media; that it is not under consideration for publication elsewhere; that its publication has been approved by all co-authors, if any, as well as (tacitly or explicitly) by the responsible authorities at the institution where the work was carried out.
- (2) We also give an assurance that the material will not be submitted for publication elsewhere until a decision has been made as to its acceptability for *Neuroscience Bulletin* in 2 months, then declare this statement becomes null and void.
- (3) I am/We are responsible for obtaining permission for the use of any material in the manuscript that may be under copyright to my/our employer(s) or other party(ies).
- (4) I have read the complete manuscript and accept responsibility for the content and completeness.
- (5) I have made a significant contribution to this work and am familiar with the contents.

Author (1) signed:                      Date:                      Author (2) signed:                      Date:

Author (3) signed:                      Date:                      Author (4) signed:                      Date:

Author (5) signed:                      Date:                      Author (6) signed:                      Date:

Author (7) signed:                      Date:                      Author (8) signed:                      Date:

Author (9) signed:                      Date:                      Author (10) signed:                      Date:

Corresponding author signed:                      Date:

Corresponding author address:

Tel:                      E-mail:

# Neuroscience Bulletin

## Editors-in-Chief

**Shumin Duan**, Zhejiang University, Hangzhou, China  
**Ru-Rong Ji**, Duke University, Durham, USA

## Deputy Editors

**Julin Du**, Center for Excellence in Brain Science and Intelligence Technology, CAS, Shanghai, China  
**Zuoren Wang**, Center for Excellence in Brain Science and Intelligence Technology, CAS, Shanghai, China

## Executive Associate Editors

**Iain C. Bruce**, Zhejiang University, Hangzhou, China  
**Guang-Yin Xu**, Institute of Neuroscience, Soochow University, Suzhou, China

## Associate Editors

**Shiqing Cai**, Center for Excellence in Brain Science and Intelligence Technology, CAS, Shanghai, China  
**Renjie Chai**, Southeast University, Nanjing, China  
**Zhong Chen**, Zhejiang University, Hangzhou, China  
**Yiru Fang**, Shanghai Mental Health Center, Shanghai, China  
**Tianming Gao**, South Medical University, Guangzhou, China  
**Yong-Jing Gao**, Nantong University, Nantong, China  
**Yong Gu**, Center for Excellence in Brain Science and Intelligence Technology, CAS, Shanghai, China  
**Shihui Han**, Peking University, Beijing, China  
**Cheng He**, Naval Medical University, Shanghai, China  
**Tianzi Jiang**, Institute of Automation, CAS, Beijing, China  
**Weidong Le**, Sichuan Academy of Medical Science • Sichuan Provincial Hospital, Chengdu, China  
**Tao Li**, Zhejiang University School of Medicine Affiliated Mental Health Center, Hangzhou, China  
**Chengyu Li**, Center for Excellence in Brain Science and Intelligence Technology, CAS, Shanghai, China  
**Chun-Feng Liu**, Second Affiliated Hospital of Soochow University, Suzhou, China  
**Minmin Luo**, National Institute of Biological Sciences, Beijing, China  
**Mengsheng Qiu**, Hangzhou Normal University, Hangzhou, China  
**Zilong Qiu**, Center for Excellence in Brain Science and Intelligence Technology, CAS, Shanghai, China  
**Fu-Dong Shi**, Tianjin Medical University General Hospital, Tianjin, China  
**Yangang Sun**, Center for Excellence in Brain Science and Intelligence Technology, CAS, Shanghai, China  
**You Wan**, Peking University, Beijing, China

**Jian-Zhi Wang**, Huazhong University of Science and Technology, Wuhan, China  
**Kai Wang**, Anhui Medical University, Hefei, China  
**Liping Wang**, Shenzhen Institute of Advanced Technology, CAS, Shenzhen, China  
**Liping Wang**, Center for Excellence in Brain Science and Intelligence Technology, CAS, Shanghai, China  
**Yanjiang Wang**, Daping Hospital, Army Medical University, Chongqing, China  
**Zheng Wang**, Peking University School of Psychological and Cognitive Sciences, Beijing, China  
**Longjun Wu**, Mayo Clinic, Rochester, USA  
**Sheng-Xi Wu**, The Fourth Military Medical University, Xi'an, China  
**Si Wu**, Peking University, Beijing, China  
**Zhi-Ying Wu**, The Second Affiliated Hospital Zhejiang University School of Medicine, Hangzhou, China  
**Ning-Long Xu**, Center for Excellence in Brain Science and Intelligence Technology, CAS, Shanghai, China  
**Tianle Xu**, Shanghai Jiao Tong University School of Medicine, Shanghai, China  
**Yun Xu**, Nanjing Drum Tower Hospital, Nanjing, China  
**Tian Xue**, University of Science and Technology of China, Hefei, China  
**Dai Zhang**, Peking University, Beijing, China  
**Hanting Zhang**, Qingdao University School of Pharmacy, Qingdao, China  
**Jie Zhang**, Xiamen University, Xiamen, China  
**Yongqing Zhang**, Institute of Genetics and Developmental Biology, CAS, Beijing, China  
**Chunjiu Zhong**, Fudan University, Shanghai, China

## Editorial Board

**Goran Angelovski**, Center for Excellence in Brain Science and Intelligence Technology, CAS, Shanghai, China  
**George Baillie**, Institute of Cardiovascular and Medical Sciences, University of Glasgow, UK  
**Guo-Qiang Bi**, University of Science and Technology of China, Hefei, China  
**Junli Cao**, Xuzhou Medical College, Xuzhou, China

**L. Judson Chandler**, Medical University of South Carolina, USA  
**Jun Chen**, The Fourth Military Medical University, Xi'an, China  
**Qing-Hui Chen**, Michigan Technological University, Houghton, USA  
**Xiaoke Chen**, Stanford University, Stanford, USA  
**Isaac M. Chiu**, Harvard Medical School, Boston, USA

**He Cui**, Center for Excellence in Brain Science and Intelligence Technology, CAS, Shanghai, China  
**Jun Ding**, Stanford University, Stanford, USA  
**Aaron Gitler**, Stanford University, Stanford, USA  
**Xiaosong Gu**, Nantong University, Nantong, China  
**Junhai Han**, Southeast University, Nanjing, China  
**Gregg E. Homanics**, University of Pittsburgh, USA  
**Zhi-An Hu**, Army Medical University, Chongqing, China

**Peter Illes**, University of Leipzig, Leipzig, Germany  
**Pierre Lavenex**, University of Fribourg, Fribourg, Switzerland  
**Juan Lerma**, Instituto de Neurociencias de Alicante, Alicante, Spain

**Wolfgang Liedtke**, Duke University School of Medicine, Durham, USA

**Stuart A. Lipton**, Sanford-Burnham Medical Research Institute and University of California at San Diego, San Diego, USA

**Jingyu Liu**, Center for Excellence in Brain Science and Intelligence Technology, CAS, Shanghai, China

**Tong Liu**, Nantong University, Nantong, China

**Lin Lu**, Peking University Sixth Hospital, Beijing, China

**Benyan Luo**, Zhejiang University School of Medicine, Hangzhou, China

**Ceng Luo**, The Fourth Military Medical University, Xi'an, China

**Jian-Hong Luo**, Zhejiang University School of Medicine, Hangzhou, China

**Zhen-Ge Luo**, ShanghaiTech University, Shanghai, China

**Lan Ma**, Fudan University, Shanghai, China

**Qiufu Ma**, Dana-Farber Cancer Institute, Boston, USA

**Quanhong Ma**, Soochow University, Suzhou, China

**Robert C. Malenka**, Stanford University, Stanford, USA

**Manuel S. Malmierca**, Universidad de Salamanca, Salamanca, Spain

**John H.R. Maunsell**, Harvard Medical School, Boston, USA

**Earl K. Miller**, Massachusetts Institute of Technology, Cambridge, USA

**Hideyuki Okano**, Keio University, Tokyo, Japan

**Vladimir Parpura**, University of Alabama at Birmingham, Birmingham, USA

**Jos Prickaerts**, School for Mental Health and Neuroscience, Maastricht University, The Netherlands

**Joshua R. Sanes**, Harvard University, Boston, USA

**Michael N. Shadlen**, Columbia University, New York, USA

**Yousheng Shu**, Fudan University, Shanghai, China

**Bai-Lu Si**, Beijing Normal University, Beijing, China

**Sangram S. Sisodia**, The University of Chicago, Chicago, USA

**Peter Somogyi**, University of Oxford, Oxford, UK

**Ron Stoop**, Lausanne University, Lausanne, Switzerland

**Feng-Yan Sun**, Fudan University, Shanghai, China

**Dick F. Swaab**, Netherlands Institute for Neuroscience, Amsterdam, The Netherlands

**Yong Tang**, Chengdu University of TCM, Chengdu, China

**Makoto Tsuda**, Kyushu University, Fukuoka, Japan

**Alexei Verkhratsky**, The University of Manchester, Manchester, UK

**Guanghui Wang**, Soochow University, Suzhou, China

**Yun Wang**, Neuroscience Research Institute, Peking University, Beijing, China

**Xu-Chu Weng**, South China Normal University, Guangzhou, China

**William Wisden**, Imperial College London, London, UK

**Jun-Xia Xie**, Qingdao University, Qingdao, China

**Zhiqi Xiong**, Center for Excellence in Brain Science and Intelligence Technology, CAS, Shanghai, China

**Lin Xu**, Kunming Institute of Zoology, CAS, Kunming, China

**Xiao-Hong Xu**, Center for Excellence in Brain Science and Intelligence Technology, CAS, Shanghai, China

**Jun Yan**, Center for Excellence in Brain Science and Intelligence Technology, CAS, Shanghai, China

**Hui Yang**, Center for Excellence in Brain Science and Intelligence Technology, CAS, Shanghai, China

**Tianming Yang**, Center for Excellence in Brain Science and Intelligence Technology, CAS, Shanghai, China

**Haishan Yao**, Center for Excellence in Brain Science and Intelligence Technology, CAS, Shanghai, China

**Shanping Yu**, Emory University School of Medicine, Atlanta, USA

**Hong Zhang**, The Second Affiliated Hospital of Zhejiang University School of Medicine, Hangzhou, China

**Xiaohui Zhang**, Beijing Normal University, Beijing, China

**Xu Zhang**, Shanghai Advanced Research Institute, CAS, Shanghai, China

**Yong Zhang**, Peking University, Beijing, China

**Yu-Qiu Zhang**, Fudan University, Shanghai, China

**Zhi-Jun Zhang**, Zhongda Hospital, Southeast University, Nanjing, China

**Ping Zheng**, Fudan University, Shanghai, China

**Jiang-Ning Zhou**, University of Science and Technology of China, Hefei, China

**Jiawei Zhou**, Center for Excellence in Brain Science and Intelligence Technology, CAS, Shanghai, China

**Jingning Zhu**, Nanjing University, Nanjing, China





Impact Factor

5.271

2021 Journal Citation Reports: Q2  
(CLARIVATE ANALYTICS, 2022)

---

NEUROSCIENCE BULLETIN 神经科学通报 (Monthly)

Vol. 38 No. 7 July 15, 2022

---

**Administrated by:** Chinese Academy of Sciences

**Sponsored by:** Center for Excellence in Brain Science and Intelligence Technology, Chinese Academy of Sciences  
Chinese Neuroscience Society

**Editors-in-Chief:** Shunmin Duan, Ru-Rong Ji

**Edited by:** Editorial Board of *Neuroscience Bulletin*

319 Yueyang Road, Building 8, Room 612, Shanghai 200031, China

Phone: +86-21-64032273; 64170853; 64032696

E-mail: nsb@ion.ac.cn; <http://www.neurosci.cn>

**Editors:** Bin Wei, Fei Dong, Ting Lyu

**Published by:** Center for Excellence in Brain Science and Intelligence Technology, Chinese Academy of Sciences

**Printed by:** Shanghai Shengtong Times Printing Co., Ltd (A6, No. 2888, Caolang Highway, Jinshan District, Shanghai)

**Overseas Distributed by:** Springer Nature

**Home Distributed by:** Local Post Offices

---

ISSN 1673-7067

CN 31-1975/R

Post Office Code Number: 4-608

Permit of Ad. Number: 3100420130051

Price: ¥ 100.00

ISSN 1673-7067





# 奥林巴斯神经科学显微成像方案

1

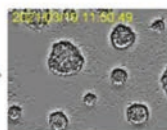
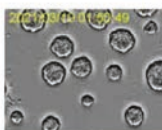
样本制备



## CM20 神经干细胞培养监控系统

适用于仪器设备的高品质光学组件

- 精确控制接种细胞数量
- 培养过程中实时观察3D培养细胞形态的变化
- 优化培养条件，精确的质量控制
- 评估实验流程节点



NSC sphere Conditions Vessel: 12 well Interval time: 1 H Measurement period: 6 Days



NSC sphere 视频



CM20 应用资料

2

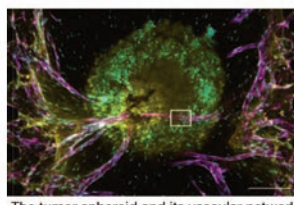
成像

完美平衡



## FV3000 激光扫描共聚焦显微镜

- TruSpectral全真光谱检测
- GaAsP高灵敏检测器
- Resonant Scanner高速成像



The tumor spheroid and its vascular network.



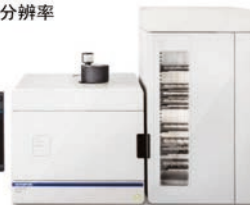
FV3000 应用资料

高通量 大视野

## VS200

全玻片成像系统

- 高速度、高通量、高效率
- 全自动、简单、智能
- 高倍镜成像、高分辨率
- 五种观察方式



深层成像

## FVMPE-RS

双光子显微成像系统

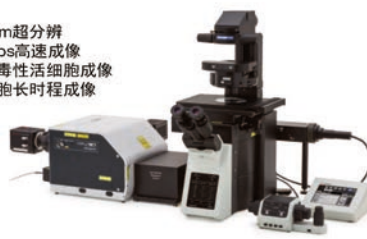


- 成像深度可达8mm
- Resonant Scanner高速成像
- 双IR激光+4通道双光子检测

超分辨

## IXplore SpinSR

转盘共聚焦高分辨成像系统

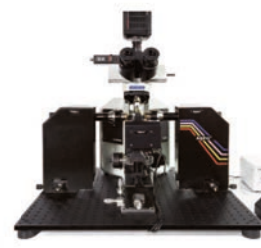


- 110nm超分辨
- 200fps高速成像
- 低光毒性活细胞成像
- 活细胞长时程成像

高速度

## Alpha<sup>3</sup>

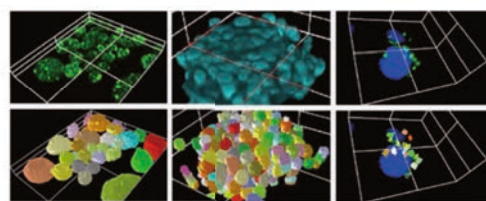
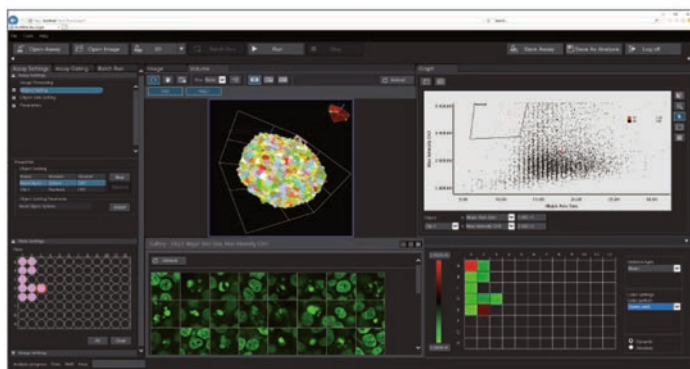
光片显微成像系统



3

分析

## NoviSight 专业三维分析软件



3D细胞分析软件，可对z序列图像进行统计分析，包括自动细胞识别、分割与计数。并对标本的体积、表面积、长度等形态学参数及荧光强度进行定量统计分析。



1

样本制备

2

成像

3

分析